The Dissertation Committee for Jae-Won Choi Certifies that this is the approved version of the following dissertation:

Modeling and Model Based Fault Diagnosis of Dry Vacuum Pumps in the Semiconductor Industry

Committee:

Michael D. Bryant, Supervisor

Matthew J. Hall

Dragan Djurdjanovic

Benito R. Fernandez

Steve Poole

Modeling and Model Based Fault Diagnosis of Dry Vacuum Pumps in the Semiconductor Industry

by

Jae-Won Choi, B.E.; M.S.

Dissertation

Presented to the Faculty of the Graduate School of

The University of Texas at Austin

in Partial Fulfillment

of the Requirements

for the Degree of

Doctor of Philosophy

The University of Texas at Austin

December 2013

Dedication

I dedicate this dissertation to my family who has supported me in many ways and showed great patience during my prolonged graduate studies far away from home. I feel a special gratitude to my mother whose words of encouragement ring in my ears.

Acknowledgements

I have received supports and encouragements from many teachers and friends during my graduate studies abroad, and I am really grateful for their invaluable advice and words of encouragement. I can't list all but I feel a special gratitude towards my supervisor, Prof. Michael D. Bryant who has given me thoughtful suggestions, academic reviews and words of wisdom and encouragements. I am also thankful to Prof. Glenn Masada for TA opportunities to teach Mechatronics Lab, and words of encouragement to navigate my prolonged Ph.D. study at UT. I thank Prof. Benito Fernandez and Prof. Dragan Djurdjanovic for academic stimulation and mentorship which improved my creativity and extended my understanding on Dynamics, Control and Fault Diagnosis.

Modeling and Model Based Fault Diagnosis of Dry Vacuum Pumps in the Semiconductor Industry

Publication No._____

Jae-Won Choi, Ph.D.

The University of Texas at Austin, 2013

Supervisor: Michael D. Bryant

Vacuum technology is ubiquitous in the high tech industries and scientific endeavors. Since vacuum pumps are critical to operation, semiconductor manufacturers desire reliable operations, ability to schedule downtime, and less costly maintenance services. To better cope with difficult maintenance issues, interests in novel fault diagnosis techniques are growing.

This study concerns model based fault diagnosis and isolation (MB-FDI) of dry vacuum pumps in the semiconductor industry. Faults alter normal operation of a vacuum pump resulting in performance deviations, discovered by measurements. Simulations using an appropriate mathematical model with suitably chosen parameters can mimic faulty behavior.

This research focuses on the construction of a detailed multi-stage dry vacuum pump model for MB-FDI, and the development of a simple and efficient FDI method to analyze common incipient faults such as particulate deposition and gas leak inside the pump. The pump model features 0-D thermo-fluid dynamics, scalable geometric

representations of Roots blower, claw pumps and inter-stage port interfaces, a unified pipe model seamlessly connecting from free molecular to turbulent regimes, sophisticated internal leakage model considering true pump geometry and tribological aspects, and systematic assembly of a multi-stage configuration using single stage pump models. Design of a simple FDI technique for the dry vacuum pump includes staged fault simulations using faulty pump models, parametric study of faulty pump behaviors, and design of a health indicator based on classification.

The main research contributions include the developments of an accurate multi-stage dry pump model with many features not found in existing pump models, and the design of a simple MB-FDI technique to detect and isolate the common faults found in dry vacuum pumps. The proposed dry pump model can pave the way for the future development of advanced MB-FDI methods, also performance improvement of existing dry vacuum pumps. The proposed fault classification charts can serve as a quick guideline for vacuum pump manufactures to isolate roots causes from faulty symptoms.

Table of Contents

List of Tables

List of Figures

Chapter 1: Introduction

1.1 INTRODUCTION

1.1.1 Model Based Fault Diagnosis of Dry Vacuum Pump

Vacuum technology is ubiquitous in the high tech industries and scientific endeavors. Semiconductor fabrication uses state-of-art dry vacuum pumps to pump down reaction chambers and eject harsh chemicals and particulates produced as bi-products. Since vacuum pumps are critical to operation, semiconductor manufacturers desire reliable operations, ability to schedule downtime, and less costly maintenance services.

To better cope with difficult maintenance issues, interests in novel fault diagnosis techniques are growing. A model based approach can tackle this problem effectively by using an accurate mathematical model to predict system's faulty behavior. Model Based Fault Detection & Isolation (MB-FDI) assesses machine health by comparing measurements with signals and fault features obtained from a model, to determine the root causes of a machine failure.

This study concerns MB-FDI of a multi-stage dry vacuum pump for semiconductor fabrication. Faults alter normal operation of a vacuum pump resulting in performance deviations such as pressure and temperature errors. These errors, discovered by measurements, can be mimicked by simulations using an appropriate mathematical model with suitably chosen parameters and parameter values. Here model parameters that deviate from nominal values can provide information about machine health. This research focuses on the construction of an accurate dry vacuum pump model, and the development of a simple FDI method to link machine health to model parameter space.

1.1.2 Vacuum Pumps in Semiconductor Fabrication

Semiconductor fabrication is a multi-step manufacturing process to create integrated circuits and micro-electronic devices. The dry vacuum pump is a key part of fabrication techniques such as ion implantation, dry etching, and chemical and physical vapor depositions, among others.

Modern semiconductor fabrication involves hundreds of micro-processes. Semiconductor manufacturing is typically automated to reduce risk of operator exposure to poisonous substances, avoid wafer contamination, and improve overall yields. Figure 1.1 depicts semiconductor manufacturing equipment, including a cassette loading station, a load lock chamber, a transfer chamber and multiple reactors (a.k.a. process chambers).

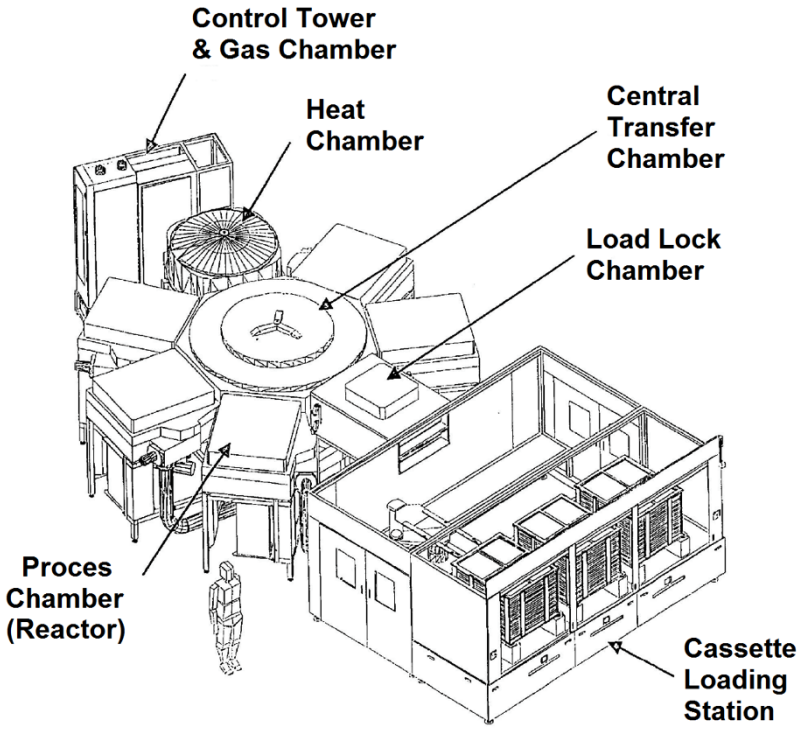

Figure 1.1: Fully Automatic Semiconductor Manufacturing Equipment [1].

A load lock chamber and reactors are connected via a polygon-shaped transfer chamber. Wafer transfer robots carry wafers between a cassette loading station at atmospheric pressure to process chambers in various vacuum environments [2]. The load lock chamber and the transfer chamber serve as an intermediate pressure buffer. Each intermediate chamber requires a vacuum pump. Each reactor requires its own vacuum environment, with vacuum pumps that meet pressure and pumping speed requirements [3]. The entire batch processing unit, including process chambers, delivery robots, cassette module, and vacuum pumps is known as cluster tools.

Performance requirements of dry vacuum pumps in the cluster tool chain are demanding [1,2]. With every new wafer installed, a high flow vacuum pump quickly pumps down the load lock chamber to equalize pressure to the transfer chamber's pressure. The transfer chamber must be evacuated before the door of a process chamber can open. After closing the door, another pump quickly evacuates the process chamber to a pressure level for a specific fabrication process. The pump then continues to pump out harsh chemicals and particulates commonly used in the deposition and etching processes. For the case of a thin film deposition process, the whole process requires multiple short treatments to achieve high film quality and uniform firm thickness. For a higher productivity, semiconductor manufacturers attach more reactors per transfer chamber, which results in a larger transfer chamber with a longer pump-down time [2]. Consequently, the likelihood of malfunction or underperformance among cluster tools can increase dramatically.

1.1.3 Overview of a Dry Vacuum Pump System

The dry vacuum pump is most common in semiconductor fabs due to oil-free operation. Semiconductor industries typically use a multi-stage configuration with four or more single-stage pumps assembled in series to achieve high vacuum [4]. A Roots blower

and claw vacuum pump is typical for a single stage. Figure 1.2 shows rotors of the Roots blower and claw pump. Roots blowers with twin lobe rotors produce the highest volumetric flow. Claw pumps with twin claw rotors have high efficiency.

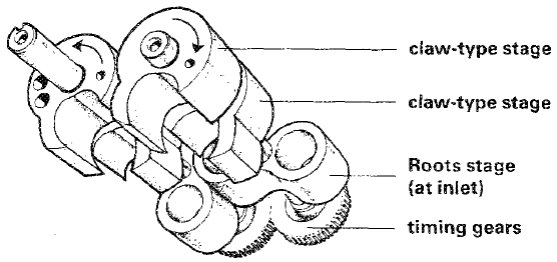

Figure 1.2: Typical Rotors in Dry Vacuum Pump in the Semiconductor Industry [5].

A multi-stage dry vacuum pump consists of individual stages including a stator component, twin rotors, and miscellaneous parts such a rubber gasket. The stator component has cavities that accommodates twin intermeshing rotors, and has intake and discharge ports cut in its side walls. The first stage inlet connects to a main suction pipe that runs to a main vacuum chamber. The first outlet port internally connects to a second stage inlet port, and the other ports internally connect in series in a similar manner. The last stage outlet connects to an exhaust pipe. The rotors attach to twin cast iron shafts, which run through all the stages and the gearbox. The shafts are supported by ball or roller bearings with gas seals at both ends. The stacked stator components are secured by long bolts and nuts on all the sides of the assembly. The pump body typically mounts on a vibration absorbing framework.

Figure 1.3 shows a cut-off view of a typical four stage dry vacuum pump to be studied in this research. The first stage is a Roots blower (a.k.a. lobe-type blower), and the second to fourth stages are claw-type pumps. The rotor type of the Roots blower is a

bi-lobe rotor and the claw rotor is of Northey type. A gear box is between the low vacuum stage and a motor. Gas enters from the top of the high vacuum stage, passes through the inner cavities and internal ports, and exits the low vacuum stage via the outlet where the main discharge port is located.

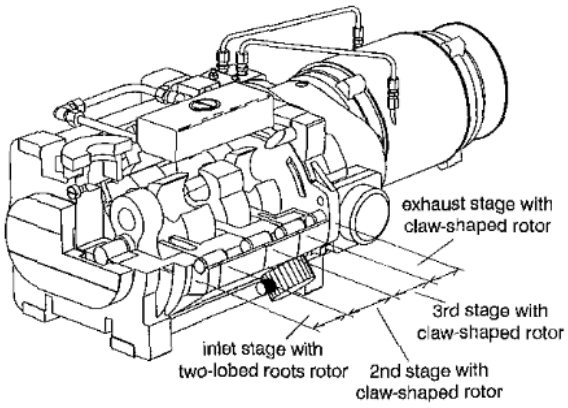

Figure 1.3: Cut-away View of a Typical Dry Pump Used in the Semiconductor Industry [6].

Pumping action occurs in any internal cavities enclosed by twin intermeshing rotors and the inner stator wall. Pumping chambers are empty spaces inside the cavities. The Roots blower has open inlet and outlet ports located at radially opposite sides. Figure 1.3 has the inlet port on the top and the outlet port concealed at the bottom. Port interfaces of claw-type pumps are areas carved into the stator side walls. Ports open and close depending on rotor position. For the port interface of Fig. 1.4, the side surfaces of interfacing rotors block the inter-stage port until the dedendum portion (not shown in the figure) of a rotor profile, overlaps and exposes the port aperture. The use of anti-symmetric interfacing rotors results in a rotor angle phase shift between opening the inlet

and outlet ports, when each rotor's dedendum portion passes over and opens (unblocks) the port aperture.

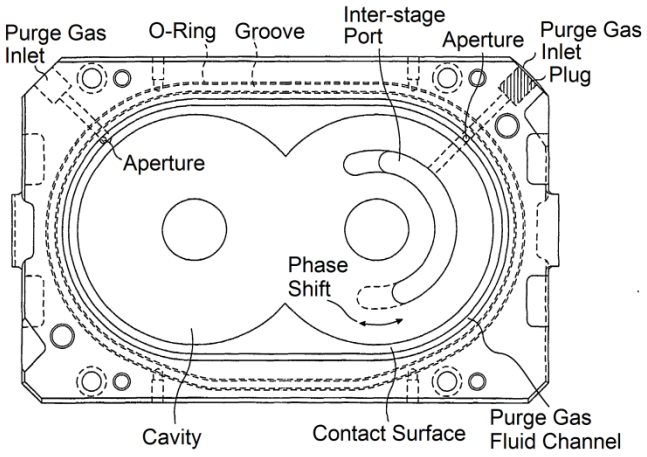

Figure 1.4: The Port Interface of a Claw Pump of Edwards BOC Corp. [7].

Internal leakage greatly compromises performance of dry vacuum pumps. Manufacturers limit air gaps between rotors and stator walls to within a few thousandths of an inch. To avoid bearing seizure, labyrinth and lip type seals prevent corrosive gasses from seeping into the lubrication chambers, and the lubrication chamber is pressurized using a purge gas such as Nitrogen or inert gases as a buffer. The gas seals are made of polytetrafluoroethylene (PTFE) with outstanding properties for high vacuum applications. High vacuum side bearings are packed with perfluoropolyether (PFPE) grease. A purge gas can escape into an intake chamber (especially at the first stage pump), which results in poor pumping efficiency.

The rotor shafts supported by ball or roller bearings are synchronized via a one to one ratio gear box. The bearings and gears are oil lubricated using a splash mechanism in

the gearbox. Typical hydrocarbon based oils in the gear box are susceptible to corrosive gas leakage and heat, which can cause gear box failure.

A rigid and efficient induction motor often drives the gearbox. Typical motor power for a medium sized dry vacuum pump is 4 to 6 kW. The operating speed, which varies from 1000 to 4500 rpm with a frequency converter, is fixed at around 3600 rpm or 3000 rpm using the power outlet [4(p.309)]. The induction motor has a steep torque speed curve at the operating point, and dry vacuum pumps for semiconductor manufacturing tend to have a more powerful motor than needed to prevent rotor seizure. Consequently, the rotational speed of a dry vacuum pump can be assumed constant under various operating conditions.

Heat is generated via cyclic compressions and expansions of pumping chambers, electrical losses in the motor, and friction in bearings and gearbox. The multi-staged dry vacuum pump in Fig. 1.3 is equipped with a hybrid cooling system. Since fans are not permitted in clean rooms, the first to third stages are air-cooled by natural convection and radiation. The gear box and the fourth stage pump actively circulate coolant through a cooling coil embedded in the pump body, and a thermostat maintains the pump body temperature. The primary coolant is cooled by a secondary cooling unit, which also removes heat from the electrical motor via a cooling jacket that covers the motor. The secondary unit connects to water pipelines.

Pump performance is gauged by a throughput defined as the product of a pressure and a pumping speed at the pump inlet. Figure 1.5 shows typical pumping speed curves of a popular multi-stage dry vacuum pump for motor speeds of 60Hz and 50Hz. The pumping speed is relatively constant over a wide vacuum range, then dramatically decreases at high vacuum. From atmospheric pressure to a rough vacuum, a vacuum pump operates efficiently. As the inlet pressure decreases, the pressure difference

between intake and exhaust pumping chambers grows, which increases internal leakage and reduces efficiency. Atmospheric pressure can push exhaust back into the pump, called back-streaming. In a high vacuum, outgassing by evaporation and sublimation from structural components also degrades performance. The ultimate inlet pressure is determined by internal leakage, back-streaming, outgassing, and pump speed.

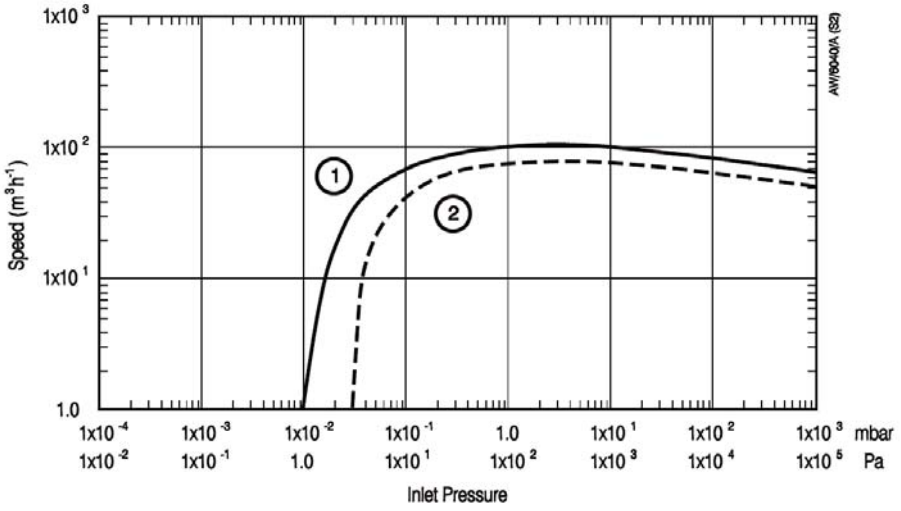

Figure 1.5: Pumping Speed Curve of a Typical Dry Vacuum Pump [8(p.2-9)].

1.2. DESCRIPTION OF PROBLEM

Dry vacuum pumps are susceptible to bearing and gear failure, rotor seizure, port blockage, and vacuum leakage, among others [9-13]. Primary causes are gas leaks and unwanted particulate deposition inside the pump [11,13]. About 30% of the injected particulates settle on the wafer surface; the vacuum pump must evacuate the rest to avoid contaminating the reactor walls. Higher performance specifications push safety margins. Failure or underperformance of a single dry vacuum pump can halt an entire

semiconductor batch process. Financial loss can far exceed pump repair cost. Early fault diagnosis and isolation (FDI) that enable scheduled maintenance can minimize losses.

Despite importance, little literature is found on health assessment of dry vacuum pumps. Most existing techniques are signal based, which often lack the holistic diagnosis of a pump malfunction. Model based FDI with accurate mathematical models can better capture the multi-physical nature of a vacuum pump system. However, existing models are deficient. Overlooked are geometric aspects of a multi-stage dry vacuum pump, and crucial dynamics of internal leakages and inter-stage flows. A detailed dry vacuum pump model would benefit understanding, and development of a health monitoring system.

The proposed FDI technique deduces machine health from machine parameters estimated by comparing model outputs to measurements. Conventionally utilized are parameter estimation (PE) techniques, such as Extended Kalman Filter (EKF) [14], Unscented Kalman Filter (UKF) [15] and Particle Filter (PF) [15,16]. The thermo-fluidic models of a dry vacuum pump are highly nonlinear. Conventional PE methods are hard to apply for highly nonlinear systems due to numerical stability [17], inefficiency [15] or structural observability issues [18]. Alternative schemes include Bayes classifier and Artificial Neural Network (ANN) [19].

1.3. LITERATURE REVIEW

1.3.1 Signal Based versus Model Based FDI

Key to fault diagnosis and isolation (FDI) are fault features sensitive enough to discriminate fault types, yet robust enough to produce consistent results. FDI techniques classify into signal based (SB-) and model based (MB-) methods [20]. Signal based methods identify dissimilarities in health indicators extracted from measurements, often without considering how different parts of a diagnosed system interact. For example,

vibration accelerometer measurements and analysis can isolate frequency components associated with specific faults, but inputs and loading conditions are not considered. MB-FDI considers all relevant details to yield a model with more realistic behavior. A model can be data driven and/or based on first principles. A data driven black box model has structure and parameters a priori unknown. After training, the resulting model is accurate within the scope of the measured training data, but usually not universally applicable. The latter approach results in a white box model, which links physical parameter space to the holistic behavior of a machine. Model fidelity depends on model sophistication: a detailed model is more desirable for a white box model based FDI. A grey box model is a white box model with a few unknown parameters, which requires parameter estimation (PE). Typical PE based FDI employs Kalman filtering and its variants.

1.3.2 FDI Methods for Dry Vacuum Pump

The Roots and claw rotor type dry vacuum pump has dominated markets since the late 1980's thanks to stringent ultra-cleanness requirements [9]. A 1991 maintenance related paper [12], based on six years' field experience, suggested "monitoring of key parameters to enable preventive maintenance". Later Abreu et al. [15] analyzed the abnormal chemical deposition caused by Richardson's annular effect, where cyclic exhaust pressure helped back-migration of rich oxygen through piping, and eventually led to unwanted chemical reaction on the wall.

Konishi and Yamasawa [7] found that the solid deposits in the sweep volumes caused abnormal rotational resistances and changed motor currents. They proposed In-Service-Life (ISL) predictor based on an ARMAX model tuned with motor current measurements and inlet valve opening levels. Results showed some success, but failed to produce consistent outcomes, often due to unstable time-varying and oscillating prediction values.

Twiddle et al. [21] proposed power ratio (PR) of an autoregressive (AR) model tuned with exhaust pressure measurements for the exhaust blockage fault. The ratio of the first to second harmonics PR_{12} via autoregressive spectrum analysis was used to evaluate free space in an exhaust pipe. Later Twiddle et al. [22] added a neuro-fuzzy classifier trained with PR_{12}, PR_{13}, and pump body temperature as inputs, and motor currents and exhaust pressure as outputs, to detect health conditions of normal, exhaust blockage (SB), and mechanical inefficiency (MI). Results successfully detected 8% MI and 29% SB.

Jiang et al. [23] proposed a SB-FDI method for ball bearing defects in a dry vacuum pump. Vibration measurements were processed with a novel wavelet clustered bandpass filter and Hilbert transformation, then fitted to an AR model for spectral analysis to isolate bearing fault frequencies. Thanagasundram et al's [24] AR model based on vibration signatures used a pole trajectory of an AR model in polar plots. A common problem is that the health indicator based on SB-FDI often lacks procedural consistency. For example, ref. [23] chose a 60^{th} order AR model, yet ref. [24] used a 10^{th} order model based on trial and error. Since the model order is critical, each solution can be considered too specific to its own applications.

Floquet et al.'s [25] grey box FDI employed a simple cooling model and a second order sliding mode observer (SO-SMO) to estimate coolant flow rate, convection coefficient of coolant, and heat generation. However, effects of pumping action on the thermal model were little discussed. Also, designing a SO-SMO requires significant hand calculations, especially for a highly nonlinear model with a large parameter set.

1.3.3 Modeling of Dry Vacuum Pump System

Dry vacuum pump modeling involves mechanical, thermo-fluid and electrical domains. A powerful motor with low speed operation, simple internal construction, and sturdy rotor and shaft allow neglect of rotor and motor dynamics. Most vacuum pump

models focus on thermo-fluid modeling, rarefied gas dynamics, and fluid dynamics in pipe flows. Geometric aspects were little considered, and pump rotor profiles were studied separately. Summarized below is the existing literature of dry vacuum pump modeling.

A simplified reversible adiabatic thermodynamic model [26,27] commonly describes the gas dynamics of pumping chambers within a dry vacuum pump. The first law [28] applied to an insulated chamber volume treated as an open system results in

$$\dot{P} = \frac{\gamma}{V}\left(-P\dot{V} + \dot{m}_{in}RT_{in} - \dot{m}_{out}RT_{out}\right),\ T = \frac{PV}{mR}. \qquad (1.1a,1.1b)$$

Here P, V and T are chamber pressure, volume and temperature; $\gamma = c_p / c_v$ where c_p and c_v are specific heats at constant pressure and volume; $\dot{m}$ is mass flow rate; subscripts refer to input and output, and R is the gas constant. Note that the internal energy of the gas is mc_vT and $c_v = mR / (\gamma - 1)$. The second equation is the ideal gas law. The rate of volume change $\dot{V}$ is specified by the shape of the pumping chamber due to the rotational speeds of the claw and lobe rotors. Inter-stage flows are based on an empirical approximation.

Ref. [26] discussed systematic modeling of a multi-stage claw vacuum pump model. Ref. [29] improved the dry vacuum pump model in [26] to model a multi-stage Roots-claw dry vacuum pump using various sub-modules via a graphic user interface (GUI) tool. However, both of the references provided little details of the vacuum pump models.

Floquet et al.'s [25] simple cooling model considered heat conduction among the electric motor, gearbox, and pump body to the coolant (each element was treated as a bulk mass) and heat convection from the pump body surfaces to the ambient air. Heat transfer to the swept air was ignored because of an inconsequential mass flow rate of air

and the adiabatic assumption. A heat transfer balance applied to the pump body and coolant within the pump gives, respectively

$$m_b C_b \dot{T}_b = P_{elec} - \dot{m}_c C_c \left(T_o - T_i\right) - h_b A_b \left(T_b - T_a\right), \tag{1.2a}$$

$$m_c C_c \dot{T}_o = \dot{m}_c C_c \left(T_o - T_b\right) + h_c A_c \left(T_b - T_o\right). \tag{1.2b}$$

Here subscripts *b*, *c*, *o* and *i* stand for body, coolant, outlet, and inlet; *C* is heat capacity; $\dot{m}$ is mass flow rate; *T* is temperature; *h* is heat convection coefficient, *A* is effective area for heat convection; and P_{elec} is the electrical input power.

Mcdougald et al. [30] studied volumetric efficiency of the Roots blower with involute rotors under atmospheric operation, based on static thermodynamic properties. Ucer and Celik [31] improved the geometry of this model and added dynamics including leakage based on an isentropic nozzle. But few details were provided.

For rotor design, Tong and Yang [32] synthesized a rotor profile given a volumetric flow rate using a deviation function. However, the method, geared towards design of general rotor shapes, resulted in complicated formulas. Joshi et al. [33] analyzed the internal leakage flow of a Roots blower using CFD under stationary operation. Hseih and Wang [34] proposed a design method for twin lobe rotors with variable trochoids. Later Hseih [35] presented the geometric study of a cycloidal claw rotor and volumetric efficiency.

1.4. RESEARCH OBJECTIVES

The objectives of this dissertation's research is to build a detailed dry vacuum pump model for fault diagnosis and isolation (FDI), and develop a simple and efficient FDI method to analyze incipient faults such as particulate deposition and gas leak inside the pump. The research includes:

1. Modeling a detailed dry vacuum pump for model-based FDI including

   a. Geometric study of a Roots blower

   b. Geometric study of a claw pump

   c. Geometric study of an inter-stage port interface of a claw pump

   d. Design of a viscous flow model in turbulent, transitional and laminar regimes

   e. Design of a molecular flow model

   f. Study of a choked flow model

   g. Unified modeling of the above flow models for pipes and internal passages

   h. Modeling internal leakage considering geometrical and tribological aspects of the above vacuum pumps models, and viscous and molecular flows models

   i. Derivation of governing dynamics based on thermodynamics and the above flow models

   j. Systematic assembly of a multi-stage configuration using single stage pump models

2. Design of a simple fault diagnosis and isolation technique for the dry vacuum pump, including

   a. Study of common vacuum pump faults and design of faulty pump models with faulty model parameters

   b. Staged fault simulation using the faulty pump model

   c. Study of the relation between parameter space and physical faults

   d. Design of a health indicator based on classification

1.5. RESEARCH CONTRIBUTIONS

Main contributions of this research include

1. Development of detailed dimensionless geometric models of the Roots blower, claw pump and the port interfaces of a multi-stage dry vacuum pump tailored for numerical simulations
2. Construction of complete internal flow models for all three viscous regimes (turbulent, transitional and laminar flows) and the molecular regime, including choking criteria.
3. Design of detailed internal leakage models for the Roots blower and claw pump
4. Systematic construction of the multi-stage dry vacuum pump using single stage pumps
5. Simulation of the detailed vacuum pump model including faults
6. Development of a model based health indicator for the dry vacuum pump based on linear classification in parameter space

1.6. DISSERTATION ORGANIZATION

Chapter 1 overviewed dry vacuum pump in semiconductor fabrication, reviewed literature on FDI of dry vacuum pump and provided motivation for better MB-FDI. Chapter 2 will review relevant thermo-fluid equations for a rarefied flow, constitutive formulas of vacuum system, also unify the internal pipe flow model and provide a novel flow choking criteria. Chapter 3 will model a 4 stage dry vacuum pump with the first stage Roots blower and the second to fourth stage claw pumps. Sections in Ch. 3 will build dimensionless pump geometry equations in detail, formulate gas mixing and gas to wall heat transfer, model internal leakages based on geometry and tribology, and study port interfaces and connecting pipes. Chapter 4 will summary equations relevant for simulation, address numerical solution technique, provide baseline simulation results, explore design space to tune a dry vacuum pump model, and validate a tuned dry vacuum

pump model with respect to manufacturer's data. Chapter 5 will simulate faulty models and propose a simple FDI method. Chapter 6 will conclude this work.

Chapter 2: Preliminaries

2.1 THROUGHPUT AND CONDUCTANCE

Pump throughput Q [W], which describes vacuum pump performance, is the product of pump inlet pressure P_p [Pa] and pumping speed S_p [m^3s^{-1}]:

$$Q = P_p S_p . \tag{2.1}$$

Pumping speed is the effective carry-away volume per unit time. The transport rate of molecules $\dot{N}$ at an imaginary cross section is the product of pumping speed S and the molecular volumetric density n_V at the cross section:

$$\dot{N} = S \cdot n_V \text{ where } n_V \equiv N/V . \tag{2.2, 2.3}$$

Here N is number of molecules. Assuming no energy accumulation and no gas leak, the transport rates at inlet and outlet are equal, and

$$\dot{N} = S_i \cdot n_{Vi} = S_o \cdot n_{Vo} \tag{2.4}$$

where n_{Vi} and n_{Vo} are densities at inlet and outlet, respectively.

Conductance measures ease of flow through a gas passage. The molecular transport rate is related to conductance as

$$\dot{N} = C \cdot \left(n_{Vi} - n_{Vo} \right). \tag{2.5}$$

Assuming a constant gas temperature, throughput Q [W] is related to the pressure drop P across a pipe and the pipe conductance C as

$$Q = P \cdot S = C \cdot (P_i - P_o) . \tag{2.6}$$

For a series gas passage, the molecular transport rate is same at all cross-sections, giving

$$\dot{N} = S_1 n_{V1} = \cdots = S_k n_{Vk} . \tag{2.7}$$

Here $\dot{N}_j = S_j n_{Vj}$ is the transport rate at the j^{th} cross-section, and k is the number of pressure nodes in a series pipe. Making an analogy between gas flow and electrical current, the conductance is equivalent to the reciprocal of a resistance. Therefore, the total conductance of a series passage is the sum of the reciprocals of the sectional conductances

$$\frac{1}{C} = \sum_{i=1}^{k-1} \frac{1}{C_i}. \tag{2.8}$$

Similarly, the total conductance of a parallel passage is

$$C = C_1 + C_2 + \cdots + C_k = \sum_{i=1}^{k} C_i \ . \tag{2.9}$$

2.2 PRESSURE AND TEMPERATURE DYNAMICS EQUATIONS

For a pumping chamber with flows in and out, variable volume V and temperature T via the first law, pressure and temperature dynamics [4,36] for P and T can be formulated similar to Eq. 1.1a of section 1.3.3, giving

$$\dot{P} = \frac{1}{V}\left[(\gamma - 1)\dot{Q}_H - \gamma P\dot{V} + \sum \gamma Q_i - \sum \gamma Q_o\right]. \tag{2.10}$$

Invoking the ideal gas law,

$$\dot{T} = (\gamma - 1)\frac{\dot{Q}_H T}{PV} - (\gamma - 1)\frac{\dot{V}T}{V} + \sum \frac{Q_i}{PV} T\left(\gamma - \frac{T}{T_i}\right) - \sum \frac{Q_o}{PV} T\left(\gamma - \frac{T}{T_o}\right). \tag{2.11}$$

Here γ (= c_p / c_v) is the specific heat ratio, $\dot{Q}_H$ is the heat power transferred across the control volume, subscripts i and o stand for inlet and outlet, Q is throughput, $Q_i/T_i = \dot{m}_i R$, $Q_o/T_o = \dot{m}_o R$, m is mass, and the second term in the influx and efflux summations came from the $\dot{m}T/m$ term in the derivative of internal energy. The RHS terms of the above equations relate to heat transfer, dynamics, influx, and efflux.

Assuming a main vacuum chamber has no heat transfer, fixed volume V_c, one outlet to pump, and constant gas temperature T_p via temperature regulation, the pressure dynamics reduce to

$$\dot{P}_c = -\frac{Q_p}{V_c} = -\frac{S_p P_p}{V_c}, \tag{2.12}$$

where subscripts c and p represent vacuum chamber and pump, and S is the pumping speed.

2.3 GAS FLOWS IN A VACUUM SYSTEM

2.3.1 Fundamental Properties

Rarefied gas flows classify into molecular, intermediate and viscous flows in increasing pressure order. Molecular flow has the mean free path of gas molecules larger than the characteristic length of a container. Gas molecules move randomly and collisions with walls are much more probable. Viscous flow occurs at higher pressure with shorter mean free path and more common inter-molecular collisions. Gas molecules move collectively as continua of infinitesimal fluid parcels and Reynolds number divides flow into laminar, transitional and turbulent. Intermediate flow transitions from viscous to molecular flow, with mean free path in between and characteristics of both flows. Inter-molecular collisions have likelihood on the same order as wall-molecule collisions. Molecular and viscous flows can be described by the Maxwell wall slip model and the Knudsen equation, and among others.

Knudsen number measures the degree of gas rarefication as a ratio of the mean free path λ of a gas to a container dimension D:

$$Kn = \frac{\lambda}{D} = \frac{\pi}{4}\frac{\eta v_{avg}}{P D} = \frac{\pi}{4}\frac{\eta}{P D}\sqrt{\frac{8RT}{\pi}}. \tag{2.13}$$

Here v_{avg}, the mean velocity of gas molecules was replaced by a statistical mechanics equivalent, and η is the dynamic viscosity. Table 1.1 classifies gas flows based on Knudsen number and gas rarefication index $\delta = Kn^{-1}$. Criteria vary from author to author.

Type of flow	Roth's Text	Jousten's Text
Molecular flow	$\delta < 1$	$Kn > 0.5$
Intermediate flow	$1 < \delta < 110$	$0.5 > Kn > 0.01$
Viscous flow	$\delta > 110$	$Kn < 0.01$

Table 2.1: Criteria of Gas Flow [4,36].

For gases on a molecular scale, thermal conductivity (heat transfer per temperature gradient per area) is corrected by the energy accommodation coefficient α_E (EAC) between gas molecules and a wall. For two plates separated by a microscopic air gap,

$$\alpha_E = \frac{\alpha_{E1}}{2 - \alpha_{E1}} \text{ where } \alpha_{E1} \text{ is the EAC for single wall.} \tag{2.14}$$

Assuming a full energy accommodation, the net heat transfer between plates in the molecular regime [4(p.51)] is

$$\dot{Q}_{H,m} = -\frac{1}{8}\frac{P}{T} v_{avg} A_w \alpha_E \frac{\gamma + 1}{\gamma - 1} \Delta T, \tag{2.15}$$

where A_w is the wall area, T_w is the wall temperature, $\Delta T = T_{w2} - T_{w1}$, and γ is the specific heat ratio.

Fourier's heat conduction law with assumption of a constant temperature gradient in every microscopic layer and Eucken's thermal conductivity [4(p.56)]

$$k_H = \frac{9\gamma - 5}{4} \eta c_v, \tag{2.16}$$

(based on empirical data) results in heat transfer for a gas in the viscous regime [4(p.57)].

$$\dot{Q}_{H,v} = -\frac{9\gamma - 5}{4}\eta\, c_v\, A_w \frac{\Delta T}{\Delta y}. \tag{2.17}$$

Here ΔT is the temperature difference, $\Delta T/\Delta y$ is the temperature gradient, c_v is the constant volume heat, and η is the dynamic viscosity.

Assuming unity EAC, and simultaneous components of viscous and molecular heat transfer $\dot{Q}_{H,v}$ and $\dot{Q}_{H,m}$, this work proposes a heat transfer formula for the entire flow regime:

$$\dot{Q}_H = \begin{cases} \dot{Q}_{H,v}\left(P/P_{atm}\right)\sqrt{T/T_{atm}} + \dot{Q}_{H,m}\left(1 - P/P_{atm}\right) & for\ P/P_{atm} < 1 \\ \dot{Q}_{H,v}\left(P/P_{atm}\right)\sqrt{T/T_{atm}} & for\ P/P_{atm} \geq 1 \end{cases}, \tag{2.18}$$

where $\dot{Q}_{H,m} = -\frac{1}{8}\frac{P}{T} v_{avg} A_w \frac{\gamma + 1}{\gamma - 1}\Delta T$. (2.19)

Here $\left(P/P_{atm}\right)$ and $\left(1 - P/P_{atm}\right)$ link continuously viscous and molecular heat transfer powers, and $\sqrt{T/T_{atm}}$ compensates for the effects of molecular mobility on viscous heat transfer [26].

2.3.2 Throughput and Conductance of a Long Pipe

Throughput and conductance of a long pipe with constant cross-section will be summarized in this section [4(p.112), 36(p.74), 37(p.342)]. For laminar viscous flow through a circular pipe, integrating the Poiseuille equation derived from the Darcy-Weisbach law, and rearranging terms for throughput Q and conductance C renders

$$Q_{LCP,Poiseuille} = \frac{\pi D^4}{256\eta L}\left(P_1^2 - P_2^2\right) = \frac{\pi D^4}{128\eta L}\overline{P}\Delta P \ , \tag{2.20}$$

$$C_{LCP,Poiseuille} = \frac{Q_{LCP,Poiseuille}}{\Delta P} = \frac{\pi D^4}{256\eta L}\left(P_1 + P_2\right) = \frac{\pi D^4}{128\eta L}\overline{P}\,, \tag{2.21}$$

where P_1 and P_2 are upstream and downstream nodal pressures, $\overline{P} = (P_1 + P_2)/2$, $\Delta P = P_1 - P_2$, D is the pipe diameter, and L is the pipe length.

For molecular flow through the long pipe, multiplying the net molecular transport rate by the Boltzmann constant k_B and the influx temperature T_1 and considering Smoluchowski's transmission probability ($P_{tr,LP} = 4D/3L$) yields the throughput and conductance

$$Q_{LCP,molecular} = \frac{\pi D^3}{12L} v_{avg} (P_1 - P_2), \tag{2.22}$$

$$C_{LCP,molecular} = \frac{\pi D^3}{12L} v_{avg}, \tag{2.23}$$

where $v_{avg} = \sqrt{8RT_1/\pi}$ is the average molecular speed.

Knudsen and Smoluchowski [4(p.134)] linked a laminar flow to a molecular flow using statistics and experiments, and produced the Knudsen equation for throughput in a long pipe with a constant cross sectional area:

$$\begin{aligned} Q_{Knudsen} &= C_{Knudsen} \Delta P = (C_{LP,Poiseuille} + C_{LP,molecular} \cdot Z) \Delta P \\ &= Q_{LP,Poiseuille} + Q_{LP,molecular} \cdot Z \end{aligned}. \tag{2.24}$$

$$\text{Here } Z = \left[1 + \sqrt{\frac{8}{\pi}} \frac{\overline{P}D}{v_{avg}\eta}\right] \left[1 + \frac{21}{17}\sqrt{\frac{8}{\pi}} \frac{\overline{P}D}{v_{avg}\eta}\right]^{-1}, \tag{2.25}$$

where $\overline{P} = (P_1 + P_2)/2$.

In terms of Knudsen number and rarefication index [4(p.150)]

$$Z = \left[1 + \sqrt{\frac{\pi}{2}} \frac{1}{Kn}\right] \left[1 + \frac{21}{17}\sqrt{\frac{\pi}{2}} \frac{1}{Kn}\right]^{-1} = \left[1 + \sqrt{\frac{\pi}{2}}\,\delta\right] \left[1 + \frac{21}{17}\sqrt{\frac{\pi}{2}}\delta\right]^{-1}. \tag{2.26}$$

For turbulent flow in a smooth pipe, integrating the Darcy-Weisbach equation with Blasius' friction factor ($f = 0.3164/\mathrm{Re}_D^{1/4}$) and rearranging gives [4(p.113)],

$$Q_{LCP,\,Blasius} = \frac{\pi}{4}\left(\frac{1}{0.3164}\right)^{4/7}\left(\frac{\pi}{8}\right)^{3/7}\frac{D^{19/7}v_{avg}^{6/7}}{\eta^{1/7}}\left(\frac{P_1^2 - P_2^2}{L}\right)^{4/7} \tag{2.27}$$

where the average molecular speed is $v_{avg} = \sqrt{8RT_1/\pi}$. The conductance of a smooth long circular pipe for turbulent flow is

$$C_{LCP,Blasius} = \frac{Q_{LCP,\,Blasius}}{P_1 - P_2} = \frac{\pi}{4}\left(\frac{1}{0.3164}\right)^{4/7}\left(\frac{\pi}{8}\right)^{3/7}\frac{D^{19/7}v_{avg}^{6/7}}{\eta^{1/7}}\frac{(P_1+P_2)^{4/7}(P_1-P_2)^{-3/7}}{L^{4/7}}. \tag{2.28}$$

For turbulent flow in a rough surface pipe, lack of a theoretical Darcy friction formula necessitates empirical data such as Moody's chart. Because Colebrook's formula requires numerical iterations, Haaland's equation, explicit and accurate within 2 percent [37(p.348)], will be used to estimate the Darcy friction factor

$$f_{Haaland}\left(\mathrm{Re}_D, \frac{\varepsilon}{D}\right) = \left\{-1.8\log_{10}\left[\frac{6.9}{\mathrm{Re}_D} + \left(\frac{\varepsilon/D}{3.7}\right)^{1.11}\right]\right\}^{-2}, \tag{2.29}$$

where Reynolds number $\mathrm{Re}_D = 4Q/(\pi D RT\eta)$ and the relative roughness ε/D involves the roughness centerline average ε. Assuming the Darcy friction factor is known, the Darcy-Weisbach equation in terms of throughput Q states

$$\frac{dP}{dL} = -\frac{f}{D}\frac{\rho V^2}{2} = -\frac{f}{2D}\frac{P}{RT}\left(\frac{4Q}{P\pi D^2}\right)^2. \tag{2.30}$$

Assuming a constant gas temperature and using the average throughput for the Darcy friction factor, integrating and rearranging the above equation gives

$$Q^2 f_{Haaland} = \frac{D}{L}RT\left(\frac{\pi\cdot D^2}{4}\right)^2\left(P_1^2 - P_2^2\right) = \frac{\pi^2 D^5}{8L}RT\,\overline{P}\Delta P. \tag{2.31}$$

Substituting into Haaland's formula Eq. (2.29), and rearranging produces

$$\frac{-1.8}{Q}\log_{10}\left[\frac{6.9\pi D R T \eta}{4Q}+\left(\frac{\varepsilon/D}{3.7}\right)^{1.11}\right]=\left[\sqrt{\frac{\pi^2 D^5}{8L}RT\,\overline{P}\Delta P}\right]^{-1}. \tag{2.32}$$

An exact solution for unknown Q of Eq. (2.32) is intractable, but a numerical solution that locally linearizes Eq. (2.29) in log-log based on the power law

$$\log_{10}\left(f_{Haaland}\right)=a\cdot\log_{10}\left(\mathrm{Re}_D\right)+\log_{10}(b) \tag{2.33}$$

can be computationally efficient. Given Blasius throughput $Q_{LCP,Blasius}$, a linearized range of Reynolds number $[R_{eD,l},\ R_{eD,u}]$ is defined with

$$\mathrm{Re}_{D,u}=\frac{4Q_{LCP,Blasius}}{\pi D R T \eta}\ \text{and}\ \mathrm{Re}_{D,l}=\max\left(4000, R_l\cdot\mathrm{Re}_{D,u}\right). \tag{2.34a, 2.34b}$$

Here $Q_{LCP,Blasius}$ overestimates real throughput because of smaller Darcy friction factor, and R_l is an arbitrary ratio to set the lower range limit. Parameters a and b are

$$a=\frac{\log_{10}\left(f_u\right)-\log_{10}\left(f_l\right)}{\log_{10}\left(\mathrm{Re}_{D,u}\right)-\log_{10}\left(\mathrm{Re}_{D,l}\right)}=\log_{10}\left(\frac{f_u}{f_l}\right)\left[\log_{10}\left(\frac{\mathrm{Re}_{D,u}}{R_{D,l}}\right)\right]^{-1}, \tag{2.35}$$

$$\log_{10}(b)=\log_{10}\left(f_l\right)-a\cdot\log_{10}\left(\mathrm{Re}_{D,l}\right), \tag{2.36}$$

where $f_u=f_{Haaland}\left(\mathrm{Re}_{D,u},\varepsilon/D\right)$ and $f_l=f_{Haaland}\left(\mathrm{Re}_{D,l},\varepsilon/D\right)$.

The estimated Darcy friction factor is

$$f_{turbulent}=f_l\cdot\left(\frac{\mathrm{Re}_D}{\mathrm{Re}_{D,l}}\right)^a=f_l\cdot\left(\frac{4Q}{\pi D R T \eta\,\mathrm{Re}_{D,l}}\right)^a. \tag{2.37}$$

Substituting the above friction factor into Eq. (2.31) and rearranging, the throughput and conductance for a turbulent flow in a rough surfaced pipe are

$$Q_{LCP,turbulent} = \left(\frac{1}{f_l} \frac{\pi^2 D^5}{8L} RT\,\overline{P}\Delta P \right)^{\frac{1}{2+a}} \cdot \left(\frac{\pi D R T \eta \,\mathrm{Re}_{D,l}}{4} \right)^{\frac{a}{2+a}}, \tag{2.38}$$

$$C_{LCP,turbulent} = \left(\frac{1}{f_l} \frac{\pi^2 D^5}{8L} RT\,\overline{P}\Delta P \right)^{\frac{1}{2+a}} \cdot \left(\frac{\pi D R T \eta \,\mathrm{Re}_{D,l}}{4} \right)^{\frac{a}{2+a}} \frac{1}{\Delta P}. \tag{2.39}$$

The transitional flow occurs at the intermediate Reynolds number defined in ($R_{eD,l}$, $R_{eD,u}$)=(2300, 4000). With lack of reliable empirical friction factor data at the intermediate Reynolds number [37(p.347)], this work proposes a similar linearized approach as for turbulent flow but with the equivalent friction factor based on Knudsen equation. The Darcy friction factor is approximated to

$$f_{transitional} = \frac{64}{2300} \cdot \left(\frac{\mathrm{Re}_{D,prev}}{2300} \right)^a = \frac{64}{2300} \cdot \left(\frac{1}{2300} \frac{4Q_{prev}}{\pi D R T \eta} \right)^a, \tag{2.40}$$

$$\text{where } a = \left[\log_{10}\left(\frac{2300}{64} \cdot f_{Haaland}\left(4000, \frac{\varepsilon}{D} \right) \right) \right] \left[\log_{10}\left(\frac{4000}{2300} \right) \right]^{-1}. \tag{2.41}$$

Throughput at the onset of transitional flow must match the Knudsen equation. Thus the lower limit of the Reynolds number is revised to

$$f_l = \left(1 + \frac{128}{3\pi} Kn \cdot Z \right)^{-1} \cdot \frac{64}{2300}, \tag{2.42}$$

and the linear fit model for a transitional flow becomes

$$f_{transitional} = f_l \cdot \left(\frac{1}{\mathrm{Re}_{D,lower}} \frac{4Q}{\pi D R T \eta} \right)^a, \tag{2.43}$$

$$\text{where } a = \left[\log_{10}\left(f_l \cdot f_{Haaland}\left(4000, \frac{\varepsilon}{D} \right) \right) \right] \left[\log_{10}\left(\frac{4000}{2300} \right) \right]^{-1}. \tag{2.44}$$

The difference is negligible in the upper viscous regime (i.e. $Kn < 0.01$), but grows as pressure decreases. Substituting the revised friction factor formula into Eq. (2.31) gives

$$Q_{LCP,transitional} = \left(\frac{1}{f_l} \frac{\pi^2 D^5}{8L} RT \overline{P} \Delta P \right)^{\frac{1}{2+a}} \cdot \left(\frac{\pi D R T \eta \mathrm{Re}_{D,l}}{4} \right)^{\frac{a}{2+a}}, \tag{2.45}$$

$$C_{LCP,transitional} = \left(\frac{1}{f_l} \frac{\pi^2 D^5}{8L} RT \overline{P} \Delta P \right)^{\frac{1}{2+a}} \cdot \left(\frac{\pi D R T \eta \mathrm{Re}_{D,l}}{4} \right)^{\frac{a}{2+a}} \frac{1}{\Delta P}. \tag{2.46}$$

2.3.3 Throughput and Conductance of Other Types of Gas Passages

Loss coefficient K_{minor}, which characterizes a gross head loss across a minor loss element such as a short pipe, orifice, or fitting, is typically constant regardless of gas rarefication, and estimates often vary because experimental conditions affect accuracy (White p. 369). Drawing an analogy with the long circular pipe model, the equivalent Darcy friction factor of a minor loss element is

$$f_{eq} = \frac{K_{minor} D}{L}, \tag{2.47}$$

where D is pipe diameter, and L is pipe length. Assuming an isothermal process, integrating the Darcy-Weisbach equation Eq.(2.30) with f_{eq} and rearranging gives throughput and conductance

$$Q_{minor} = \left(\frac{\pi D^2}{4} \right) \left(\frac{2RT_1}{K_{minor}} \frac{P_1^2 - P_2^2}{2} \right)^{1/2}, \tag{2.48}$$

$$C_{minor} = \frac{Q_{minor}}{P_1 - P_2} = \left(\frac{\pi D^2}{4} \right) \left(\frac{2RT}{K_{minor}} \frac{P_1 + P_2}{2(P_1 - P_2)} \right)^{1/2}. \tag{2.49}$$

where subscripts 1 and 2 denote upstream and downstream.

In the molecular regime, transmission probability of gas molecules dictates throughput and conductance and depends only on geometries of gas passage. Unity transmission probability of an aperture (i.e. $P_{tr,AP}$=1) implies that all influx molecules pass through. The molecular transport rate is proportional to the inlet cross sectional area A_c and inlet pressure P_1, assuming an isothermal process. Then throughput and conductance of an aperture are [4(p.129)]:

$$Q_{AP} = \frac{1}{4} v_{avg1} A_c \, P_1 \text{ , and } \quad C_{AP} = \frac{1}{4} v_{avg1} A_c \text{ ,} \tag{2.50, 2.51}$$

where v_{avg1} is the average molecular velocity of influx.

Formulas that do not depend on the outlet pressure are called intrinsic. Using the intrinsic transmission probability $P_{tr,intrinsic}$ and the throughput and conductance of an aperture (AP), general intrinsic throughput and conductance are

$$Q_{intrinsic} = P_{tr,intrinsic} \cdot Q_{AP} \text{, and } C_{intrinsic} = P_{tr,intrinsic} \cdot C_{AP} \text{ .} \tag{2.52, 2.53}$$

Intrinsic transmission probability only depends on pipe geometry. For a short pipe, the rate of molecules impinging the inner surface can be approximated to be half the impinging rate on the inlet cross sectional area. Assuming random collisions between gas molecules and the inner surface, half the gas molecules hitting the inner surface will move toward the inlet. The transmission probability of a short circular pipe (SCP) with diameter D and length L [4(p.134)] is

$$P_{tr,SCP} = 1 - \frac{A_i}{4A_c} = 1 - \frac{\pi DL}{4\pi D^2/4} = 1 - \frac{L}{D}, \tag{2.54}$$

where A_c and A_i are the cross sectional and inner areas.

The transmission probability of medium sized pipes can be approximated based on a modification of the long pipe solution [4(p.136)].

$$\frac{1}{P_{tr,MCP}} = \frac{1}{P_{tr,AP}} + \frac{1}{P_{tr,LCP}} = 1 + \frac{3L}{4D} \tag{2.55}$$

The modern approach allows more accurate results based on numerical simulations. The following are intrinsic transmission probability formulas for a circular pipe and a narrow slot with an arbitrary length (ALCP and ALNS) [4(pp.136-137)],

$$P_{tr,ALCP} = \frac{14 + 4\frac{L}{D}}{14 + 18\frac{L}{D} + 3\left(\frac{L}{D}\right)^2} \quad \text{and} \quad P_{tr,ALNS} = \frac{1 + \ln\left(0433\frac{L}{b} + 1\right)}{\frac{L}{b} + 1} \tag{2.56, 2.57}$$

where L is pipe length, D is pipe diameter, and b is the width of a narrow slot.

Combining the above viscous and molecular throughput formulas requires experimental data, but with little available, this work proposes linking variable Z in the Knudsen equation Eq. (2.24), assuming trends similar to the Knudsen equation of throughput variations in the intermediate regimes. Hence the throughput of minor loss elements can be stated as

$$Q_{other\ pipes} = Q_{minor} + Q_{intrinsic} \cdot Z \tag{2.58}$$

$$\text{where } Q_{minor} = \left(\frac{\pi D^2}{4}\right)\left(\frac{2RT_1}{K_{minor}}\frac{P_1^2 - P_2^2}{2}\right)^{1/2}, \quad Q_{intrinsic} = P_{tr,intrinsic} C_{AP} P_1, \tag{2.59, 2.60}$$

P_1 and P_2 are the upstream and downstream pressures, and T_1 is the influx temperature.

2.3.4 Considerations of Compressibility in a Viscous Flow

For an isentropic nozzle from a gas reservoir (i.e. V_1=0), rearranging Bernoulli's equation for outlet flow speed V_2 and applying the Poisson equations for an isentropic flow yields

$$V_2 = \sqrt{\frac{2\gamma}{\gamma\text{-}1} RT_1 \left[1 - \left(\frac{P_2}{P_1} \right)^{(\gamma-1)/\gamma} \right]} \tag{2.61}$$

where subscripts 1 and 2 denote upstream and downstream. The mass flux is the product of outlet density ρ_2 and flow speed V_2 [4(p.93)]:

$$j_m = \rho_2 V_2 = \frac{4}{\sqrt{\pi}} \frac{P_1}{v_{avg1}} \psi\left(\frac{P_2}{P_1} \right), \tag{2.62}$$

where the dimensionless flow function

$$\psi\left(\frac{P_2}{P_1} \right) = \sqrt{\frac{\gamma}{\gamma - 1} \left[\left(\frac{P_2}{P_1} \right)^{2/\gamma} - \left(\frac{P_2}{P_1} \right)^{(k+1)/k} \right]}. \tag{2.63}$$

The throughput of an isentropic nozzle (IN) is

$$Q_{IN} = A_{\min} \sqrt{\frac{\pi}{4}} P_1 v_{avg1} \psi\left(\frac{P_2}{P_1} \right) \tag{2.64}$$

where A_{min} is the minimum cross sectional area due to vena contracta. Since the theory of vena contracta is not well established, the following guideline estimates the minimum area [37(p.371)]

$$A_{min} = \begin{cases} 0.60\, A_c \ \text{for}\ P_2 \approx P_1 \ \text{(low pressure drop)} \\ 0.86\, A_c \ \text{for}\ P_2 < P^* \ \text{(choked flow)} \end{cases} \tag{2.65}$$

The mass flow rate maximizes when $d\psi / dP_2 = 0$, which results in the critical pressure

$$P_2^* = P_1 \left(\frac{2}{\gamma + 1} \right)^{\gamma/(\gamma-1)}. \tag{2.66}$$

Average speed of the critical flow

$$V_2^* = \sqrt{\frac{2\gamma}{\gamma\text{-}1}\frac{P_1}{\rho_1}\left[1-\left(\frac{P_2^*}{P_1}\right)^{(\gamma-1)/\gamma}\right]} = \sqrt{\frac{P_2^*}{\rho_2^*}\left(\frac{2}{\gamma+1}\right)^{-1}\left(\frac{2\gamma}{\gamma+1}\right)} = \sqrt{\gamma\frac{P_2^*}{\rho_2^*}} = \sqrt{\gamma RT_2^*} = a_2^* \quad (2.67)$$

reaches the local speed of sound a^*, where superscript * denotes critical, subscripts 1 and 2 represent upstream and downstream, and γ is the specific heat ratio.

During choking inside an isentropic nozzle, an influx accelerates until the cross sectional area minimizes at the vena contracta. The mass flux then attains a maximum behind the vena contracta, and the average flow velocity reaches the local speed of sound. Since a choked flow is unaffected by the outlet pressure, any information behind a choking point cannot be transmitted to the inlet. For choking the throughput of an isentropic nozzle must be revised to

$$Q_{IN,unchoked} = A_{\min}\sqrt{\frac{\pi}{4}}P_1 v_{avg1}\psi\left(\frac{P_2}{P_1}\right), \quad \text{for } \frac{P_2}{P_1} > \left(\frac{2}{\gamma+1}\right)^{\gamma/(\gamma-1)}, \quad (2.68a)$$

$$Q_{IN,choked} = A_{\min}\sqrt{\frac{\pi}{4}}P_1 v_{avg1}\psi\left(\frac{P_2^*}{P_1}\right), \quad \text{for } \frac{P_2}{P_1} \le \left(\frac{2}{\gamma+1}\right)^{\gamma/(\gamma-1)}. \quad (2.68b)$$

Choking of non-isentropic passages (NIP) with constant cross sectional area is similar, except that the flow accelerates due to wall friction. The effects of wall friction on flow choking and the pressure distribution within a choked pipe are the subject of Fanno flow. For simple 0-D modeling, a choked flow is assumed when the outlet pressure decreases to the critical pressure. A choked flow emerges at the pipe exit as the speed of efflux reaches the local speed of sound. Therefore, the choked throughput is

$$Q_{NIP}^* = P_2^* A_c a^* = P_2^* A_c\sqrt{\gamma RT_2^*} = P_2^* A_c\sqrt{RT_1\, 2\gamma/(\gamma+1)}\,. \quad (2.69)$$

Finding the critical pressure requires solving

$$Q_{NIP}\left(P_1, P_2^*, \ldots\right) = P_2^* A_c\sqrt{RT_1\, 2\gamma/(\gamma+1)} \quad (2.70)$$

for P_2^*. Assuming outlet pressure much smaller than inlet pressure during choking, (outlet pressure is neglected), the critical pressure [4(p.113)]

$$P_2^* = \frac{Q_{NIP}\left(P_1,\ P_2^* = 0,...\right)}{A_c\sqrt{RT_1\, 2\gamma/(\gamma+1)}}. \tag{2.71}$$

The above approach values computation efficiency over accuracy. The ratio of the critical pressure to the inlet pressure for air in an isentropic nozzle is about 52.8%, thus the error cannot be ignored. Also simulation has shown that Eq. (2.71) greatly overestimates the discharge critical pressure (greater than inlet pressure P_1) when throughput is large and a flow is turbulent.

This work proposes to utilize turbulent throughput formula Eq. (2.38) for critical pressure calculation. Choked flow occurs at high Reynolds number where parameter *a* of Eq. (2.35) is very small (e.g. $a \approx 0.05$). Assuming parameter *a* is nil, Eq. (2.38) approximates to

$$Q_{LCP,turbulent} \approx \sqrt{\frac{1}{f_l}\frac{\pi^2 D^5}{8L} RT_1\, \overline{P}\Delta P} = \sqrt{F\cdot\left(P_1^2 - P_2^2\right)}. \tag{2.72}$$

where pre-factor $F = \frac{1}{f_l}\frac{\pi^2 D^5}{8L}\frac{RT_1}{2}$. (2.73)

Solving

$$P_2^* = \frac{Q_{LCP,turbulent}\left(P_1, P_2^*,...\right)}{A_c\sqrt{RT_1\, 2\gamma/(\gamma+1)}} \tag{2.74}$$

for critical discharge pressure P_2^* renders an critical pressure ratio estimate

$$\frac{P_2^*}{P_1} = \sqrt{\frac{F}{S_2^{*2} + F}} \tag{2.75}$$

where $S_2^* = A_c\sqrt{RT_1\,2\gamma/(\gamma+1)}$ is the critical pumping speed. (2.76)

Blasius' throughput formula Eq. (2.27) also produces a similar result through slightly overestimated. Unlike the algebraic solution in Eq. (2.75), the use of Eq. (2.27) requires solving a nonlinear equation

$$P_2^* = \frac{Q_{LCP,\,Blasius}(P_1, P_2^*, ...)}{S_2^*} = \frac{1}{S_2^*}\frac{\pi}{4}\left(\frac{1}{0.3164}\right)^{4/7}\left(\frac{\pi}{8}\right)^{3/7}\frac{D^{19/7}\nu_{avg}^{6/7}}{\eta^{1/7}}\left(\frac{P_1^2 - P_2^{*2}}{L}\right)^{4/7} \tag{2.77}$$

for P_2^*. Eq. (2.77) is useful for the validation of Eq. (2.75).

With critical pressure estimate P_2^* known, the throughput of a non-isentropic passage with choking criteria is

$$Q_{NIP} = \begin{cases} Q_{NIP}(P_1,\, P_2,\, ...)\ if\ \ P_2 > P_2^* \\ Q_{NIP}^*(P_1,\, P_2^*,\, ...)\ if\ \ P_2 \le P_2^* \end{cases}. \tag{2.78}$$

Chapter 3: Vacuum Pump Modeling

3.1 INTRODUCTION

3.1.1 Overview of the Vacuum Pump Model

Figure 3.1 shows the four stage dry vacuum pump model. The first stage is a Roots blower, and the other stages are claw type pumps. Each stage consists of an intake and exhaust pumping chamber, represented by vacuum pump symbols. The subscript indicates the stage number, and *i* or *e* indicates intake or exhaust chamber.

The vacuum pump connects to the main vacuum chamber via a suction pipe, and to the exhaust system via a silencer with a check valve and an exhaust pipe. Throughputs Q_{sp} and Q_{ep} are at pump inlet and outlet. The main vacuum chamber with volume V_c is maintained at a constant temperature T_c using a temperature regulator, required to meet manufacturing specifications. Thus pressure dynamics only matter. The exhaust system is modeled as a thermal reservoir at atmospheric pressure P_{atm} and temperature T_{atm}.

Gas transports in the Stage 1 Roots blower by a carry-over volume. The initial conditions for a new cycle are the equilibrium states that result after mixing the prior carry-over volume with the exhaust volume. A similar transition happens for claw pumps. Roots blowers differ from claw pumps in that pumping chambers switch from intake to exhaust every transition.

A pumping chamber has a variable volume V with rate of volume change $\dot{V}$ dependent on rotor angle θ. A powerful induction motor and an inverter (motor speed controller) render constant pump speed Ω. Pressure and temperature dynamics of a pumping chamber will be studied. Also considered will be flank leakage Q_{FL} and radial leakage Q_{RL}, subdivided into intake and exhaust components Q_{FLi} and Q_{FLe}, and Q_{RLi} and Q_{RLe}; heat transfer between pump body and pumping chambers $\dot{Q}_H$; and pump body temperature T_{pbw} regulated via a cooling system. The inter-stage throughput is Q_{PI}.

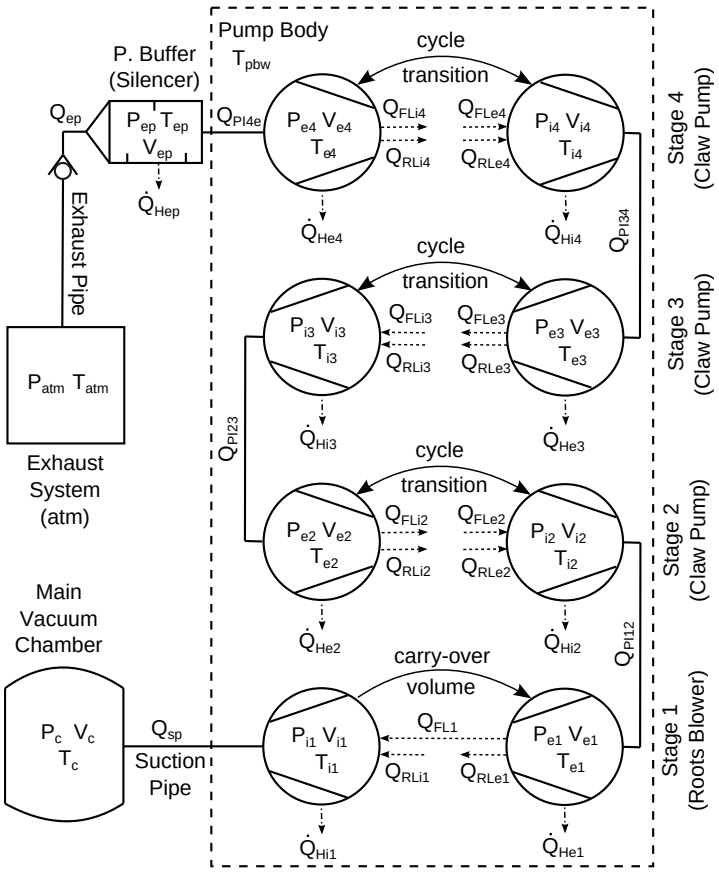

Figure 3.1: Four Stage Dry Vacuum Pump Model.

3.1.2 Chapter Structure

Section 2 will formulate a Roots blower model based on geometry and dynamics for a bi-lobe rotor pump. Included are heat transfer within a pumping chamber based on the two-plate transfer model in Ch.2, and internal leakage based on geometry and a rarefied gas bearing theory including Maxwell's wall slip model.

Section 3 will develop a claw pump model with methods similar to Section 2. Section 4 will model gas passage via a suction pipe model based on the conductance formulas in Ch. 2 and an inter-stage port interface model including dimensionless port

area, geometry and flow dynamics. The resulting nonlinear equations will be numerically solved. Lastly, an exhaust pipe model will be modeled based on a long pipe model.

3.2 ROOTS VACUUM PUMP MODEL

3.2.1 Construction and Operating Principles

Figure 3.2 defines the internal structure of the Roots blower with bi-lobe rotors. The blower consists of intake and exhaust pumping chambers, twin counter-rotating rotors driven by gears with one to one gear ratio, and the stator. For bi-lobe rotors, the phase angle between rotors is 90 degrees. The rotor angle θ defines the rotor position for both rotors.

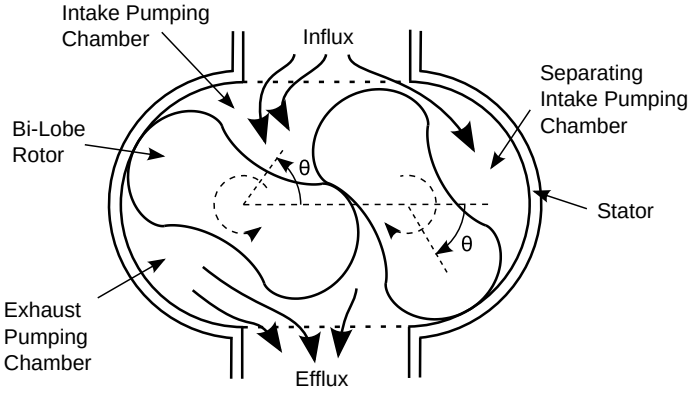

Figure 3.2: Cross-sectional View of a Roots Blower with Twin Bi-lobe Rotors.

Pumping actions are illustrated in Fig. 3.3. As the rotors turn, the intake pumping chamber expands to create a partial vacuum, and gas flows in from a main suction pipe atop Figs. 3.2 and 3.3. Meanwhile the exhaust pumping chamber diminishes and squeezes the gas out to an exhaust pipe at the bottom of Figs. 3.2 and 3.3. The intake and exhaust cycle repeats for every 90 degree rotation of the bi-lobe rotors. During a cyclic transition (a), the intake volume CV_i separates into (b) volumes $CV_{i,i}$ and $CV_{i,e}$; here (d) $CV_{i,e}$

merges with the exhaust pumping chamber, and and $CV_{i,i}$ remerges with the intake chamber.

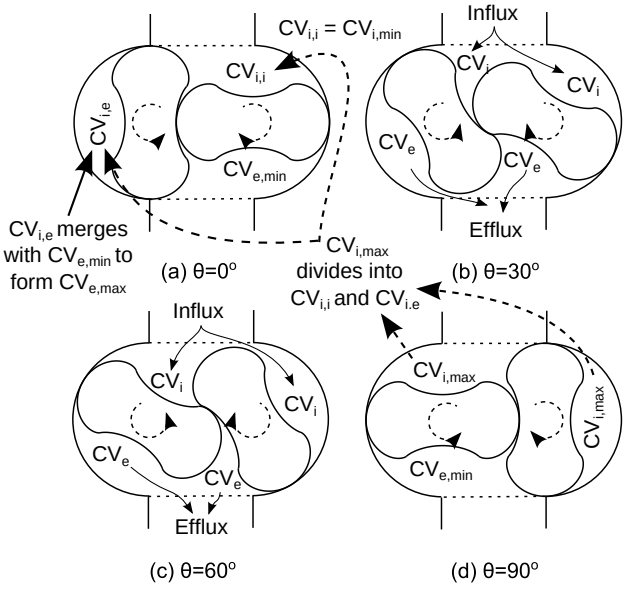

Figure 3.3: Definition of CV's with Timing Diagrams for 2CV Model.

3.2.2 Lobe Rotor and Stator Designs

Shape of lobes is critical to successful pumping. Involute type lobes and epitrochoidal lobes are common for the Roots blower [32]. Epitrochoidal lobes produce a more stable flow than involute lobes. Simplest is the cycloidal bi-lobe, assumed in this research.

Figure 3.4 (a) shows the construction of a bi-lobe rotor, having convex epicycloid ends and concave hypocycloid mid-sections. In (b) are shown stator dimensions for twin bi-lobe rotors. The intermeshing of the twin rotors, permitted by the conforming convex epicycloid and concave hypocycloid sections, is key to the rotor design, see Appendix A1.1.

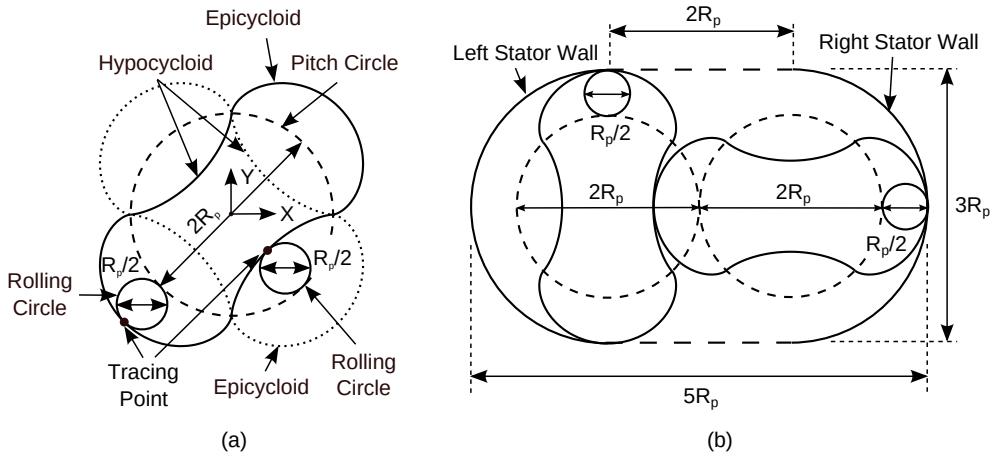

Figure 3.4: The Geometries of a Bi-Lobe Rotor and a Stator.

The x-y coordinates of an epicycloid end surface related to the origin in Fig. 3.4 (a) are

$$\begin{aligned} x_{eo} &= R_p\left(1+\frac{1}{2N_{Lobe}}\right)\cos\theta_e - \frac{R_p}{2N_{Lobe}}\cos\left(\left(2N_{Lobe}+1\right)\theta_e\right) \\ y_{eo} &= R_p\left(1+\frac{1}{2N_{Lobe}}\right)\sin\theta_e - \frac{R_p}{2N_{Lobe}}\sin\left(\left(2N_{Lobe}+1\right)\theta_e\right) \end{aligned} \tag{3.1}$$

and the coordinates of a hypocycloid corresponding mid surface are

$$\begin{aligned} x_{ho} &= R_p\left(1-\frac{1}{2N_{Lobe}}\right)\cos\theta_h + \frac{R_p}{2N_{Lobe}}\cos\left(\left(2N_{Lobe}-1\right)\theta_h\right) \\ y_{ho} &= R_p\left(1-\frac{1}{2N_{Lobe}}\right)\sin\theta_h - \frac{R_p}{2N_{Lobe}}\sin\left(\left(2N_{Lobe}-1\right)\theta_h\right) \end{aligned} \tag{3.2}$$

Here the number of lobes is N_{Lobe} (N_{Lobe} = 2 in Fig. 3.4), R_p is the pitch radius, R_r is the radius of a rolling circle, and θ_e and θ_h are angles to the centerline of the pitch and rolling circles.

The stator walls are half-circles separated by intake and exhaust ports of diameter $2R_p$. For bi-lobe rotors, the stator height H and width W are 1.5 and 2.5 times the pitch diameter, respectively. For a multi-lobe rotor,

$$H = 2R_p\left(1+\frac{1}{N_{Lobe}}\right) \text{ and } W = 2R_p\left(2+\frac{1}{N_{Lobe}}\right) \quad (3.3, 3.4)$$

3.2.3 The Two Control Volume (2CV) Model for Twin Bi-Lobe Rotors

Figure 3.3 shows the control volume definitions of the 2CV (two control volume) model in a cycle. Figure 3.3 (a) shows the end of an intake process and the start of an exhaust process in terms of the carry-over volume. Here the carry-over volume labeled as $CV_{i,e}$ accepts flow from the intake. After an instant of rotation, the carry-over volume carries flow to the exhaust side, and becomes an exhaust control volume (CV_e) which maximizes in volume.

Figures 3.3 (b) and (c) depict intake and exhaust as the rotors turn. No distinction is made between the original pumping chambers and the carry-over volume, even though the carry-over volume has different flow dynamics due to the changing gas passages and expanding and contracting volumes. Arrows indicate flow paths.

When the intake and exhaust cycles finish, a same transition of control volumes from intake to exhaust occurs, see Fig. 3.3 (d). Considering the symmetry between the left and the right of the pump geometry, Fig. 3.3 (a) is technically identical to Fig. 3.3 (d). New intake and exhaust cycles start from (d) and the processes repeat every 90 degrees of rotor rotation.

The carry-over volume contains gas with thermodynamic properties for intake volume CV_i different from exhaust volume $CV_{e,min}$. The 2CV model assumes that during transition, gas in the carry-over volume instantaneously mixes with gas in $CV_{e,min}$. The proposed mixing model has two caveats. First, gas passage between the intake and

exhaust control volumes is non-existent during a transition, and second, even if gas could pass, a mixing process requires finite time to reach equilibrium. Consequences of the simplifying assumptions are discontinuity of pressure and temperature of CV_e during a transition, and underestimation of initial pressure and temperature every cycle.

The simplified mixing model makes computer simulations more manageable. The thermodynamic properties for equilibrium are expressed by algebraic equations. The detailed calculations are provided in Appendix A1.2. A summary of the mixing process is tabulated below.

	Process	Rotor Angle	
		$\theta = n\cdot\pi/4 - \varepsilon$	$\theta = n\cdot\pi/4 + \varepsilon$
Volume	Intake	$V_i\big\vert_{final} = V_{i,\max}$	$V_i\big\vert_{initial} = V_{i,\min} = V_e\big\vert_{final}$
	Exhaust	$V_e\big\vert_{final} = V_{e,\min}$	$V_e\big\vert_{initial} = V_{e,\max} = V_i\big\vert_{final}$
Temperature	Intake	$T_i\big\vert_{final}$	$T_i\big\vert_{initial} = T_i\big\vert_{final}$
	Exhaust	$T_e\big\vert_{final}$	$T_e\big\vert_{initial} = \left.\dfrac{P_i(V_i - V_e) + P_eV_e}{P_i(V_i - V_e)/T_i + P_eV_e/T_e}\right\vert_{final}$
Pressure	Intake	$P_i\big\vert_{final}$	$P_i\big\vert_{initial} = P_i\big\vert_{final}$
	Exhaust	$P_e\big\vert_{final}$	$P_{e1,initial} = \left.\dfrac{P_i(V_i - V_e) + P_eV_e}{V_i}\right\vert_{final}$

Table 3.1: Changes of Thermodynamic Properties During a Transition for Reversely-Symmetric Intake and Exhaust Chamber Volumes.

3.2.4 Computation of Internal Volumes and Areas

The product of base area and stator height defines an intake or exhaust control volume. Cross-sectional areas within the stator confines, but not part of either lobe cross-sectional areas are base areas. Axial length of a stage is stage height. Base areas can be calculated analytically and numerically. The analytical method produces an approximate base area, but the error is negligible. The analytical approach will be presented, followed by the numerical approach.

A lobe consists of an epicycloid and two halves of a hypocycloid. The areas under the cycloids were calculated as described in Appendix A1.3. The general rotor area is the product of the number of lobes and a base area per lobe:

$$A_{rotor\_N\,lobes} = N_{lobe}\left(A_{epi\_N\,lobes} + 2\cdot\frac{1}{2}A_{hypo\_N\,lobes} \right) = \frac{\pi\left(2N_{lobe}^2+1\right)}{2N_{lobe}^2}R_p^2 \ . \tag{3.5}$$

The base area of a carry-over volume can be calculated using

$$A_{carry} = \frac{1}{N_{lobe}}\left[\pi\left(R_p + \frac{R_p}{N_{lobe}} \right)^2 - A_{rotor\_N\,lobes} \right] = \frac{\pi\left(4N_{lobe}+1\right)}{2N_{lobe}^3}R_p^2 . \tag{3.6}$$

For a bi-lobe rotor (N_{lobe}=2),

$$A_{rotor} = \frac{9\pi}{8}R_p^2 \text{ and } A_{carry} = A_{c,L} = A_{c,R} = \frac{9\pi}{16}R_p^2 \ . \tag{3.7, 3.8}$$

Referring to Fig. 3.4 (b), the area within the stator profile for bi-lobe rotors is

$$A_{stator} = \pi\left(R_p + \frac{R_p}{2} \right)^2 + 2R_p\cdot\left(2R_p + 2\frac{R_p}{2} \right) = \frac{\left(9\pi+24\right)}{4}R_p^2 . \tag{3.9}$$

Figure 3.5 depicts the base areas at (a) θ = 0°, (b) 45° and (c) 90°. The minimum base area (see Fig. 3.3 (a) or (b)) for the anti-symmetric intake and exhaust volumes is, via Eqs. (3.7-3.9)

$$A_{i,\min} = A_{e,\min} = \frac{A_{stator} - A_{carry} - 2A_{rotor}}{2} = \frac{(96 - 9\pi)}{32} R_p^2 \ . \tag{3.10}$$

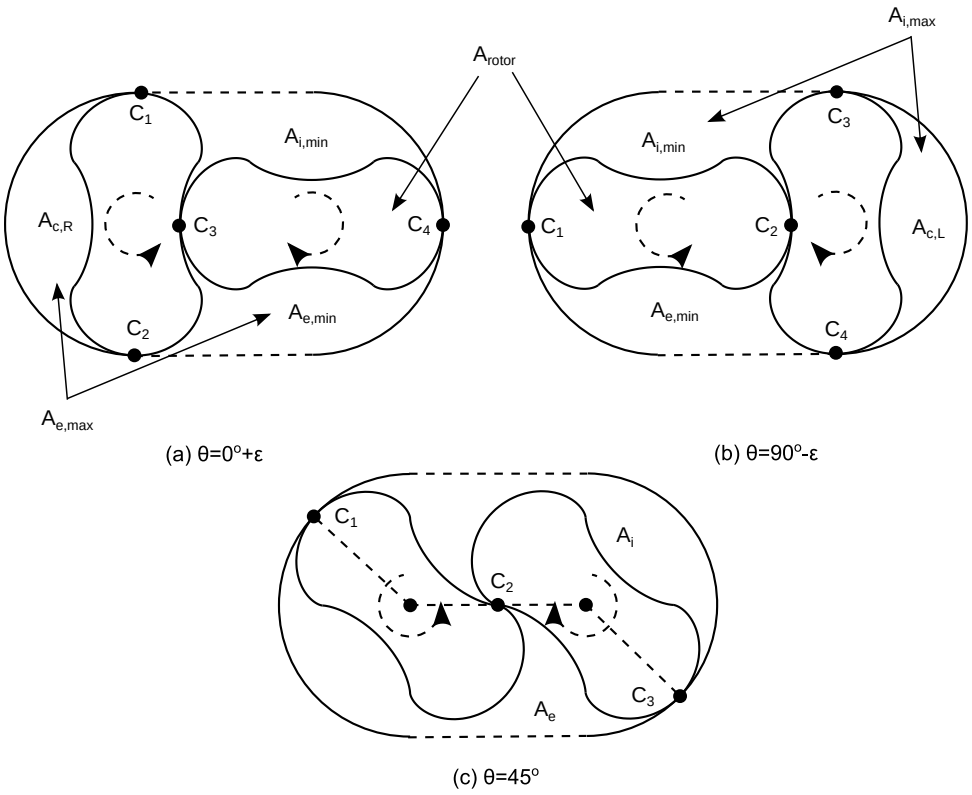

Figure 3.5: Base Area Definitions at the Rotor Angle $\theta = 0$, 45 and 90 Degrees.

Similarly, via Fig. 3.5 (b), the maximum base area for the pumping chambers is

$$A_{i,\max} = A_{i,\min} + A_{c,L} = A_{e,\min} + A_{c,R} = A_{e,\max} = \frac{(96 + 9\pi)}{32} R_p^2 \ . \tag{3.11}$$

The sum of the intake and exhaust base areas is constant and independent of angle,

$$A_i(\theta) + A_e(\theta) = A_{stator} - 2A_{rotor} = 6R_p^2 \ . \tag{3.12}$$

Differentiating the above equation with respect to θ yields

$$\frac{dA_i(\theta)}{d\theta} = -\frac{dA_e(\theta)}{d\theta}, \tag{3.13}$$

which asserts that the increment of A_i equals the decrement of A_e. Because the intake base area A_i equals the exhaust base area A_e at $\theta = 45^o$, the intake and exhaust base areas are anti-symmetric about 45°, giving

$$A_e(\theta) = A_i\left(\frac{\pi}{2} - \theta\right) \text{ or } A_i(\theta) = A_e\left(\frac{\pi}{2} - \theta\right). \tag{3.14}$$

Figure 3.6 shows points, lines and angles relevant to the base area calculation for $45^o < \theta < 90^o$. The contact point C_2 between lobes is always above the horizontal dashed centerline of pitch circles $\overline{o_L o_R}$. As θ increases, the contact points C_1 and C_3 approach P_1 and P_4, respectively, and the angles from the centerline of pitch circles to $\overline{o_L p_7}$ and $\overline{o_R p_8}$ θ_e and θ_h vary according to the rotor angle θ.

The composite area enclosed by *p1, c1, p2, p3, c3, p4, oR, p5, p6, oL* and *p1* consists of three fourths of the stator's circular sectors and rectangle *oL-oR-p3-p2*. Subtracting the two circular sections enclosed by *p1-c1-oL*, and *p4-c3-oR* from the composite area gives

$$A_o = \left[\frac{3}{4}\pi\left(\frac{3}{2}R_p\right)^2 + 2R_p \cdot \frac{3}{2}R_p\right] - 2\cdot\underbrace{\left[\frac{1}{2}\left(\frac{\pi}{2} - \theta\right)\left(\frac{3}{2}R_p\right)^2\right]}_{pie\ \ shaped\ \ \text{sec}tion} = \frac{3(3\pi + 12\theta + 16)}{16}R_p^2. \tag{3.15}$$

There are two sub rotor areas to be removed A_o: A_1 enclosed by o_L-c_1-p_7-c_2-p_6-o_L, i.e.,

$$A_1 = \frac{1}{2}A_{epi\_2lobes} + A_{hypo\_2lobes} + \int_0^{\theta e^*}\frac{1}{2}r_{pe}^2\left(\frac{d\theta_{pe}}{d\theta_e}\right)d\theta_e = \frac{21\pi}{64}R_p^2 + \frac{15\left(4\theta_e^* - \sin\left(4\theta_e^*\right)\right)}{64}R_p^2 \tag{3.16}$$

where $\theta_{pe}\left(\theta_e^*\right) = \theta_e = \theta - \frac{\pi}{4}$ and $\theta_{pe}\left(\theta_e\right) = \tan^{-1}\left(\frac{\sin(5\theta_e) - 5\sin(\theta_e)}{\cos(5\theta_e) - 5\cos(\theta_e)}\right)$; and A_2 enclosed by o_R-c_3-p_8-c_2-p_5-o_R, i.e.,

$$A_2 = \frac{3}{2}A_{epi\_2lobes} + A_{hypo\_2lobes} + \int_0^{\theta h^*} \frac{1}{2} r_{ph}^2 \left(\frac{d\theta_{ph}}{d\theta_h}\right) d\theta_h = \frac{3\left(17\pi + 4\theta_h^* - \sin\left(4\theta_h^*\right)\right)}{64} R_p^2 . \quad (3.17)$$

In the preceding equation $\theta_{ph}\left(\theta_h^*\right) = \theta_h = \theta - \frac{\pi}{4}$ and $\theta_{ph} = -\tan^{-1}\left(\frac{\sin(3\theta_h) - 3\sin\theta_h}{4\cos^3\theta_h}\right)$.

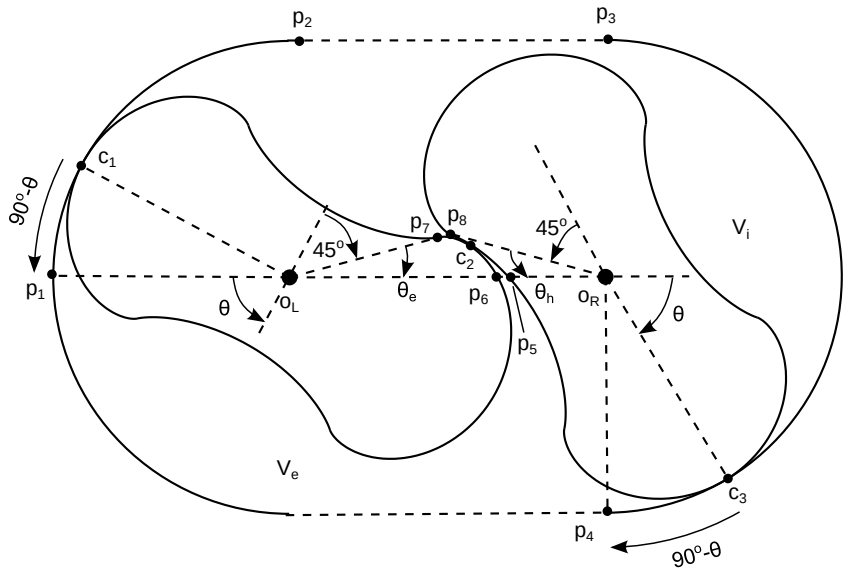

Figure 3.6: Diagram for the Calculation of a Intake Base Area from $\theta = 45$ to 90 Degrees.

Here the integrands represent the infinitesimal pie area calculated using a varying radius for epicycloid r_{pe} and hypocycloid r_{ph} and angular conversion from the rolling circle's centerline angle θ_e or θ_h to tracer's angle θ_{pe} or θ_{ph}. For details, see Fig. A1.2 in A1.3.

The tiny area inside p_5-p_6-c_2 will be neglected. Therefore, the analytical method will produce an approximate solution, though error is small. Finally subtracting Eqs. (3.16) and (3.17) from Eq. (3.15) gives the intake base area for $\pi/4 \le \theta \le \pi/2$

$$A_i(\theta) = \frac{3\left(48\theta - 12\pi - 20\theta_e^* - 4\theta_h^* + 5\sin\left(4\theta_e^*\right) + \sin\left(4\theta_h^*\right) + 64\right)}{64} R_p^2 . \tag{3.18}$$

Using anti-symmetry, the intake base area for $0 \le \theta_{as} \le \pi/4$ is

$$A_i(\theta_{as}) = A_i\left(\frac{\pi}{2} - \theta\right) = 6R_p^2 - A_i(\theta) \text{ , } \pi/4 \le \theta \le \pi/2. \tag{3.19}$$

After the intake base area has been obtained, the exhaust base area can be obtained using the anti-symmetry expressed by the first of Eq. (3.14).

Solution requires numerically solving nonlinear equations for θ_e^* and θ_h^* every time step. To improve computational efficiency, a polynomial is fit to the base area,

$$A_i(\theta) = R_p^2 \, f_{BA,lobe}(\theta), \tag{3.20}$$

where $f_{BA,lobe}(\theta)$ is a dimensionless base area function for the Roots blower. After trial and error, the best fit is a fifth order polynomial with mean square error 7.0367×10^{-7}:

$$f_{BA,lobe}(\theta) = c_5\theta^5 + c_4\theta^4 + c_3\theta^3 + c_2\theta^2 + c_1\theta + c_0$$
$$\textit{where} \quad c_5=0.3053,\ c_4=-1.1989,\ c_3=1.4565,\ c_2=-0.473,\ c_1=1.0656 \ \textit{and}\ c_0=2.1146 \tag{3.21}$$

Figure 3.7 shows overlay between the analytical, polynomial-fit and numerical dimensionless base area functions. The numerical approach of Appendix A1.4 produces a technically identical dimensionless area function that is easy to implement and has high accuracy regardless of geometric complexity of rotor profile.

The intake and exhaust volumes are calculated using the dimensionless base area function as below

$$V_{Li}(\theta) = H_s R_p^2 f_{BA,lobe}(\theta), \tag{3.22}$$

$$V_{Le}(\theta) = V_{Li}(\pi/2 - \theta), \tag{3.23}$$

where H_s is the out of plane height of a stator component.

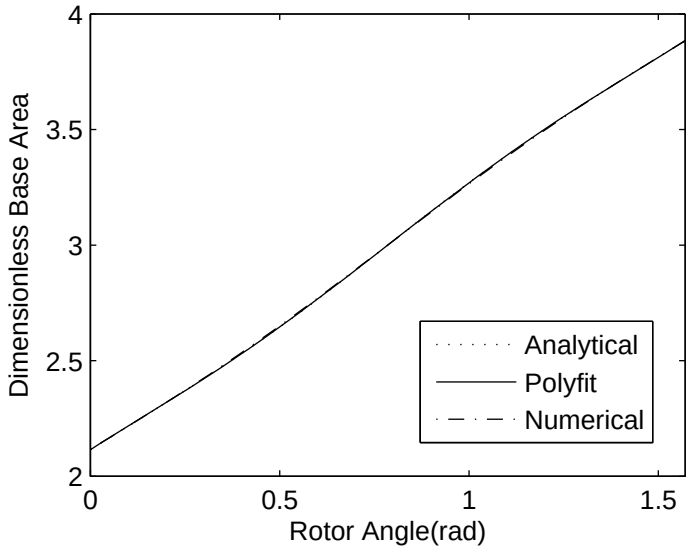

Figure 3.7: Comparison of Dimensionless Base Area Functions.

Heat transfer calculation requires the boundary area of a pumping chamber. Similarly, To calculate the dimensionless boundary length $f_{BL,lobe}$ for the intake base area, a numerical curve fit with a 5^{th} order polynomial and mean square error of 3.5312×10^{-4} renders

$$f_{BL,lobe}(\theta) = c_5\theta^5 + c_4\theta^4 + c_3\theta^3 + c_2\theta^2 + c_1\theta + c_0$$
$$\textit{where}\quad c_5 = -4.3418,\ c_4 = 17.0502,\ c_3 = -21.1329,\ .$$
$$c_2 = 7.7235,\ c_1 = 5.8655\ \textit{and}\ c_0 = 8.3896 \tag{3.24}$$

The inner area of a pumping chamber is the sum of the side area and two base areas. Anti-symmetry applies to the inner intake and exhaust boundary areas A_{Li} and A_{Le}, giving

$$A_{Li}(\theta) = H_s R_p f_{BL,lobe}(\theta) + 2R_p^2 f_{BA,lobe}(\theta), \tag{3.25}$$

$$A_{Le}(\theta) = A_{Li}(\pi/2 - \theta) \ . \tag{3.26}$$

3.2.5 Heat Transfer Model

Heat transfers between the trapped gas and the stator and rotor assembly. Treating the gas mass as a plate with a different temperature on the opposite side, the heat formulas Eqs. (2.18), (2.17), and (2.19) in Ch. 2 describe heat transfer inside a pumping chamber. The wall surface A_w becomes the inner areas of the pumping chambers A_{Li} and A_{Le} developed in the previous section. The inner wall temperature of a pump body T_{pbw}, represented by the equal stator and rotor temperature, is regulated via an automatic cooling system. Also the thermal capacity of a pump body is much larger than gases inside pumping chambers, hence the pump mass filters temperature shocks. Here T_{pbw} is assumed constant. ΔT is the temperature difference between the trapped gas T_{i1} or T_{e1} and T_{pbw}. The thermal distance between gas and a pump body Δy is a undetermined value to be validated via simulation. A typical heat transfer coefficient of an air to water heat exchanger ranges from 10 to 50 W/K·m^2 [38(p.663)], which gives $\Delta y \approx 2$ to 4 mm. But the true Δy may vary depending on pump structure and operating conditions.

3.2.6 Internal Leakage Modeling of 2CV Model

The Roots blower internally leaks because dry sealing via custom made rotors limit radial and axial gaps to a few thousandths of an inch. This section develops a leakage model from geometric, thermodynamic and tribological aspects.

3.2.6.1 Overview of Internal Leakages

A positive displacement pump can internally leak via flank leakage through a radial clearance, and radial leakage through an axial clearance, see Figs. 3.8 and 3.9, which also show nominal flow directions for the bi-lobe Roots blower.

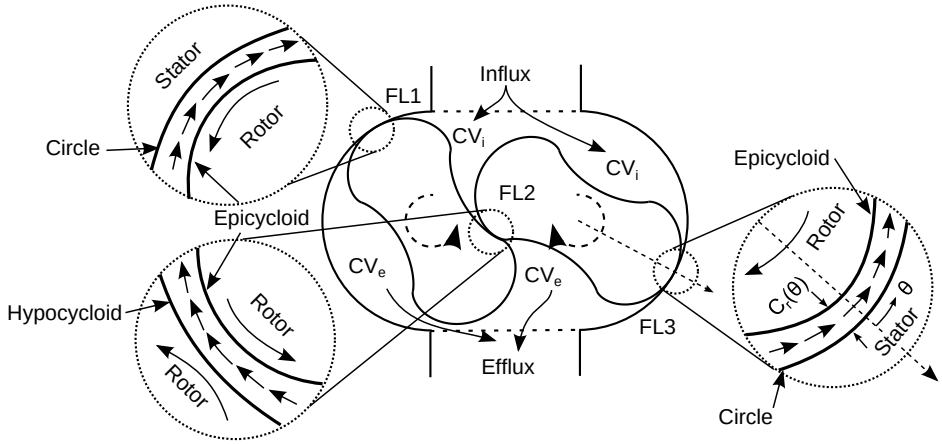

Figure 3.8: Flank Leakages of Bi-Lobe Rotors for 2CV Model.

Leakage flows FL1 and FL3 are through the radial clearance between the stator wall and the moving lobe face. Leakage FL2 is through the radial clearance between two lobe faces under a rolling sliding contact. Since flank leakage resembles the thin film flow of a gas journal bearing, a review of relevant gas bearing theory and Reynolds equation is summarized in Appendix A1.5. Since leakage across the sliding lobe surface can alter pressure distribution, especially around the minimum clearance, Couette flow is just as important as Poiseuille flow to describe flank leakage.

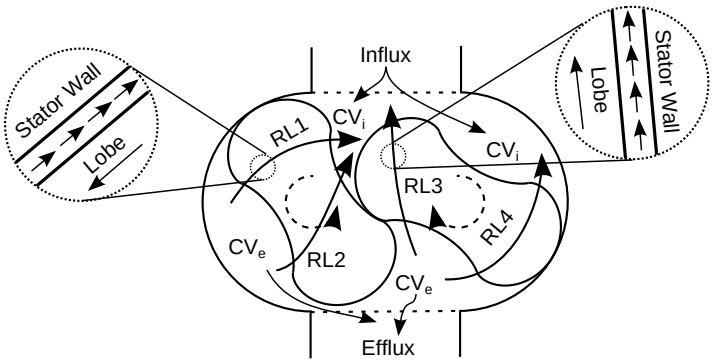

Figure 3.9: Radial Leakages of Bi-Lobe Rotors for 2CV Model.

Eight radial leakage paths exist: $RL1_{f,b}$, $RL2_{f,b}$,$\cdots$,$RL4_{f,b}$ are four radial leakage paths between front and back stator walls and mating surfaces of the rotor, see Fig. 3.9. Subscripts *f* and *b* stand for front and back. The axial clearance between a stator wall and rotor is assumed uniform, but the sliding directions of the lobes are different. For RL1 and RL4, the lobes move towards high pressure, and vice versa for RL2 and RL3. Gas compressibility is minimal because of uniform clearances. A smaller pressure gradient drives the Poiseuille flow, and the flow boundaries are several times longer than for flank leakage.

3.2.6.2 Preliminaries

Pseudo $r - \varphi$ coordinates that switch roles of the rotor and stator circumvents issues related to application of Reynolds equation to the leakage model, see Appendix A1.5. The paragraphs below describe additional revisions required to solve the Reynolds equation.

An approximate clearance function inspired by the journal bearing eccentricity function will be employed. Near the contact line between rotors, this approximate function is almost identical to the actual functions, see Eqs. (A1.33a and b). Also, this

approximate function produces explicit solutions of the integrals alluded to in Appendix A1.5. The dimensionless form of the approximate clearance function is

$$\overline{C}_r(\varphi) = \frac{C_r(\varphi)}{C_{r0}} = 1 + \frac{2}{3}\left(\frac{R_p}{C_{r0}}\right) - \frac{2}{3}\left(\frac{R_p}{C_{r0}}\right)\cos\left(\frac{4}{3}\varphi\right) \tag{3.27}$$

where C_{r0} is the minimum radial clearance, φ is a boundary angle defined in the rotor body fixed frame, and the origin of φ is located at the minimum clearance.

Based on the bi-lobe rotor geometry, the boundary angles of the flank leakage can be set to [-π/2, π/2]. However, at the thickest part of the clearance the local compressibility is negligible, since

$$\Lambda(\varphi = \pm\pi/2) = \frac{6\eta_o\Omega}{P_o}\left(\frac{9}{4}\frac{R_p^2}{\left(C_r(\pm\pi/2)\right)^2}\right) = \frac{6\eta_o\Omega}{P_o}\left(\frac{9}{4}\frac{R_p^2}{R_p^2}\right) = \frac{6\eta_o\Omega}{P_o}\left(\frac{9}{4}\right) \approx 0\,, \tag{3.28}$$

the region can be reduced by half. The regions with negligible compressibility effect coincide with the half hypocycloids, which are [-π/2, -π/4] and [π/4, π/2]. Invoking Eq. (A1.30) with $\overline{h} = \overline{Cr}(\cdot)$ and substituting Eq. (3.28) gives

$$\frac{\partial}{\partial\varphi}\left(\xi\,\overline{P}\overline{C}_r^3\frac{\partial\overline{P}}{\partial\varphi}\right) = \overline{\eta}\Lambda\frac{\partial}{\partial\varphi}\left(\overline{P}\overline{C}_r\right) \approx 0\,. \tag{3.29}$$

Solving Eq. (3.29) gives $\overline{P} = const$. Thus pressure changes within [-π/2, -π/4] and [π/4, π/2] are negligible, which greatly reduces the boundary region to [-π/4, π/4].

3.2.6.3 Throughput of Flank Leakage

The local volumetric flow rate at the minimum clearance is

$$\dot{V}\Big|_{\varphi=0} = H_s C_{r0}\,\overline{u}\Big|_{\varphi=0} = H_s C_{r0}\left[\frac{C_{r0}^2}{12\eta}\left(\frac{2}{3R_p}\right)\left(-\frac{\partial P}{\partial\varphi}\right)\Big|_{\varphi=0}\xi\Big|_{\varphi=0} + \left(\frac{3R_p}{2}\right)\frac{\Omega}{2}\right] \tag{3.30}$$

where $\bar{u}$ is the mean flow speed averaged over the film thickness, H_s is the stator height, $\xi = 1 - 6\left(2 - \sigma_{1t}\right)/\sigma_{1t} \cdot f_r(Kn)$, and $f_r(\cdot) = -Kn$ using Maxwell's wall slip model [40(p.216)].

The pressure at the minimum clearance is the average of the intake and exhaust pressures $P_m = \left(P_e + P_i\right)/2$ because of symmetry at the upstream and downstream of the flank leakage. The pressure solution with the variable gas rarefication along the leakage path produces a positive dimensionless pressure gradient, because the momentum exchange with the walls is greatly overestimated for a small clearance. Consequently, the direction of a leakage flow contradicts common observation (i.e. from exhaust to intake chamber). Instead, the Knudsen number is assumed unchanged along a leakage path. Then the dimensionless pressure gradient at the minimum clearance is

$$\left.\frac{\partial \overline{P}(\varphi)}{\partial \varphi}\right|_{\varphi=0} = \frac{\overline{P}_i - \overline{P}_e}{I_2(\pi/4) - I_2(-\pi/4)} = \frac{P_r - 1}{I_2(\pi/4) - I_2(-\pi/4)} \tag{3.31}$$

where $I_2 = \int \overline{C}_r^{-2} d\varphi$, $\overline{P}_e = P_e/P_e = 1$, $\overline{P}_i = P_i/P_e$ and $P_r = P_i/P_e$.

As a result, the flank leakage

$$Q_{FL1} = Q_{FL3} = P_m \dot{V}\Big|_{\varphi=0} = H_s C_{r0} R_p P_m \left[\frac{\xi_0 P_e}{12\eta}\left(\frac{2C_{r0}^2}{3R_p^2}\right)\frac{1 - P_r}{I_2(\varphi_f) - I_2(\varphi_i)} + \left(\frac{3}{2}\right)\frac{\Omega}{2}\right] \tag{3.32a}$$

where $P_m = \left(P_e + P_i\right)/2$, $\xi_0 = 1 + 6\left(2 - \sigma_{1t}\right)/\sigma_{1t} \cdot Kn_0$ and $Kn_0 = \frac{\pi}{4}\frac{\eta}{C_{r0} P_m}\sqrt{\frac{8RT_e}{\pi}}$.

For FL2, assuming negligible movement of the contact line, the total surface speed in the Couette flow term becomes $2R_p\Omega$. Therefore, the leakage throughput for FL2 is

$$Q_{FL2} = H_s C_{r0} R_p P_m \left[\frac{\xi_0 P_e}{12\eta} \left(\frac{2C_{r0}^2}{3R_p^2} \right) \frac{1 - P_r}{I_2(\varphi_f) - I_2(\varphi_i)} + 2\frac{\Omega}{2} \right]. \tag{3.32b}$$

Assuming the lobe to lobe radial clearance is twice the lobe to stator clearance, the total flank leakage is

$$Q_{FL} = Q_{FL1} + Q_{FL2} + Q_{FL3} = H_s C_{r0} R_p P_m \left[\frac{\xi P_e}{\eta} \left(\frac{C_{r0}^2}{3R_p^2} \right) \frac{1 - P_r}{I_2(\varphi_f) - I_2(\varphi_i)} + \left(\frac{7}{2} \right) \frac{\Omega}{2} \right]. \tag{3.33}$$

3.2.6.4 Throughput of Radial Leakage

For radial leakage, the product of the dimensionless pressure and pressure gradient is

$$\overline{P} \frac{\partial \overline{P}}{\partial \varphi} = \left(\frac{1 - \overline{P}_i}{\varphi_i - \varphi_f} \right)^2 \varphi + \frac{\overline{P}_i \varphi_i - \varphi_f}{\varphi_i - \varphi_f} \left(\frac{1 - \overline{P}_i}{\varphi_i - \varphi_f} \right) \quad \text{where } \overline{P}_i = P_i / P_e = P_r . \tag{3.34}$$

The infinitesimal radial leakage leaving the exhaust chamber or entering the intake chamber is

$$dQ_{RL} = dr\, C_{a0} \left[\xi \frac{C_{a0}^2}{12\eta} \left(\frac{P_e^2}{r} \right) \left(-\overline{P} \frac{\partial \overline{P}}{\partial \varphi} \right) \Bigg|_{\varphi = \varphi_i \text{ or } \varphi_f} + \overline{P}(\varphi_{i \text{ or } f}) P_e \frac{\Omega}{2} r \right]. \tag{3.35}$$

Assuming the direction of the positive rotor speed Ω drags fluid parcels from the exhaust pumping chamber to the intake pumping chamber, integrating the above equation from $R_p/2$ to $3R_p/2$ yields the radial leakage formulas for a single side of a lobe, described below. The radial leakage removed from the exhaust pumping chamber is

$$Q_{RLe/unit} = \int_{R_p/2}^{3R_p/2} dQ_{RLe} = \frac{\xi C_{a0}^3 P_e^2}{12\eta} \left[0.474 \cdot (1 - P_r) \right] + \left(P_e C_{a0} \frac{\Omega}{2} \right) R_p^2 , \tag{3.36a}$$

and the leakage entering to the intake pumping chamber is

$$Q_{RLi/unit} = \int_{R_p/2}^{3R_p/2} dQ_{RLi} = \frac{\xi C_{a0}^3 P_e^2}{12\eta}\left[0.474 \cdot P_r\left(1-P_r\right)\right] + \left(P_i C_{a0}\frac{\Omega}{2}\right)R_p^2 . \quad (3.36b)$$

For RL1 and RL4, the shearing effects work favorably to increase the leakage flow. Therefore, the sign of the rotor speed Ω should be positive. However, the sign of the rotational speed should be negative for RL2 and RL3. When the rotors are perpendicular to each other, either of RL2 and RL3 is effective. As the rotors turn, RL2 and RL3 sometimes overlap each other. To reduce model complexity, RL2 and RL3 are treated as a single radial leakage RL23. Considering the above and assuming the same axial clearance, the total radial leakage is

$$Q_{RLi} = Q_{RL1i} + Q_{RL4i} + Q_{RL23i} = \frac{\xi C_{a0}^3 P_e^2}{2\eta}\left[0.474 \cdot \left(1-P_r\right)\right] + \left(P_i C_{a0}\Omega\right)R_p^2 , \quad (3.37a)$$

$$Q_{RLe} = Q_{RL1e} + Q_{RL4e} + Q_{RL23e} = \frac{\xi C_{a0}^3 P_e^2}{2\eta}\left[0.474 \cdot P_r\left(1-P_r\right)\right] + \left(P_e C_{a0}\Omega\right)R_p^2 . \quad (3.37b)$$

3.3 CLAW-TYPE VACUUM PUMP MODEL

3.3.1 Claw Pump Overview

Figure 3.10 depicts the internal construction of a Northey type claw vacuum pump. The surrounding stator accommodates twin claw rotors, rotating in opposite directions and synchronously driven by a one-to-one ratio gear box. The claws partition the left and right stators—identical truncated and joined hollow cylinders—to form intake and exhaust pumping chambers. During rotation, as claws move away from each other, intake volume between the separating claws increases; as claws approach each other, exhaust volume between the approaching claws is squeezed and decreases. The inlet and outlet ports are located respectively on the front and back side walls of the left and right stators. Port opening and claw positions are controlled by rotor angle θ.

Figure 3.11 illustrates that a cycle begins at (a) $\theta = 0^o$ with claws interlaced, causing minimum intake volume (between claws) and maximum exhaust volume (surrounding claws). The initial exhaust volume is mostly carried over from the final intake volume of the previous cycle. The initial intake volume enclosed by the claws is inherited from the previous intake cycle. As rotation angle θ increases and the claws separate from (a) to (b), volume changes are negligible. The inlet and outlet ports start to open at (b) (as the dedendum portion of a claw overlaps the port), and intake and exhaust processes through the now open ports continue through (c) until the dedendum passes and the ports fully close at (d). The inter-stage flow is restricted by the partially open port, confined by the dedendum area of the rotor as depicted in (c). Transition from (d) to (a) involves negligible volume change, and the processes repeat every 360 degrees. Port geometry in the figure may not reflect real world apparati.

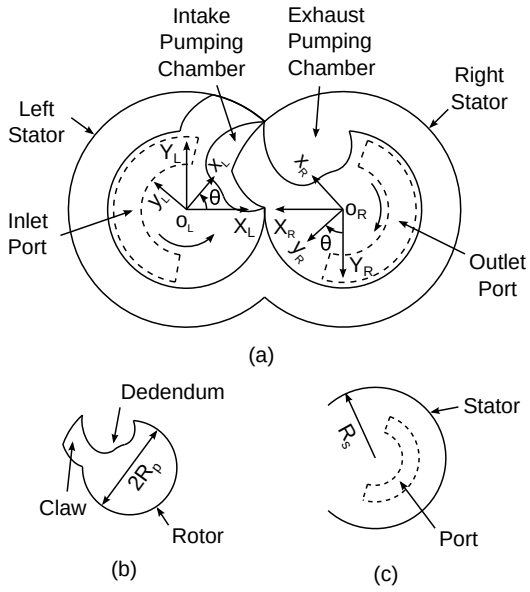

Figure 3.10: The Internal Construction of Claw Vacuum Pump.

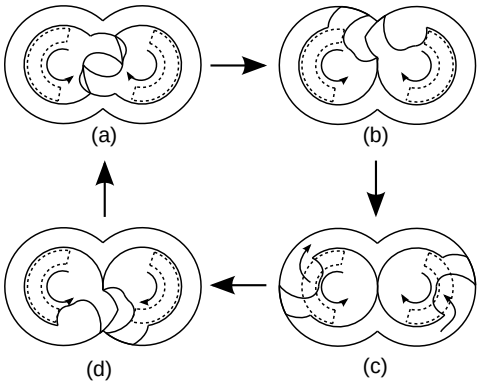

Figure 3.11: Pumping Cycles of Claw Vacuum Pump.

3.3.2 Design of the Northey Type Claw Rotor

The Northey-type claw rotor profile [42,43] is made of epitrochoid, epicycloid and circular arcs. Figure 3.12 shows the initial rotor position with tracing points p_{AL} and p_{BL} (both at radii R_s from the left rotor center) on the left rotor profile. Point p_{CB} is stationary on the stator. Characteristic angles that define boundaries of Fig. 3.12 are

$$\theta_{c1} = \theta_{op} = \cos^{-1}\left(\frac{3R_p^2 + R_s^2}{4R_pR_s}\right),\ \theta_{c2} = \theta_{po} = \cos^{-1}\left(\frac{5R_p^2 - R_s^2}{4R_p^2}\right), \tag{3.38, 3.39}$$

$$\theta_{c3} = \cos^{-1}\left(\frac{R_p}{R_s}\right), \tag{3.40}$$

where R_p and R_s are the radii of the pitch circle and the stator circle. With the left rotor at θ_{c1} and the right rotor at θ_{c2}, intake and exhaust of Fig. 3.10 (b) commences, and ends with the right rotor at θ_{c3}.

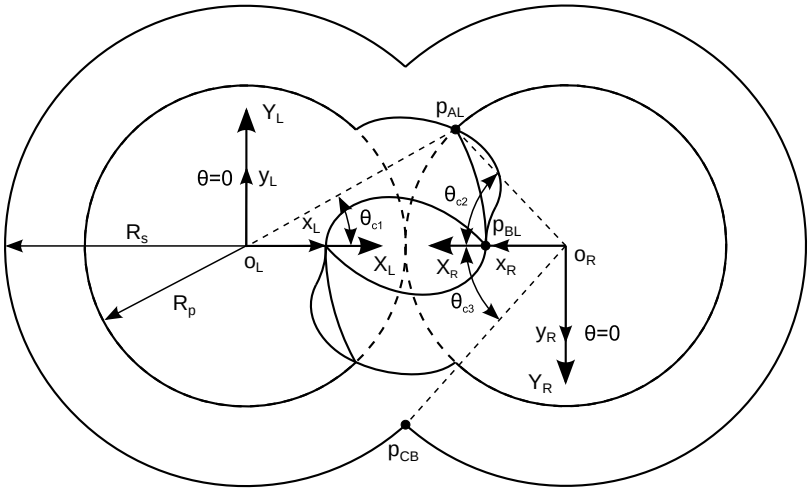

Figure 3.12: Characteristic Angles of Northey Type Claw Rotor.

Figure 3.13 illustrates epitrochoidal curves A_R and B_R on the right rotor profile. Points p_{AL} and p_{BL} rotate with the left rotor and define rotor profile curves A_R and B_R. Attached to the center of each rotor are inertial coordinate frames X_L-Y_L and X_R-Y_R identified by upper case letters, and frames x_L-y_L and x_R-y_R identified by lower case letters that rotate with the rotor. The segment of circular arc between points p_{AL} and p_{BL} has radius R_s, to fit within the stator. The position vector to p_{AL} relative to the rotating x_R-y_R frame is

$$P_{AL}^{xyR} = R(\theta)\left(-P_{AL}^{XYL} + P_{oL}^{XYR}\right) = \begin{bmatrix} 2R_p\cos\theta - R_s\cos(2\theta+\theta_{c1}) \\ 2R_p\sin\theta - R_s\sin(2\theta+\theta_{c1}) \end{bmatrix}, \tag{3.41}$$

where $R(\theta) = \begin{bmatrix} \cos\theta & -\sin\theta \\ \sin\theta & \cos\theta \end{bmatrix}$ is the 2-D rotational matrix, $P_{oL}^{XYR} = \begin{bmatrix} 2R_p \\ 0 \end{bmatrix}$ is the position vectors of the origin o_L in the X_R-Y_R frame, and and $P_{AL}^{XYL} = \begin{bmatrix} R_s\cos(\theta+\theta_{c1}) \\ R_s\sin(\theta+\theta_{c1}) \end{bmatrix}$ is the position vector of p_{AL} in the X_L-Y_L frame.

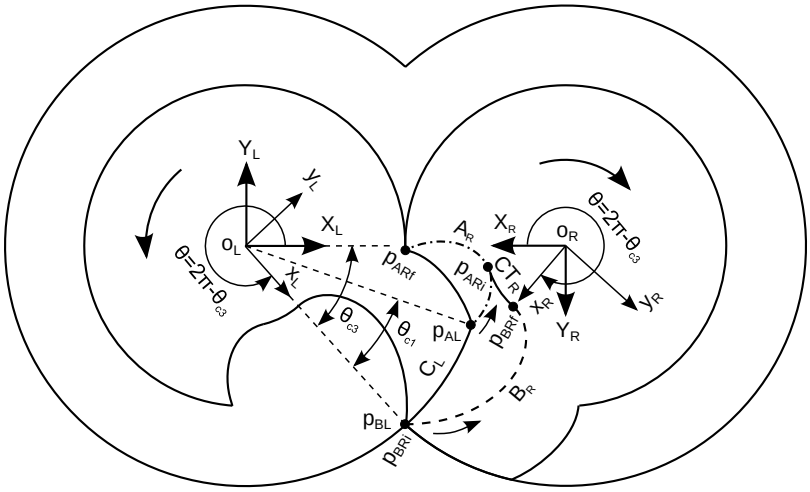

Figure 3.13: Drawing of A_R, B_R and CT_R.

Similarly, the position vector to p_{BL} in the x_R-y_R frame is

$$P_{BL}^{xyR} = R(\theta)\cdot\left(-P_{BL}^{XYL} - P_{oL}^{XYR}\right) = \begin{bmatrix} 2R_p\cos\theta - R_s\cos(2\theta) \\ 2R_p\sin\theta - R_s\sin(2\theta) \end{bmatrix}. \tag{3.42}$$

Here the subscript indicates curve name and rotor, and the superscript denotes the reference coordinate frames.

The epitrochoidal curve B_R that forms the inner claw section on the right rotor extends from p_{BRi} to p_{BRf}, and the rotor position θ corresponds from $\theta = -\theta_{c3}$ to $\theta = 0$. Similarly A_R spans from p_{ARi} at $\theta = -\theta_{c1}$ to p_{ARf} at $\theta = 0$.

$$A_R = \widehat{P}_{AL}^{xyR} = \begin{bmatrix} 2R_p\cos\theta - R_s\cos(2\theta+\theta_{c1}) \\ 2R_p\sin\theta - R_s\sin(2\theta+\theta_{c1}) \end{bmatrix} \quad for \ -\theta_{c1} \le \theta \le 0\,, \tag{3.43}$$

$$B_R = \widehat{P}_{BL}^{xyR} = \begin{bmatrix} 2R_p\cos\theta - R_s\cos(2\theta) \\ 2R_p\sin\theta - R_s\sin(2\theta) \end{bmatrix} \quad for \ -\theta_{c3} \le \theta \le 0\,. \tag{3.44}$$

Although curves A_R and B_R can be connected many ways, herein, a circular arc CT_R with radius $2R_p - R_s$ in $-\theta_{c1} \le \theta \le 0$ will interconnect, via

$$CT_R = \widehat{P}_{CTR}^{xyR} = \begin{bmatrix} (2R_p - R_s)\cos\theta \\ (2R_p - R_s)\sin\theta \end{bmatrix} \quad for \quad -\theta_{c1} \le \theta \le 0\,. \tag{3.45}$$

Figure 3.14 illustrates the drawing of epicycloidal curve D_R (which must fit inside the left rotor's claw during rotation), and circular arcs C_R and E_R.

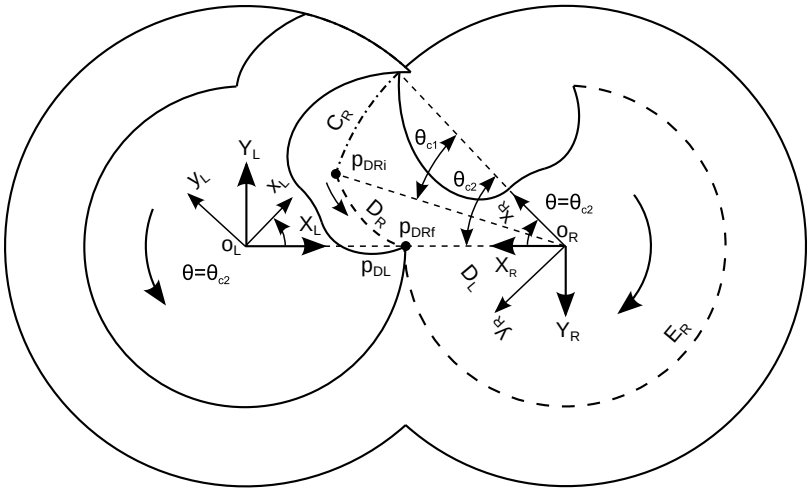

Figure 3.14: Drawing of C_R, D_R and E_R.

The position vector to p_{DL} on the left rotor profile in the x_L-y_L frame is converted to the x_R-y_R frame via

$$P_{DL}^{xyR} = R(\theta)\left(R(\pi+\theta)P_{DL}^{xyL} + P_{oL}^{XYR}\right) = \begin{bmatrix} 2R_p\cos(\theta) - R_p\cos(2\theta - \theta_{c2}) \\ 2R_p\sin(\theta) - R_p\sin(2\theta - \theta_{c2}) \end{bmatrix}. \tag{3.46}$$

The epicycloidal curve D_R, defined in $0 \le \theta \le \theta_{c2}$ is the loci of the above tracer:

$$D_R = \widehat{P}_{DL}^{xyR} = \begin{bmatrix} 2R_p\cos(\theta) - R_p\cos(2\theta - \theta_{c2}) \\ 2R_p\sin(\theta) - R_p\sin(2\theta - \theta_{c2}) \end{bmatrix} for\ 0 \le \theta \le \theta_{c2}\,. \tag{3.47}$$

The circular arcs C_R and E_R are simply defined as

$$C_R = \widehat{P}_{CR}^{xyR} = \begin{bmatrix} R_s \cos\theta \\ R_s \sin\theta \end{bmatrix} \quad for \ 0 \le \theta \le \theta_{c1}, \tag{3.48}$$

$$E_R = \widehat{P}_{ER}^{xyR} = \begin{bmatrix} R_p \cos\theta \\ R_p \sin\theta \end{bmatrix} \quad for \ \theta_{c2} \le \theta \le 2\pi - \theta_{c2}. \tag{3.49}$$

3.3.3 Control Volume Definitions and Cycle Transition

Figure 3.15 shows the control volumes of the intake and exhaust pumping chambers V_i and V_e. A cycle starts at $\theta = 0 + \varepsilon$ where $\varepsilon > 0$ is infinitesimal. The exhaust volume is initially comprised of three sub-volumes $V_{e,a}$, $V_{e,\mathrm{b}}$ and $V_{e,c}$ (Fig. 3.15(a)). Volumes $V_{e,a}$ and $V_{e,\mathrm{c}}$ are inherited from intake sub-volumes $V_{i,a}$ and $V_{i,c}$ of the previous cycle (Fig 3.15(d)), and V_i and $V_{e,b}$ are the carry-over volumes $V_{i,b}$ and V_e from the previous intake and exhaust processes. Strictly speaking, gas mixing occurs while the exhaust sub-volumes merge to form single exhaust volume V_e from (a) to (b). For simplicity, the sub-volumes will be assumed to have identical equilibrium pressure and temperature after mixing. During the processes from (b) to (c), the exhaust volume V_e monotonically shrinks while the intake volume V_i monotonically expands. The intake volume divides into three sub-volumes $V_{i,a}$, $V_{i,b}$ and $V_{i,c}$ between (c) and (d), while the exhaust control volume decreases to a minimum at (d).

The cycle transition occurs from $\theta = 2\pi - \varepsilon$ to $\theta = 0 + \varepsilon$. The thermodynamic changes during the transition are summarized in Table 3.2. Herein the subscripts final and initial represent the final and initial time of a cycle. Energy conservation and the ideal gas law apply to derive the above initial exhaust pressure and temperature.

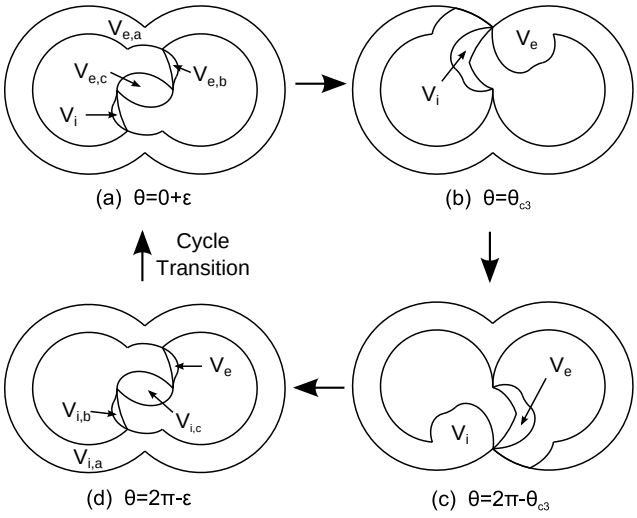

Figure 3.15: Control Volume Definitions of the Claw Pump.

	Process	Rotor Angle	
		$\theta = n\cdot 2\pi - \varepsilon$	$\theta = n\cdot 2\pi + \varepsilon$
Volume	Intake	$V_i\big\|_{final} = \left(V_{i,a} + V_{i,b} + V_{i,c}\right)\big\|_{final}$	$V_i\big\|_{initial} = V_{i,b}\big\|_{final}$
	Exhaust	$V_e\big\|_{final}$	$V_e\big\|_{initial} = \left(V_{i,a} + V_{i,c}\right)\big\|_{final} + V_e\big\|_{final}$
Temperature	Intake	$T_i\big\|_{final}$	$T_i\big\|_{initial} = T_i\big\|_{final}$
	Exhaust	$T_e\big\|_{final}$	$T_e\big\|_{initial} = \left.\dfrac{P_i\left(V_{i,a} + V_{i,c}\right) + P_e V_e}{P_i\left(V_{i,a} + V_{i,c}\right)/T_i + P_e V_e / T_e}\right\|_{final}$
Pressure	Intake	$P_i\big\|_{final}$	$P_i\big\|_{initial} = P_{i2}\big\|_{final} = P_i\big\|_{final}$
	Exhaust	$P_e\big\|_{final}$	$P_e\big\|_{initial} = \left.\dfrac{P_i\left(V_{i,a} + V_{i,c}\right) + P_e V_e}{V_{i,a} + V_{i,c} + V_e}\right\|_{final}$

Table 3.2: Changes of Thermodynamic Properties During a Cycle Transition.

3.3.4 Computation of Internal Volumes and Areas

Like the Roots blower model, the volume and internal area of a pumping chamber can be calculated using a base area and the out of plane stator height. Due to issues with the analytical method summarized in Appendix A2.1, the numerical approach employed for the Roots blower model is adopted here.

First the constituent curves of the claw rotor profile are converted to the dimensionless forms listed in Appendix A2.2. Any area under the above curves can be defined by

$$A_u = R_s^2 f_u\left(\theta,\, r_{ps}\right), \tag{3.50}$$

where $f_u(\cdot) = \left[\int_{\theta_i}^{\theta_f} \frac{1}{2}\bar{r}_\alpha^2 \frac{d\theta_\alpha}{d\theta} d\theta\right]$ is the dimensionless area function, θ_i and θ_f are the initial and final rotor angles for the curve definition, $\bar{r}_\alpha = \bar{r}_\alpha\left(\theta,\, r_{ps}\right) = \sqrt{\bar{x}_\alpha^2 + \bar{y}_\alpha^2}$ is the dimensionless radial distance, $r_{ps} = R_p / R_s$, and $\theta_\alpha\left(\theta,\, r_{ps}\right) = \tan^{-1}\left(\bar{y}_\alpha / \bar{x}_\alpha\right)$ is the angle conversion formula between the rotor angle and the angle to a tracing point on a curve.

For volumes V_i and V_e, the intake and exhaust base areas A_i and A_e can be constructed by adding and subtracting the unit areas of Eq. (3.50), i.e.,

$$A_{i.e}\left(\theta, r_{ps}\right) = \sum \pm A_u\left(\theta, r_{ps}\right) = R_s^2 \sum \pm f_u\left(\theta, r_{ps}\right) = R_s^2 f_{BA,claw}\left(\theta, r_{ps}\right), \tag{3.51}$$

where $f_{BA,claw}$ denotes the dimensionless base area function for claw pumps.

The dimensionless base area function can be estimated numerically using Eq. (3.51) with $R_s = 1$. Figure 3.16 shows the intake and exhaust dimensionless base functions with $r_{ps} = 2/3$ as a function of rotation angle θ. As Fig. 3.11 of sec. 3.3.1 suggests, since the plots are anti-symmetric about $\theta = \pi$ rad, only the intake function must be computed.

The base area function is divided into three regions separated at θ_{c3} and $2\pi - \theta_{c3}$. For computational efficiency, a polynomial curve fit is performed. For r_{ps}=2/3, Table 3.3 summarizes the resulting coefficients up to a fourth order polynomial and errors.

Given r_{ps}, the intake and exhaust pumping volumes are obtained from

$$V_{Ci}(\theta) = H_s R_s^2 f_{BA,claw}(\theta) = H_s R_s^2 \left(\sum_i c_i \theta^i \right), \tag{3.52}$$

$$V_{Ce}(\theta) = R_s^2 f_{BA,claw}(2\pi - \theta), \tag{3.53}$$

where H_s is the out of plane height of a stator component.

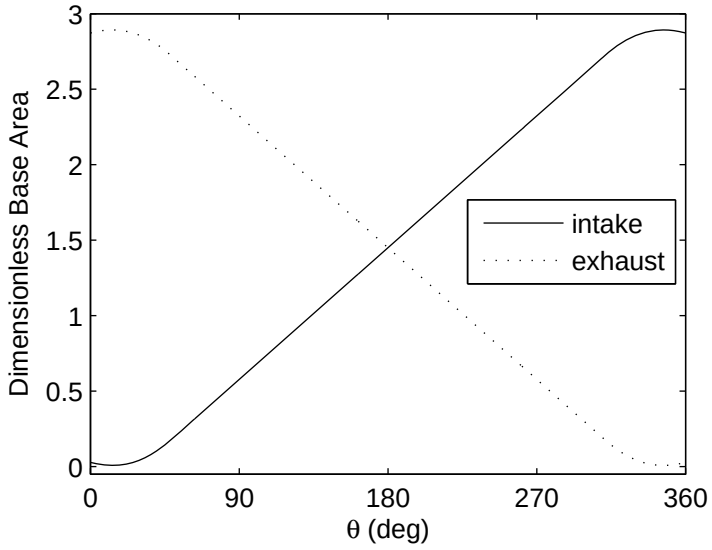

Figure 3.16: Intake and Exhaust Base Area Functions with r_{ps} = 2/3.

Region	Polynomial Coefficients					RMS Error
	c_4	c_3	c_2	c_1	c_0	
$0 \le \theta \le \theta_{c3}$	-0.03646	0.126636	0.320944	-0.16647	0.028311	1.692×10^{-6}
$\theta_{c3} \le \theta \le 2\pi-\theta_{c3}$	0	0	2.39×10^{-8}	0.555554	-0.29483	4.93×10^{-7}
$2\pi-\theta_{c3} \le \theta \le 2\pi$	0.036468	-0.78988	5.929851	-17.3167	16.66915	1.701×10^{-6}

Table 3.3: Dimensionless Base Area Function for r_{ps} = 2/3.

Heat transfer calculation requires the boundary area of a control volume. Like the Roots blower model, a numerical approach and curve fit results in a dimensionless boundary length $f_{BL,claw}$ for the intake base area, which consist of three linear lines. For r_{ps} = 2/3, results are summarized in Table 3.4.

Region	Polynomial Coefficients		RMS Error
	c_1	c_0	
$0 \le \theta \le \theta_{c3} + \theta_{c1}$	1.47177	1.08264	3.55×10^{-2}
$\theta_{c3} + \theta_{c1} \le \theta \le 2\pi-\theta_{c3} + \theta_{c1}$	3.3529	-1.44542	4.9×10^{-2}
$2\pi-\theta_{c3} + \theta_{c1} \le \theta \le 2\pi$	1.58036	9.104	6.6×10^{-3}

Table 3.4: Dimensionless Boundary Length Function for r_{ps} = 2/3.

The inner chamber area consists of the side area and two base areas except for the port opening area that varies with rotor position. For simplicity, the port opening area is neglected. Anti-symmetry applies to the inner area calculation for the exhaust chamber. The intake and exhaust boundary areas A_{Ci} and A_{Ce} are

$$A_{Ci}(\theta) = H_s R_s f_{BL,claw}(\theta) + 2R_s^2 f_{BA,claw}(\theta), \text{ and } A_{Ce}(\theta) = A_{Ci}(2\pi - \theta). \quad (3.54, 3.55)$$

3.3.5 Heat Transfer Model

An approach similar to the Roots blower is employed to formulate heat transfer inside the claw pump. The wall surface A_w is the inner areas A_{Ci} or A_{Ce} developed in the previous section, ΔT is temperature difference between pumping chamber temperatures (i.e. T_{i2}, T_{i3}, T_{i4}, T_{e2}, T_{e3} and T_{e4}) and the inner wall temperature of a pump body T_{pbw}. Thermal thickness Δy is the same as the Roots blower's Δy, which is to be validated via simulation.

3.3.6 Internal Leakage Model

3.3.6.1 Overview of Internal Leakages and Simplifying Assumptions

Figure 3.17 shows the radial and flank leakages for the claw pump. FL1 to FL7 denote flank leakages, and R1 and R2 indicate radial leakages.

Flank leakages FL1, FL2, FL6 and FL7 flow between the sharp edges of the claws, thus fluid shearing is neglected due to low compressibility factor. Leakage FL3 is through counter-rotating pitch circles. The transition from FL1 to FL3 occurs as the pitch circles start to make a line contact at $\theta = \theta_{c2}$. The transition is assumed to occur at $\theta = \theta_{c3}$ for computational efficiency; with error of about 1 or 2 degrees. Similarly the transition from FL3 to FL6 is assumed to occur at $\theta = 2\pi - \theta_{c3}$ rather than $\theta = 2\pi - \theta_{c2}$. FL4 and FL5, defined in the interval $[\theta_{c3}, 2\pi - \theta_{c3}]$, flow between the stator wall and the claw top face. The leakage path of FL4 increases from $\theta = \theta_{c3}$ to $\theta = \theta_{c3} + \theta_{c1}$, and remains unchanged until the end of the range 2π-θ_{c3}. Conversely, FL5's path initially maintains then decreases from $\theta = 2\pi - \theta_{c3} - \theta_{c1}$ to $\theta = 2\pi - \theta_{c3}$.

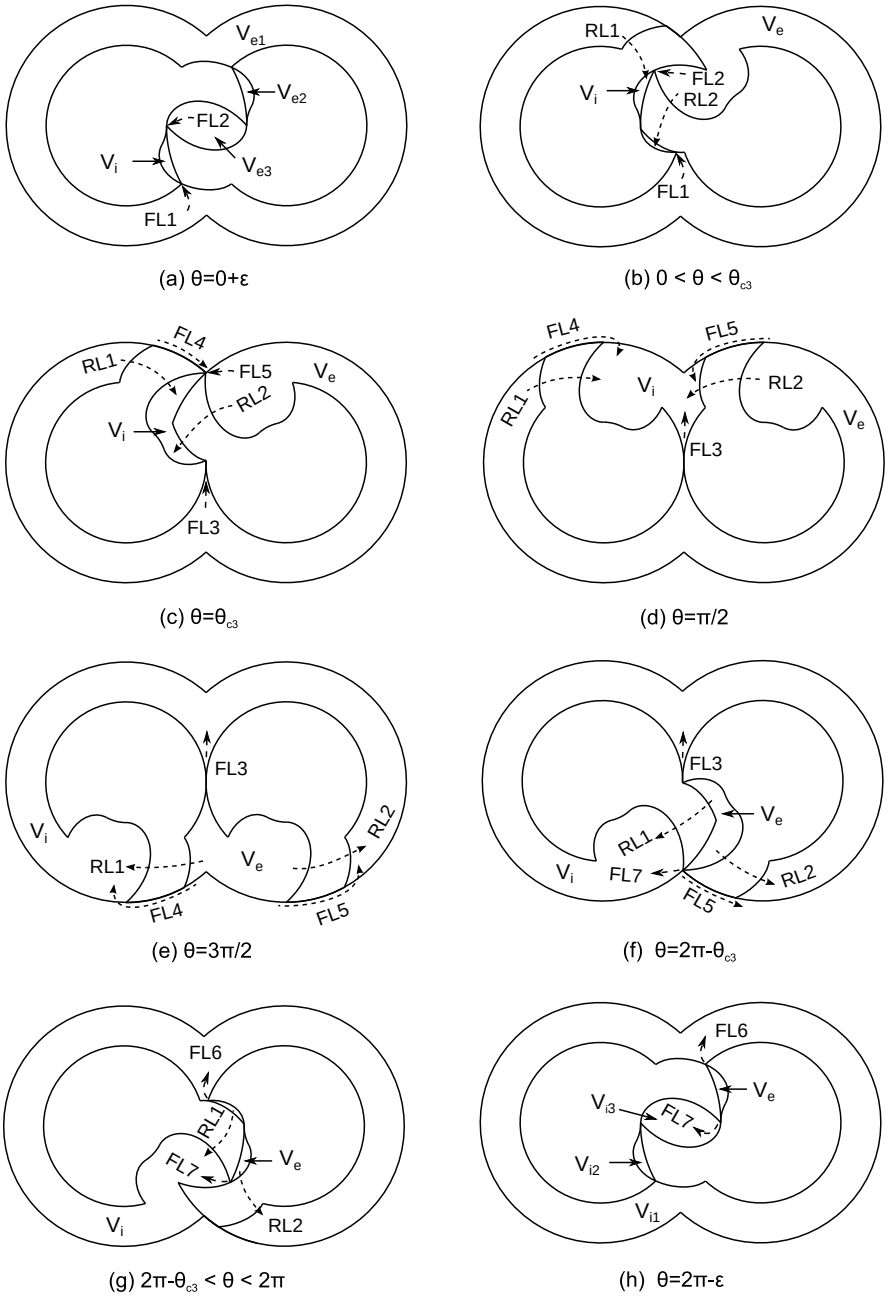

Figure 3.17: Definitions of Internal Leakages Inside the Claw Pump.

The radial leakage path is assumed to be concentric with the pitch circle. Thus the effective leakage path is the addendum portion of a rotor where the claw is located. The leakage paths are evident from $\theta = \theta_{c3}$ to $\theta = 2\pi - \theta_{c3}$, but not defined at $\theta = 0$ and 2π. Thus no radial leakage is shown in (a) and (e). During (b) and (g), the inlet and outlet boundaries change as the claws intermesh. For simplicity, the combined leakage quantity in (b) and (g) is prorated between no leakage and a full leakage according to the rotor position.

3.3.6.2 Throughput of Flank Leakage

Flank leakages FL1, FL2, FL6 and FL7, collectively identified by FL1, is modeled as an isentropic nozzle flow with a narrow slit. Experimental data [4] and numerical simulation [44] of a rarefied gas flow through an orifice showed that for most cases, transition from viscous to molecular flow occurs continuously between $\delta = 50$ and 0.5, where δ is gas rarefication factor (i.e. $\delta = Kn^{-1}$). This work proposes a weighting function $f_L(\delta)$ based on hyperbolic tangent, which asymptotically converges to unity at high δ and to zero at low δ. Figure 3.18 shows that the conductance ratio estimated using $f_L(\delta)$ agrees with experimental data [4] and numerical simulation results [44].

The leakage throughput is defined as:

$$Q_{FL1} = Q_{FL1,viscous} \cdot f_L + Q_{FL1,molecular}\left(1 - f_L\right) \ for \ 0 \le \theta \le \theta_{c3} \ and \ 2\pi - \theta_{c3} \le \theta \le 2\pi \quad (3.56)$$

where $f_L(\delta) = \frac{1}{2}\left[1 + \tanh\left(\frac{\log_{10}\left(\delta^2/\delta_L\delta_H\right)}{\log_{10}\left(\delta_H/\delta_L\right)}\right)\right]$, and the lower and upper limits of gas rarefication factors are set to δ_L=1 and δ_H=25.

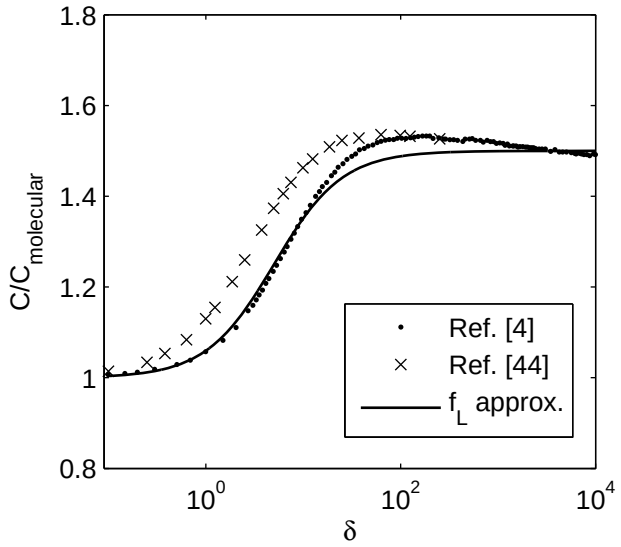

Figure 3.18: Weighting Function $f_L(\delta)$ Compared with Experimental Data [4] and Numerical Simulation [44].

The viscous leakage based on the isentropic nozzle model (see. Eq. 2.68) in Ch.2 is

$$Q_{FL1,viscous} = \begin{cases} \left(A_{c,v}\right)_{\min} \cdot \sqrt{\frac{\pi}{4}} P_e \sqrt{\frac{8RT_e}{\pi}}\, \psi\left(P_r\right) & for\ P_r > \left(\frac{2}{\gamma+1}\right)^{\gamma/(\gamma-1)} \\ \left(A_{c,v}\right)_{\min} \cdot \sqrt{\frac{\pi}{4}} P_e \sqrt{\frac{8RT_e}{\pi}} \sqrt{\frac{\gamma}{2}\left(\frac{2}{\gamma+1}\right)^{(\gamma+1)/(\gamma-1)}} & for\ P_r \le \left(\frac{2}{\gamma+1}\right)^{\gamma/(\gamma-1)} \end{cases}, \quad (3.57)$$

where the cross section area due to vena contracta is $\left(A_{c,v}\right)_{\min} = \frac{\pi}{4}\left(\frac{2H_s C_{r0}}{H_s + C_{r0}}\right)^2$ and $P_r = P_i / P_e$.

Similarly, the molecular leakage is

$$Q_{FL1,molecular} = P_{tr,ALNS}\frac{A_{c,m}}{4}\sqrt{\frac{8RT_e}{\pi}}P_e, \tag{3.58}$$

where $P_{tr,ALNS} = \left[1+\ln\left(0.433\frac{H_s}{C_{r0}}+1\right)\right]\left[\frac{H_s}{C_{r0}}+1\right]^{-1}$ and $A_{c,m} = H_s \cdot C_{r0}$.

Leakage FL3 is between the counter-rotating pitch circles. The dimensionless radial clearance can be defined as

$$\overline{C}_r = \frac{C_r(\varphi)}{C_{r0}} = 1+2\left(\frac{R_p}{C_{r0}}\right)-2\left(\frac{R_p}{C_{r0}}\right)\cos(\varphi). \tag{3.59}$$

Herein φ, defined in the body fixed frame, locates a fluid parcel around the contact of the pitch circles, and the origin of φ is set at the minimum clearance whether the contact line is located.

Since leakage between counter-rotating lobes FL3 of the claw pump resembles FL2 of the Roots blower, the same formula applies but with different surface sliding speed and radial clearance function. The throughput is

$$Q_{FL3} = H_s C_{r0} R_p P_m\left[\frac{\xi_0 P_e}{12\eta}\left(\frac{C_{r0}^2}{R_p^2}\right)\frac{1-P_r}{I_2(\varphi_f)-I_2(\varphi_i)}+2\cdot\frac{\Omega}{2}\right], \tag{3.60}$$

where $P_m = (P_e+P_i)/2$, $P_r = P_i/P_e$, $I_2 = \int \overline{C}_r^{-2} d\varphi$, $\xi_0 = 1+6(2-\sigma_{1t})/\sigma_{1t}\cdot Kn_0$ and $Kn_0 = \frac{\pi}{4}\frac{\eta}{C_{r0}P_m}\sqrt{\frac{8RT_e}{\pi}}$.

Here φ_i and φ_f are the relative angles at which the leakage flow starts and ends, respectively. For consistency with the Roots blower leakage model, φ_i and φ_f are set to $-\pi/4$ and $\pi/4$.

Leakages FL4 and FL5 are similar to the radial leakage of the Roots blower, except for a constant sliding speed and fixed length of the leakage path. With a constant radial clearance, the product of the dimensionless pressure and its gradient is

$$\overline{P}\frac{\partial \overline{P}}{\partial \varphi}=\left(\frac{1-\overline{P}_i}{\theta_{c1}}\right)^2\varphi+\frac{\overline{P}_i\varphi_i-\varphi_f}{\theta_{c1}}\left(\frac{1-\overline{P}_i}{\theta_{c1}}\right), \tag{3.61}$$

where a leakage flow starts at $\varphi = \varphi_i$ and ends at $\varphi = \varphi_f$, and $\overline{P}_i = P_i/P_e = P_r$.

Therefore, the radial leakage entering the intake chamber is

$$Q_{FL4i}=H_s\,C_{r0}\left[\frac{\xi_0\,C_{r0}^2}{12\eta}\left(\frac{P_e^2}{R_s}\right)\left(P_r\left(1-P_r\right)\right)f_X\left(\theta\right)+P_iR_s\,\frac{\Omega}{2}\right], \tag{3.62a}$$

and the radial leakage leaving the exhaust chamber is

$$Q_{FL4e}=H_sC_{r0}\left[\frac{\xi_0\,C_{r0}^2}{12\eta}\left(\frac{P_e^2}{R_s}\right)\left(1-P_r\right)f_X\left(\theta\right)+P_eR_s\,\frac{\Omega}{2}\right] \tag{3.62b}$$

where f_X is defined differently for FL4 and FL5:

$$f_{FL4}\left(\theta\right)=\begin{cases}\theta_{c1}^{-1} & for\ \theta_{c3}\le\theta<2\pi-\theta_{c3}-\theta_{c1}\\ \left(2\pi-\theta_{c3}-\theta\right)^{-1} & for\ \ 2\pi-\theta_{c3}-\theta_{c1}\le\theta<2\pi-\theta_{c3}\end{cases} \tag{3.63a}$$

$$f_{FL5}\left(\theta\right)=\begin{cases}\left(\theta-\theta_{c3}\right)^{-1} & for\ \ \theta_{c3}<\theta\le\theta_{c3}+\theta_{c1}\\ \theta_{c1}^{-1} & for\ \theta_{c3}+\theta_{c1}<\theta\le2\pi-\theta_{c3}\end{cases}. \tag{3.63b}$$

3.3.6.3 Throughput of Radial Leakage

The radial leakage model is based on the radial leakages of the Roots blower but with a different integration interval, [R_p, R_s] for the claw pump, compared to [R_p/2, 3R_p/2] for the Roots blower, and a constant arc angle. The concentric arc represents the path of

an infinitesimal radial leakage dQ_{RL}. The arc length is arc angle times radius. Due to the complex claw geometry mentioned in Appendix A2.1, the arc angle is assumed equal to θ_{c1} (i.e. $\theta_f - \theta_i = \theta_{c1}$).

The radial leakage removed from the exhaust pumping chamber through single boundary on a claw in $\theta_{c3} < \theta < 2\pi - \theta_{c3}$ is

$$\begin{aligned}\left(Q_{RLe/unit}\right)_{full} &= \int_{R_p}^{R_s} dQ_{RLe} = \frac{\xi_0 C_{a0}^3 P_e^2}{12\eta}\frac{P_r\left(1-P_r\right)}{\varphi_f - \varphi_i}\int_{R_p}^{R_s}\frac{dr}{r} + \left(P_e C_{a0}\frac{\Omega}{2}\right)\int_{R_p}^{R_s} r\,dr \\ &= \frac{\xi_0 C_{a0}^3 P_e^2}{12\eta}\frac{1-P_r}{\theta_{c1}}\ln\left(\frac{1}{r_{ps}}\right) + \left(P_e C_{a0}\frac{\Omega}{2}\right)\frac{1}{2}R_s^2\left(1-r_{ps}^2\right)\end{aligned} . \tag{3.64a}$$

Similarly, the radial leakage entering to the intake pumping chamber is

$$\begin{aligned}\left(Q_{RLi/unit}\right)_{full} &= \int_{R_p}^{R_s} dQ_{RLi} = \frac{\xi_0 C_{a0}^3 P_e^2}{12\eta}\frac{P_r\left(1-P_r\right)}{\varphi_f - \varphi_i}\int_{R_p}^{R_s}\frac{dr}{r} + \left(P_i C_{a0}\frac{\Omega}{2}\right)\int_{R_p}^{R_s} r\,dr \\ &= \frac{\xi_0 C_{a0}^3 P_e^2}{12\eta}\frac{P_r\left(1-P_r\right)}{\theta_{c1}}\ln\left(\frac{1}{r_{ps}}\right) + \left(P_i C_{a0}\frac{\Omega}{2}\right)\frac{1}{2}R_s^2\left(1-r_{ps}^2\right)\end{aligned} , \tag{3.64b}$$

where $\xi_0 = 1 - 6\dfrac{2-\sigma_t}{\sigma_t}Kn_o$, $Kn_0 = \dfrac{\pi}{4}\dfrac{\eta}{C_{r0}P_m}\sqrt{\dfrac{8RT_e}{\pi}}$, $P_r = P_i/P_e$ and $P_o = \left(P_i + P_e\right)/2$.

To account for variation of leakage boundaries in Figure 3.15 (b) and (g) and promote computation efficiency, the combined radial leakage is prorated between no and full leakage according to rotor position. Considering four boundaries per stage, the radial leakages per stage are

$$Q_{RLi} = 4\left(Q_{RLi/unit}\right)_{full} f_{RL}(\theta) \text{ and } Q_{RLe} = 4\left(Q_{RLe/unit}\right)_{full} f_{RL}(\theta), \tag{3.65a, 3.65b}$$

$$\text{where } f_{RL}(\theta) = \begin{cases} \left(\theta_{c3} - \theta\right)/\theta_{c3} & for\ 0 \le \theta \le \theta_{c3} \\ 1 & for\ \theta_{c3} \le \theta \le 2\pi - \theta_{c3} \\ \left(2\pi - \theta\right)/\theta_{c3} & for\ 2\pi - \theta_{c3} \le \theta \le 2\pi \end{cases}. \tag{3.66}$$

3.4 MODELING CONNECTING PIPES

This section models gas passages that connect the main vacuum chamber, the individual pump stages, and the exhaust system.

3.4.1 Inter-Stage Gas Passages

3.4.1.1 Overview of Port Interfaces

Figure 3.19 shows the port interfaces and connections of a four stage dry vacuum pump. The solid and dashed profiles indicate an intake port and exhaust port, respectively. Hereafter a port interface PI_{ij} has first and second subscripts that identify connected stages 1, 2, 3, 4 or exhaust system e.

Rotor angle locates the port opening of claw pumps. A single rotor controls the ports on PI_{12} and PI_{4e}, but PI_{23} and P_{34} rely on both the interfacing rotors. An anti-symmetric rotor arrangement across PI_{23} and P_{34} leads to the angular shift by θ_{c1} between the inlet and outlet port profiles. Also, the symmetric cycloidal curves in the dedendum portion of the claw rotor profile open a port irrespective of rotational direction. Thus a unified port model applies to both side ports.

The blower outlet connects to the second stage claw pump inlet through a circuitous internal cavity, which is treated as a part of the blower exhaust chamber. This treatment leads to one less energy storage element and a smaller pressure and temperature change during a cyclic transition. The short gas passage into the second intake chamber can be modeled similar to the port interface between claw pumps.

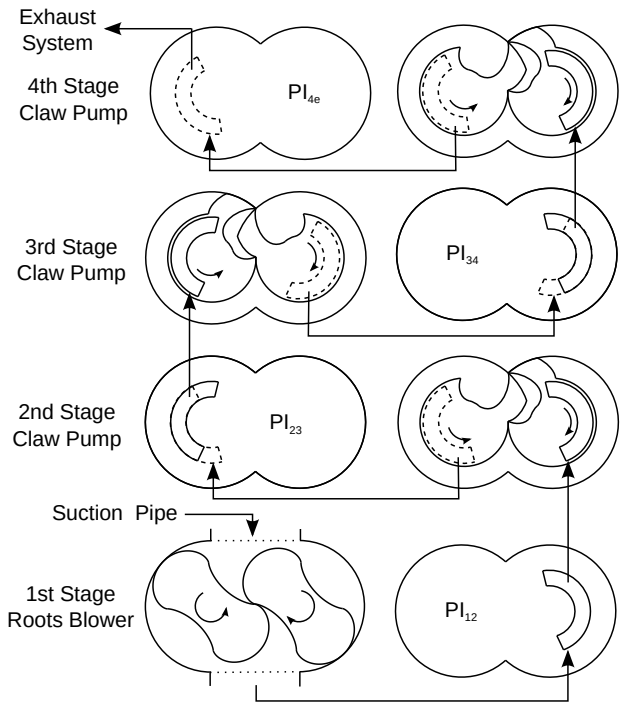

Figure 3.19: Inter-Stage Port Interfaces.

3.4.1.2 Nominal Port Area Calculation

The inter-stage flows resemble orifice flow, wherein the cross sectional area determines flow characteristics. Figure 3.20 depicts an inter-stage viscous flow entering the port interface at an angle θ_{ePI}, approximated as

$$\theta_{ePI} \approx \tan^{-1}\left(\frac{L_{tPI}}{L_{dPI}}\right), \tag{3.67}$$

where L_{tIS} is the interface thickness, and L_{dIS} is the average arc length of the phase delay, which in Fig. 3.20 appears as the length of the end-piece of the interface wall.

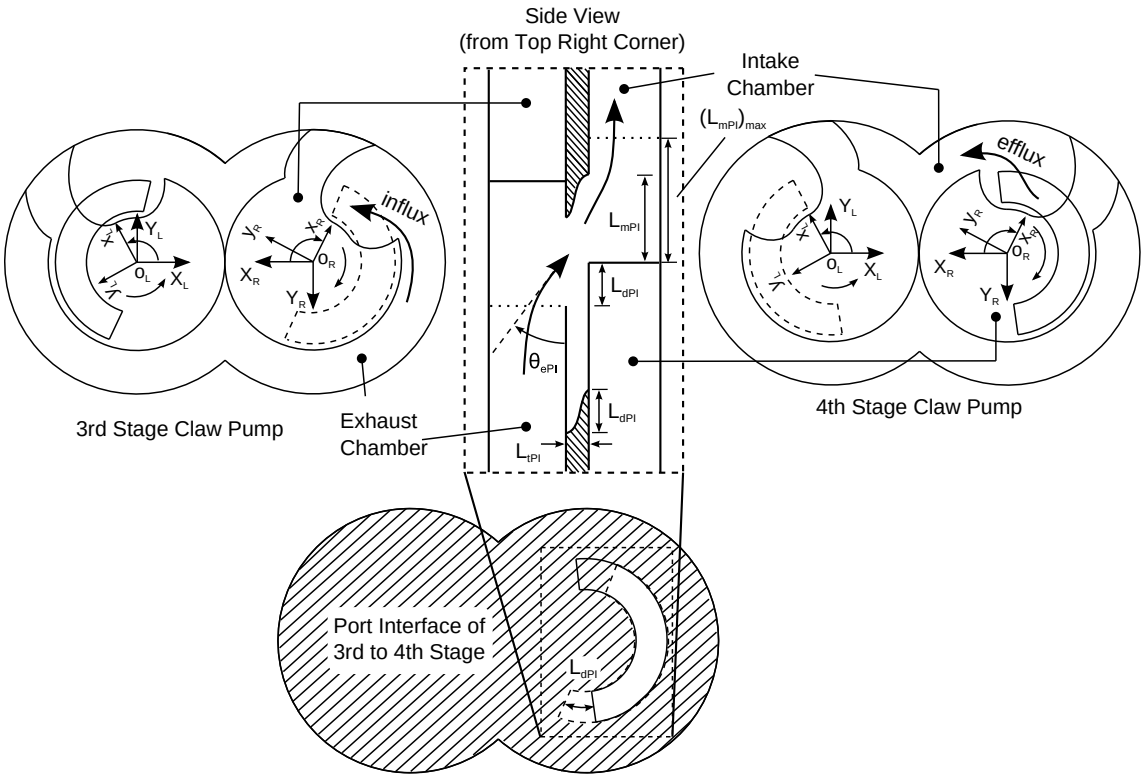

Figure 3.20: Description of the Inter-Stage Viscous Flow Between Claw Pumps.

Figure 3.21 defines geometric parameters of the nominal port opening area A_{PI}. Here R_{oPI} and R_{iPI} are outer and inner radii of the port profile and R_{mPI} is the mean radius. The characteristic angles for the port area are

$$\theta_{oPI} = 2\cos^{-1}\left(\frac{1+2r_{ps}^2}{3r_{ps}}\right) + \theta_{c1} \ , \tag{3.68}$$

$$\theta_{iPI} = 2\theta_{c2} - \theta_{c1}, \tag{3.69}$$

$$\left(\theta_{mPI}\right)_{\max} = \left(\frac{\theta_{oPI} + \theta_{iPI}}{2}\right), \tag{3.70}$$

where $r_{ps} = R_s / R_p$, $\theta_{c1} = \cos^{-1}\left(\dfrac{3R_p^2 + R_s^2}{4R_p R_s}\right)$ and $\theta_{c2} = \cos^{-1}\left(\dfrac{5R_p^2 - R_s^2}{4R_p^2}\right)$.

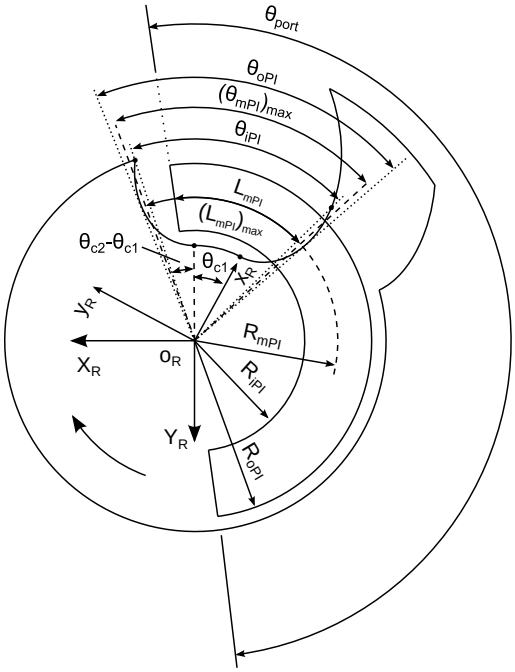

Figure 3.21: Definitions of Parameters of Port Area A_{PI}.

Then the entrance angle can be rewritten as

$$\theta_{ePI} = \tan^{-1}\left(\frac{L_{tPI}}{R_{mPI}\,\theta_{c1}}\right) = \tan^{-1}\left(\frac{r_{ts}}{r_{ms}\theta_{c1}}\right) \tag{3.71}$$

where $R_{mPI} = \left(\dfrac{R_{oPI} + R_{iPI}}{2}\right), r_{ts} = L_{tPI} / R_s$ and $r_{ms} = R_{mPI} / R_s$.

The nominal port arc length L_{mPI} depends on rotor angle. The maximum value is

$$\left(L_{mPI}\right)_{\max} = R_{mPI}\left(\theta_{mPI}\right)_{\max} \ . \tag{3.72}$$

The maximum port area can be estimated by

$$\left(A_{PI}\right)_{\max}=\pi(R_{oPI}^2-R_{iPI}^2)\frac{\left(L_{mPI}\right)_{\max}}{2\pi R_{mPI}}=\frac{R_{oPI}^2-R_{iPI}^2}{2}\left(\theta_{mPI}\right)_{\max}. \tag{3.73}$$

If the port is fully open, the rate change of the opening area with respect to rotor angle is

$$\frac{dA_{PI}}{d\theta_{rel}}=\frac{R_{oPI}^2-R_{iPI}^2}{2}, \tag{3.74}$$

where θ_{rel} is the relative rotor angle, with origin defined by the onset of a port opening.

The port opening process undergoes three phases: initial interval θ_{ab}, accelerating interval θ_{bc} and ending interval θ_{cd}. Assuming the shape of the port areas in θ_{ab} and θ_{cd} to be wedges (isosceles triangle with base length $(R_{oPI}\text{-}R_{iPI})\cdot\theta_{rel}/\theta_{ab}$ and height $\theta_{rel}\cdot(R_{oPI}\text{-}R_{iPI})/2$) spanning angle θ_{rel}, the port area for θ_{ab} is

$$A_{PI,ab}\left(\theta_{rel}\right)=\frac{\left(R_{oPI}^2-R_{iPI}^2\right)}{2\theta_{ab}}\frac{\theta_{rel}^2}{2}. \tag{3.75}$$

Applying anti-symmetry between opening and closing phases gives

$$\begin{aligned}A_{PI,cd}\left(\theta_{rel}\right)&=\left(A_{PI}\right)_{\max}-\frac{R_{oPI}^2-R_{iPI}^2}{2\theta_{ab}}\frac{\left(\theta_{oPI}-\theta_{rel}\right)^2}{2}\\&=\frac{R_{oPI}^2-R_{iPI}^2}{2}\cdot\left(\frac{\theta_{oPI}+\theta_{iPI}}{2}\right)-\frac{R_{oPI}^2-R_{iPI}^2}{2\theta_{ab}}\frac{\left(\theta_{oPI}-\theta_{rel}\right)^2}{2}\end{aligned}. \tag{3.76}$$

Integrating Eq. (3.74) over θ_{rel} and applying the boundary conditions

$$A_{PI,ab}\left(\theta_{rel}=\theta_{ab}\right)=A_{PI,bc}\left(\theta_{rel}=\theta_{ab}\right), \tag{3.77}$$

$$A_{PI,cd}\left(\theta_{rel}=\theta_{oPI}-\theta_{ab}\right)=A_{PI,bc}\left(\theta_{rel}=\theta_{oPI}-\theta_{ab}\right), \tag{3.78}$$

render the area formula for θ_{bc} as

$$A_{PI,bc}\left(\theta_{rel}\right)=\frac{R_{oPI}^2-R_{iPI}^2}{2}\left(\theta_{rel}-\frac{\theta_{ab}}{2}\right), \tag{3.79}$$

where $\theta_{ab} = \theta_{cd} = \dfrac{\theta_{oPI} - \theta_{iPI}}{2}$ and $\theta_{bc} = \theta_{iPI}$.

Dimensionless radii can be defined as

$$r_{os} = R_{oPI} / R_s \le r_{ps} \text{ and } r_{is} = R_{iPI} / R_s \ge \left(2r_{ps} - 1\right) \tag{3.80a, 3.80b}$$

Diving the nominal port area formulas by R_s^2 give the dimensionless nominal port area functions

$$f_{PI,ab}\left(\theta_{rel}\right) = \frac{\left(r_{os}^2 - r_{is}^2\right)}{2} \frac{\theta_{rel}^2}{2\theta_{ab}} \quad for \;\; 0 \le \theta_{rel} \le \theta_{ab}, \tag{3.81}$$

$$f_{PI,bc}\left(\theta_{rel}\right) = \frac{r_{os}^2 - r_{is}^2}{2}\left(\theta_{rel} - \frac{\theta_{ab}}{2}\right) \quad for \;\; \theta_{ab} \le \theta_{rel} \le \theta_{oPI} - \theta_{ab} \;\;, \tag{3.82}$$

$$f_{PI,cd}\left(\theta_{rel}\right) = \frac{r_{os}^2 - r_{is}^2}{2} \cdot \left[\left(\frac{\theta_{oPI} + \theta_{iPI}}{2}\right) - \frac{\left(\theta_{oPI} - \theta_{rel}\right)^2}{2\theta_{ab}}\right] for \;\; \theta_{oPI} - \theta_{ab} \le \theta_{rel} \le \theta_{oPI}. \tag{3.83}$$

Denoting the port angular span as θ_{port}, the nominal port area maximizes at $\theta_{rel} = \theta_{oPI}$, and sustains the maximum until $\theta_{rel} = \theta_{port}$.

$$f_{PI,de}\left(\theta_{rel}\right) = \frac{r_{os}^2 - r_{is}^2}{2} \cdot \left(\frac{\theta_{oPI} + \theta_{iPI}}{2}\right) for \;\; \theta_{oPI} \le \theta_{rel} \le \theta_{port} \tag{3.84}$$

The port closing process from $\theta_{rel} = \theta_{port}$ to $\theta_{rel} = \theta_{port} + \theta_{oPI}$ is the reverse of the opening process. The dimensionless area formulas in the above phases are summarized below

$$f_{PI,ef}\left(\theta_{rel}\right) = \frac{r_{os}^2 - r_{is}^2}{2} \cdot \left[\left(\frac{\theta_{oPI} + \theta_{iPI}}{2}\right) - \frac{\left(\theta_{oPI} - \left(\theta_{port} + \theta_{oPI} - \theta_{rel}\right)\right)^2}{2\theta_{ab}}\right], \tag{3.85}$$

$$for \;\; \theta_{port} \le \theta_{rel} \le \theta_{port} + \theta_{ab}$$

$$f_{PI,fg}(\theta_{rel}) = \frac{r_{os}^2 - r_{is}^2}{2}\left(\left(\theta_{port} + \theta_{oPI} - \theta_{rel}\right) - \frac{\theta_{ab}}{2} \right) \quad , \qquad (3.86)$$
$$for \;\; \theta_{port} + \theta_{ab} \le \theta_{rel} \le \theta_{port} + \theta_{oPI} - \theta_{ab}$$

$$f_{PI,gh}(\theta_{rel}) = \frac{\left(r_{os}^2 - r_{is}^2\right)}{2} \frac{\left(\theta_{port} + \theta_{oPI} - \theta_{rel}\right)^2}{2\theta_{ab}} \quad . \qquad (3.87)$$
$$for \;\; \theta_{port} + \theta_{oPI} - \theta_{ab} \le \theta_{rel} \le \theta_{port} + \theta_{oPI}$$

3.4.1.3 Effective Port Area for a Viscous Flow

For a viscous flow through, the angled flow entrance reduces the cross sectional area. For PI_{23} and PI_{34}, the area reduction factor is $sin\ \theta_{ePI}$, which also applies for PI_{12} and PI_{4e} though the entrance angle may differ in the strict sense. Also the rectangular shape port area needs correcting with use of the hydraulic diameter. Then the effective cross sectional area for the inter-stage flow is

$$\left(A_{PI,H}\right)_{eff} = A_{PI,H}(\theta_{rel}) \cdot \sin\theta_{ePI} \;\text{ and }\; A_{PI,H}(\theta_{rel}) = \frac{\pi}{4}\left(\frac{4A_{PI}(\theta_{rel})}{L_p(\theta_{rel})} \right)^2 \quad , \qquad (3.88)$$

where $A_{PI,H}$ is the corrected nominal port area, L_p is the perimeter of the nominal port area. The dimensionless form of the effective cross sectional area is

$$\begin{aligned} \left(f_{PI,H}(\theta_{rel})\right)_{eff} &= \frac{\left(A_{PI,H}\right)_{eff}}{R_s^2} = \frac{A_{PI,H}(\theta_{rel}) \cdot \sin\theta_{ePI}}{R_s^2} = \pi\left(2\frac{A_{PI}(\theta_{rel})}{R_s^2} \frac{R_s}{L_p(\theta_{rel})} \right)^2 \cdot \sin\theta_{ePI} \\ &= \pi\left(2\frac{f_{PI}(\theta_{rel})}{r_{ps}(\theta_{rel})} \right)^2 \cdot \sin\theta_{ePI} = f_{PI,H}(\theta_{rel}) \cdot \sin\theta_{ePI} \end{aligned} \qquad (3.89)$$

where $f_{PI,H}$ is the dimensionless hydraulic cross sectional area, and $r_{ps} = L_p / R_s$.

The shape at the ends of the port profile is approximated as an obtuse triangle with the vertex of the dull angle on the epitrochoidal curve, as depicted in Fig. 3.22. The following geometric parameters are defined

$$L_r = R_{oPI} - R_{iPI} \ , \tag{3.90}$$

$$L_{tri} = 2\sqrt{\left(R_{mPI}\theta_{ab}\right)^2 + \left(L_r/2\right)^2} \ . \tag{3.91}$$

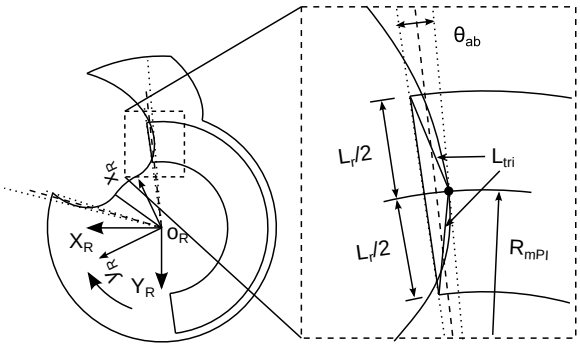

Figure 3.22: Definitions of Geometric Parameters in $0 \le \theta_{rel} \le \theta_{ab}$

Then the perimeter of a nominal port area during an opening phase becomes

$$L_{p,ab} = \left(L_{tri} + L_r\right)\theta_{ref}/\theta_{ab} \ , \tag{3.92}$$

$$L_{p,bc} = L_{tri} + L_r + 2R_{mPI}\left(\theta_{ref} - \theta_{ab}\right) , \tag{3.93}$$

$$\begin{aligned} L_{p,cd} &= L_{tri} + 2R_{mPI}\theta_{iPI} + L_r\left(\frac{\theta_{ab} + \left(\left(\theta_{iPI} + \theta_{ab}\right) - \theta_{ref}\right)}{\theta_{ab}}\right) \\ &\quad + L_{tri}\left(1 - \frac{\theta_{ab} + \left(\left(\theta_{iPI} + \theta_{ab}\right) - \theta_{ref}\right)}{\theta_{ab}}\right) \\ &= 2L_{tri} + 2R_{mPI}\theta_{iPI} + \left(L_r - L_{tri}\right)\left(\theta_{oPI} - \theta_{ref}\right)/\theta_{ab} \end{aligned} \ , \tag{3.94}$$

$$L_{p,de} = 2L_{tri} + 2R_{mPI}\theta_{iPI} \ , \tag{3.95}$$

$$L_{p,ef} = 2L_{tri} + 2R_{mPI}\theta_{iPI} + (L_r - L_{tri})\left(\frac{\theta_{oPI} - (\theta_{port} + \theta_{oPI} - \theta_{ref})}{\theta_{ab}}\right), \quad (3.96)$$
$$= 2L_{tri} + 2R_{mPI}\theta_{iPI} + (L_r - L_{tri})(\theta_{ref} - \theta_{port})/\theta_{ab}$$

$$L_{p,fg} = L_{tri} + L_r + 2R_{mPI}\left((\theta_{port} + \theta_{oPI} - \theta_{ref}) - \theta_{ab}\right), \quad (3.97)$$

$$L_{p,gh} = (L_{tri} + L_r)(\theta_{port} + \theta_{oPI} - \theta_{ref})/\theta_{ab}. \quad (3.98)$$

Similarly, the dimensionless perimeter formulas are

$$r_{ps,ab} = [r_{tris} + r_{rs}]\theta_{ref}/\theta_{ab}, \quad (3.99)$$

$$r_{ps,bc} = r_{tris} + r_{rs} + 2r_{ms}(\theta_{ref} - \theta_{ab}), \quad (3.100)$$

$$r_{ps,cd} = 2r_{tris} + 2r_{ms}\theta_{iPI} + (r_{rs} - r_{tris})(\theta_{oPI} - \theta_{ref})/\theta_{ab}, \quad (3.101)$$

$$r_{ps,de} = 2r_{tris} + 2r_{ms}\theta_{iPI}, \quad (3.102)$$

$$r_{ps,ef} = 2r_{tris} + 2r_{ms}\theta_{iPI} + (r_{rs} - r_{tris})(\theta_{ref} - \theta_{port})/\theta_{ab}, \quad (3.103)$$

$$r_{ps,fg} = r_{tris} + r_{rs} + 2r_{ms}\left((\theta_{port} + \theta_{oPI} - \theta_{ref}) - \theta_{ab}\right), \quad (3.104)$$

$$r_{ps,gh} = (r_{tris} + r_{rs})(\theta_{port} + \theta_{oPI} - \theta_{ref})/\theta_{ab}, \quad (3.105)$$

where $r_{tris} = \frac{L_{tri}}{R_s} = 2\sqrt{(r_{ms}\theta_{ab})^2 + (r_{rs}/2)^2}$, $r_{ms} = \frac{R_{mPI}}{R_s} = \frac{r_{os} + r_{is}}{2}$ and $r_{rs} = \frac{L_r}{R_s} = r_{os} - r_{is}$.

Figure 3.23 shows an example of the dimensionless port profile functions for r_{ps} = 2/3, $r_{os} = 0.9 \cdot r_{ps}$, $r_{is} = 0.6 \cdot r_{ps}$, $\theta_{port} = \pi$. Because of the use of the hydraulic diameter, the transient phase of $f_{PI,H}$ is curved inside. One of the main issues is that its first derivative becomes discontinuous at $\theta_{rel} = \theta_b$ and $\theta_{rel} = \theta_c$ during an opening phase and a closing phase. For computational efficiency, fewer discrete functions are desirable.

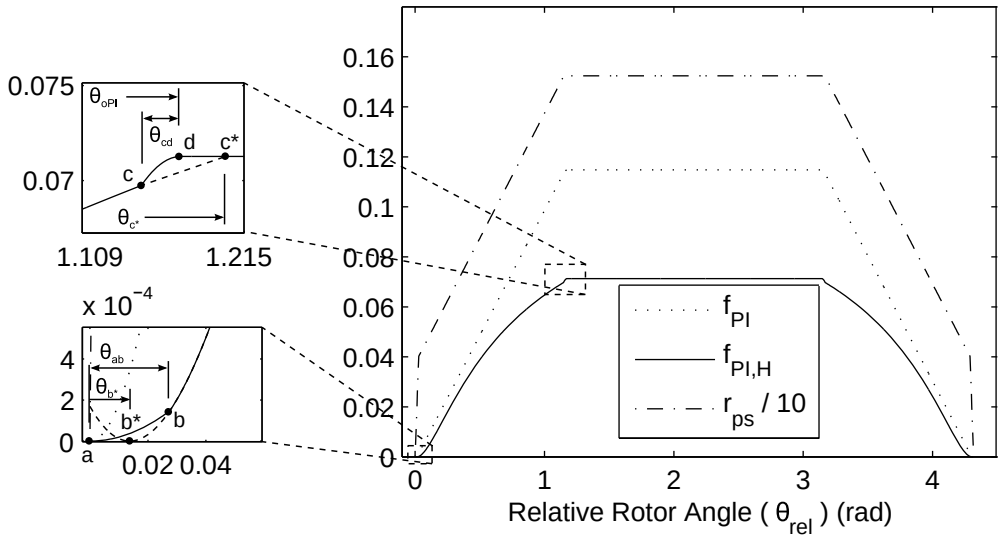

Figure 3.23: Example of Dimensionless Port Profile.

Considering θ_{ab} and θ_{cd} negligibly small, $f_{PI,H,ab}$ and $f_{PI,H,cd}$ can be replaced by the extrapolated curves of $f_{PI,H,bc}$ where the last subscript represents the corresponding segment of $f_{PI,H}$. The new extended segments denote $\overline{b^*b}$ and $\overline{cc^*}$; consequently, the opening phase starts at $\theta_{rel} = \theta_{b*}$ and ends at $\theta_{rel} = \theta_{c*}$. The new starting and ending relative rotor angles are

$$\theta_{b^*} = \frac{\theta_{ab}}{2} \text{ and } \theta_{c^*} = \left[2\theta_{ab} + \frac{\theta_{oPI} + \theta_{iPI}}{r_{tris} + r_{ms}\theta_{iPI}}\left(r_{tris} + r_{rs} - 2r_{ms}\theta_{ab}\right)\right]\left[4 - \frac{\theta_{oPI} + \theta_{iPI}}{r_{tris} + r_{ms}\theta_{iPI}}\left(2r_{ms}\right)\right]^{-1}.$$

(3.106, 3.107)

Similarly, new starting and ending relative rotor angles for a closing phase are

$$\theta_{f^*} = \theta_{port} + \theta_{oPI} - \left[2\theta_{ab} + \frac{\theta_{oPI} + \theta_{iPI}}{r_{tris} + r_{ms}\theta_{iPI}}\left(r_{tris} + r_{rs} - 2r_{ms}\theta_{ab}\right)\right]\left[4 - \frac{\theta_{oPI} + \theta_{iPI}}{r_{tris} + r_{ms}\theta_{iPI}}\left(2r_{ms}\right)\right]^{-1},$$

$$\theta_{g^*} = \theta_{port} + \theta_{oPI} - \frac{\theta_{ab}}{2}. \qquad (3.108, 3.109)$$

Then the simplified dimensionless hydraulic nominal port area function for an inter-stage flow is

$$f_{PI,H}(\theta_{rel}) = \pi\left(2\frac{f_{PI,i}(\theta_{rel})}{r_{ps,i}(\theta_{rel})}\right)^2 \quad for\ \ i = 1,\ 2,\ 3 \tag{3.110}$$

$$\text{where } f_{PI,1}(\theta_{rel}) = r_{ms}r_{rs}\left(\theta_{rel} - \frac{\theta_{ab}}{2}\right) \ \ for\ \ \theta_{b*} \le \theta_{rel} \le \theta_{c*}, \tag{3.111}$$

$$f_{PI,2}(\theta_{rel}) = r_{ms}r_{rs}\left(\frac{\theta_{oPI} + \theta_{iPI}}{2}\right) for\ \theta_{c*} \le \theta_{rel} \le \theta_{f*}, \tag{3.112}$$

$$f_{PI,3}(\theta_{rel}) = r_{ms}r_{rs}(\theta_{g*} - \theta_{rel}) \ \ for\ \ \theta_{f*} \le \theta_{rel} \le \theta_{g*}, \tag{3.113}$$

$$r_{ps,1} = r_{tris} + r_{rs} + 2r_{ms}(\theta_{ref} - \theta_{ab}), \tag{3.114}$$

$$r_{ps,2} = 2r_{tris} + 2r_{ms}\theta_{iPI}, \tag{3.115}$$

$$r_{ps,3} = r_{tris} + r_{rs} + 2r_{ms}(\theta_{g*} - \theta_{ab}/2 - \theta_{ref}). \tag{3.116}$$

3.4.1.4 Transmission Probability for Molecular Throughput

The transmission probability of a series-connected tube with different cross sectional areas can be obtained from [4(p.143)],

$$\frac{1}{A_{c,1}}\left(\frac{1}{P_{tr,1n}} - 1\right) = \sum_{i=1}^{n}\frac{1}{A_{c,i}}\left(\frac{1}{P_{tr,i}} - 1\right) + \sum_{i=1}^{n-1}\left(\frac{1}{A_{c,i+1}} - \frac{1}{A_{c,i}}\right)\delta_{i,i+1} \tag{3.117}$$

where $P_{tr,1n}$ is the total intrinsic transmission probability (ITP), $P_{tr,i}$ is the ITP of the i^{th} tube, $A_{c,i}$ is the cross section area of the i^{th} the tube, n is the total number of tubes, and $\delta_{i,i+1}$ is a geometric parameter for the interface between the i^{th} and $(i+1)^{th}$ tubes, defined as

$$\delta_{i,i+1} = \begin{cases} 1 \ \ for\ \ A_{c,i} > A_{c,i+1} \ \ (decreasing\ A_c) \\ 0 \ \ for\ \ A_{c,i} \le A_{c,i+1} \ \ (non-decreasing\ A_c) \end{cases}. \tag{3.118}$$

For the three tube cases, the general transmission probability formula reduces to

$$P_{tr,13} = \left[\frac{1}{P_{tr,1}} + \frac{A_{c,1}}{A_{c,2}} \left(\frac{1}{P_{tr,2}} - 1 \right) + \frac{A_{c,1}}{A_{c,3}} \left(\frac{1}{P_{tr,3}} - 1 \right) + \left(\frac{A_{c,1}}{A_{c,2}} - \frac{A_{c,1}}{A_{c,1}} \right) \delta_{1,2} + \left(\frac{A_{c,1}}{A_{c,3}} - \frac{A_{c,1}}{A_{c,2}} \right) \delta_{2,3} \right]^{-1} . \tag{3.119}$$

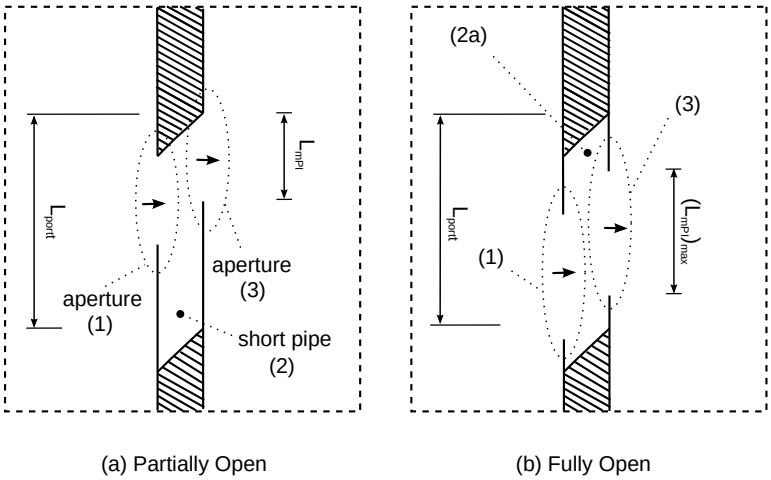

Figure 3.24: Definitions of Geometric Parameters for Molecular Throughput Model.

Figure 3.24 shows definitions of geometric parameters for the transmission probability of inter-stage molecular throughput for PI_{23} and PI_{34}. The hashed area represents the wall of a port interface. The inter-stage gas passage in the molecular regime is modeled as a tube with two identical apertures (1, 3) connected in series with a short pipe (2) with an angled side wall. The cross sectional area of the aperture is equal to the nominal port area defined previously. The cross sectional area of the short pipe does not change but the centerline moves upward in the flow direction.

The transmission probability of an aperture is unity. The transmission probability of a short pipe with an angled wall can be calculated by integrating the transmission probability of an infinitesimal short pipe with the same cross sectional area. The transmission probability of an infinitesimally short pipe is

$$P_{tr,2dx} = 1 - \frac{\left[2R_s r_{ms}\theta_{port} + R_s r_{rs}\right]}{4R_s^2 r_{ms} r_{rs}\theta_{port}} dx \tag{3.120}$$

where *dx* is the wall thickness. For an infinitesimal *dx*, an approximation

$$\frac{1}{P_{tr,2dx}} \cong 1 + \frac{\left[2R_s r_{ms}\theta_{port} + R_s r_{rs}\right]}{4R_s^2 r_{ms} r_{rs}\theta_{port}} dx \ . \tag{3.121}$$

The following integral estimates the transmission probability of a short pipe with an angled wall [4(p.145)]:

$$\frac{1}{P_{tr,2}} = 1 + \int_0^{L_{tPI}} \left(\frac{1}{P_{tr,2dx}} - 1 \right) dx = 1 + \frac{\left[2R_s r_{ms}\theta_{port} + R_s r_{rs}\right]}{4R_s^2 r_{ms} r_{rs}\theta_{port}} L_{tPI} \ . \tag{3.122}$$

In dimensionless form the above solution is

$$\frac{1}{P_{tr,2}} = 1 + \frac{\left[2r_{ms}\theta_{port} + r_{rs}\right]}{4r_{ms} r_{rs}\theta_{port}} r_{ts} \ . \tag{3.123}$$

Considering the geometries of the above port model,

$$A_{c,1} = A_{c,3} = A_{PI}\left(\theta_{ref}\right),\ A_{c,2} = R_s^2 r_{ms} r_{rs}\theta_{port}\ ,\ \delta_{1,2} = 0\ ,\ \delta_{2,3} = 1 \text{ and } P_{tr1} = P_{tr,3} = 1$$

(3.124, 3.125, 3.126 and 3.127)

Therefore, the transmission probability through PI_{23} and PI_{34} reduces to

$$P_{tr,13}\left(\theta_{ref}\right) = \left[2 + \frac{A_{PI}\left(\theta_{ref}\right)}{A_{c,2}} \left(\frac{1}{P_{tr,2}} - 2 \right) \right]^{-1} = \frac{A_{c,2} P_{tr,2}}{A_{PI}\left(\theta_{ref}\right)\left(1 - 2P_{tr,2}\right) + 2A_{c,2} P_{tr,2}} \tag{3.128a}$$

where A_{PI} is the simplified nominal port area developed in the previous section.

Similarly, the transmission probability for PI_{12} and PI_{4e} are:

$$P_{tr,13} = \left[\left(\frac{1}{P_{tr,2}} - 1 \right) + \left(\frac{A_{c,1}}{A_{c,3}} \right) \right]^{-1} = \frac{A_{PI}(\theta_{ref}) P_{tr,2}}{A_{PI}(\theta_{ref}) \cdot (1 - P_{tr,2}) + A_{c,2} P_{tr,2}} \quad \text{for } PI_{12} \tag{3.128b}$$

$$P_{tr,13} = \left[\frac{1}{1} + \frac{A_{c,1}}{A_{c,2}} \left(\frac{1}{P_{tr,2}} - 1 \right) \right]^{-1} = \frac{A_{c,2} P_{tr,2}}{A_{PI}(\theta_{ref}) \cdot (1 - P_{tr,2}) + A_{c,2} P_{tr,2}} \quad \text{for } PI_{4e} \tag{3.128c}$$

A reverse flow has the same transmission probability because of geometric symmetry. Also, the cross sectional area in the molecular throughput formula should be the nominal port area. Therefore, the original throughput formula revises to

$$Q_{PI,molecular} = P_{tr,PI} \frac{A_{PI}}{4} \sqrt{\frac{8RT_s}{\pi}} P_s \quad \text{where } P_{tr,PI}(\theta_{ref}) = P_{tr,13}(\theta_{ref}) = P_{tr,31}(\theta_{ref}) . \tag{3.129}$$

3.4.1.5 Throughput Across an Inter-Stage Gas Passage

Considering the thin inter-stage interface and streamlined flow, the internal cavity in a port interface is treated as an isentropic nozzle for viscous flow. In the molecular regime, gas passage is modeled as a series connected tube consisting of two apertures and a short pipe in between.

Then the throughput of a port interface is

$$Q_{PI} = Q_{PI,viscous} \cdot f_L + Q_{PI,molecular} \cdot (1 - P_2/P_1) \cdot (1 - f_L) \ , \tag{3.130}$$

where $f_L(\delta) = \frac{1}{2} \left[1 + \tanh \left(\frac{\log_{10}(\delta^2 / \delta_L \delta_H)}{\log_{10}(\delta_H / \delta_L)} \right) \right]$, and $\delta_L = 1 \le \delta \le \delta_H = 25$,

$$Q_{PI,viscous} = \begin{cases} \left(A_{c,v}\right)_{\min} \cdot \sqrt{\frac{\pi}{4}} P_1 \sqrt{\frac{8RT_1}{\pi}} \psi\left(\frac{P_2}{P_1}\right) & for \ \frac{P_2}{P_1} > \left(\frac{2}{\gamma+1}\right)^{\gamma/(\gamma-1)} \\ \left(A_{c,v}\right)_{\min} \cdot \sqrt{\frac{\pi}{4}} P_1 \sqrt{\frac{8RT_1}{\pi}} \sqrt{\frac{\gamma}{2}\left(\frac{2}{\gamma+1}\right)^{(\gamma+1)/(\gamma-1)}} & for \ \frac{P_2}{P_1} \le \left(\frac{2}{\gamma+1}\right)^{\gamma/(\gamma-1)} \end{cases}, \quad (3.131)$$

$$Q_{PI,molecular} = P_{tr,PI} \frac{A_{c,m}}{4} \sqrt{\frac{8RT_1}{\pi}} P_1 \ , \quad (3.132)$$

where subscripts *1* and *2* denote upstream and downstream, $(A_{c,v})_{min}$ is the minimum cross section area for the viscous flow, $A_{c,m,}$ is the nominal port area for the molecular flow, and $P_{tr,PI}$ is the transmission probability of a port interface.

Vena contract restricts a viscous flow through a sharp-edged port opening. Considering lack of experimental data and established theory, the minimum cross sectional area A_c is linearly approximated based on two limit values [37]:

$$\left(A_{c,v}\right)_{\min} = \begin{cases} A_{c,v}\left[0.60 + 0.26\left(1 - \sqrt{\frac{\gamma}{2}\left(\frac{2}{\gamma+1}\right)^{(\gamma+1)/(\gamma-1)}}\right)^{-1}\left(1 - \frac{P_2}{P_1}\right)\right] & for \ \frac{P_2}{P_1} > \left(\frac{2}{\gamma+1}\right)^{\gamma/(\gamma-1)} \\ A_{c,v} \cdot 0.86 & for \ \frac{P_2}{P_1} \le \left(\frac{2}{\gamma+1}\right)^{\gamma/(\gamma-1)} \end{cases}. \quad (3.133)$$

3.4.2 Main Suction Pipe Model

A continuously expanding intake chamber keeps pump inlet pressure P_{i1} lower than chamber outlet pressure P_c; therefore, a gas always flows from the vacuum chamber to the pump. Low thermal conductivity of rarefied gases leads to an isothermal flow assumption [45,46], commonly accepted in the vacuum society. Hence throughput across the main suction pipe is a conserved quantity.

The suction pipe consists of long pipes, fittings and assorted parts in series. Here pressure at the joint of pipe component refers to nodal pressure. The overall throughput of a suction pipe equals to total conductance C_{sp} times pressure difference $P_c - P_{i1}$.

$$Q_{sp} = C_{sp} \cdot \left(P_c - P_{i1}\right) \text{ where } \quad C_{sp} = \left(\sum_i \left(C\right)_i^{-1} \right)^{-1} \tag{3.134, 3.135}$$

The conductance of a pipe component $(C)_i$ varies with surrounding nodal pressures. Applying the conservation of throughput to pipe components results in a set of nonlinear algebraic equations with unknown nodal pressures. Solving the nonlinear equations analytically is intractable. A numerical approach via Newton's equation (Appendix A3.1) was initially proposed, however, the numerical method failed due to convergence issues.

This work proposes an alternative approach where an intermediate volume is inserted at each joint of pipe components to model a nodal pressure. For a fixed volume with one inlet and one outlet, the pressure and temperature dynamics equations of a pumping chamber in Eqs. (2.10) and (2.11) simplify to

$$\dot{P}_{spk} = \frac{1}{V_{spk}} \left[\left(\gamma - 1\right) \dot{Q}_{Hspk} + \gamma Q_{spki} - \gamma Q_{spko} \right] \tag{3.136}$$

$$\dot{T}_{spk} = \left(\gamma - 1\right) \frac{\dot{Q}_{Hspk} T_{spk}}{P_{spk} V_{spk}} + \frac{Q_{spki} T_{spk}}{P_{spk} V_{spk}} \left(\gamma - \frac{T_{spk}}{T_{spki}} \right) - \frac{Q_{spko} T_{spk}}{P_{spk} V_{spk}} \left(\gamma - \frac{T_{spk}}{T_{spko}} \right). \tag{3.137}$$

Here subscript *sp* stands for suction pipe, followed by a subscript *k* which indicates a nodal pressure index (i.e. *k=1, 2, ...*), subscripts *i* and *o* stand for inlet and outlet, γ (= c_p / c_v) is the specific heat ratio, $\dot{Q}_H$ is the heat power transferred across the pipe, Q is throughput.

Heat transfer through a pipe differs from the heat transfer of a pumping chamber. The thermal boundary layer of a duct flow resembles its velocity boundary layer, and

Colburn's analogy which relates Nusselt number to Reynolds number Re_D and Prandtl number Pr can be used to formulate an average convective heat transfer coefficient [47,48]. For a turbulent flow, heat transfer power through a suction pipe is

$$\dot{Q}_{Hsp} = -h_H \cdot A_{sp} \cdot \left(T_{spk} - T_{spw}\right) \tag{3.138}$$

$$h_H = \begin{cases} 0.023 \dfrac{k_H}{D} \mathrm{Re}_D^{0.8} \mathrm{Pr}^{0.4} & \textit{for gas cooling} \\ 0.023 \dfrac{k_H}{D} \mathrm{Re}_D^{0.8} \mathrm{Pr}^{0.3} & \textit{for gas heating} \end{cases} \tag{3.139}$$

where $k_H = \dfrac{9\gamma - 5}{4} \eta c_v$, $\mathrm{Re}_D = \dfrac{4Q}{\pi D R T \eta}$ and $\mathrm{Pr} = \dfrac{c_p \eta}{k_H} = \dfrac{4\gamma}{9\gamma - 5}$.

Here k_H is Eucken's thermal conductivity, γ is specific heat ratio, η is dynamic viscosity, c_v and c_p are constant volume and constant pressure specific heats, D is pipe diameter, Q is pipe throughput, T_{spw} is pipe wall temperature, and A_{sp} is the surface area of a pipe.

A main suction pipe designed for maximum pumping speed excludes anything that restricts flow, such as an orifice. Flow choking occurs at any long pipe section, thus each pipe element requires a choking test. Based on the choking test in Sec. 2.3.4 of Ch.2, the choking test for a pipe element is summarized below:

1. *Calculate the critical discharge pressure of* k^{th} *pipe*

$$\left(P_2^*\right)_k = \left(P_1\right)_k \sqrt{\frac{\left(F\right)_k}{\left(S_2^*\right)_k + \left(F\right)_k}} \quad \textit{where} \quad \left(S_2^*\right)_k = A_c \sqrt{R\left(T_1\right)_k 2\gamma/(\gamma+1)}$$

$$\left(F\right)_k = \frac{1}{\left(f_l\right)_k} \frac{\pi^2 \left(D\right)_k^5}{8\left(L\right)_k} \frac{R\left(T_1\right)_k}{2} \tag{3.140}$$

2. *Perform choking test*

$$\left(Q_{NIP}\right)_k = \begin{cases} Q_{NIP}\left((P_1)_k, (P_2)_k, ...\right) \textit{ if } \left(P_2\right)_k > \left(P_2^*\right)_k \textit{ ; no choking} \\ Q_{NIP}^*\left((P_1)_k, (P_2^*)_k, ...\right) \textit{ if } \left(P_2\right)_k \le \left(P_2^*\right)_k \textit{ ; choking} \end{cases}$$

where $\left(Q_{NIP}\right)_k$ is the throughput formula for the k^{th} non-isentropic passage (see. Eqs. (2.24), (2.27), (2.38) and (2.45))

If choking occurs in any element of the long pipe, the solution of the nodal pressure distribution is technically invalid. As an approximation, the throughput of a main suction pipe is assumed limited by the throughput of any choked element.

3.4.3 Main Exhaust Pipe

The main exhaust pipe connects the outlet of the vacuum pump to the exhaust system, which post-processes harmful chemicals before release to the atmosphere. Unlike a suction pipe, an exhaust pipe has smaller conductance to maintain a high vacuum at the pump inlet. An exhaust pipe also includes a check valve to prevent a back flow. A cavity between the outlet of the last pump stage and the check valve functions as a pressure buffer which reduces acoustic emission (i.e. silencer). The pressure drop across the check valve in the designed flow direction can be neglected because of a large pressure drop in the long pipe.

To sum up, the main exhaust pipe can be modeled as a pressure buffer and a long circular pipe with flow direction always from pump outlet to exhaust system. The long circular pipe model is similar to the suction pipe model. Pressure and temperature dynamics for pressure buffers in an exhaust pipe state

$$\dot{P}_{epk} = \frac{1}{V_{epk}}\left[(\gamma-1)\dot{Q}_{Hepk} + \gamma Q_{epki} - \gamma Q_{epko}\right] \tag{3.141}$$

$$\dot{T}_{epk} = (\gamma-1)\frac{\dot{Q}_{Hepk}T_{epk}}{P_{epk}V_{epk}} + \frac{Q_{epki}T_{epk}}{P_{epk}V_{epk}}\left(\gamma - \frac{T_{epk}}{T_{epki}}\right) - \frac{Q_{epko}T_{epk}}{P_{epk}V_{epk}}\left(\gamma - \frac{T_{epk}}{T_{epko}}\right). \tag{3.142}$$

Here subscript *ep* stands for exhaust pipe, subscript *k* denotes a nodal pressure index (i.e. *k=1, 2, ...*) and subscripts *i* and *o* indicate inlet and outlet.

Chapter 4: Simulation

4.1 INTRODUCTION

This chapter summarizes equations of healthy pump dynamics and operation, specifies pump geometry, introduces the numerical simulation technique, and presents simulation results.

4.2 VACUUM PUMP SIMULATION

4.2.1 Simulation Equations

Equation (2.12) describes the pressure dynamics of a main vacuum chamber, and Eqs. (2.10) and (2.11) concern pressure and temperature dynamics of eight pumping chambers inside a vacuum pump. With induction motor speed assumed constant due to a steep torque-speed curve and a speed controller (a.k.a. inverter), time derivatives in these equations can be expressed as angle derivatives via $d(\cdot)/dt = \Omega\, d(\cdot)/d\theta$, where Ω is motor speed. The aforementioned dynamics equations become:

for vacuum chamber,

$$\frac{dP_c}{d\theta} = -\frac{Q_p}{\Omega V_c} = -\frac{S_p P_p}{\Omega V_c}, \tag{4.1}$$

and for pumping chamber,

$$\frac{dP}{d\theta} = \frac{1}{\Omega V}\left[(\gamma-1)\dot{Q}_H - \gamma P\Omega\frac{dV}{d\theta} + \sum \gamma Q_i - \sum \gamma Q_o\right], \tag{4.2}$$

$$\frac{dT}{d\theta} = \frac{1}{\Omega V}\left[(\gamma-1)\frac{\dot{Q}_H T}{P} - (\gamma-1)T\,\Omega\frac{dV}{d\theta} + \sum \frac{Q_i}{P}T\left(\gamma - \frac{T}{T_i}\right) - \sum \frac{Q_o}{P}T\left(\gamma - \frac{T}{T_o}\right)\right]. \tag{4.3}$$

Here, definitions are omitted for brevity (refer to sec. 2.2).

Equations (2.17) – (2.19) and (3.138)

$$\dot{Q}_H = \begin{cases} \dot{Q}_{H,v}\left(P/P_{atm}\right)\sqrt{T/T_{atm}} + \dot{Q}_{H,m}\left(1 - P/P_{atm}\right) & for\ P/P_{atm} < 1 \\ \dot{Q}_{H,v}\left(P/P_{atm}\right)\sqrt{T/T_{atm}} & for\ P/P_{atm} \geq 1 \end{cases},$$

$$\dot{Q}_{H,v} = -\frac{9\gamma - 5}{4}\eta\, c_v\, A_w \frac{\Delta T}{\Delta y},\ \dot{Q}_{H,m} = -\frac{1}{8}\frac{P}{T} v_{avg} A_w \frac{\gamma + 1}{\gamma - 1}\Delta T\ ,\ \dot{Q}_{Hsp} = h_H \cdot A_{sp} \cdot \left(T_{spk} - T_{spw}\right)$$

calculate heat transfer power $\dot{Q}_H$ of a pumping chamber and a suction pipe.

For Roots blower, Eqs. (3.25) and (3.26)

$$A_{Li}(\theta) = H_s R_p f_{BL,lobe}(\theta) + 2R_p^2 f_{BA,lobe}(\theta) \text{ and } A_{Le}(\theta) = A_{Li}(\pi/2 - \theta)$$

estimate heat transfer areas A_W of intake and exhaust chambers, respectively. Similarly, Eqs. (3.54) and (3.55)

$$A_{Ci}(\theta) = H_s R_s f_{BL,claw}(\theta) + 2R_s^2 f_{BA,claw}(\theta) \text{ and } A_{Ce}(\theta) = A_{Ci}(2\pi - \theta)$$

determine intake and exhaust areas for a claw pump. Equations (3.22), (3.23), (3.52) and (3.53)

$$V_{Li}(\theta) = H_s R_p^2 f_{BA,lobe}(\theta),\ V_{Le}(\theta) = V_{Li}(\pi/2 - \theta),$$

$$V_{Ci}(\theta) = H_s R_s^2 f_{BA,claw}(\theta) = H_s R_s^2\left(\sum_i c_i \theta^i\right),\ V_{Ce}(\theta) = R_s^2 f_{BA,claw}(2\pi - \theta)$$

estimate intake and exhaust chamber volumes $V_i(\theta)$ and $V_e(\theta)$ for Roots blower and claw pump, respectively. Taking a derivative of a polynomial fit base area function (refer to Eq. (3.24) for Roots blower and Table 3.3 for claw pump) with respect to θ estimates $dV/d\theta$.

Equations (3.130)-(3.132)

$$Q_{PI} = Q_{PI,viscous} \cdot f_L + Q_{PI,molecular} \cdot \left(1 - P_2/P_1\right) \cdot \left(1 - f_L\right),$$

$$Q_{PI,viscous} = \begin{cases} \left(A_{c,v}\right)_{\min} \cdot \sqrt{\frac{\pi}{4}} P_1 \sqrt{\frac{8RT_1}{\pi}} \psi\left(\frac{P_2}{P_1}\right) & for \ \frac{P_2}{P_1} > \left(\frac{2}{\gamma+1}\right)^{\gamma/(\gamma-1)} \\ \left(A_{c,v}\right)_{\min} \cdot \sqrt{\frac{\pi}{4}} P_1 \sqrt{\frac{8RT_1}{\pi}} \sqrt{\frac{\gamma}{2}\left(\frac{2}{\gamma+1}\right)^{(\gamma+1)/(\gamma-1)}} & for \ \frac{P_2}{P_1} \le \left(\frac{2}{\gamma+1}\right)^{\gamma/(\gamma-1)} \end{cases},$$

$$Q_{PI,molecular} = P_{tr,PI} \frac{A_{c,m}}{4} \sqrt{\frac{8RT_1}{\pi}} P_1 \ ,$$

estimate inter-stage flows. Equations (3.88) and (3.89)

$$\left(A_{PI,H}\right)_{eff} = \frac{\pi}{4}\left(\frac{4A_{PI}\left(\theta_{rel}\right)}{L_p\left(\theta_{rel}\right)}\right)^2 \cdot \sin\theta_{ePI} \ , \ \left(f_{PI,H}\left(\theta_{rel}\right)\right)_{eff} = \pi\left(2\frac{f_{PI}\left(\theta_{rel}\right)}{r_{ps}\left(\theta_{rel}\right)}\right)^2 \cdot \sin\theta_{ePI}$$

determine effective port cross-sectional area and port opening timing, and Eqs. (3.106)-(3.109)

$$\theta_{b*} = \frac{\theta_{ab}}{2}, \ \theta_{c*} = \left[2\theta_{ab} + \frac{\theta_{oPI}+\theta_{iPI}}{r_{tris}+r_{ms}\theta_{iPI}}\left(r_{tris}+r_{rs}-2r_{ms}\theta_{ab}\right)\right]\left[4 - \frac{\theta_{oPI}+\theta_{iPI}}{r_{tris}+r_{ms}\theta_{iPI}}\left(2r_{ms}\right)\right]^{-1},$$

$$\theta_{f*} = \theta_{port} + \theta_{oPI} - \left[2\theta_{ab} + \frac{\theta_{oPI}+\theta_{iPI}}{r_{tris}+r_{ms}\theta_{iPI}}\left(r_{tris}+r_{rs}-2r_{ms}\theta_{ab}\right)\right]\left[4 - \frac{\theta_{oPI}+\theta_{iPI}}{r_{tris}+r_{ms}\theta_{iPI}}\left(2r_{ms}\right)\right]^{-1},$$

$$\theta_{g*} = \theta_{port} + \theta_{oPI} - \frac{\theta_{ab}}{2},$$

$$f_{PI,H}\left(\theta_{rel}\right) = \pi\left(2\frac{f_{PI,i}\left(\theta_{rel}\right)}{r_{ps,i}\left(\theta_{rel}\right)}\right)^2 \quad for \ \ i = 1, \ 2, \ 3$$

define the simplified dimensionless hydraulic nominal port area function.

Carry-over gas mixes with exhaust gas during a cyclic transition. Tables 3.1 and 3.2 determine thermodynamic property changes of the first stage Roots blower and the remaining claw pump stages, respectively.

	Process	Rotor Angle	
		$\theta = n\cdot\pi/4 - \varepsilon$	$\theta = n\cdot\pi/4 + \varepsilon$
Volume	Intake	$V_i\big\|_{final} = V_{i,\max}$	$V_i\big\|_{initial} = V_{i,\min} = V_e\big\|_{final}$
	Exhaust	$V_e\big\|_{final} = V_{e,\min}$	$V_e\big\|_{initial} = V_{e,\max} = V_i\big\|_{final}$
Temperature	Intake	$T_i\big\|_{final}$	$T_i\big\|_{initial} = T_i\big\|_{final}$
	Exhaust	$T_e\big\|_{final}$	$T_e\big\|_{initial} = \left.\dfrac{P_i(V_i - V_e) + P_eV_e}{P_i(V_i - V_e)/T_i + P_eV_e/T_e}\right\|_{final}$
Pressure	Intake	$P_i\big\|_{final}$	$P_i\big\|_{initial} = P_i\big\|_{final}$
	Exhaust	$P_e\big\|_{final}$	$P_{e1,initial} = \left.\dfrac{P_i(V_i - V_e) + P_eV_e}{V_i}\right\|_{final}$

	Process	Rotor Angle	
		$\theta = n\cdot 2\pi - \varepsilon$	$\theta = n\cdot 2\pi + \varepsilon$
Volume	Intake	$V_i\big\|_{final} = \left(V_{i,a} + V_{i,b} + V_{i,c}\right)\big\|_{final}$	$V_i\big\|_{initial} = V_{i,b}\big\|_{final}$
	Exhaust	$V_e\big\|_{final}$	$V_e\big\|_{initial} = \left(V_{i,a} + V_{i,c}\right)\big\|_{final} + V_e\big\|_{final}$
Temperature	Intake	$T_i\big\|_{final}$	$T_i\big\|_{initial} = T_i\big\|_{final}$
	Exhaust	$T_e\big\|_{final}$	$T_e\big\|_{initial} = \left.\dfrac{P_i(V_{i,a} + V_{i,c}) + P_eV_e}{P_i(V_{i,a} + V_{i,c})/T_i + P_eV_e/T_e}\right\|_{final}$
Pressure	Intake	$P_i\big\|_{final}$	$P_i\big\|_{initial} = P_{i2}\big\|_{final} = P_i\big\|_{final}$
	Exhaust	$P_e\big\|_{final}$	$P_e\big\|_{initial} = \left.\dfrac{P_i(V_{i,a} + V_{i,c}) + P_eV_e}{V_{i,a} + V_{i,c} + V_e}\right\|_{final}$

Equations (3.33), (3,37a) and (3.37b)

$$Q_{FL} = Q_{FL1} + Q_{FL2} + Q_{FL3}$$
$$= H_s C_{r0} R_p P_m \left[\frac{\xi_0 P_e}{4\eta} \left(\frac{2C_{r0}^2}{3R_p^2} \right) \frac{1 - P_r}{I_2(\varphi_f) - I_2(\varphi_i)} + \left(\frac{7}{2} \right) \frac{\Omega}{2} \right]$$

$$Q_{RLi} = Q_{RL1i} + Q_{RL4i} + Q_{RL23i} = \frac{\xi C_{a0}^3 P_e^2}{2\eta} \left[0.474 \cdot (1 - P_r) \right] + \left(P_i C_{a0} \Omega \right) R_p^2$$

$$Q_{RLe} = Q_{RL1e} + Q_{RL4e} + Q_{RL23e} = \frac{\xi C_{a0}^3 P_e^2}{2\eta} \left[0.474 \cdot P_r (1 - P_r) \right] + \left(P_e C_{a0} \Omega \right) R_p^2$$

calculate the first stage (Roots blower) flank and radial leakages. For the second to fourth claw pump stages, Eqs. (3.56)-(3.58)

$$Q_{FL1} = Q_{FL1,viscous} \cdot f_L + Q_{FL1,molecular} (1 - f_L) \quad for \;\; 0 \le \theta \le \theta_{c3} \;\; and \;\; 2\pi - \theta_{c2} \le \theta \le 2\pi$$

$$Q_{FL1,viscous}$$
$$= \begin{cases} \left(A_{c,v} \right)_{\min} \cdot \sqrt{\frac{\pi}{4}} P_e \sqrt{\frac{8RT_e}{\pi}} \psi(P_r) & for \;\; P_r > \left(\frac{2}{\gamma + 1} \right)^{\gamma/(\gamma - 1)} \\ \left(A_{c,v} \right)_{\min} \cdot \sqrt{\frac{\pi}{4}} P_e \sqrt{\frac{8RT_e}{\pi}} \sqrt{\frac{\gamma}{2} \left(\frac{2}{\gamma + 1} \right)^{(\gamma+1)/(\gamma-1)}} & for \;\; P_r \le \left(\frac{2}{\gamma + 1} \right)^{\gamma/(\gamma - 1)} \end{cases}$$

$$Q_{FL1,molecular} = P_{tr,ALNS} \frac{A_{c,m}}{4} \sqrt{\frac{8RT_e}{\pi}} P_e,$$

where $P_{tr,ALNS} = \left[1 + \ln\left(0.433 \frac{H_s}{C_{r0}} + 1 \right) \right] \left[\frac{H_s}{C_{r0}} + 1 \right]^{-1}$ and $A_{c,m} = H_s \cdot C_{r0}$

estimate flank leakage when the claws are interwoven, and Eqs. (3.60), (3.62a) and (3.62b)

$$Q_{FL3} = H_s C_{r0} R_p P_m \left[\frac{\xi_0 P_e}{12\eta} \left(\frac{C_{r0}^2}{R_p^2} \right) \frac{1 - P_r}{I_2(\varphi_f) - I_2(\varphi_i)} + 2 \cdot \frac{\Omega}{2} \right],$$

$$Q_{FL4i} = H_s\, C_{r0}\left[\frac{\xi_0\, C_{r0}^2}{12\eta}\left(\frac{P_e^2}{R_s}\right)\left(P_r\left(1-P_r\right)\right)f_X\left(\theta\right)+P_i R_s\,\frac{\Omega}{2}\right],$$

$$Q_{FL4e} = H_s C_{r0}\left[\frac{\xi_0\, C_{r0}^2}{12\eta}\left(\frac{P_e^2}{R_s}\right)\left(1-P_r\right)f_X\left(\theta\right)+P_e R_s\,\frac{\Omega}{2}\right]$$

compute flank leakages flowing in parallel as the claws rotate separately. Equations (3.65a), (3.65b) and (3.66)

$Q_{RLi} = 4\left(Q_{RLi/unit}\right)_{full} f_{RL}\left(\theta\right)$ and $Q_{RLe} = 4\left(Q_{RLe/unit}\right)_{full} f_{RL}\left(\theta\right)$,

where $f_{RL}\left(\theta\right) = \begin{cases} \left(\theta_{c3}-\theta\right)/\theta_{c3} & for\ 0 \le \theta \le \theta_{c3} \\ 1 & for\ \theta_{c3} \le \theta \le 2\pi-\theta_{c3} \\ \left(2\pi-\theta\right)/\theta_{c3} & for\ \ 2\pi-\theta_{c3} \le \theta \le 2\pi \end{cases}$

calculate radial leakages.

Equations (3.136), (3.137), (3.141) and (3.142) govern intermediate pressure buffers in suction and exhaust pipes. Because of the constant motor speed assumption, time derivatives in aforementioned equations can convert to angle derivatives via $d(\cdot)/dt = \Omega\, d(\cdot)/d\theta$. Therefore, the governing equations of pressure buffers are:

$$\frac{dP_{spk}}{d\theta} = \frac{1}{\Omega V_{spk}}\left[\left(\gamma-1\right)\dot{Q}_{Hspk} + \gamma Q_{spko} - \gamma Q_{spko}\right], \tag{4.4}$$

$$\frac{dT_{spk}}{d\theta} = \frac{1}{\Omega V_{spk}}\left[\left(\gamma-1\right)\frac{\dot{Q}_{Hspk}T_{spk}}{P_{spk}} + \frac{Q_{spki}T_{spk}}{P_{spk}}\left(\gamma-\frac{T_{spk}}{T_{spki}}\right) - \frac{Q_{spko}T_{spk}}{P_{spk}}\left(\gamma-\frac{T_{spk}}{T_{spko}}\right)\right], \tag{4.5}$$

$$\frac{dP_{epk}}{d\theta} = \frac{1}{\Omega V_{epk}}\left[\left(\gamma-1\right)\dot{Q}_{Hepk} + \gamma Q_{epki} - \gamma Q_{epko}\right], \tag{4.6}$$

$$\frac{dT_{epk}}{d\theta} = \frac{1}{\Omega V_{epk}}\left[\left(\gamma-1\right)\frac{\dot{Q}_{Hepk}T_{epk}}{P_{epk}} + \frac{Q_{epki}T_{epk}}{P_{epk}}\left(\gamma-\frac{T_{epk}}{T_{epki}}\right) - \frac{Q_{epko}T_{epk}}{P_{epk}}\left(\gamma-\frac{T_{epk}}{T_{epko}}\right)\right]. \tag{4.7}$$

Equations (2.20), (2.22) and (2.24) give pipe throughput in the laminar and molecular flow regimes.

$$Q_{LCP,Poiseuille} = \frac{\pi D^4}{256\eta L}\left(P_1^2 - P_2^2\right),\ Q_{LCP,molecular} = \frac{\pi D^3}{12L} v_{avg}\left(P_1 - P_2\right),$$

$$Q_{Knudsen} = Q_{LCP,Poiseuille} + Q_{LCP,molecular} \cdot Z .$$

Equations (2.38) and (2.45) produce pipe throughputs in the transitional and turbulent flow regimes, respectively.

$$Q_{LCP,turbulent} = \left(\frac{1}{f_l}\frac{\pi^2 D^5}{8L} RT \frac{P_1^2 - P_2^2}{2}\right)^{\frac{1}{2+a}} \cdot \left(\frac{\pi D R T \eta \,\mathrm{Re}_{D,l}}{4}\right)^{\frac{a}{2+a}},$$

$$Q_{LCP,transitional} = \left(\frac{1}{f_l}\frac{\pi^2 D^5}{8L} RT \frac{P_1^2 - P_2^2}{2}\right)^{\frac{1}{2+a}} \cdot \left(\frac{\pi D R T \eta \,\mathrm{Re}_{D,l}}{4}\right)^{\frac{a}{2+a}}.$$

Equations (2.58)-(2.60) determines throughput via a fitting and assorted parts of a suction or exhaust pipe.

$$Q_{other\ pipes} = Q_{minor} + Q_{intrinsic} \cdot Z \ ,\ Q_{minor} = \left(\frac{\pi D^2}{4}\right)\left(\frac{2RT_1}{K_{minor}}\frac{P_1^2 - P_2^2}{2}\right)^{1/2}$$

$$Q_{intrinsic} = P_{tr,intrinsic} C_{AP} P_1 .$$

Here P_1 and P_2 are upstream and downstream nodal pressures of a pipe component, D is a pipe diameter and L is a pipe length. Equation (3.140) describes the choking criteria for suction and exhaust pipe components.

1. *Calculate the critical discharge pressure of* k^{th} *pipe*

$$\left(P_2^*\right)_k = \left(P_1\right)_k \sqrt{\frac{\left(F\right)_k}{\left(S_2^*\right)_k + \left(F\right)_k}} \qquad \textit{where} \quad \left(S_2^*\right)_k = A_c \sqrt{R\left(T_1\right)_k 2\gamma/(\gamma+1)} \quad \textit{and}$$

$$\left(F\right)_k = \frac{1}{\left(f_l\right)_k} \frac{\pi^2 \left(D\right)_k^{\,5}}{8\left(L\right)_k} \frac{R\left(T_1\right)_k}{2}$$

2. *Perform choking test*

$$\left(Q_{NIP}\right)_k = \begin{cases} Q_{NIP}\left(\left(P_1\right)_k, \left(P_2\right)_k, \ldots\right) \textit{ if } \left(P_2\right)_k > \left(P_2^*\right)_k \textit{ ; no choking} \\ Q_{NIP}^*\left(\left(P_1\right)_k, \left(P_2^*\right)_k, \ldots\right) \textit{ if } \left(P_2\right)_k \le \left(P_2^*\right)_k \textit{ ; choking} \end{cases}$$

Figure 4.1 overviews the vacuum pump model including states, parameters, and primary equation and table numbers.

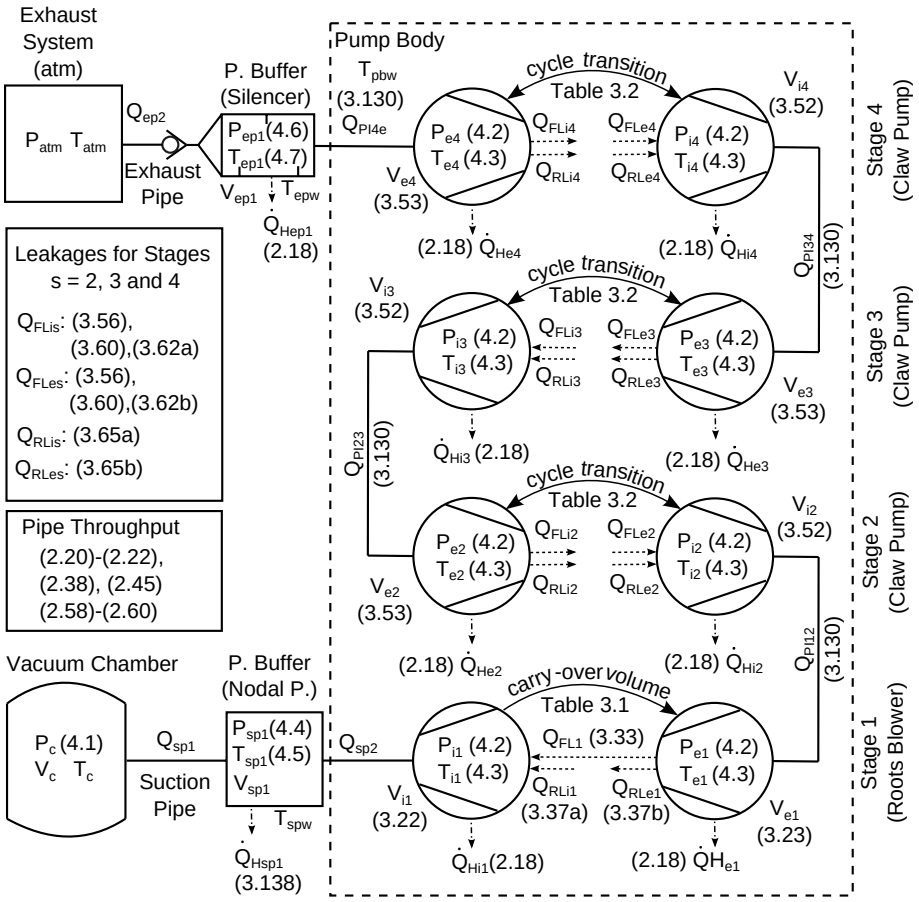

Figure 4.1: Pump Model with References.

4.2.2 Baseline Model Parameters

Baseline model parameters associated with a healthy vacuum pump are given below. The steep torque-speed curve of an induction motor [49] and the use of an inverter (speed controller) [8] and a powerful motor render constant pump speed Ω. Here the frequency of power lines is 60Hz and the number of rotor poles is two. Considering a small slip speed of about 2 ~ 5%, the motor speed is set to 3520 rpm. Table 4.1 summarizes the motor specifications.

Parameter	Value	Unit
Motor Speed Ω	3520 (368.61)	rpm (rad/s)
Power Frequency	60	Hz
Num. of Rotor Poles	2	n/a

Table 4.1: Motor Drive Specifications.

Table 4.2 summaries the properties of evacuated gas, which is atmospheric air at room temperature.

Parameter	Value	Unit
Specific Heat Ratio γ	1.4	n/a
Specific Gas Constant R	287.058	J/kg·K
Constant Volume Specific Heat c_v	717.645	J/kg·K
Constant Pressure Specific Heat c_p	1004.703	J/kg·K
Ref. Dynamic Viscosity η_o	1.83643×10^{-5}	Pa·s
Prandtl Number P_r	0.73684	n/a
Atmospheric Pressure P_{atm}	100	kPa
Atmospheric Temperature T_{atm}	298	K

Table 4.2: Evacuated Gas Properties.

The vacuum chamber is initially filled with atmospheric air at room temperature. The vacuum chamber volume is set to 5 m^3 (≈1.7m×1.7m×1.7m).

Parameter	Value	Unit
Chamber Pressure P_c	100	kPa
Chamber Temperature T_c	298	K
Chamber Volume V_c	5	m^3

Table 4.3: Vacuum Chamber Specifications.

Little data about vacuum pump dimensions is available in the literature. Table 4.4 was constructed via educated guessing based on Refs. [8,50] and the pump geometry analysis in Chapter 3. V_{add1} is an intermediate volume, which connects Roots blower's outlet port to the inlet port of the second stage claw pump, and A_{add1} is the area of V_{add1}.

Parameter	Value	Unit
Stator Radius R_s	0.06	m
Pitch Radius of Stage 1 R_{p1}	0.04	m
Pitch Radius of Stage 2 R_{p2}	0.04	m
Pitch Radius of Stage 3 R_{p3}	0.04	m
Pitch Radius of Stage 4 R_{p4}	0.04	m
Stator Height of Stage 1 H_{s1}	0.03	m
Stator Height of Stages 2 H_{s2}-	0.02	m
Stator Height of Stage 2 H_{s3}	0.02	m
Stator Height of Stage 4 H_{s4}	0.02	m
Intermediate Vol. for Roots Blower V_{add1}	0.001	m^3
Area of Intermediate Vol. A_{add1}	0.072	m^2

Table 4.4: Vacuum Pump Dimensions.

The suction pipe diameter is set to 0.04m, which is the inner diameter specification of a NW40 pipe which can attach to the inlet flange ISO63 in manufacturer's manuals [8,50]. The suction pipe (*sp*) comprises two circular pipes identified with subscripts *sp1* and *sp2*. The pressure buffer at the pipe joint has an arbitrary volume V_{sp1} and area A_{sp1}.

Parameter	Value	Unit
Pipe Diameter (NW40) D_{sp}	0.04	m
Pipe Surface Roughness ε/D	10^{-3}	n/a
Component 1's Length L_{sp1}	1.0	m
Component 2's Length L_{sp2}	1.0	m
Pressure Buffer 1's Volume V_{sp1}	0.001	m^3
Pressure Buffer 1's Area A_{sp1}	0.2513	m^2

Table 4.5: Suction Pipe Specifications.

The exhaust pipe has a smaller conductance than the suction pipe. The exhaust pipe diameter specification is NW40 [8,50], and the pipe length is several times longer than the suction pipe. A cavity V_{ep1} between the outlet of the fourth stage claw pump stage and a check valve is large enough to reduce a peak-to-peak pressure variation.

Parameter	Value	Unit
Pressure Buffer 1's Volume V_{ep1}	0.0081	m^3
Pressure Buffer 1's Area A_{ep1}	0.294	m^2
Pipe Diameter (NW40) D_{ep2}	0.04	m
Pipe Surface Roughness ε/D	10^{-3}	n/a
Component 2's Length L_{ep2}	10.0	m

Table 4.6: Exhaust Pipe Specifications.

The same port interface was used for all four stages to reduce model complexity. The outer and inner port radii were set to 90% and 60% of the pitch radius, respectively. The port interface is thin; the port thickness was set to 0.01 m. Table 4.7 summarizes the port interface related dimensions.

Parameter	Value	Unit
Outer Port Radius R_{oPI}	0.024	m
Inner Port Radius R_{iPI}	0.036	m
Median Port Radius R_{mPI}	0.03	m
Port Thickness L_{tPI}	0.01	m

Table 4.7: Port Interface Dimensions.

All four stages have the same ratio of pitch radius to stator radius (i.e. r_{ps} = 2/3). The claw rotors have the same shape and characteristic angles.

Parameter	Value	Unit
Rotor Profile Ch. Angle θ_{c1}	0.5053 (28.95)	rad (degree)
Rotor Profile Ch. Angle θ_{c2}	0.8127 (46.56)	rad (degree)
Rotor Profile Ch. Angle θ_{c3}	0.8410 (48.18)	rad (degree)

Table 4.8: Claw Rotor Characteristic Angles.

Table 4.9 summarizes port interface related angles. A port opening angle θ_{po} equals to θ_{c3}. Port angular span θ_{port} was set to 180 degrees. The flow entrance angle θ_{ePI} was calculated based on the port dimensions in Table 4.8.

Dry vacuum pumps require small clearances to work efficiently. Dry vacuum pumps warm up for 10 to 20 minutes to achieve a typical operational clearance [8, 50]. During a normal operation, thermal expansion of internal components can be neglected, thus leakage clearances can be assumed constant. A typical internal clearance of a dry vacuum pump is about 0.1 mm (4 mils) [4,45]. The internal clearances were assumed identical for all four stages except for the claw to claw clearance. Table 4.10 summarizes clearance parameters.

Parameter	Value	Unit
Port Opening Angle θ_{po}	0.8410 (48.18)	rad (degree)
Port Span Angle θ_{port}	3.1415 (180)	rad (degree)
θ_{oPI}	1.1751 (67.32)	rad (degree)
θ_{iPI}	1.1201 (64.17)	rad (degree)
Flow Entrance Angle θ_{ePI}	0.5830 (33.40)	rad (degree)
Port Profile Angle θ_{b*}	0.0137 (0.785)	rad (degree)
Port Profile Angle θ_{c*}	1.1976 (68.61)	rad (degree)
Port Profile Angle θ_{f*}	3.1191 (178.71)	rad (degree)
Port Profile Angle θ_{g*}	4.3029 (246.53)	rad (degree)

Table 4.9: Port Interface Angles.

Parameter	Value		Unit
	Roots Blower	Claw Pumps	
Radial Clearance C_{r0} *for* $\theta_{c3} \le \theta \le 2\pi - \theta_{c3}$	0.0001	0.0001	m
Radial Clearance C_{r0} *for* $-\theta_{c3} \le \theta \le \theta_{c3}$	0.0001	0.001	m
Axial Clearance C_{a0}	0.0001	0.0001	m

Table 4.10: Internal Clearance Specifications of Claw Pump.

When claws engage at the beginning of an intake cycle and the end of an exhaust cycle (i.e. $-\theta_{c3} \le \theta \le \theta_{c3}$), chamber pressure increases excessively due to high volume efficiency of claw pumps. Vacuum pump manufacturers revise the dedendum section of a claw rotor profile to induce large leakage and avoid an excessive pressure build-up. Indeed simulations without a profile change from the ideal cycloidal rotor exhibited a large pressure, which could indicate either numerical instability and/or physical rotor issues. Here radial clearance was set to 30 times larger for $-\theta_{c3} \le \theta \le \theta_{c3}$, as listed in

Table 4.10. Figure 4.2 shows the revised dimensionless base area function, which reflects the rotor profile change. Table 4.11 tabulates the coefficients of the revised base area function.

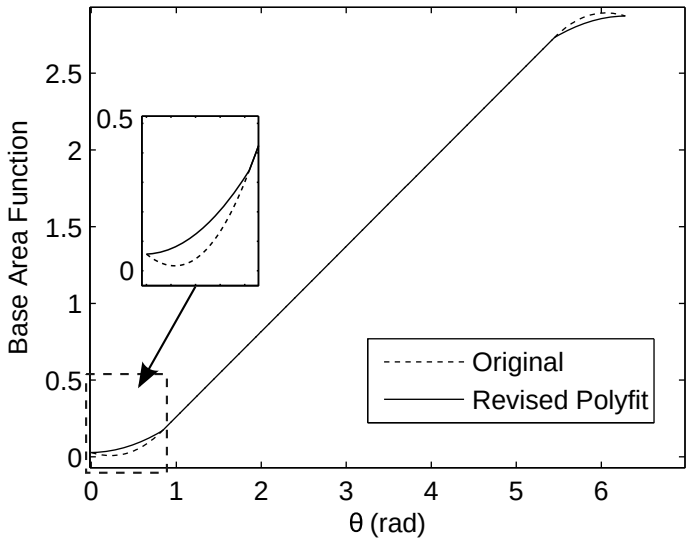

Figure 4.2: Revised Base Area Functions with $r_{ps} = 2/3$.

Region	Polynomial Coefficients		
	c_2	c_1	c_0
$0 \le \theta \le \theta_{c3}$	1.9492×10^{-1}	6.5336×10^{-3}	2.8315×10^{-2}
$\theta_{c3} \le \theta \le 2\pi-\theta_{c3}$	2.39×10^{-8}	5.5555×10^{-1}	-2.9483×10^{-1}
$2\pi-\theta_{c3} \le \theta \le 2\pi$	-1.9492×10^{-1}	2.4560	-4.8638

Table 4.11: Revised Dimensionless Base Area Function for $r_{ps} = 2/3$.

Dry vacuum pumps employ an automatic cooling system [8,50] to maintain a constant temperature and prevent rotor seizure. Calculation of heat transfer in working chambers requires a temperature gradient. But little experimental data was found in the

literature, and heat transfer coefficients found in some literature varied considerably. Ref. [38] listed 10 to 50 W/K·m^2 for a typical gas to water heat exchanger. Ref. [51] reported the heat transfer coefficient of positive displacement compressors running at 3000 rpm ranged from 500 to 1600 W/K·m^2. Ref. [52] proposed an empirical formula for a reciprocal compressor,

$$h_H = 0.053 \frac{k_H}{D_{eq}} Re_{eq}^{0.8} Pr^{0.6} \quad . \tag{4.8}$$

Here $D_{eq} = Volume/\left(Area/6\right)$ is the equivalent diameter, $\mathrm{Re}_{eq} = \rho D_{eq}(D_{eq} 2\Omega)/\eta$ is the equivalent Reynolds number, and Pr is Prandtl number. Using the above pump parameters, D_{eq} = 0.044 m and h_H = 223 W/K·m^2 for a Roots blower, and D_{eq} = 0.029 m and h_H =190 W/K·m^2 for the second stage claw pump.

By comparison, the suction pipe with a turbulent flow (R_{eD} = 8.3×10^4) has a convective heat transfer coefficient of 241 W/K·m^2. However, the fact that a pipe without an active cooling mechanism has a higher heat transfer coefficient contradicts physical intuition. Based on preliminary simulation results, the heat transfer coefficient for pumping chambers was set to 400 W/K·m^2. Equating the heat transfer power of a pumping chamber to convective heat transfer power renders

$$h_H = \frac{9\gamma - 5}{4} \frac{\eta c_v}{\Delta y} . \tag{4.9}$$

Here γ is the specific heat ratio, η is dynamic viscosity, c_v is constant volume specific heat and Δy is a undetermined distance to match the above two heat transfer coefficients. For h_H=400 W/K·m^2, $\Delta y \approx 0.001 \times R_s$.

Ref. [50] states the normal operating temperature of a similar sized dry vacuum pump ranges from 50 to 60 ^{o}C. The pump body wall temperature was set to 328 K (55 ^{o}C). Since the suction pipe is exposed to open air, the suction pipe wall temperature was

set equal to atmospheric temperature. The silencer directly attached to the pump exit is typically enclosed in a pump housing [8, 50]. The wall temperature of an exhaust silencer (part of an exhaust pipe) was set to a median temperature between T_{pbw} and T_{spw}. Table 4.12 summarizes the heat transfer parameters.

Parameter	Value	Unit
Thermal Distance $\Delta y / R_s$	0.001	n/a
Pump Body Temperature T_{pbw}	328	K
Suction Pipe Wall Temperature T_{spw}	297	K
Silencer Wall Temperature T_{epw}	315	K

Table 4.12: Heat Transfer Parameters.

4.2.3 Simulation Technique

The vacuum pump model's equations are highly nonlinear and very stiff, due to thermodynamics, gas mixing, highly variable throughput, and choking, among others. A stiff system requires a stiff solver. This work used the numerical solver CVODE of the SUNDIALS (SUite of Nonlinear and DIfferential/ALgebraic equation Solvers) numerical package publically available via Lawrence Livermore National Laboratory [53]. The CVODE solver varies order from 1st to 5th using Backward Differentiation Formula, and steps using Modified Newton's iteration to solve a stiff ODE system efficiently [54].

After a user defines a fixed integration interval, a stiff solver selects optimal order and sub-steps to perform an accurate integration. However, an abrupt change of states and inputs during integration can make a simulation numerically unstable. For instance, gas mixing during a cyclic transition requires an instantaneous re-initialization of states, which renders a discontinuity. To avoid the discontinuity pitfall, state re-initialization

must occur between integration processes. Propagating simulation through rotor angle θ instead of time t allowed a precise control over the timing of a cyclic transition.

Large differences in the magnitude of states also influence numerical stability, especially for a stiff system. To make the pressure computations order of magnitude comparable to the temperature computations, the pressure and temperature states were divided by 10^5 and 10^2, respectively.

4.3 HEALTHY VACUUM PUMP SIMULATION AND VALIDATION

4.3.1 Simulation Results with Baseline Parameters

Figures 4.3 to 4.8 show the pressures and temperature of vacuum pump simulations under three different initial conditions. The total number of states is 21, which include the pressures and temperatures of eight pumping chambers and two pressure buffers, and the pressure of a main vacuum chamber. Subscripts *i* and *e* denote intake and exhaust chambers, and subscript number indicates stage number. Subscripts *sp* and *ep* stand for suction pipe and exhaust pipe, and a number followed by the subscript denotes an index number of nodal pressure buffers.

Figures 4.3 and 4.4 show the results of the first case where all initial pressures were set to atmospheric pressure P_{atm} (≈ 100kPa). The vacuum chamber evacuates as the chamber pressure P_c slowly decreases. The first stage pressures P_{i1} and P_{e1}, and the nodal pressure of the suction pipe P_{sp1} oscillate 4 times every revolution due to the pumping action of the Roots blower. Here P_{e1} slowly increases then stays slightly above P_{atm}. The second to fourth intake chamber pressures P_{i2}, P_{i3} and P_{i4} initially decrease as chamber volumes expand. They increase rapidly during port opening, maintain the max level, and decrease during port closing. The second to fourth exhaust pressures P_{e2}, P_{e3} and P_{e4} exhibit a large peak of about 5 times P_{atm} as claws start to interact and trapped gases

squeeze out. The exhaust pipe pressure P_{ep1} pulsates as the fourth exhaust chamber releases gas into the exhaust pressure buffer. Temperatures show similar trends but the variations are smaller. The temperatures stay slightly above the corresponding wall temperatures, except that the temperatures in the second to fourth exhaust chambers peak at about 400K.

In the second case, the initial pressures were set to 10 kPa except for P_{ep1} which remains at P_{atm} (=100 kPa). Otherwise, the silencer only accumulates gas till the pressure reaches P_{atm}. Figures 4.5 and 4.6 show the second case results. Here pressures and temperatures become 10 times smaller, but the overall trends do not change much from the previous case ($P_{initlal}$ =100 kPa). In general, a throughput transfers to the next stages, but the throughput across the last port interface temporarily reverses to equalize P_{e4} and P_{ep1}. As a result, P_{ep1} dips when P_{e4} is smaller than P_{ep1}. As claws engage in the last stage, a large pressure difference between P_{e4} and P_{i4} increases leakage, to cause distinguishable peaks on P_{i4}. However, P_{e2} and P_{e3} have smaller peaks, thus P_{i2} and P_{i3} do not show any peak. Also, P_{e1} rapidly goes through a transition period. The temperature trends resemble the aforementioned pressure characteristics. T_{e2} and T_{e3} reduce dramatically.

In the last case, the initial pressures were set to 1 kPa. Because a smaller throughput transfers through, the pressure and temperature changes are even smaller. However the peak P_{e4} remains at 400 kPa and a pressure difference $P_{e4} - P_{i4}$ becomes relatively larger. A leakage from *i4* to *e4* causes a more pronounced peak on P_{i4}

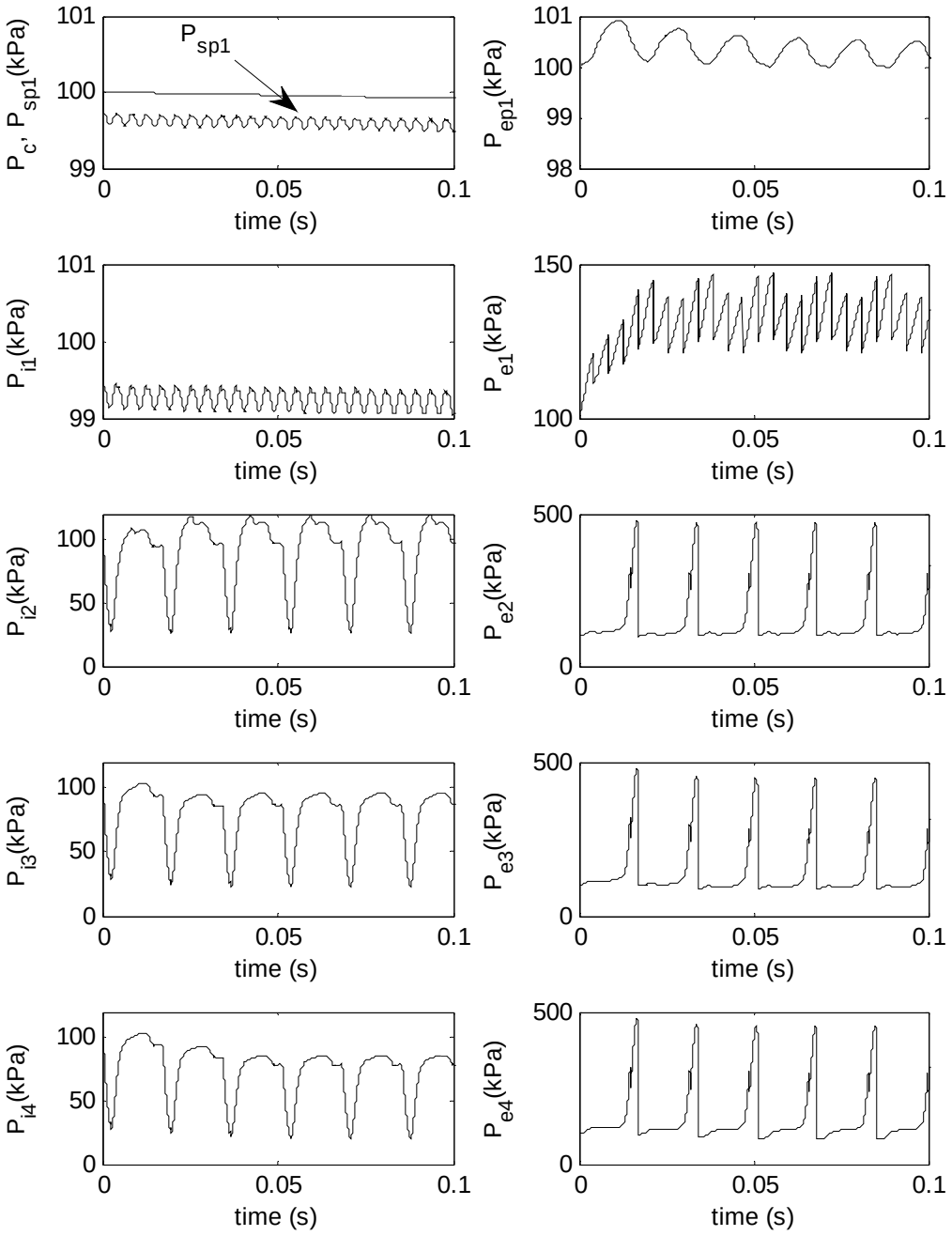

Figure 4.3: Baseline Pressures for P_{in} = 100 kPa.

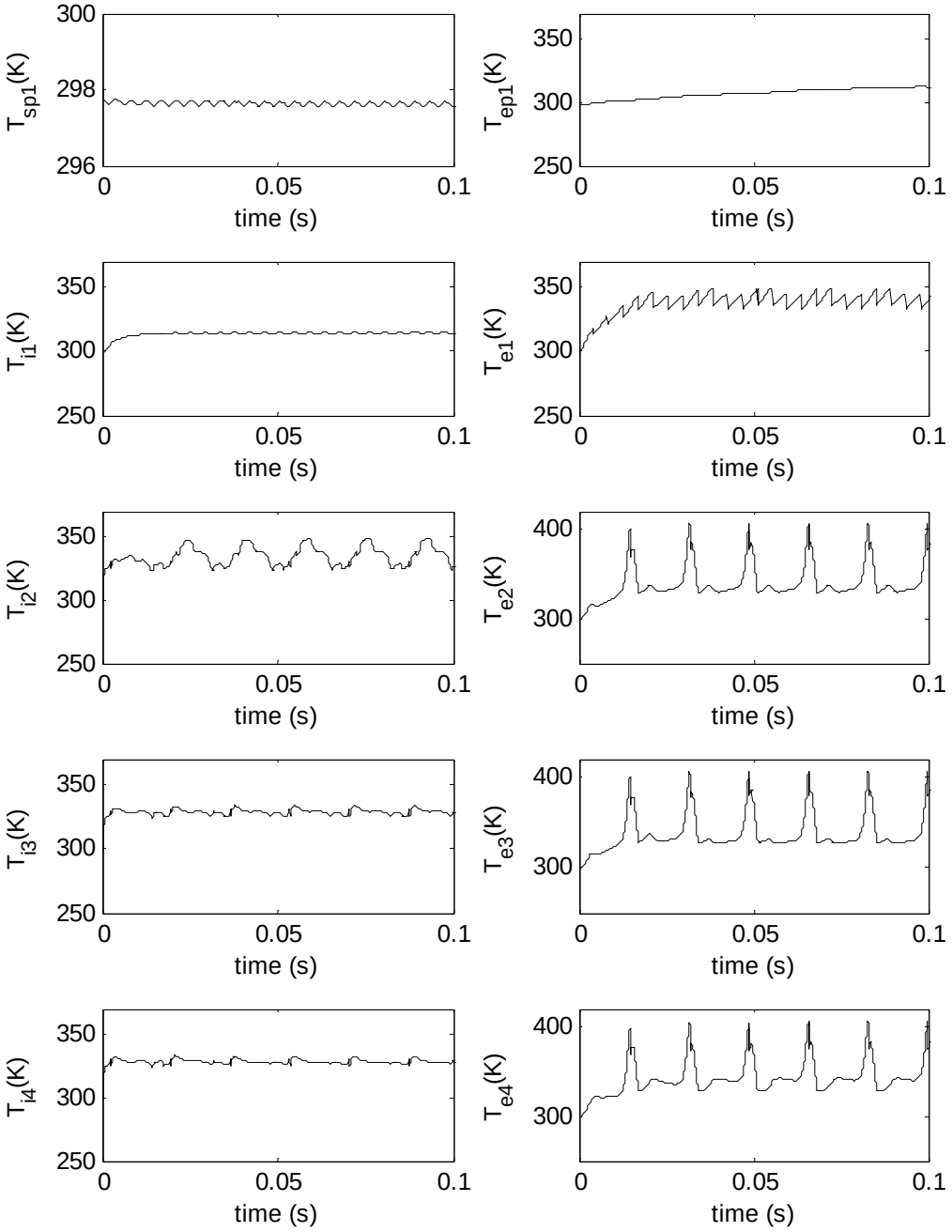

Figure 4.4: Baseline Temperatures for P_{in} = 100 kPa.

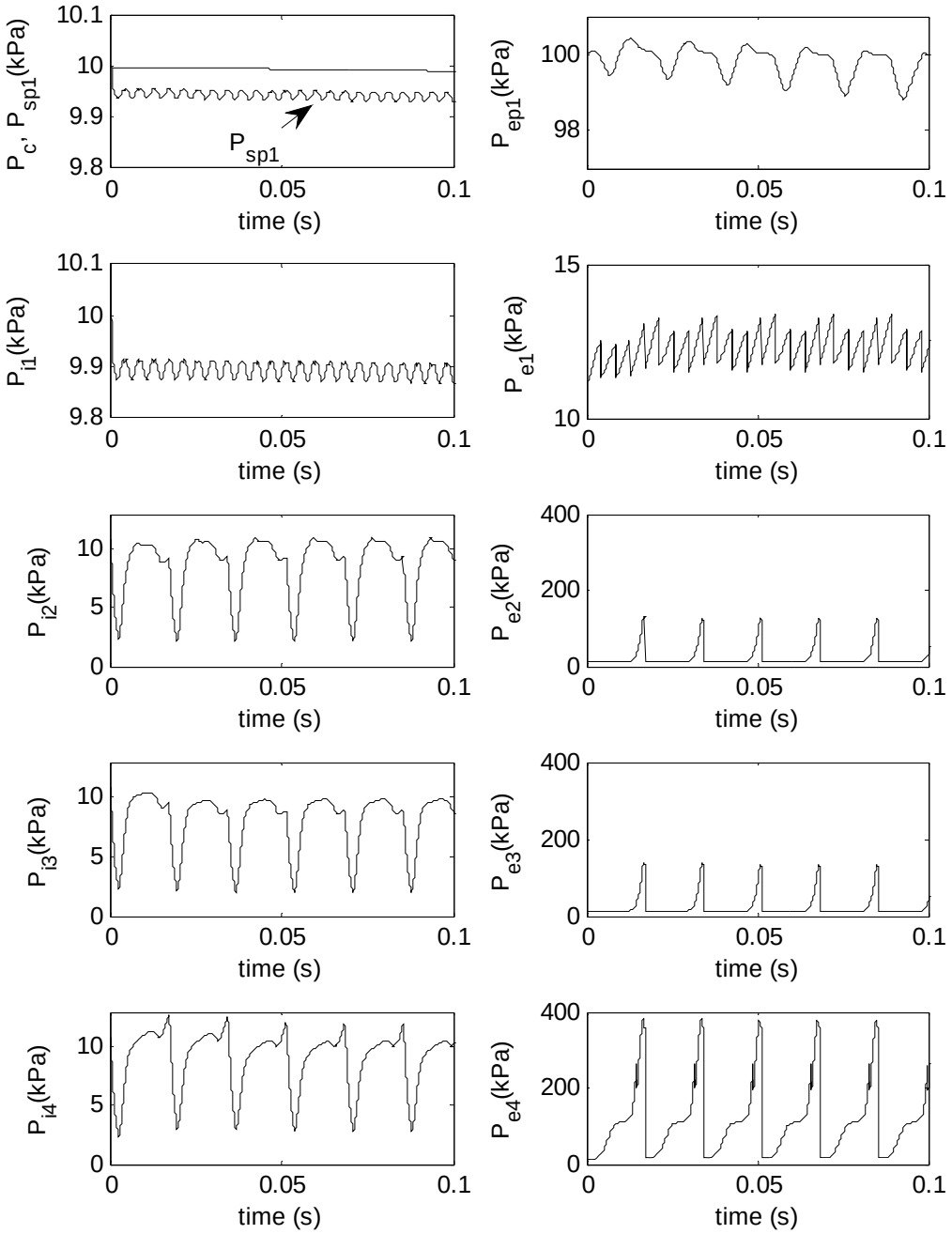

Figure 4.5: Baseline Pressures for P_{in} = 10 kPa.

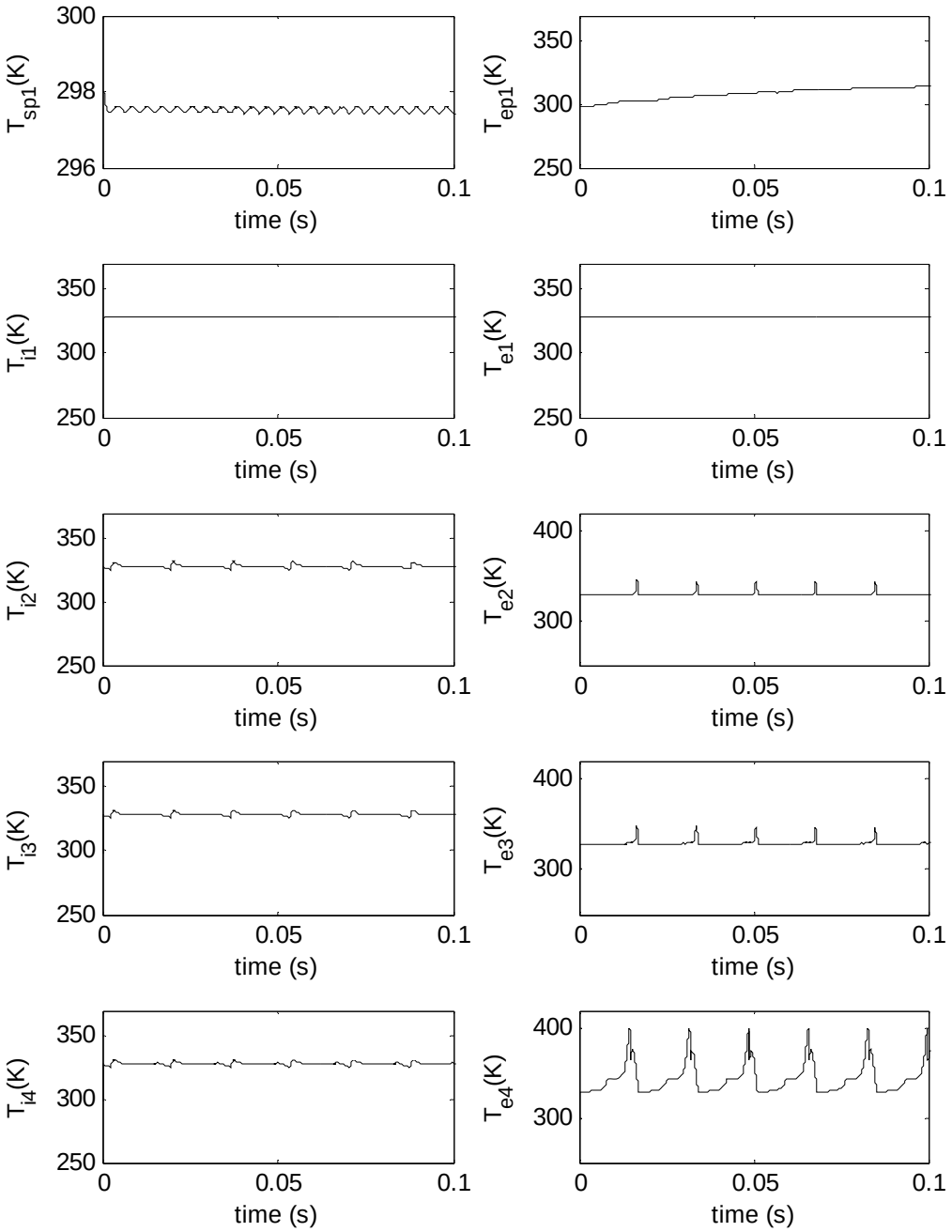

Figure 4.6: Baseline Temperatures for P_{in} = 10 kPa.

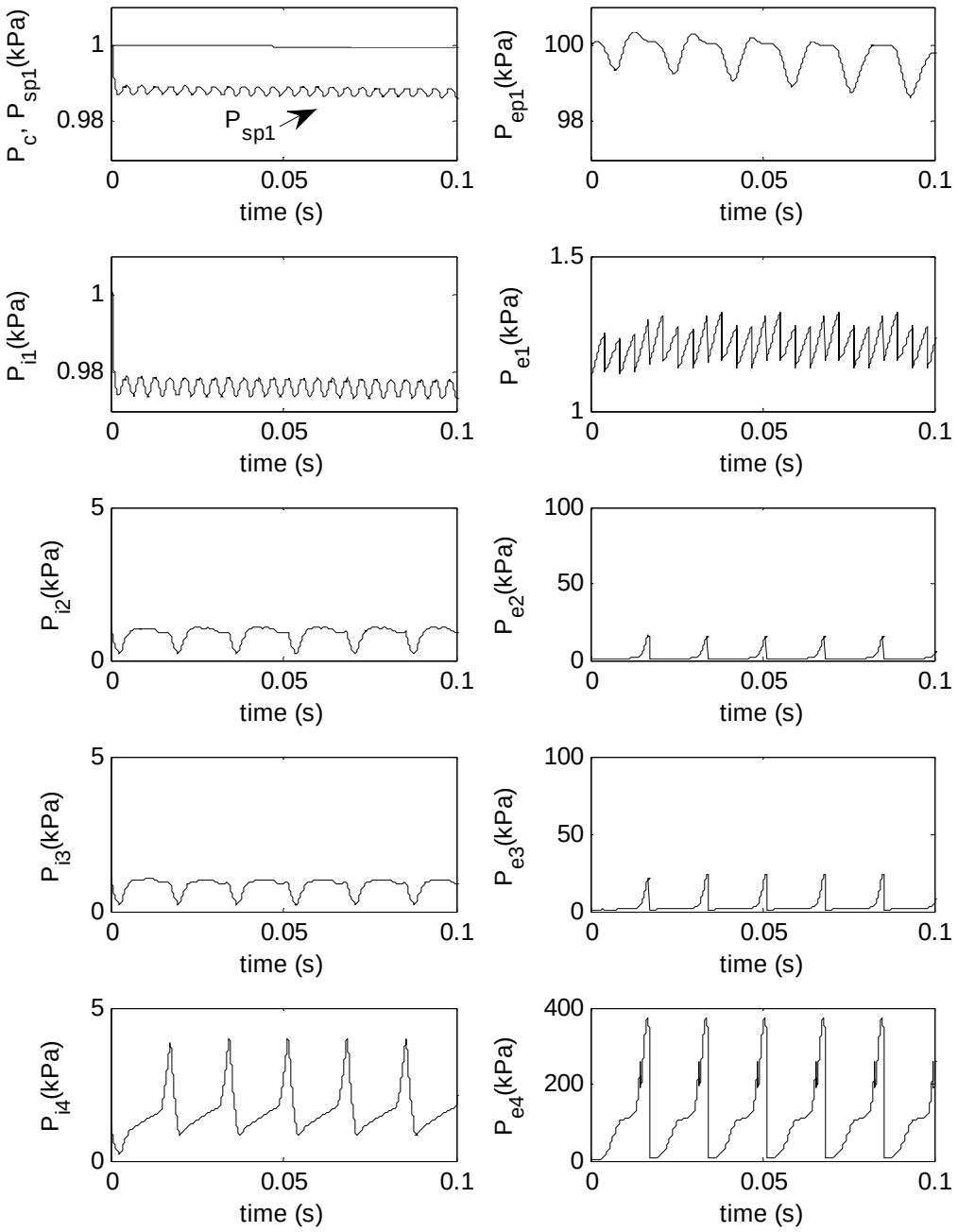

Figure 4.7: Baseline Pressure for P_{in} = 1 kPa.

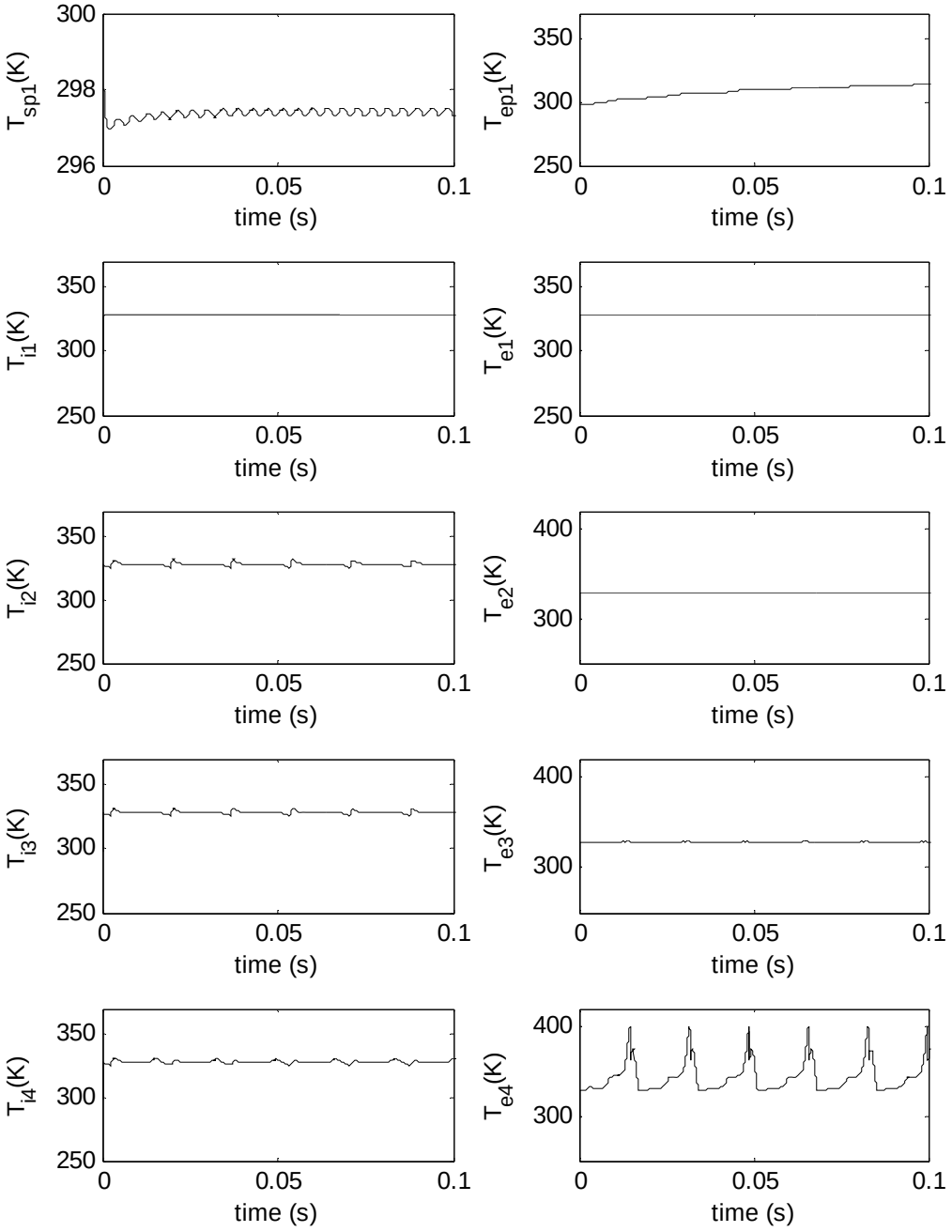

Figure 4.8: Baseline Temperatures for P_{in} = 1 kPa.

Figure 4.9 shows simulated performance curves versus pump inlet pressure. Also included for comparison are reference performance curves of a similarly-sized dry vacuum pump extracted from a manufacturer's manual [8].

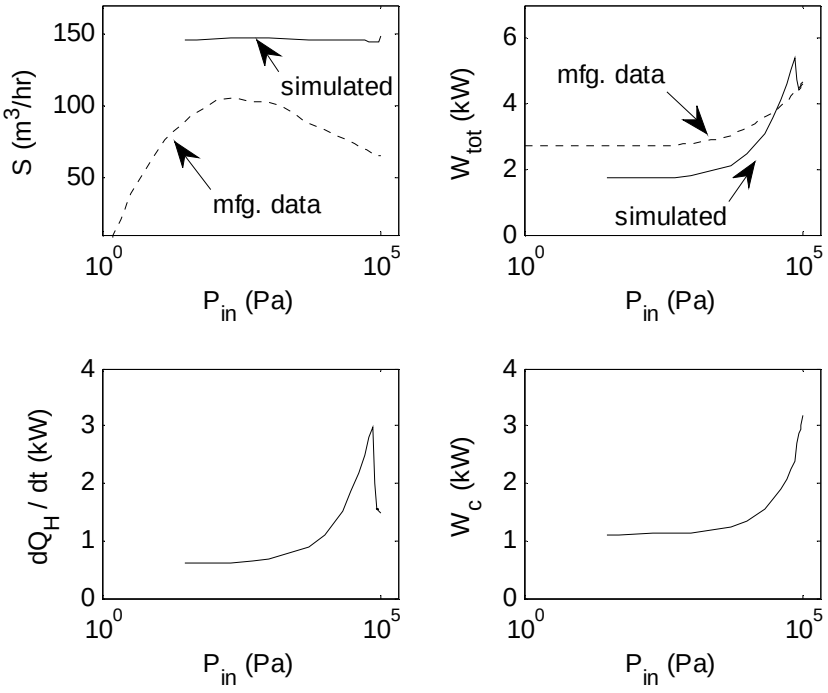

Figure 4.9: Baseline Performance Curves Compared with Reference Performance Curves (Dashed Lines).

Pumping speed S remains steady at about 145 m^3/hr, while the manufacturer's pumping speed curve peaks at about 1 kPa. Here total power W_{tot} denotes the sum of heat dissipation power dQ_H/dt and compression power W_c. Strictly speaking, total power must include power losses in auxiliary systems such as a gear box, a temperature control system, and an induction motor. The general trend of total power W_{tot} disagrees with manufactuer's power consumption curve in a high pressure range. Heat dissipation

power increases exponentially up to 70 kPa, then decreases between 70 kPa and 100 kPa. Compression power W_c increases exponentially up to 100 kPa.

4.3.2 Exploring the Design Space

Parameter tuning can minimize the discrepancies in pumping speed and total power curves, shown in Figure 4.9. This section summarizes some findings of a parametric study based on the baseline dry vacuum pump model.

The size of a Roots blower largely influences pumping speed *S*. Pump manufacturers typically provide an attachable booster vacuum pump (i.e. a large capacity Roots blower) if a high pumping speed is desired. Because of a fixed stator radius in the model, a larger stage height H_{s1} can simulate the increased capacity of the Roots blower. Figure 4.10 compares pumping speed curves with different stator heights H_{s1}. Pumping speed generally declines with a smaller capacity first stage Roots blower.

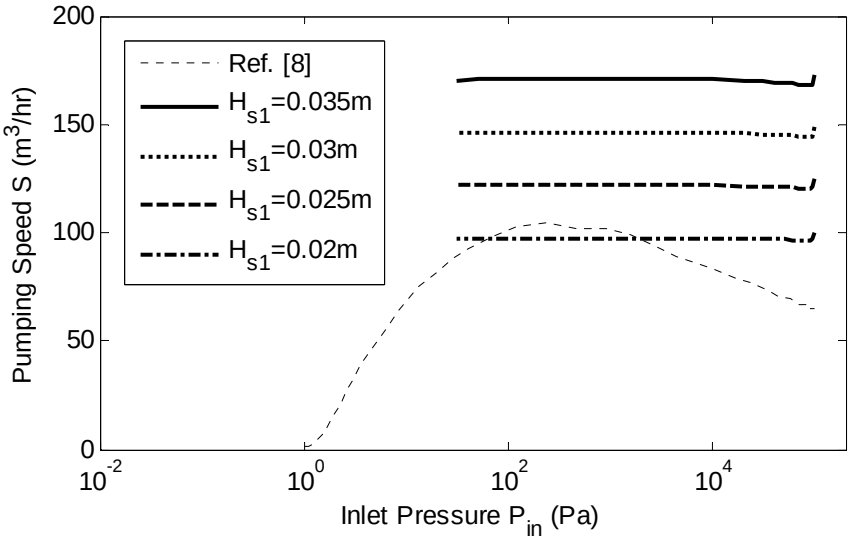

Figure 4.10: Effect of Roots Blower's Stator Height on Pumping Speed in Comparison with Manufacturer's Pumping Speed.

The internal leakage of the first stage Roots blower is largely responsible for a decreasing reference pumping speed from P_{in} = 1 kPa to 100 kPa. Figures 4.11 and 4.12 show the effects of clearance size on pumping speed. Here H_{s1} is set to 0.02 m. The pumping speed curve becomes close to the reference with increased internal clearances.

The size of the intermediate volume V_{add1} between the Roots blower outlet and the second stage input influences heat dissipation power at a high pressure. Figures 4.13 and 4.14 show that a smaller V_{add1} slightly increases a peak heat dissipation power and reduces the peak pressure. Here H_{s1} is set to 0.02 m while the other parameters remain unchanged.

The radial clearance between claws to the dedendum section of a claw rotor affects compression power. Here the second to fourth stage claw pumps have the same radial clearance. Figure 4.15 shows that a larger radial clearance reduces compression power.

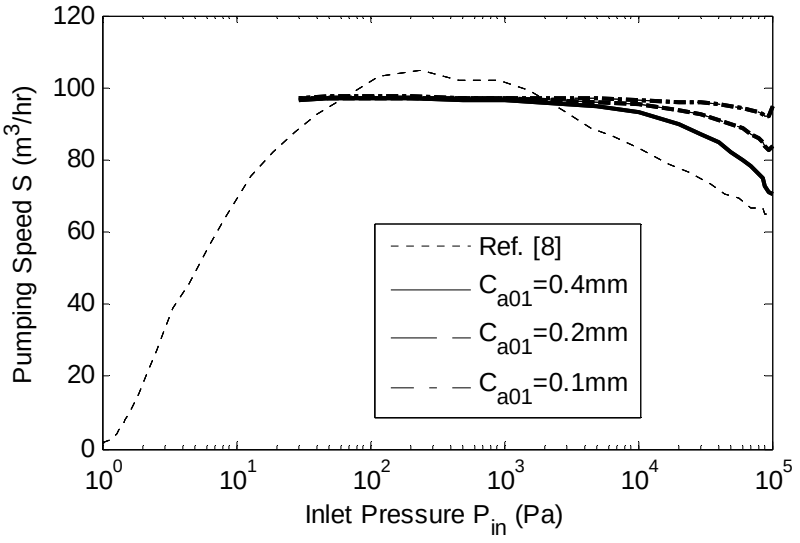

Figure 4.11: Effect of Roots Blower's Clearances on Pumping Speed for C_{r01} = 0.1 mm Compared with Manufacturer's Pumping Speed.

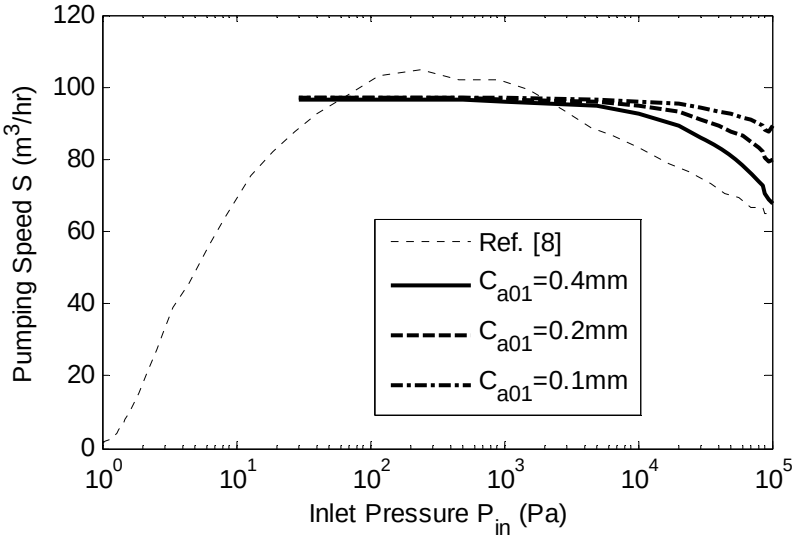

Figure 4.12: Effect of Roots Blower's Clearances on Pumping Speed for C_{r01} = 0.2 mm Compared with Manufacturer's Pumping Speed.

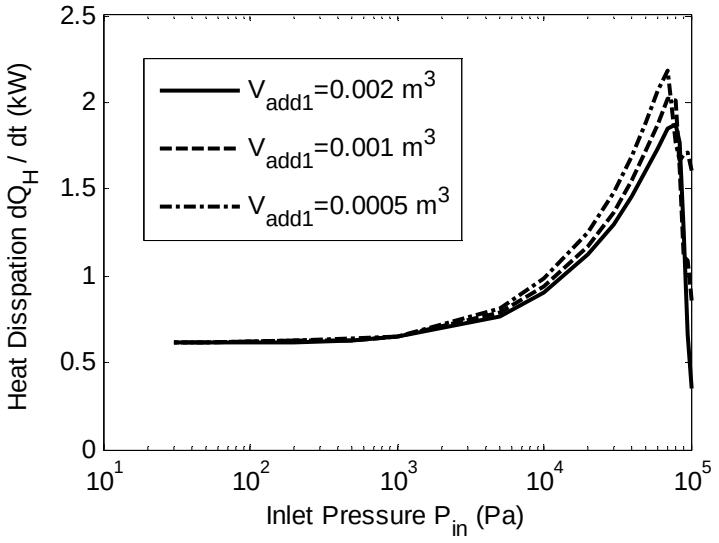

Figure 4.13: Heat Dissipation Power versus Intermediate Volume Size.

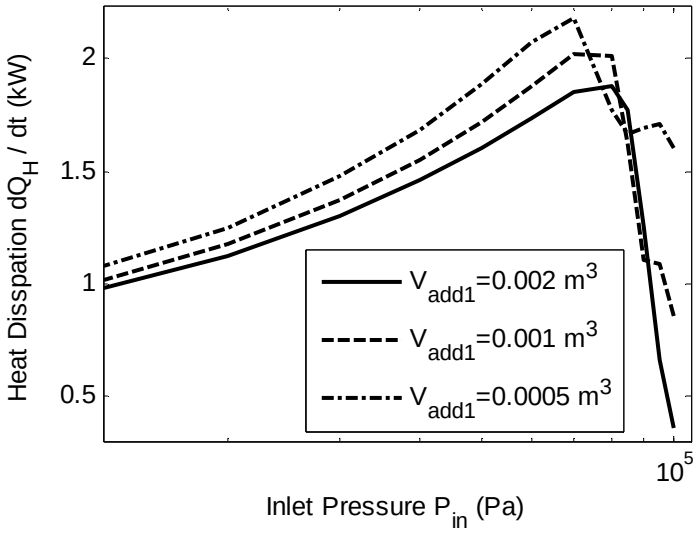

Figure 4.14: Heat Dissipation Power versus Intermediate Volume Size (Zoomed).

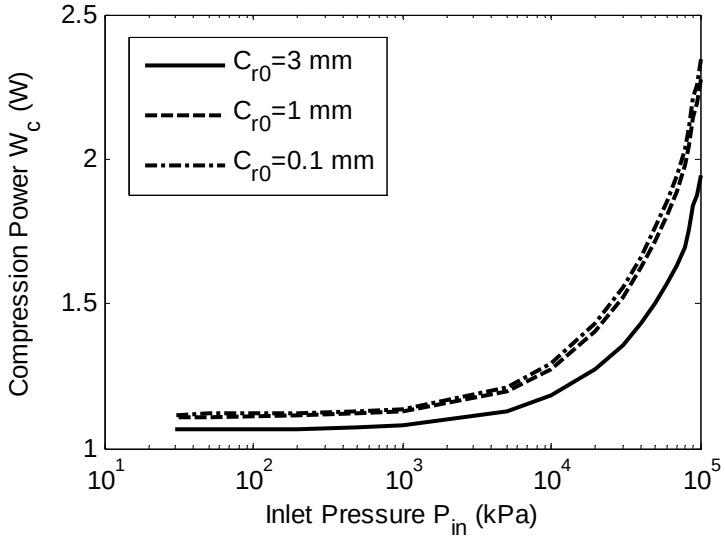

Figure 4.15: Compression Power vs. Radial Clearance between Claws to Rotor Dedendum.

The pipe length and relative roughness has a minimal effect on pumping speed, if a pipe is short and the surface is smooth. A 2 meter long stainless suction pipe with relative roughness $\varepsilon/D = 5.0\times10^{-5}$ generate a pumping speed S of 100.307 m^3/hr while a iron cast pipe with relative roughness $\varepsilon/D = 1.0\times10^{-3}$ yields S = 100.174 m^3/hr at the atmospheric inlet pressure.

Tinkering other model parameters also affected pump performance and altered pressure and temperature plots. However, due to limited space these results were omitted. Results regarding the internal clearances of claw pumps, and heat transfer coefficients will be saved for the next chapter.

4.3.3 Model Validation

Figure 4.16 compares performance curves of the tuned pump model versus manufacturer's data [8], simulated over the inlet pressure range between 30 Pa and 100 kPa. Parameter tuning was based on limited manufacturer's data and educated guessing, considering little performance specifications are available for accurate model validation. The parameter changes from the baseline model discussed in the previous section are tabulated in Table 4.13.

The Pumping speed differs from the manufacturer's data for pressures below 100Pa because of the inherent limit of the vacuum pump model. Molecular mobility changes in a low pressure as inter-molecular actions weaken. Fast rotating impellers of the Roots blower hinder molecular mobility, so that the pressure of a separating volume in the intake chamber decreases. Consequently, a pressure build-up occurs at the pump inlet and pumping speed suffers [4(p.313)]. Furthermore, desorption of absorbed gases from the vacuum chamber and the suction pipe increases pump inlet pressure, which degrades pumping speed.

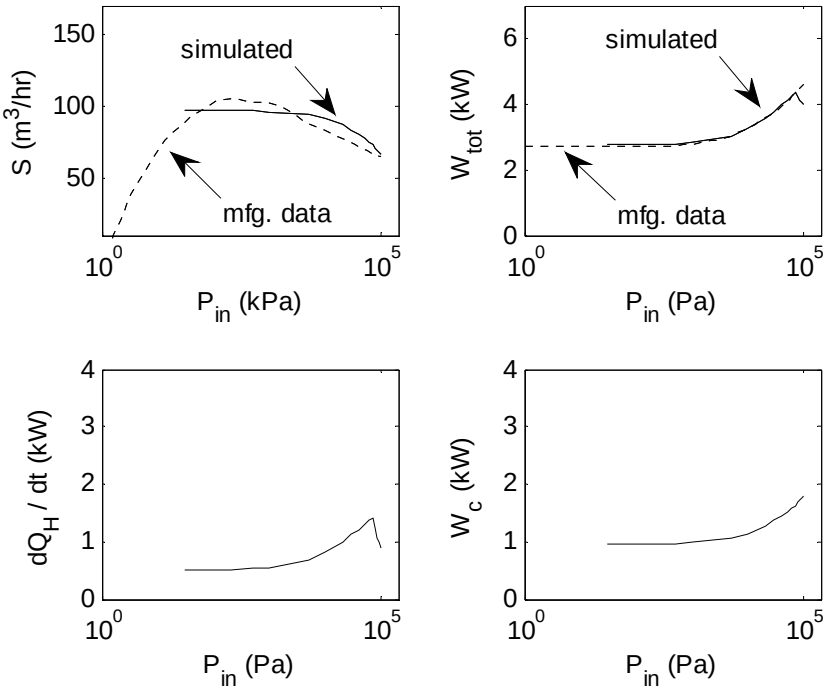

Figure 4.16: Performance Curves of Tuned Model Compared with Manufacturer's Data.

Parameter	Value		Unit
	Baseline	Tuned	
Roots Blower's Stator Height H_{s1}	0.03	0.02	m
Claw Pump's Stator Height H_{s2}, H_{s3}, H_{s4}	0.02	0.018	m
Roots Blower Radial Clearance C_{r01}	0.1	0.16	mm
Roots Blower Axial Clearance C_{a01}	0.1	0.2	mm
Claw to Dedendum Clearance C_{r02}, C_{r03}, C_{r04}	1.0	2.5	mm
Intermediate Volume V_{add1}	0.001	0.00035	m^3
Heat Transfer Area of V_{add1}	0.072	0.06	m^2
Pipe Relative Roughness ε/D (stainless steel)	0.001	5.0×10^{-5}	n/a
Flow Entrance Angle θ_{ePI} for PI_{12} *and* PI_{4e}	33.4	66.8	degree

Table 4.13: Tuned Parameter Values.

Total power W_{tot} in Fig. 4.16 was scaled by adding 1.3 kW uniformly across the pressure range to match the reference power consumption. During a steady state, the power consumption of the auxiliary systems (such as an induction motor and a gear box) can account for most of the discrepancy. The additional 1.3 kW that was added to the simulated curve of Figure 4.16 can be justified as follows: small induction motors with efficiency of about 85 to 90% [55] accounts for about 500 W power loss, and a gear pair of comparable size including bearings consumes about 700 W [56]. Manufacturer's manual [8] indicates that the maximum heat removal via a built-in cooling system is 2.5 kW, which is comparable to the sum of the maximum heat transfer power of approximately 1.5 kW and the additional power loss of 1.3 kW for scaling, presented earlier in this section.

The clearance changes increase Roots blower's leakage and reduce the peak pressures and compression power of claw pumps. Hollows on real-world rotor surfaces increase leakage [4(p.313)], which can justify the large clearances of the Roots blower.

Vacuum tubing is typically made of stainless steel, which has a roughness of 0.002 mm [37]. The port interfaces between the 1st to 2nd stages (PI_{12}), and the 4th to silencer (PI_{4e}) have a different port structure, and a viscous flow may enter at a higher angle. The doubled flow entrance angle was set based on an educated guess, since experimental data is not easily found in the literature.

4.3.4 Slow Dynamics and FFT Plots

Figures 4.17 and 4.18 show pressures and temperatures simulated for 10 seconds to reveal the slower dynamics of the tuned vacuum pump model. Large data hides details of cyclic pressure and temperature variations. However, the envelopes enclosing the pressure signals in Fig. 4.17 clearly show a slowly descending trend except, for P_{ep1}. Meanwhile the temperatures in Fig. 4.18 remain steady. Also, the thicker line in the plot

indicates a larger cyclic variation. Pressure and temperature variations per cycle in the exhaust chambers are larger than ones in the intake chambers. Here P_c and P_{sp1} are indistinguishable as P_c technically overlays P_{sp1}.

Figures 4.19 and 4.20 show the frequency contents of the above simulated pressures and temperatures. The original time signals were pre-processed to remove large DC contents before Fast Fourier Transformation (FFT), then the frequency components were normalized using the maximum amplitude (i.e. the maximum amplitude in the plot is 0 dB). Large frequency peaks in the plots are harmonics of the fundamental frequency component at 58.66 Hz (=3520 rpm / 60). The frequency envelope reveals that most energy lies in the low frequency range while non-trivial high frequency harmonics also reveal the nature of a complex thermo-fluid process inside pumping chambers. In Fig. 4.19, FFT of P_c is virtually identical to FFT of P_{sp1} except that P_c does not contain frequency peaks.

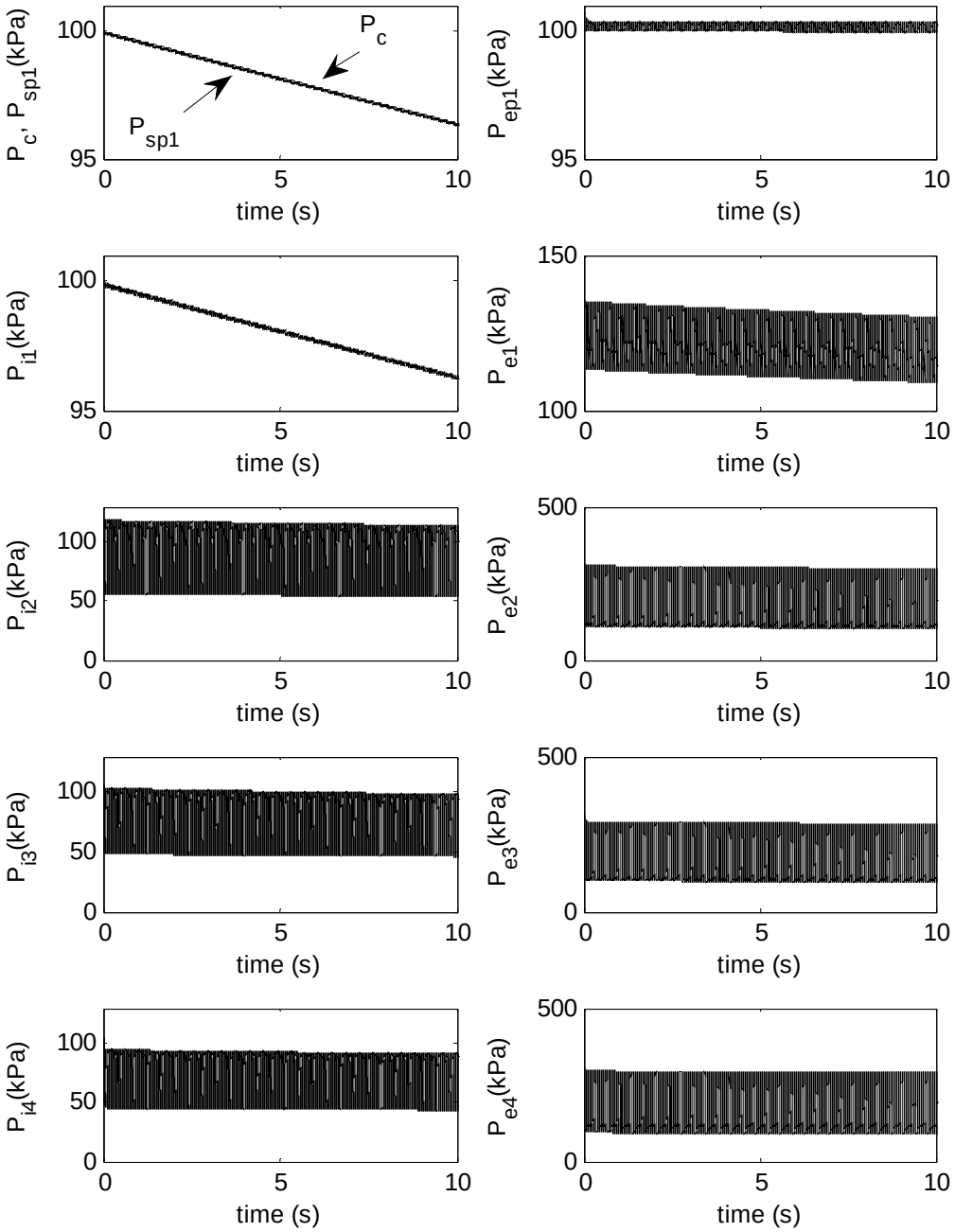

Figure 4.17: Slow Pressure Dynamics of Tuned Model for P_{in}=100 kPa.

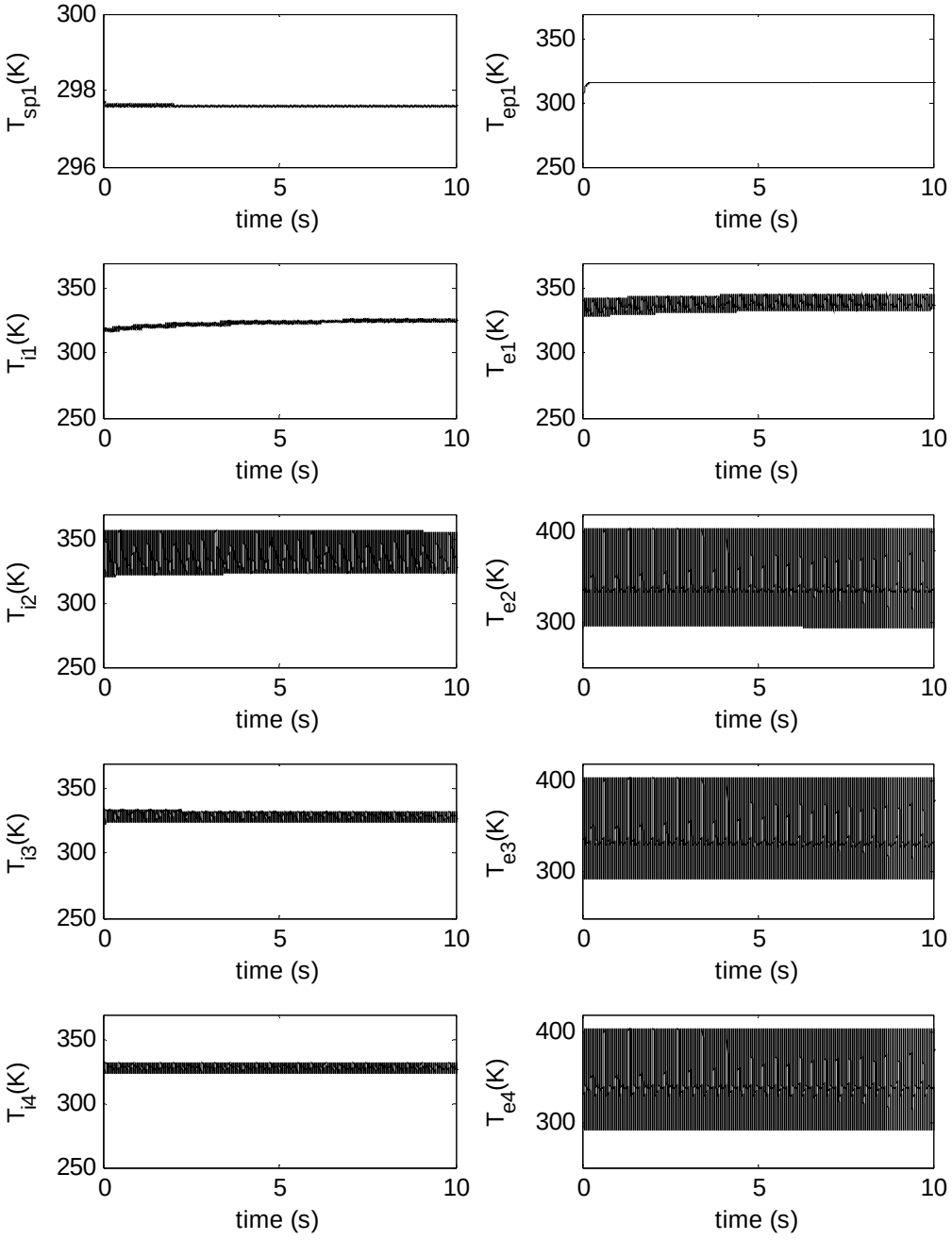

Figure 4.18: Slow Temperature Dynamics of Tuned Model for P_{in}=100 kPa.

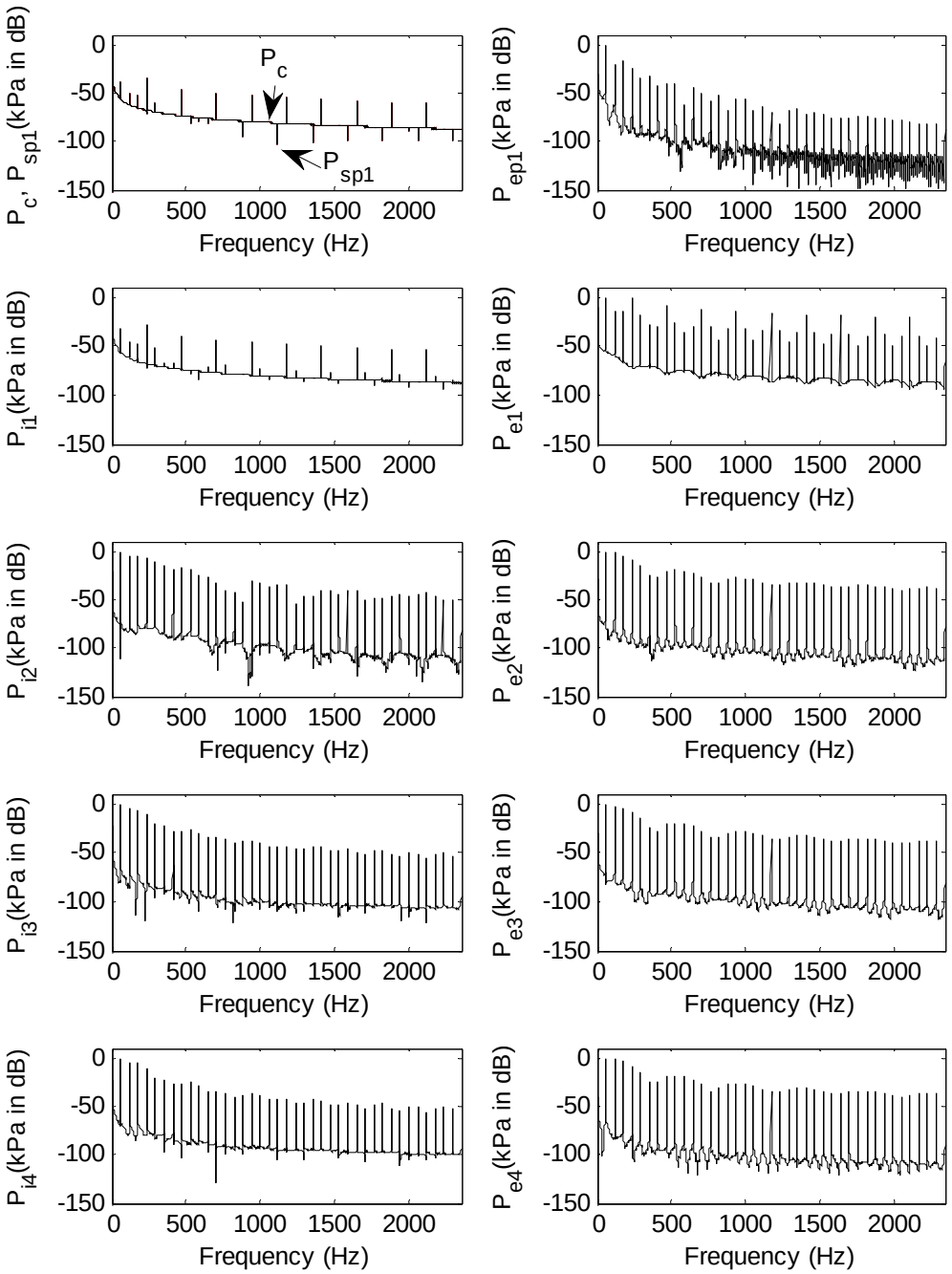

Figure 4.19: FFT Plots of Normalized Pressures for P_{in}=100 kPa.

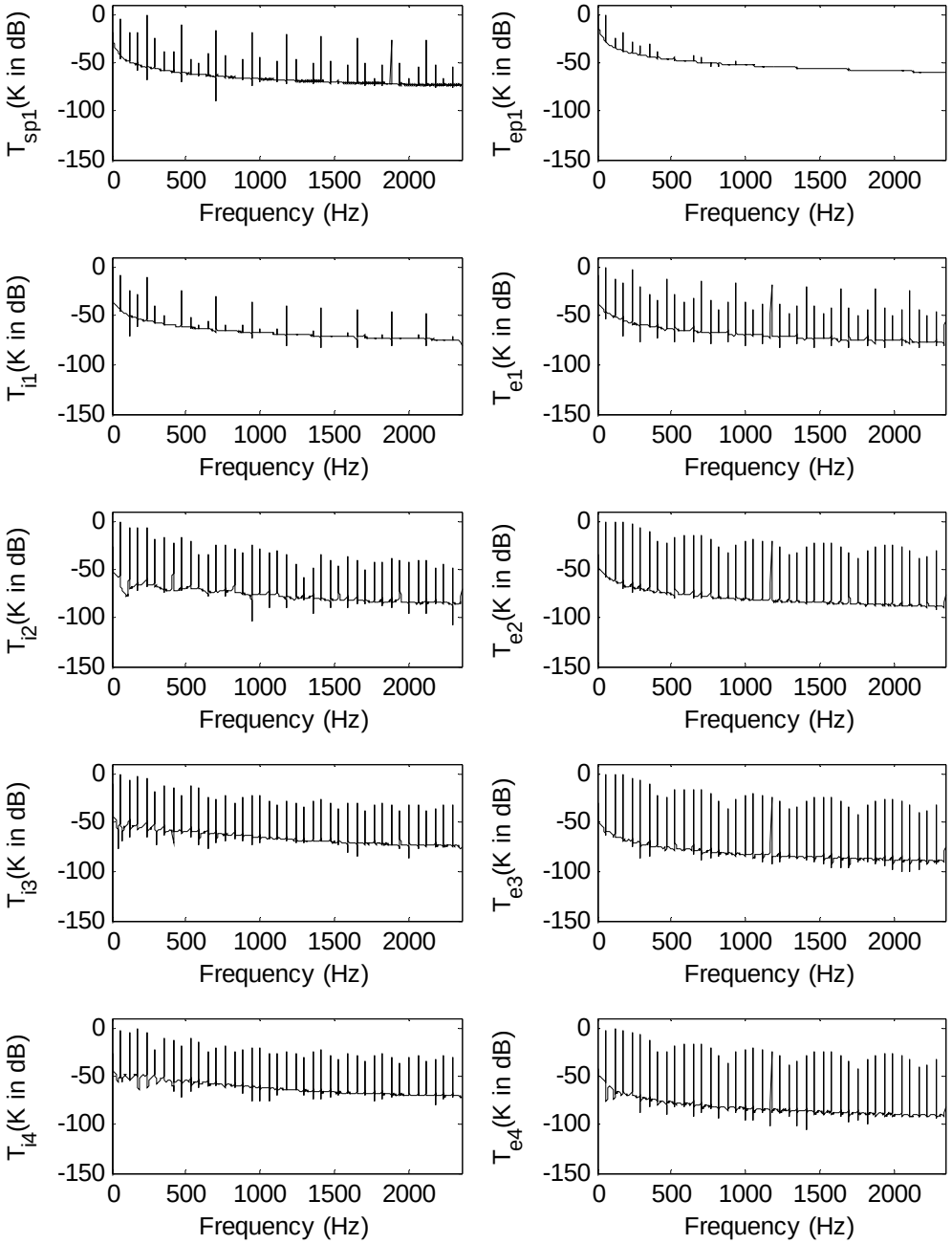

Figure 4.20: FFT Plots of Normalized Temperatures for P_{in}=100 kPa.

Chapter 5: Fault Diagnosis

5.1 INTRODUCTION

This chapter will overview the sensor technology of the state of art dry vacuum pump, discuss three common faults of dry vacuum pumps in the semiconductor industry and introduce a possible health indicator for the fault diagnosis of dry vacuum pumps using simulated faults.

5.2 SENSORS IN A VACUUM SYSTEM

5.2.1 Sensor Technology

Typical temperature sensors include thermistor, thermocouple (TC), resistance temperature detector (RTD), and infrared sensors [57,58]. Thermistors, which are inexpensive but suffer from poor linearity and a lower operating temperature range, are not suitable for precision measurements. TC and RTD offer excellent linearity and a wide temperature range from -200 to 850 ^{o}C, but the response times are too slow for temperature measurements of pumping chambers. The time constant of TC varies from 1 to 10 seconds depending on wire diameter [58], and RTD has a typical response time of four minutes for air temperature measurements [57]. Infrared temperature sensors have a wide temperature range from -70 to 1000 ^{o}C [57] and a fast response time up to 1 ms [59]. Even a state of art infrared temperature sensor [60] has a bandwidth below 40 Hz (a time constant of 1ms and a minimum sample holding time of 25 ms), which is well below the required Nyquist rate of chamber temperature signals to avoid aliasing. By comparison, thermal cycles of the first stage Roots blower runs at four times the motor speed, approximately 240 Hz, thus the Nyquist rate must be above 480 Hz even if the chamber temperature stays constant throughout a cycle. As a result, continuous fast

sampling of working chamber temperature is not possible with the current sensor technology.

Commercial pressure transducers for fast dynamic pressure measurements are diaphragm or thermal dissipation based. Diaphragm pressure sensors include piezo-resistive, resonance based, capacitive, and piezo-electric types, among others [4]. Piezo-resistive and resonance based sensors utilize relations between electric resistance of crystalline silicon and the resonance frequency change of two MEMS resonators embedded on a diaphragm versus a mechanical strain exerted by a vacuum pressure. Similarly, capacitive pressure sensors are based on the change of capacitance due to a diaphragm deflection caused by a pressure force. Piezo-electric pressure transducers use the piezo-electric effect of quartz crystal or PZT to convert pressure to electricity. Piezo-electric pressure sensors dominate the market for dynamic pressure sensing. The state of art piezo-electric pressure transducer [61] can measure pressure up to 300 bars at a sampling frequency above 100 kHz under the maximum static temperature of 316 ^{o}C and flash temperature of 1600 ^{o}C. For a high temperature and high bandwidth application such as measuring a turbine engine's pressure, a fiber optic sensor based on optical interference has been tested [62]. Thermal dissipation based sensors such as Pirani pressure sensors and thermocouple vacuum gauges are sensitive to surrounding temperature [4]. Also, the state of art Pirani pressure sensor has a much slower response time than piezo-electric pressure sensors [63].

In sum, the current sensor technology enables measuring transient pressures of the main vacuum chamber and pumping chambers at a high sampling frequency above 100 kHz if the static temperatures do not exceed about 300 ^{o}C. Dynamic temperature sensing of pumping chambers is not possible, but the state of the art temperature sensor can

measure temperatures of a main vacuum chamber, pipes, a silencer, and a pump body at the maximum sampling rate of 40 Hz or below.

5.2.2 Sensors in State of the Art Dry Vacuum Pump

The state of the art dry vacuum pump [8] has some diagnostic capabilities using various sensors mounted on the pump body and auxiliary systems. Pressure transducers measure static purging gas pressures and exhaust pressure, and thermistors sense the temperatures of a pump body, motor stator and coolant. A flow meter records a coolant flow rate, and a power meter measures a motor's power consumption.

5.3 FAULT TYPES

A dry vacuum pump manual [8] provides a list of warnings that an on-board diagnostic system can produce. This section describes some of the fault symptoms and possible causes, except for sensor faults:

- High motor current and/or power – gas leak and/or debris
- High motor temperature – cooling failure if pump inlet pressure is low
- High or low purge flow or pressure – purging gas module failure and/or gas seal failure
- High pump body temperature – cooling failure and/or debris
- High exhaust pressure – debris or condensation in the exhaust pipe

Harsh chemicals and particulates during semiconductor fabrication are primary causes of a ripple effect, resulting in the aforementioned faults and symptoms. Excessive particulates and undesired chemical reaction can clog internal air gaps between rotors and stators and block an exhaust pipe. Reduced clearances consequently increase pressures and temperatures inside working chambers, which can portend impending rotor seizure. High motor current, power, and temperature can link to a gas seal failure, first caused by

an excessive pressure build-up. Corrosive byproducts can leak through failed gas seals to corrode bearings and gears, contaminate lubricant, and overload a motor. Also, a failed gas seal negatively affects the performance of a purging gas system, which can cause a pre-mature system failure. Excessive pressure build-up can cause gas leaks into cooling channels embedded in the stators, which introduces gas bubbles into a cooling system and degrades cooling performance. Condensed particulates can block an exhaust pipe, which further slows exhaust throughput and increases the likelihood of more particulate build-up.

The above discussion leads to the simulated faults studied in this research.

- Excessive pressure and temperature build-up
    - simulated with reduced clearances between rotors and stators, emulating the presence of undesired particulates within air gaps inside the pumping chambers.
- Gas leaks in stators and/or failed gas seals
    - simulated with leak throughputs in pumping chambers.
- Exhaust pipe blockage
    - simulated with a reduced exhaust pipe diameter to emulate a dramatically reduced pipe conductance.

5.4 Simulation Results and Discussions

5.4.1 Excessive Pressure and Temperature Build-up

Excessive pressure and temperature caused by faulty clearances can forewarn of an incipient rotor seizure. This section summarizes a parametric study using the dry vacuum pump model with faulty clearances in eight scenarios. The baseline clearance of

claw pumps is 0.1 mm, and the baseline radial and axial clearance of the first stage Roots blower are 0.16 mm and 0.2 mm, respectively. Table 5.1 summarizes clearance changes in the eight scenarios.

Scenario	Fault Location	Clearances
Clearance Fault 1 (CF1)	Roots Blower	C_{r01}= C_{a01}=0.02 mm
Clearance Fault 2 (CF2)	Roots Blower	C_{r01}= C_{a01}=0.004 mm
Clearance Fault 3 (CF3)	2nd Stage Claw Pump	C_{r02}= C_{a02}=0.02 mm
Clearance Fault 4 (CF4)	2nd Stage Claw Pump	C_{r02}= C_{a02}=0.004 mm
Clearance Fault 5 (CF5)	3rd Stage Claw Pump	C_{r03}= C_{a03}=0.02 mm
Clearance Fault 6 (CF6)	3rd Stage Claw Pump	C_{r03}= C_{a03}=0.004 mm
Clearance Fault 7 (CF7)	4th Stage Claw Pump	C_{r04}= C_{a04}=0.02 mm
Clearance Fault 8 (CF8)	4th Stage Claw Pump	C_{r04}= C_{a04}=0.004 mm

Table 5.1: Summary of Clearance Fault Scenarios.

Figures 5.1 – 5.4 show the performance curves for four mild fault cases: CF1, CF3, CF5 and CF7. Here thick solid and dashed lines represent healthy and faulty models, respectively. Thin dashed lines indicate manufacturer's data [8]. The other four severe fault cases produce slightly worse but almost identical results, hence additional plots are not shown here.

Clearance fault emulating debris in working chambers yields higher power consumption in a high pressure range for CF1, CF2 and CF3, and across the pressure range for CF4. A relatively higher pressure in the fourth exhaust chamber accounts for the difference. For CF1, pumping speed increases in a high pressure range while pumping speeds in the other three cases remain unchanged.

Figures 5.5 – 5.12 show simulated pressures and temperatures of healthy and faulty models in the above scenarios at pump inlet pressure P_{in} = 100 kPa, which is representative of a high pressure range where differences are the greatest. In the plots, solid and dashed lines indicate healthy and faulty models, respectively. Some of the solid line healthy plots overlay the dashed line faulty performance curves. For CF1, the increased exhaust pressure P_{e1} in the first stage Roots blower produces a trickling effect on pressures in the downstream. However, the corresponding temperature changes are relatively mild. For CF2, the second exhaust pressure P_{e2} increases by about 2.5 times, which causes a large leakage that results in small bumps appearing on the second intake pressure P_{i2}. Also a cascading effect increases pressures and temperatures in the downstream, but not in the upstream. The results of CF5 and CF7 are similar to the previous results except that P_{e3} and P_{e4} are the sources of changes, respectively. Pressures and temperatures in the main vacuum chamber (*c*), suction pipe (*sp1*), exhaust pipe (*ep1*) and first intake chamber (*i1*) remain virtually unchanged for all the cases.

Tables 5.2 – 5.5 tabulate mean and peak-to-peak pressure errors and temperature errors per cycle. Undesired particulate build-ups in pumping chambers increase exhaust pressure and temperature of an affected pump stage, which suggests the physical correlation between errors in an exhaust chamber and a fault location. For example, pressure errors suddenly jump between P_{i2} and P_{e2} for CF3 and CF4, which are mild and severe clearance faults in stage 2. This work proposes to utilize the maximum mean and peak-to-peak errors in a column of Tables 5.2 – 5.5 to indicate a fault location. In the tables, a grey shading marks the maximum value in each fault case. The maximum mean pressure and temperature errors correctly detect a fault location for all the cases. The maximum peak-to-peak pressure and temperature errors fail for CF1 and CF2. For CF1 and CF2, the maximum error is much less pronounced because the Roots blower has

open ports. Instead, a sudden jump of peak-to-peak pressure error from P_{i1} = 0.14 kPa to P_{e1} = 24 kPa can be used as a health indicator.

The simulation results show that fault severity has a little effect on additional increases of pressure and temperature errors. Though the faulty clearances for CF2, CF4, CF6 and CF8 are set four times smaller than the ones in the other mind fault cases, pressure and temperature errors increase by less than 1%.

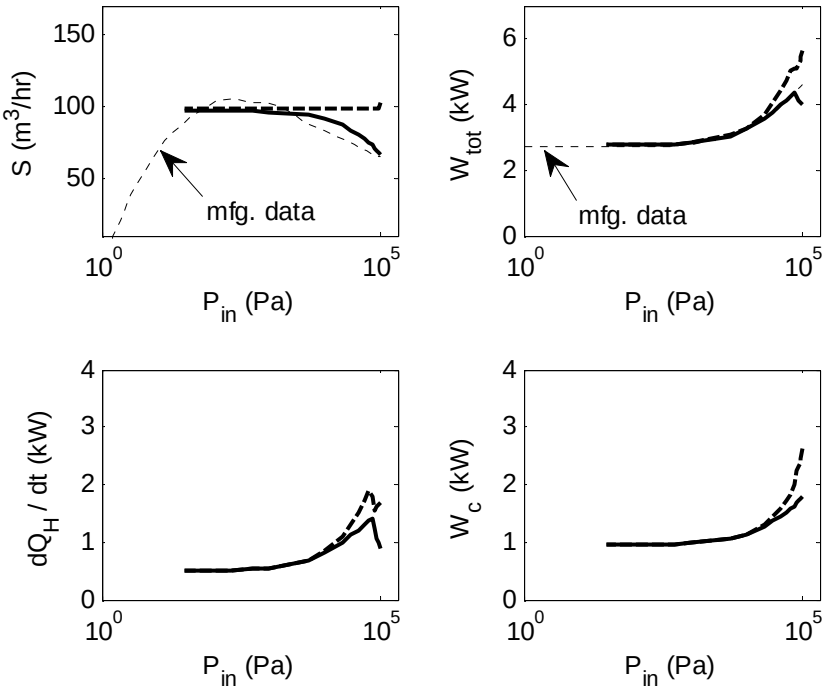

Figure 5.1: Performance Curve Comparisons for CF1 (C_{r01} = C_{a01} = 0.02 mm) where Solid Indicates Healthy and Dashed Indicates Faulty.

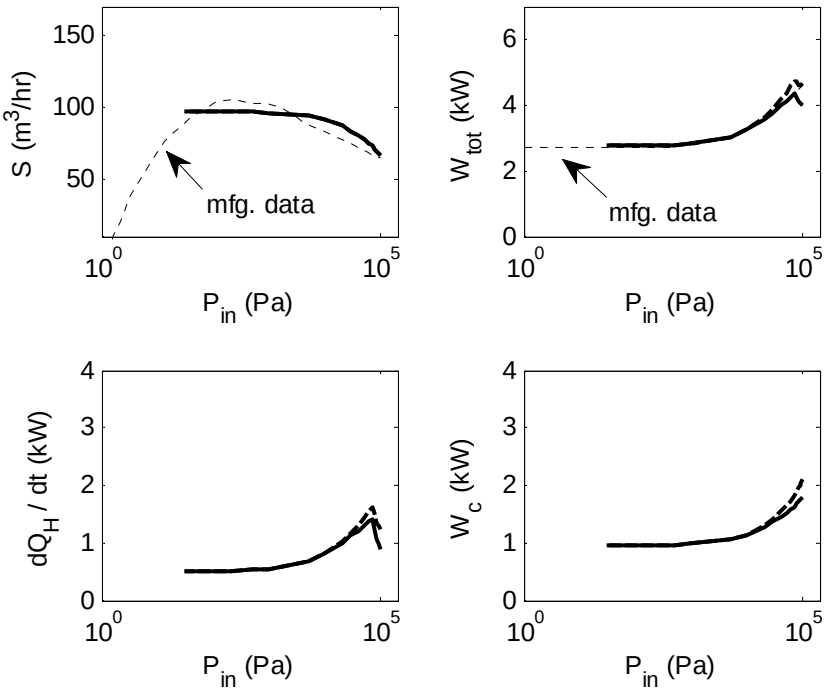

Figure 5.2: Performance Curve Comparisons for CF3 ($C_{r02} = C_{a02} = 0.02$ mm) where Solid Indicates Healthy and Dashed Indicates Faulty.

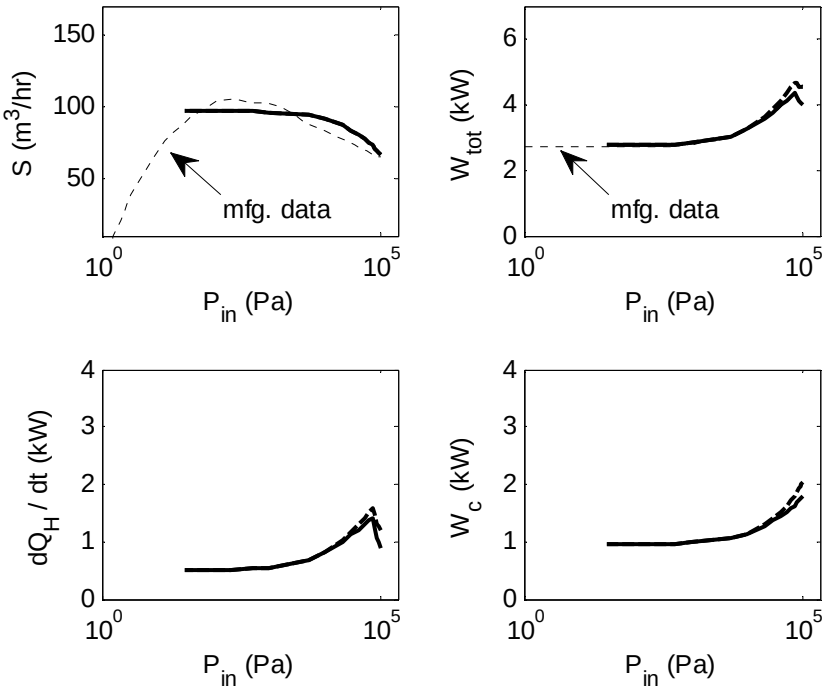

Figure 5.3: Performance Curve Comparisons for CF5 ($C_{r03} = C_{a03} = 0.02$ mm) where Solid Indicates Healthy and Dashed Indicates Faulty.

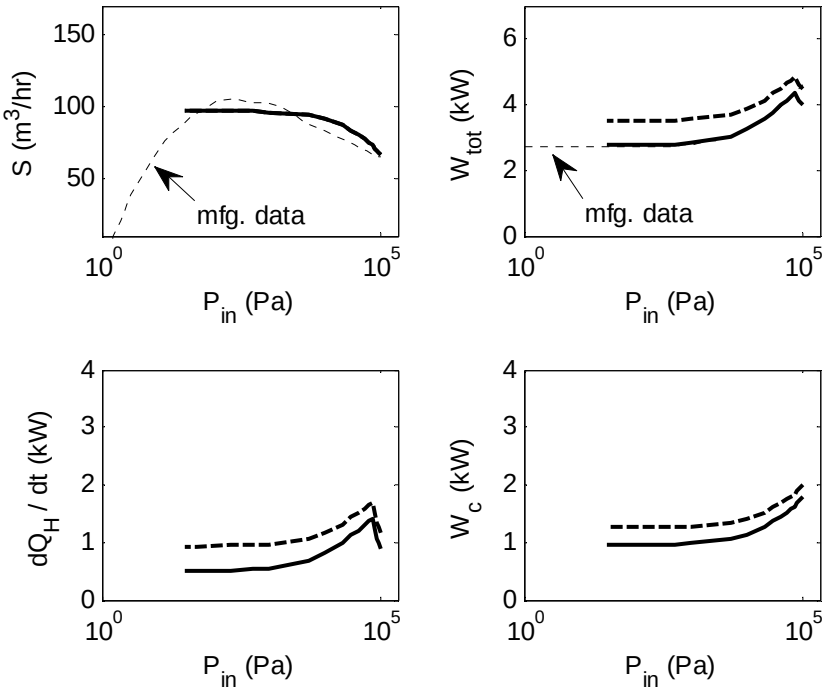

Figure 5.4: Performance Curve Comparisons for CF7 ($C_{r04} = C_{a04} = 0.02$ mm) where Solid Indicates Healthy and Dashed Indicates Faulty.

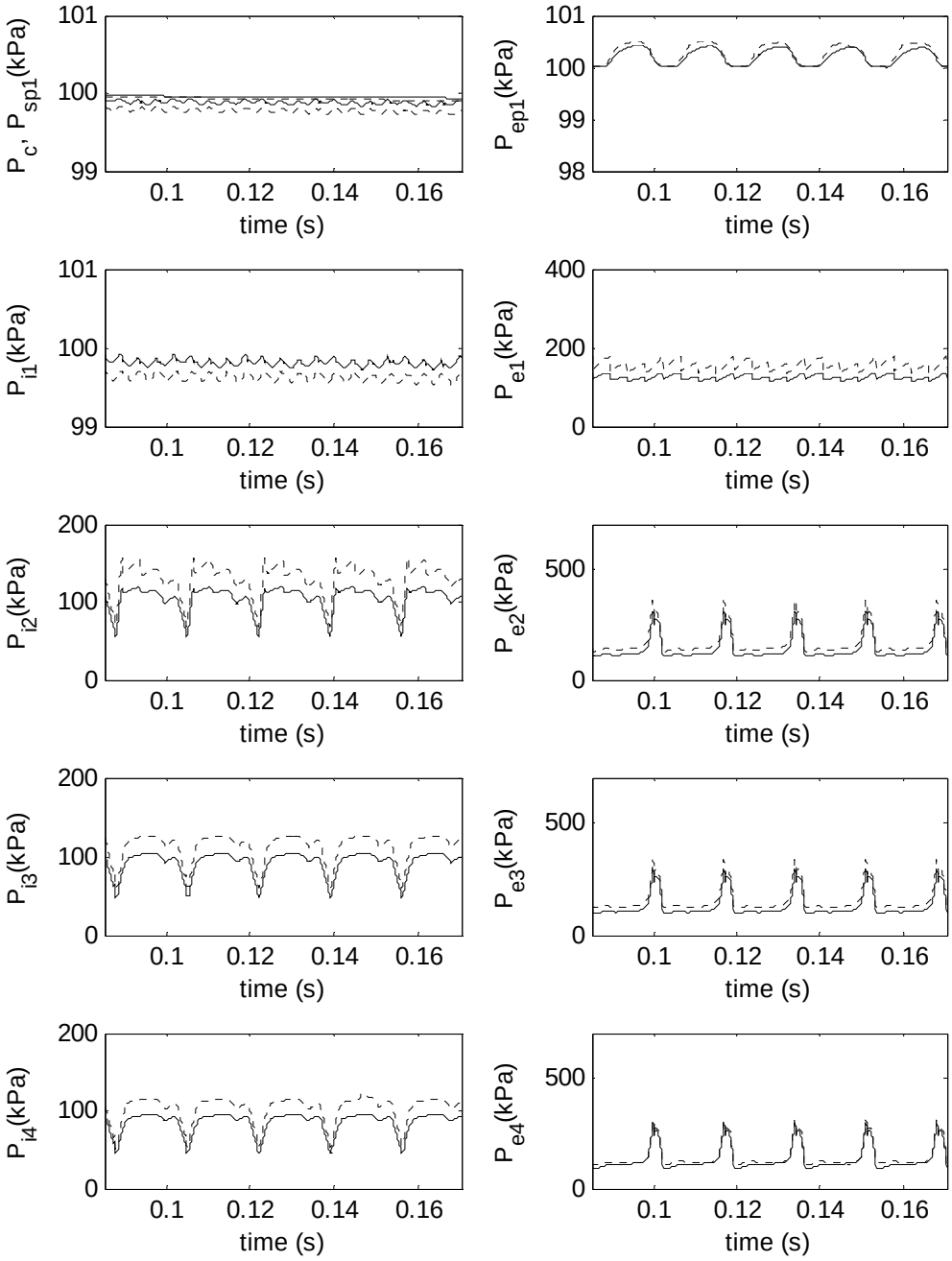

Figure 5.5: Pressure Comparisons for CF1 ($C_{r01} = C_{a01} = 0.02$ mm) at $P_{in} = 100$ kPa where Solid Indicates Healthy and Dashed Indicates Faulty.

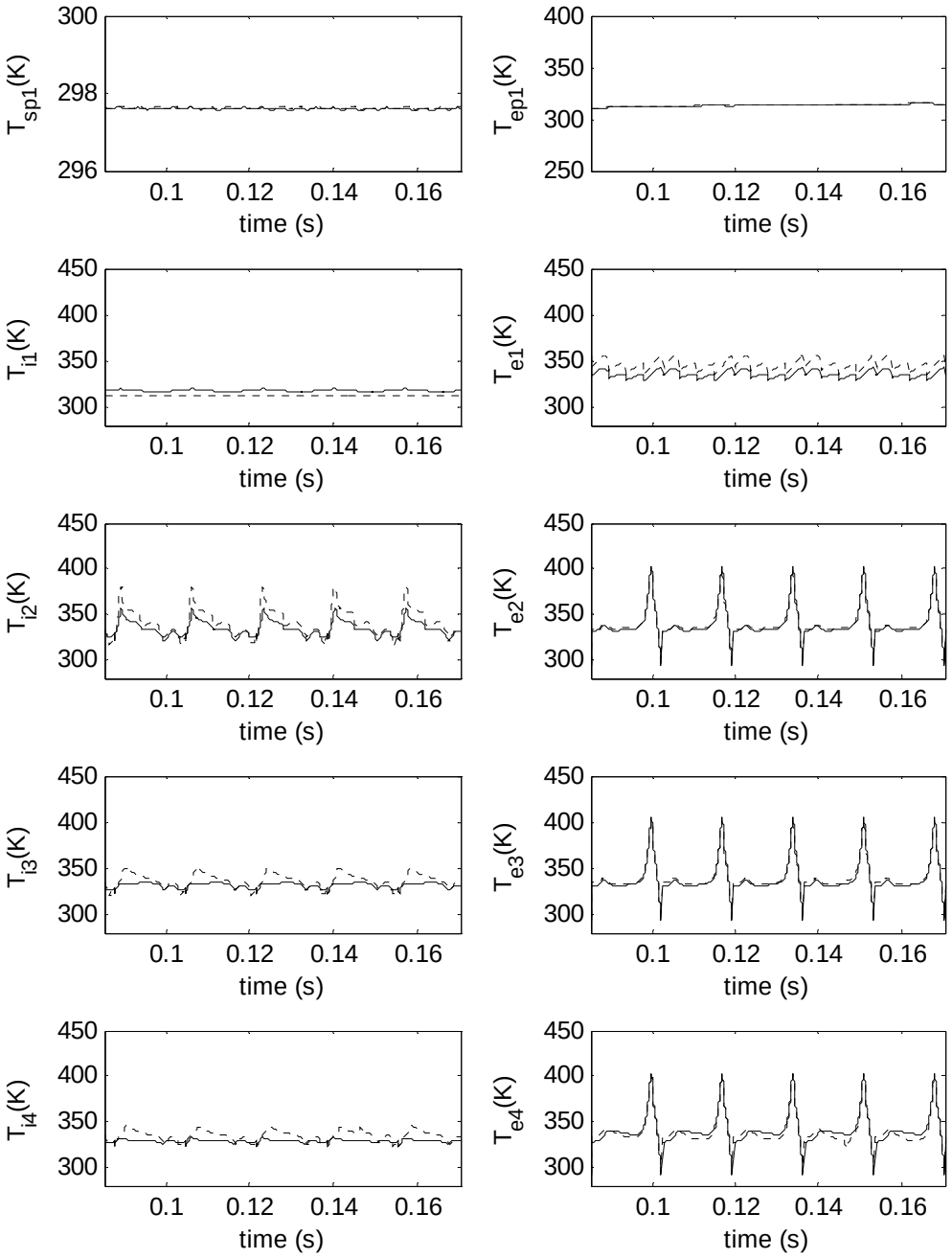

Figure 5.6: Temperature Comparisons for CF1 ($C_{r01} = C_{a01} = 0.02$ mm) at $P_{in} = 100$ kPa where Solid Indicates Healthy and Dashed Indicates Faulty.

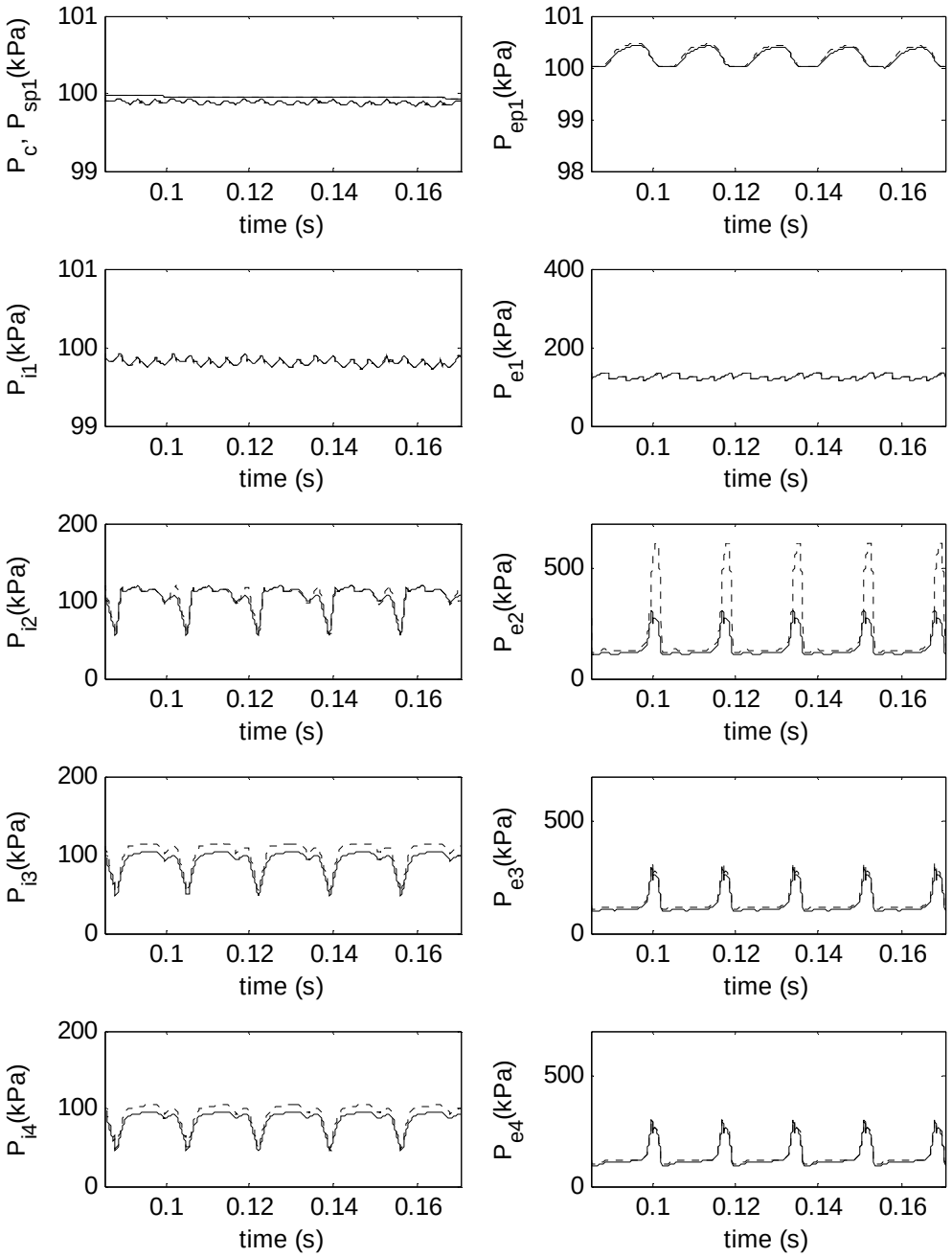

Figure 5.7: Pressure Comparisons for CF 3 (C_{r02} = C_{a02} = 0.02 mm) at P_{in} = 100 kPa where Solid Indicates Healthy and Dashed Indicates Faulty.

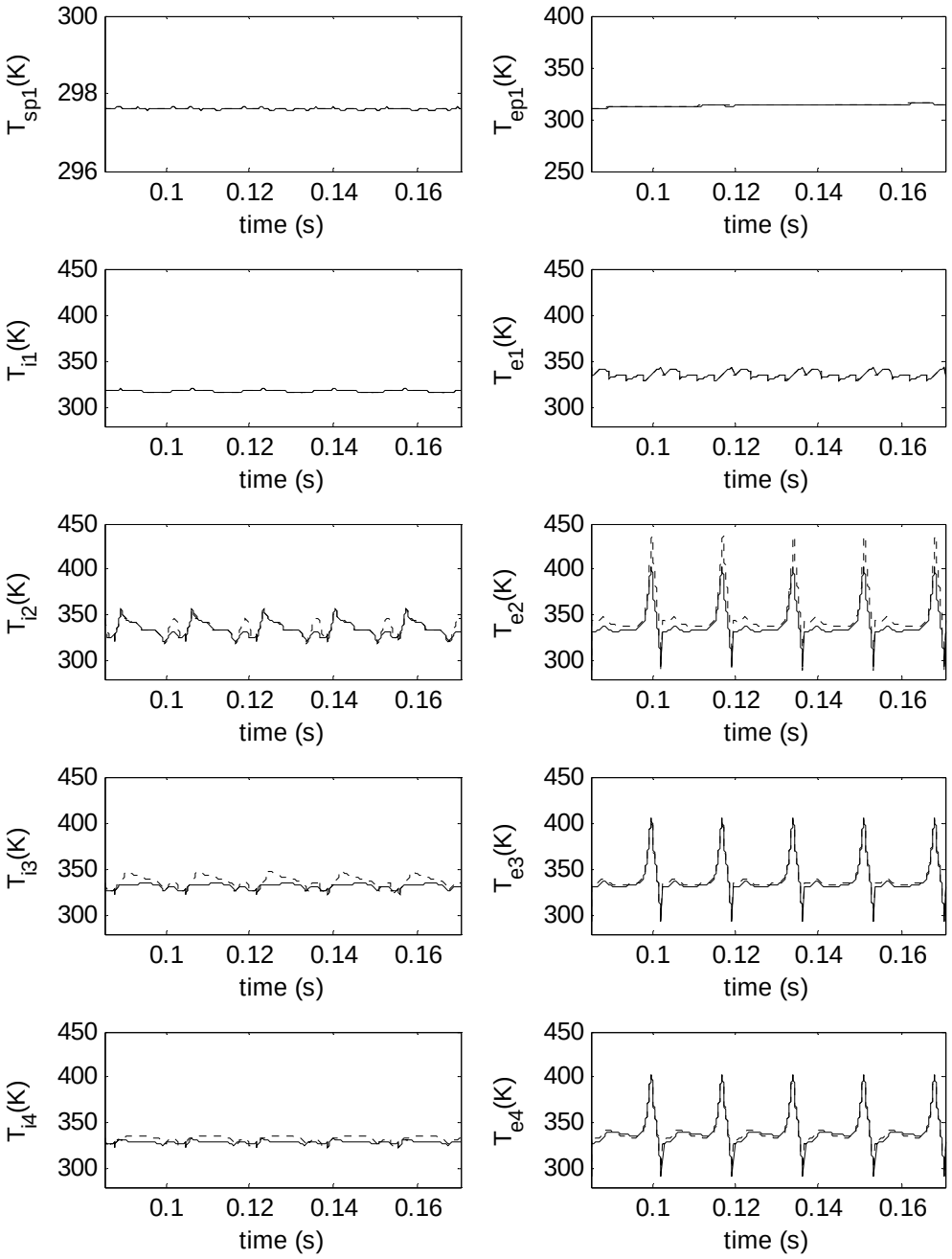

Figure 5.8: Temperature Comparisons for CF3 (C_{r02} = C_{a02} = 0.02 mm) at P_{in} = 100 kPa where Solid Indicates Healthy and Dashed Indicates Faulty.

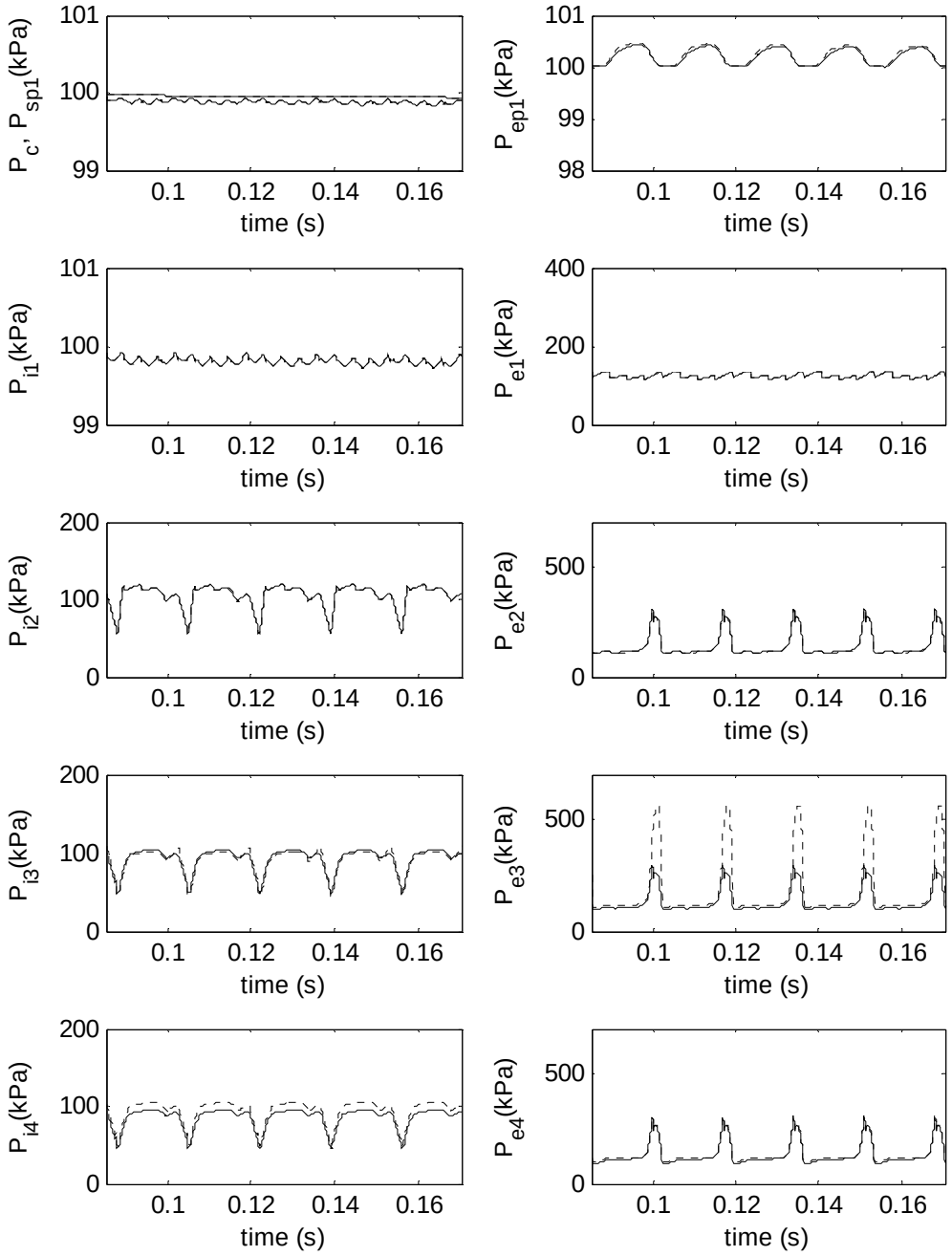

Figure 5.9: Pressure Comparisons for CF5 ($C_{r03} = C_{a03} = 0.02$ mm) at $P_{in} = 100$ kPa where Solid Indicates Healthy and Dashed Indicates Faulty.

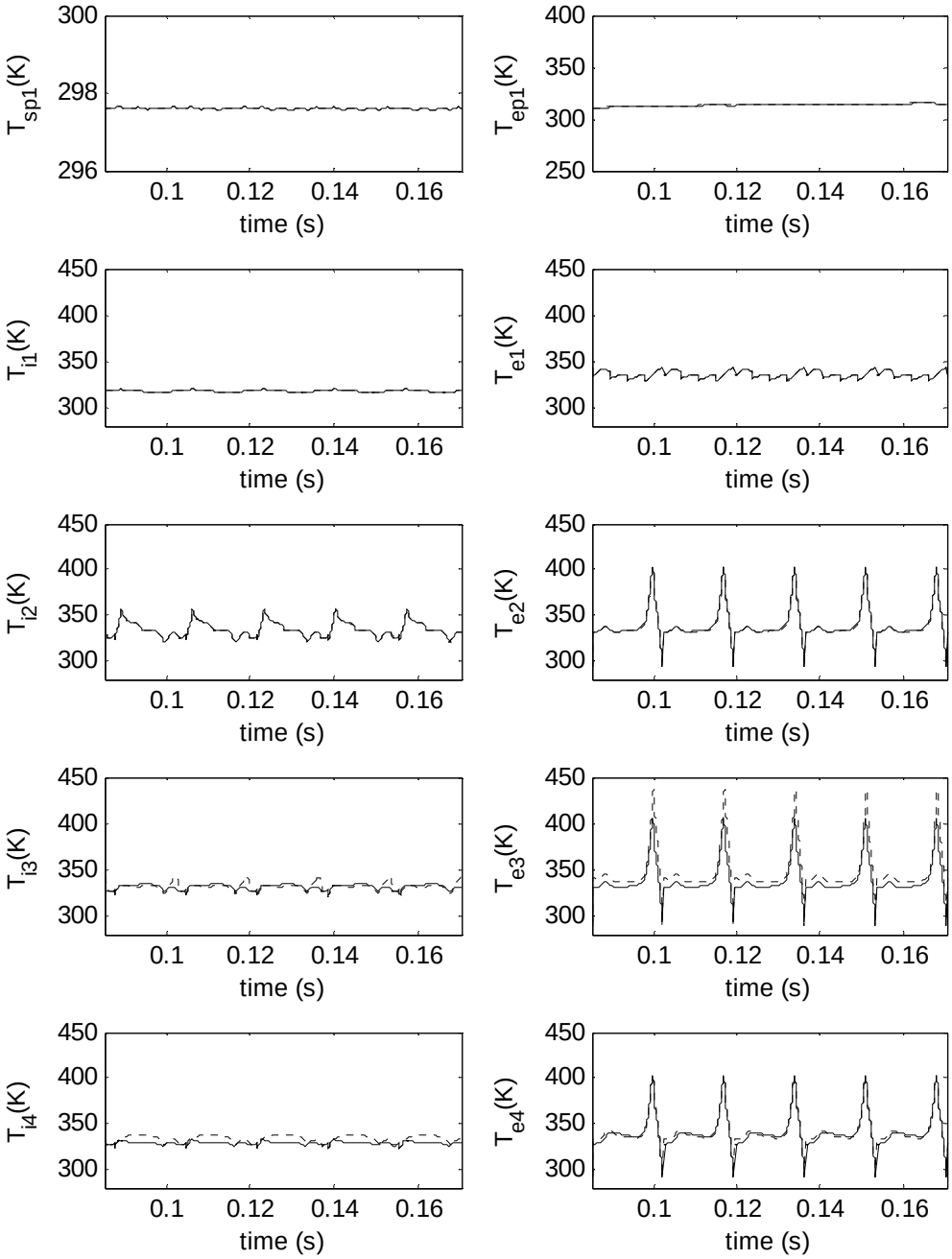

Figure 5.10: Temperature Comparisons of CF5 (C_{r03} = C_{a03} = 0.02 mm) at P_{in} = 100 kPa where Solid Indicates Healthy and Dashed Indicates Faulty.

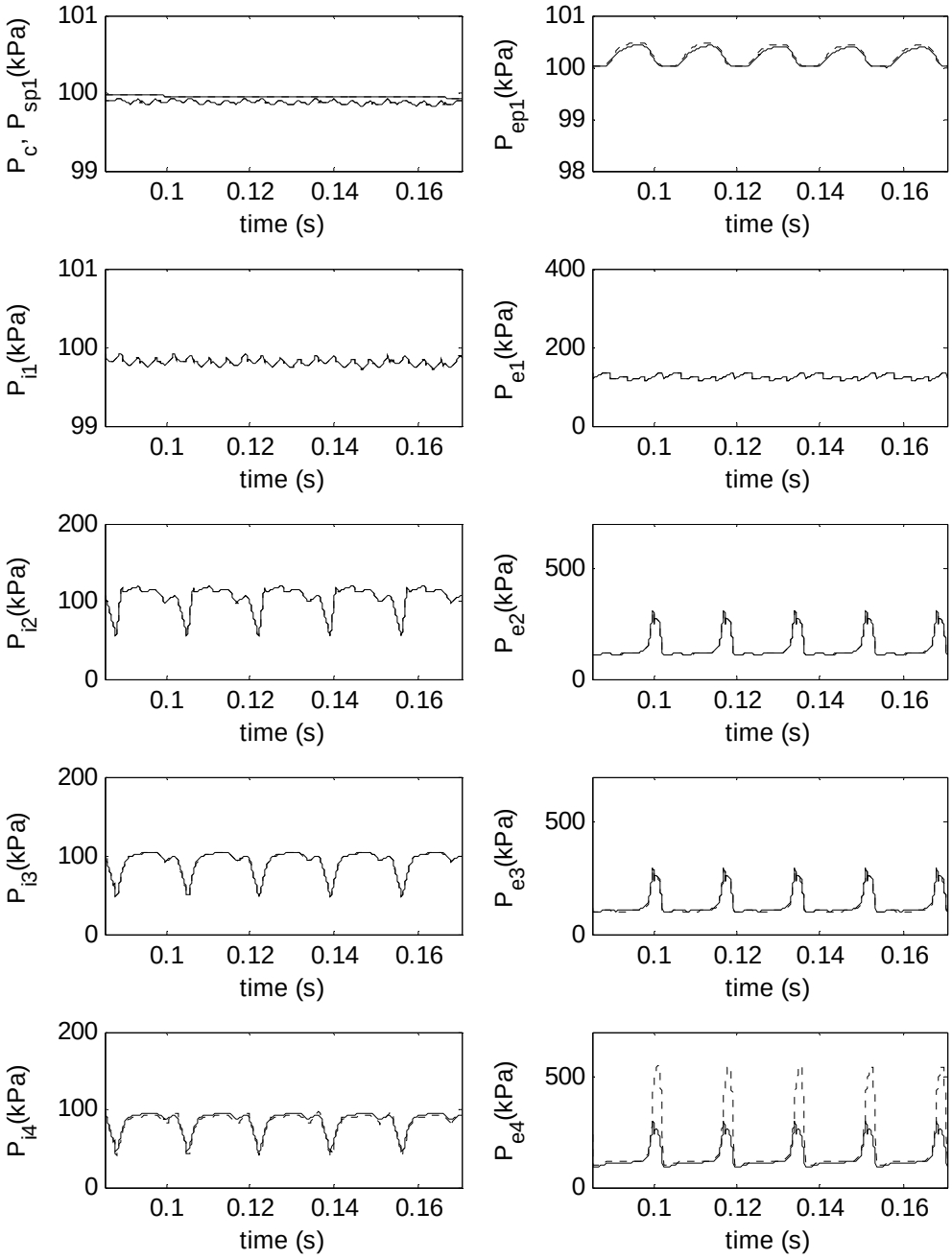

Figure 5.11: Pressure Comparisons of CF7 ($C_{r04} = C_{a04} = 0.02$ mm) at $P_{in} = 100$ kPa where Solid Indicates Healthy and Dashed Indicates Faulty.

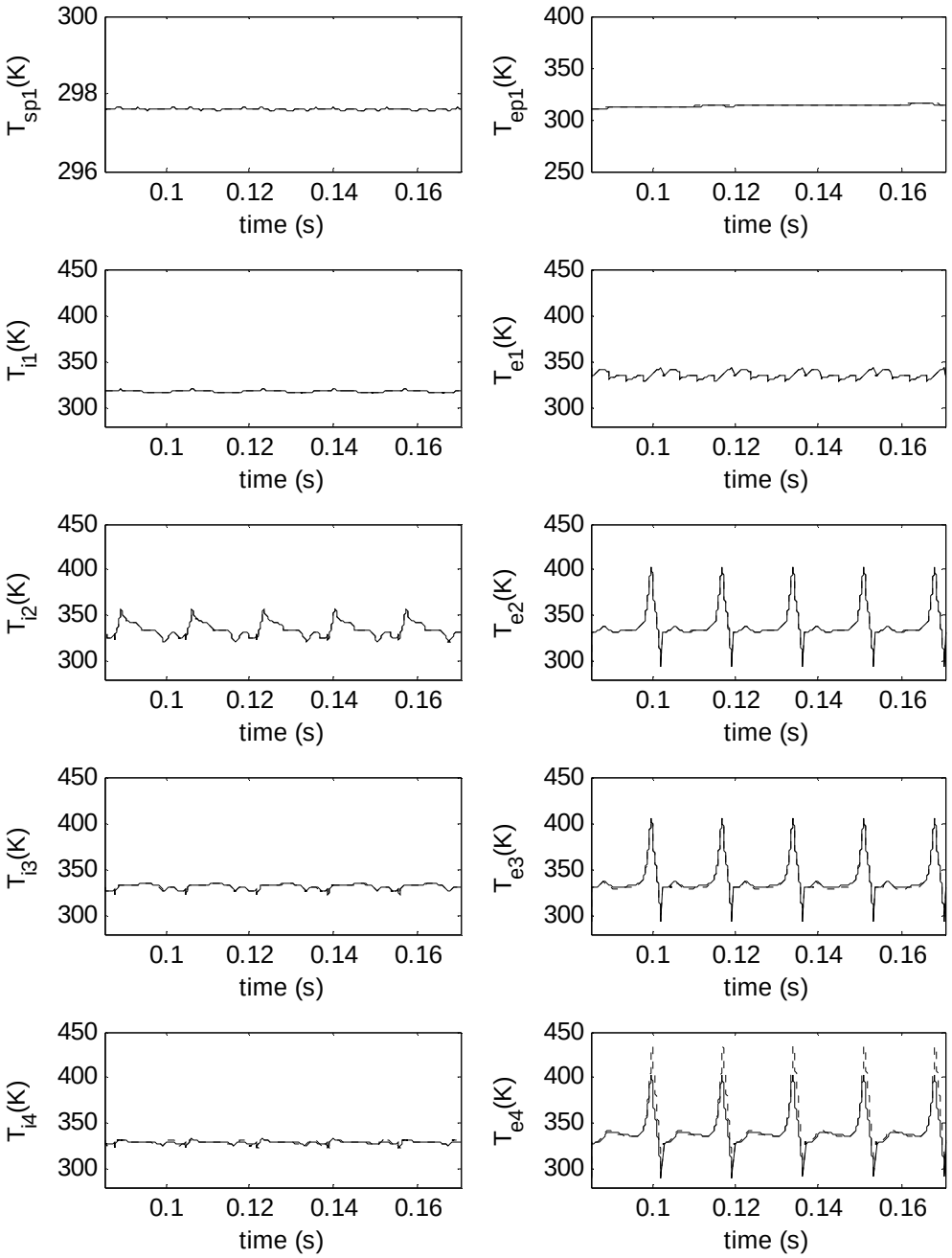

Figure 5.12: Temperature Comparisons of CF7 (C_{r04} = C_{a04} = 0.02 mm) at P_{in} = 100 kPa where Solid Indicates Healthy and Dashed Indicates Faulty.

State (kPa)	Stage 1		Stage 2		Stage 3		Stage 4	
	CF1	CF2	CF3	CF4	CF5	CF6	CF7	CF8
P_{i1}	-0.19	-0.19	0.00	0.00	0.00	0.00	0.00	0.00
P_{e1}	29.92	29.99	-0.05	-0.07	-0.02	-0.02	0.00	0.00
P_{i2}	24.63	24.68	1.25	1.11	-0.09	-0.10	-0.01	-0.01
P_{e2}	26.59	26.51	54.83	57.52	-1.33	-1.49	-0.14	-0.08
P_{i3}	20.49	20.27	10.03	10.65	-0.55	-0.88	-0.27	-0.14
P_{e3}	24.48	23.60	11.39	12.12	48.56	50.65	-2.11	-2.74
P_{i4}	17.37	16.74	8.01	8.55	8.43	8.81	-1.96	-2.51
P_{e4}	8.29	8.10	3.81	4.09	3.99	4.19	39.25	40.76
P_{ep1}	0.06	0.06	0.03	0.03	0.03	0.03	0.03	0.04

Table 5.2: Mean Pressure Errors for CF at P_{in}=100 kPa.

State (K)	Stage 1		Stage 2		Stage 3		Stage 4	
	CF1	CF2	CF3	CF4	CF5	CF6	CF7	CF8
T_{i1}	-5.44	-5.46	-0.02	-0.03	-0.01	-0.01	0.00	0.00
T_{e1}	10.56	10.59	-0.04	-0.05	-0.02	-0.02	0.00	0.00
T_{i2}	6.59	6.60	1.73	1.78	-0.02	-0.03	0.00	0.00
T_{e2}	0.51	0.48	9.47	9.85	-0.44	-0.49	-0.05	-0.03
T_{i3}	5.21	5.18	5.16	5.41	0.21	0.12	-0.14	-0.01
T_{e3}	1.24	1.18	1.76	1.79	9.08	9.36	-0.97	-1.23
T_{i4}	5.90	5.71	3.43	3.69	4.62	4.86	0.03	0.00
T_{e4}	-1.31	-1.30	0.25	0.29	0.32	0.36	4.25	4.42
T_{ep1}	0.08	0.09	0.07	0.08	0.08	0.09	0.16	0.17

Table 5.3: Mean Temperature Errors for CF at P_{in} = 100 kPa.

State (kPa)	Stage 1		Stage 2		Stage 3		Stage 4	
	CF1	CF2	CF3	CF4	CF5	CF6	CF7	CF8
P_{i1}	0.14	0.14	0.00	0.00	0.00	0.00	0.01	0.00
P_{e1}	25.06	25.09	0.27	0.28	0.03	0.04	0.00	0.02
P_{i2}	25.48	25.56	16.97	17.55	0.17	0.19	0.03	0.37
P_{e2}	32.04	31.71	346.54	363.32	3.15	3.54	0.41	8.68
P_{i3}	11.88	12.41	7.71	8.07	14.52	14.91	0.48	11.70
P_{e3}	32.93	29.54	13.38	14.22	312.34	326.81	4.91	21.33
P_{i4}	21.47	13.26	5.45	5.81	5.89	6.11	11.05	14.01
P_{e4}	30.93	19.71	7.99	8.54	8.35	8.76	302.48	314.87
P_{ep1}	0.17	0.15	0.07	0.07	0.07	0.07	0.07	0.07

Table 5.4: Peak-to-Peak Pressure Errors for CF P_{in} = 100 kPa.

State (K)	Stage 1		Stage 2		Stage 3		Stage 4	
	CF1	CF2	CF3	CF4	CF5	CF6	CF7	CF8
T_{i1}	2.97	2.97	0.03	0.03	0.01	0.01	0.01	0.01
T_{e1}	9.07	9.10	0.20	0.20	0.02	0.03	0.00	0.01
T_{i2}	38.04	38.10	18.93	19.46	0.15	0.17	0.02	0.23
T_{e2}	9.67	9.70	65.20	65.78	1.59	1.78	0.19	4.38
T_{i3}	22.97	22.45	15.25	16.00	15.93	16.18	0.63	10.31
T_{e3}	10.93	10.11	7.44	7.73	61.08	61.53	2.44	14.67
T_{i4}	17.51	16.47	7.25	7.93	9.23	9.70	6.97	7.23
T_{e4}	22.57	12.91	7.21	7.69	7.60	7.96	61.78	62.88
T_{ep1}	0.24	0.21	0.09	0.09	0.09	0.10	0.10	0.10

Table 5.5: Peak-to-Peak Temperature Errors for CF at P_{in} = 100 kPa.

5.4.2 Gas Leak

This section shows results of a parametric study about gas leak detection using the vacuum pump model, with a gas leak in 16 scenarios, see Table 5.6. Leak throughput

$$Q_{leak} = C_{leak}\left(P_{pc} - P_{atm}\right) \tag{5.1}$$

equals choked leak conductance C_{leak} times the difference between pumping chamber pressure P_{pc} and atmospheric pressure P_{atm}. C_{leak} is set to 0.1 or 1.0 L/s, which corresponds to conductance of an 0.85 or 2.5 mm dia. aperture [4(p.99)].

Scenario	Fault Location	C_{leak}
Leak Fault 1 (LF1)	1st Stage Intake Chamber	0.0001 m^3/s
Leak Fault 2 (LF2)	1st Stage Exhaust Chamber	0.0001 m^3/s
Leak Fault 3 (LF3)	2nd Stage Intake Chamber	0.0001 m^3/s
Leak Fault 4 (LF4)	2nd Stage Exhaust Chamber	0.0001 m^3/s
Leak Fault 5 (LF5)	3rd Stage Intake Chamber	0.0001 m^3/s
Leak Fault 6 (LF6)	3rd Stage Exhaust Chamber	0.0001 m^3/s
Leak Fault 7 (LF7)	4th Stage Intake Chamber	0.0001 m^3/s
Leak Fault 8 (LF8)	4th Stage Exhaust Chamber	0.0001 m^3/s
Leak Fault 9 (LF9)	1st Stage Intake Chamber	0.001 m^3/s
Leak Fault 10 (LF10)	1st Stage Exhaust Chamber	0.001 m^3/s
Leak Fault 11 (LF11)	2nd Stage Intake Chamber	0.001 m^3/s
Leak Fault 12 (LF12)	2nd Stage Exhaust Chamber	0.001 m^3/s
Leak Fault 13 (LF13)	3rd Stage Intake Chamber	0.001 m^3/s
Leak Fault 14 (LF14)	3rd Stage Exhaust Chamber	0.001 m^3/s
Leak Fault 15 (LF15)	4th Stage Intake Chamber	0.001 m^3/s
Leak Fault 16 (LF16)	4th Stage Exhaust Chamber	0.001 m^3/s

Table 5.6: Summary of Leak Fault Scenarios.

Figures 5.13 and 5.14 show the comparisons of performance curves for LF1 and LF9 where a gas leak is present at the intake pumping chamber of the first stage Roots blower. Thick solid and dashed lines in the plots indicate healthy and faulty models, respectively. As pump inlet pressure increases, pumping speed rises significantly for LF1 and LF9 because a gas leak causes pump inlet pressure to rise, which consequently reduces throughput in a suction pipe. Total power increases slightly in a low pressure range for LF9. However, a gas leak does not affect performance curves for the other cases, and pressures and temperatures remain virtually unchanged.

The mean and peak-to-peak pressure errors for small leak cases (LF1-8) at P_{in} = 100 kPa, tabulated in Tables 5.7 and 5.8 show a strong correlation between the column-wise maximum pressure error and a fault location except for LF1 and LF2, which denote gas leaks in the intake and exhaust chambers of the Roots blower. For large leak cases (LF9-16) in Tables 5.9 and 5.10, the above correlation becomes even pronounced while the correlation weakens for small leak cases (LF1-8) at a lower pressure P_{in} = 10 kPa in Tables 5.11 and 5.12.

Temperature errors are practically insignificant, and the corresponding tables are omitted here.

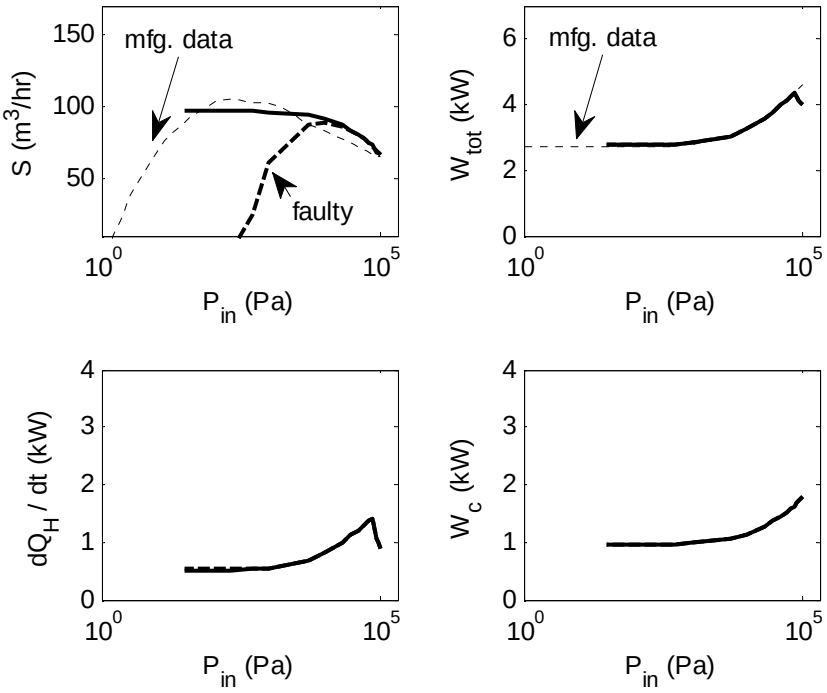

Figure 5.13: Performance Curve Comparisons for LF1 (Mild Gas Leak in the 1st Stage Intake Chamber) where Solid Indicates Healthy and Dashed Indicates Faulty.

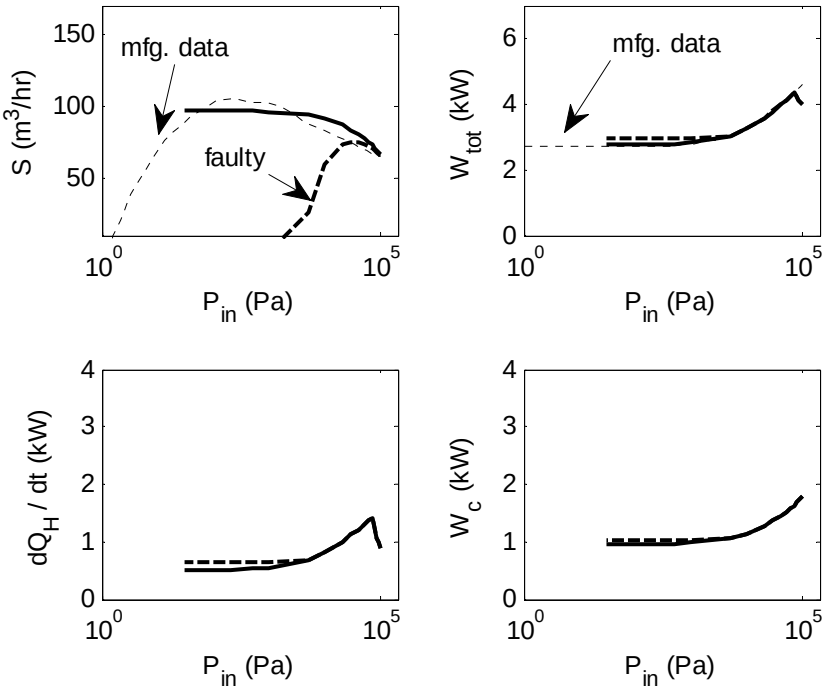

Figure 5.14: Performance Curve Comparisons for LF9 (Severe Gas Leak in the 1st Stage Intake Chamber) where Solid Indicates Healthy and Dashed Indicates Faulty.

State (kPa)	Stage 1		Stage 2		Stage 3		Stage 4	
	LF1	LF2	LF3	LF4	LF5	LF6	LF7	LF8
P_{i1}	0.000	0.000	0.000	0.000	0.000	0.000	0.000	0.000
P_{e1}	0.000	-0.021	-0.003	-0.005	0.001	0.000	0.000	0.000
P_{i2}	0.000	-0.016	0.020	-0.059	0.004	-0.002	0.000	0.001
P_{e2}	0.000	-0.018	-0.013	-0.663	0.069	-0.023	0.007	0.007
P_{i3}	0.000	-0.015	-0.009	-0.232	0.139	-0.076	0.013	0.006
P_{e3}	-0.002	-0.019	-0.012	-0.266	0.099	-0.595	0.101	0.002
P_{i4}	-0.001	-0.013	-0.009	-0.176	0.068	-0.163	0.185	-0.033
P_{e4}	-0.001	-0.006	-0.004	-0.080	0.031	-0.075	0.065	-0.434
P_{ep1}	0.000	0.000	0.000	-0.001	0.000	-0.001	0.001	-0.001

Table 5.7: Mean Pressure Errors for Small Leak Cases at P_{in} = 100 kPa.

State (kPa)	Stage 1		Stage 2		Stage 3		Stage 4	
	LF1	LF2	LF3	LF4	LF5	LF6	LF7	LF8
P_{i1}	0.003	0.004	0.003	0.004	0.003	0.006	0.003	0.003
P_{e1}	0.003	0.021	0.021	0.008	0.004	0.004	0.003	0.004
P_{i2}	0.016	0.028	0.314	0.232	0.021	0.013	0.013	0.024
P_{e2}	0.017	0.034	0.036	3.818	0.130	0.060	0.027	0.031
P_{i3}	0.014	0.021	0.021	0.156	0.333	0.245	0.023	0.033
P_{e3}	0.025	0.033	0.038	0.272	0.114	3.619	0.208	0.034
P_{i4}	0.012	0.017	0.018	0.141	0.060	0.131	0.343	0.163
P_{e4}	0.020	0.025	0.029	0.181	0.070	0.175	0.160	3.676
P_{ep1}	0.000	0.000	0.000	0.002	0.001	0.002	0.001	0.001

Table 5.8: Peak-to-Peak Pressure Errors for Small Leak Cases at P_{in} = 100 kPa.

State (kPa)	Stage 1		Stage 2		Stage 3		Stage 4	
	LF9	LF10	LF11	LF12	LF13	LF14	LF15	LF16
P_{i1}	0.000	-0.001	0.000	0.000	0.000	0.000	0.000	0.000
P_{e1}	0.000	-0.211	-0.032	-0.048	0.011	-0.003	0.001	0.000
P_{i2}	0.000	-0.159	0.185	-0.524	0.038	-0.012	0.005	-0.001
P_{e2}	0.000	-0.171	-0.124	-5.788	0.604	-0.182	0.072	-0.007
P_{i3}	0.000	-0.141	-0.082	-1.916	1.230	-0.601	0.127	-0.012
P_{e3}	-0.002	-0.164	-0.103	-2.152	0.866	-5.011	0.944	-0.088
P_{i4}	-0.002	-0.109	-0.069	-1.452	0.606	-1.308	1.677	-0.369
P_{e4}	-0.001	-0.049	-0.031	-0.667	0.275	-0.612	0.605	-3.883
P_{ep1}	0.000	0.000	0.000	-0.005	0.002	-0.004	0.005	-0.006

Table 5.9: Mean Pressure Errors for Large Leak Cases at P_{in} = 100 kPa.

State (kPa)	Stage 1		Stage 2		Stage 3		Stage 4	
	LF9	LF10	LF11	LF12	LF13	LF14	LF15	LF16
P_{i1}	0.003	0.004	0.005	0.003	0.003	0.004	0.003	0.003
P_{e1}	0.003	0.189	0.194	0.069	0.020	0.006	0.003	0.004
P_{i2}	0.019	0.207	2.947	2.022	0.100	0.026	0.019	0.011
P_{e2}	0.023	0.254	0.207	33.139	1.069	0.439	0.206	0.024
P_{i3}	0.015	0.101	0.068	1.231	3.077	1.824	0.200	0.032
P_{e3}	0.028	0.170	0.110	2.302	0.901	31.163	1.767	0.178
P_{i4}	0.012	0.089	0.062	1.010	0.472	0.920	3.100	1.271
P_{e4}	0.024	0.114	0.078	1.483	0.603	1.387	1.411	31.749
P_{ep1}	0.000	0.001	0.001	0.015	0.007	0.015	0.017	0.015

Table 5.10: Peak-to-Peak Pressure Errors for Large Leak Cases at P_{in} = 100 kPa.

State (kPa)	Stage 1		Stage 2		Stage 3		Stage 4	
	LF1	LF2	LF3	LF4	LF5	LF6	LF7	LF8
P_{i1}	0.003	0.000	0.000	0.000	0.000	0.000	0.000	0.000
P_{e1}	0.003	0.149	0.111	0.009	0.007	0.000	0.000	0.000
P_{i2}	0.003	0.125	0.500	0.074	0.033	0.001	0.001	0.000
P_{e2}	0.005	0.191	0.724	1.469	0.755	0.028	0.012	0.000
P_{i3}	0.003	0.113	0.435	0.652	0.928	0.084	0.033	0.000
P_{e3}	0.004	0.185	0.697	1.238	1.630	1.504	0.757	0.001
P_{i4}	0.003	0.110	0.412	0.736	0.980	0.692	0.809	-0.008
P_{e4}	0.002	0.070	0.260	0.471	0.628	0.513	0.567	-0.215
P_{ep1}	0.000	0.004	0.013	0.023	0.028	0.024	0.027	0.005

Table 5.11: Mean Pressure Errors for Small Leak Cases at P_{in} = 10 kPa.

State (kPa)	Stage 1		Stage 2		Stage 3		Stage 4	
	LF1	LF2	LF3	LF4	LF5	LF6	LF7	LF8
P_{i1}	0.001	0.000	0.000	0.001	0.000	0.000	0.000	0.000
P_{e1}	0.001	0.101	0.147	0.010	0.008	0.001	0.000	0.000
P_{i2}	0.002	0.105	7.057	0.278	0.128	0.004	0.003	0.001
P_{e2}	0.012	0.391	1.958	5.980	2.942	0.093	0.043	0.003
P_{i3}	0.002	0.071	0.420	0.510	5.579	0.277	0.110	0.001
P_{e3}	0.012	0.381	1.809	2.499	3.606	5.895	2.531	0.006
P_{i4}	0.002	0.076	0.390	0.489	0.720	0.582	1.077	0.074
P_{e4}	0.020	0.143	0.647	0.947	1.317	1.033	1.199	2.696
P_{ep1}	0.001	0.009	0.037	0.061	0.078	0.065	0.072	0.013

Table 5.12: Peak-to-Peak Pressure Errors for Small Leak Cases at P_{in} = 10 kPa.

5.4.3 Exhaust Pipe Blockage

The reduced diameter of an exhaust pipe can simulate an exhaust blockage fault. The baseline diameter is 0.04m. Table 5.13 summarizes the three cases studied.

Scenario	Fault Location	Pipe Diameter
Exhaust Blockage Fault 1 (EBF1)	Exhaust Pipe	D_{ep} = 0.01 m
Exhaust Blockage Fault 2 (EBF2)	Exhaust Pipe	D_{ep} = 0.005 m
Exhaust Blockage Fault 3 (EBF3)	Exhaust Pipe	D_{ep} = 0.003 m

Table 5.13: Summary of Exhaust Blockage Fault Scenarios

Figures 5.15-5.17 compare performance curves for EBF. In the plots, thick solid and dashed lines represent healthy and faulty models, respectively. Exhaust blockage fault dramatically increases power consumption at a higher pressure range, and slightly decreases heat dissipation, which is more pronounced for EBF1. However, pumping speeds are unaffected.

Figures 5.18 – 5.21 show simulated pressures and temperatures for EBF1 and EBF3 at pump inlet pressure P_{in} =100 kPa where the contrasts become the largest. Solid and dashed lines indicate healthy and faulty models, respectively. Pressures and temperatures in the exhaust pipe and the fourth exhaust chamber increase noticeably while other states remain virtually unchanged. Severe pipe blockage further increases exhaust pressures for EBF3, but the changes are relatively small, compared to the pipe diameter change.

Tables 5.14 and 5.15 summarize the mean and peak-to-peak errors of pressures and temperatures for EBF. Fault isolation based on the column-wise maximum mean error correctly predicts that the exhaust blockage fault occurs at the exhaust pipe. However, the column-wise maximum peak-to-peak error incorrectly points to the exhaust

chamber though the peak to peak error of P_{ep1} is the second largest. The mean and peak-to-peak errors increase monotonically along with fault severity, however the increments are small.

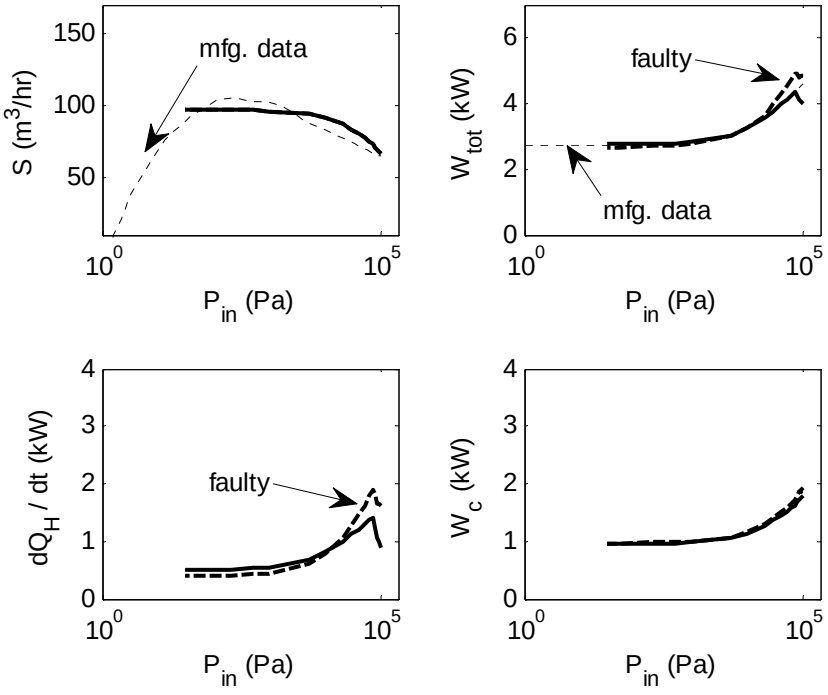

Figure 5.15: Performance Curve Comparisons for EBF1 (D_{ep} = 0.01 m) where Solid Indicates Healthy and Dashed Indicates Faulty.

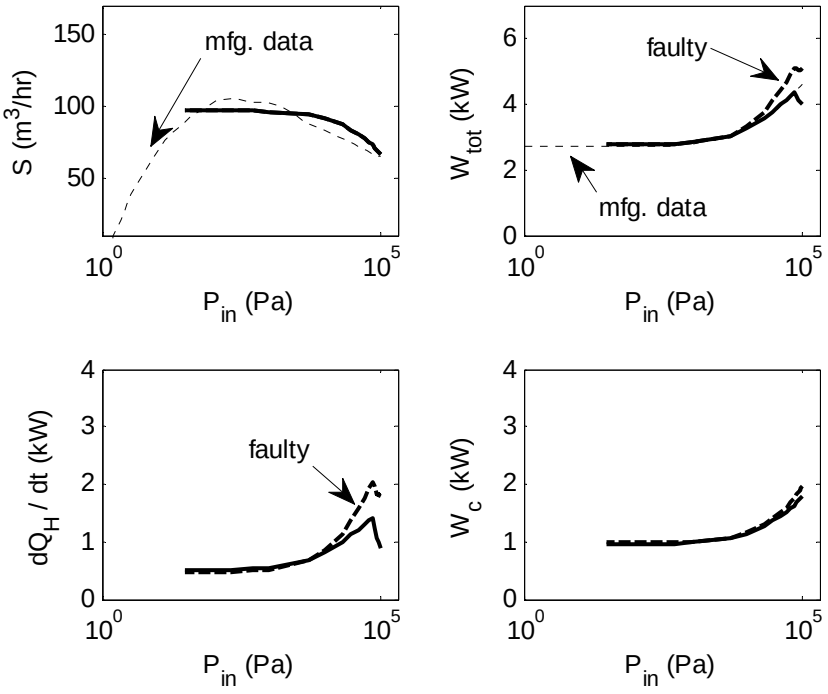

Figure 5.16: Performance Curve Comparisons for EBF2 (D_{ep} = 0.005 m) where Solid Indicates Healthy and Dashed Indicates Faulty.

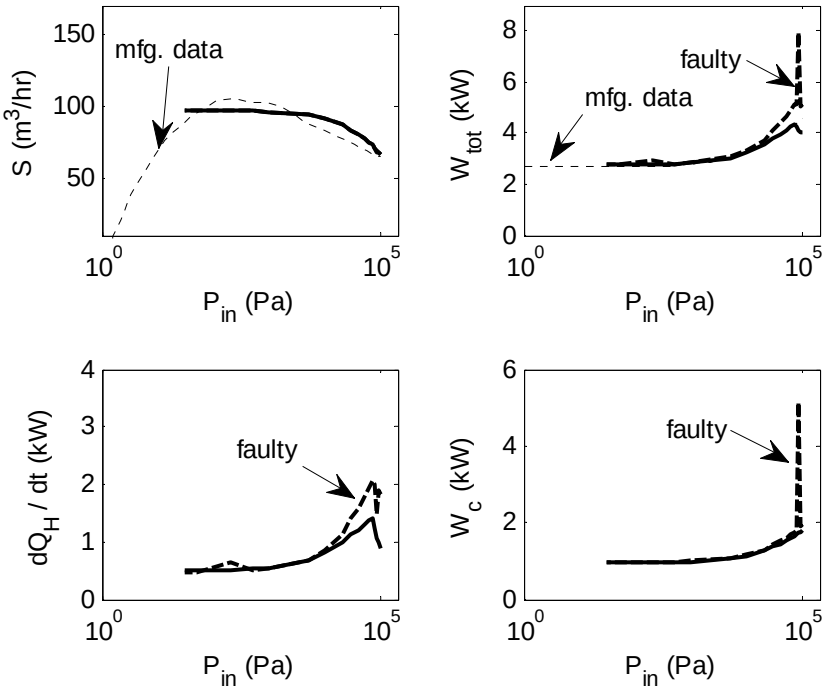

Figure 5.17: Performance Curve Comparisons for EBF3 (D_{ep} = 0.003 m) where Solid Indicates Healthy and Dashed Indicates Faulty.

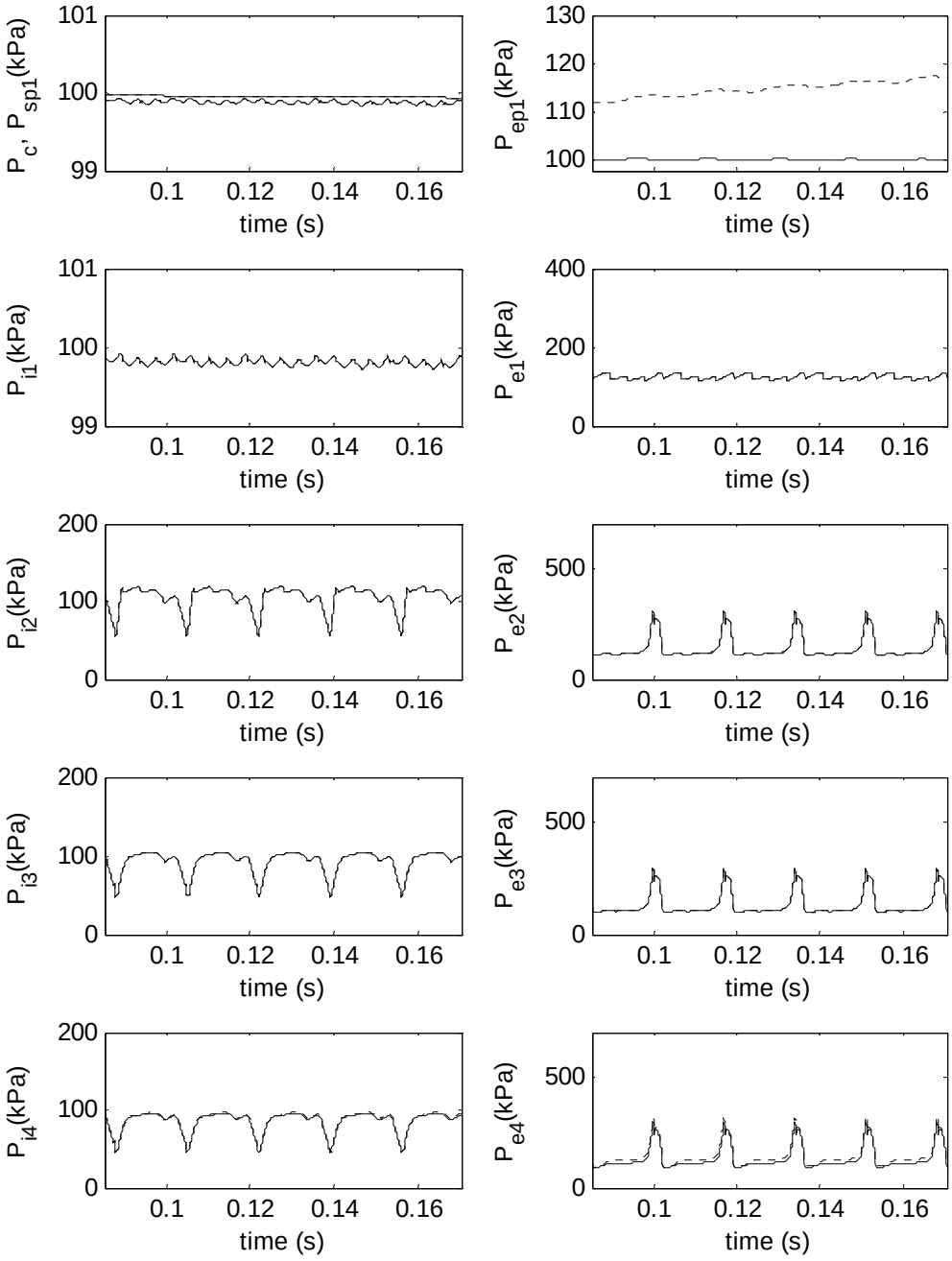

Figure 5.18: Pressure Comparisons for EBF1 (D_{ep} = 0.01 m) at P_{in} = 100 kPa where Solid Indicates Healthy and Dashed Indicates Faulty.

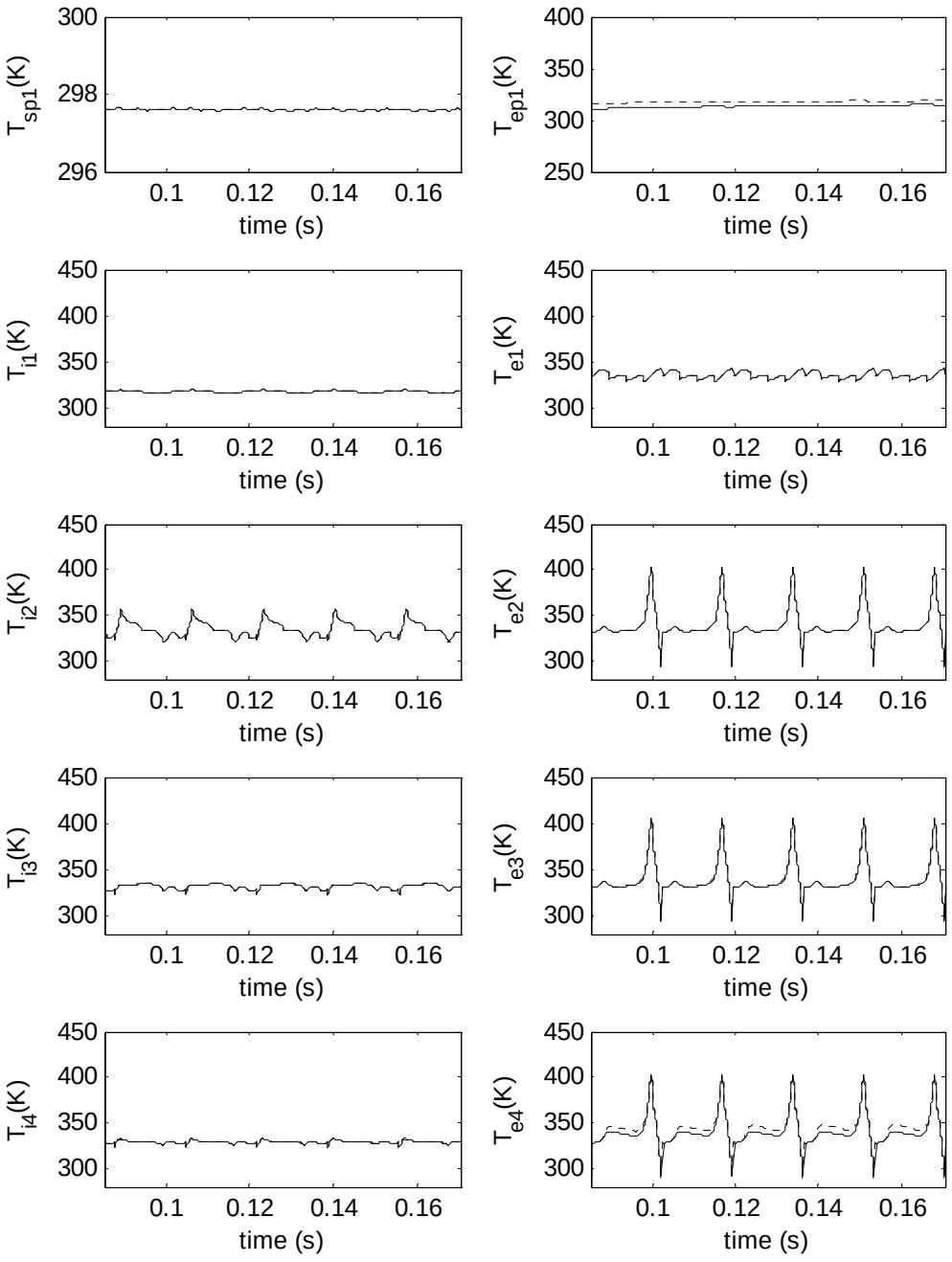

Figure 5.19: Temperature Comparisons for EBF1 (D_{ep} = 0.01 m) at P_{in} = 100 kPa where Solid Indicates Healthy and Dashed Indicates Faulty.

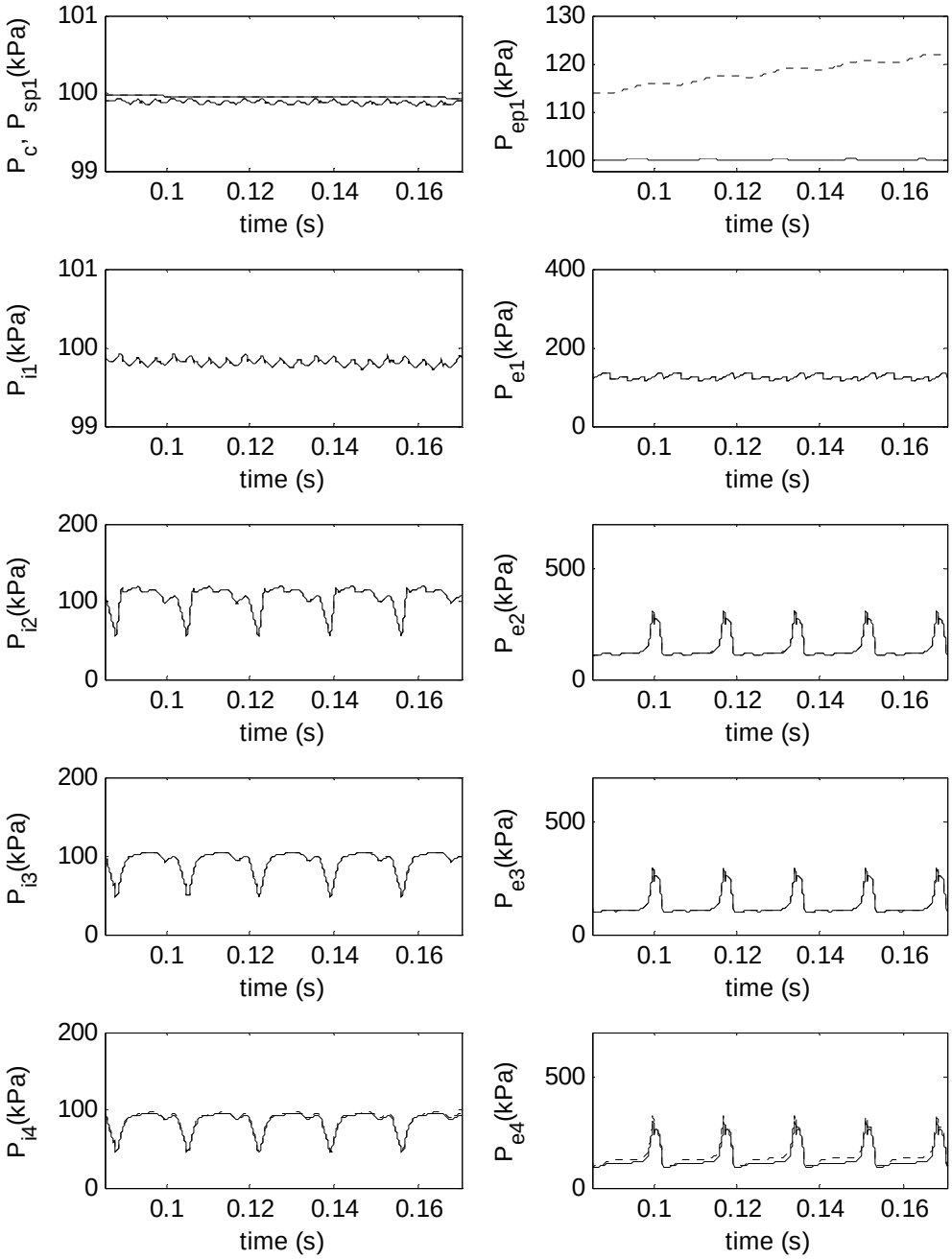

Figure 5.20: Pressure Comparisons for EBF3 (D_{ep} = 0.003 m) at P_{in} = 100 kPa where Solid Indicates Healthy and Dashed Indicates Faulty.

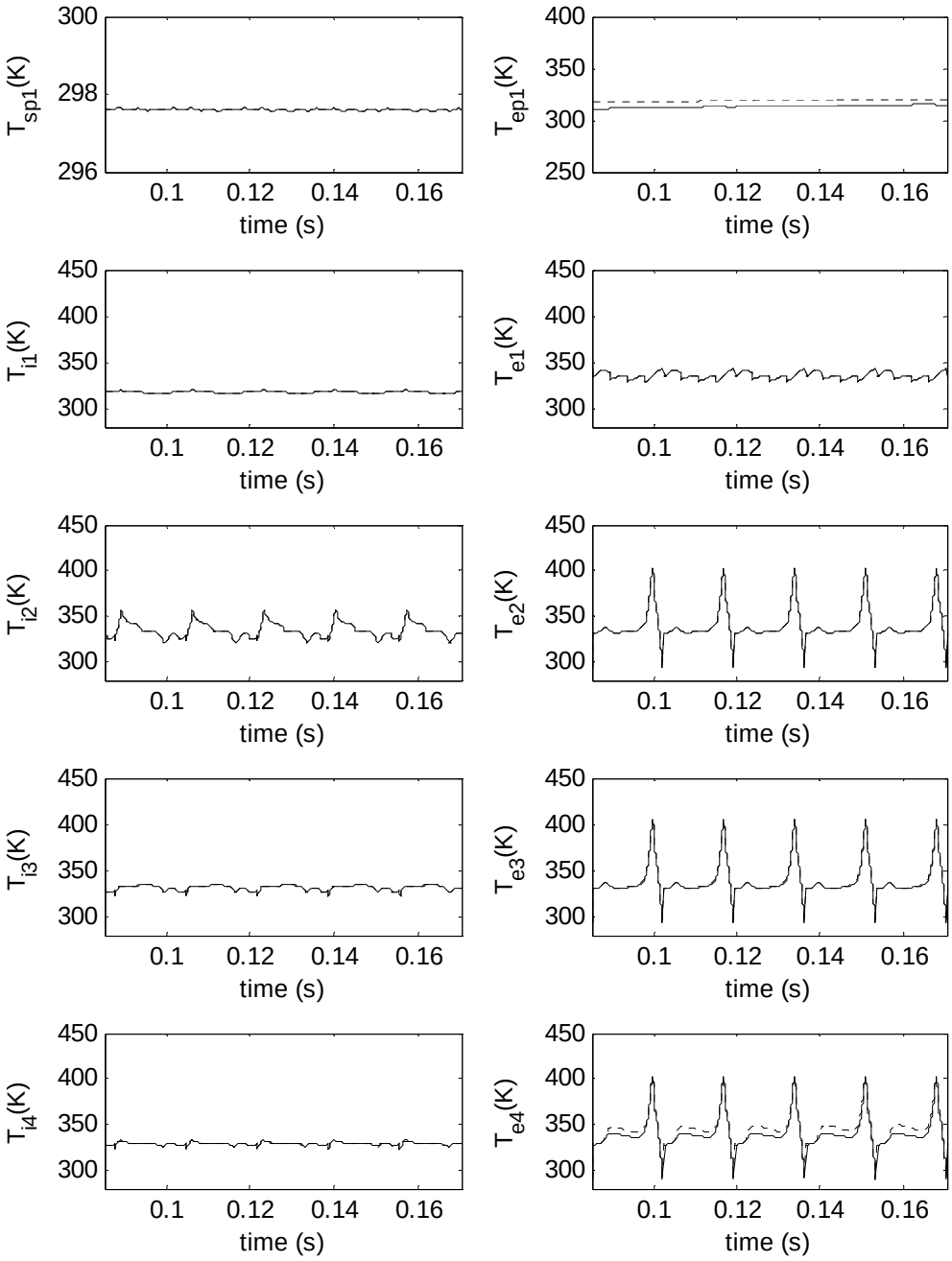

Figure 5.21: Temperature Comparisons for EBF3 (D_{ep} = 0.003 m) at P_{in} = 100 kPa where Solid Indicates Healthy and Dashed Indicates Faulty.

State (kPa)	Mean Pressure Error			Peak-to-Peak Pressure Error		
	EBF1	EBF2	EBF3	EBF1	EBF2	EBF3
P_{i1}	0.000	0.000	0.000	0.003	0.005	0.004
P_{e1}	0.000	0.001	0.001	0.004	0.004	0.004
P_{i2}	0.003	0.004	0.003	0.015	0.034	0.108
P_{e2}	0.045	0.056	0.054	0.156	0.215	0.199
P_{i3}	0.091	0.111	0.110	0.213	0.279	0.274
P_{e3}	0.753	0.904	0.920	2.331	2.924	2.975
P_{i4}	1.193	1.425	1.453	1.957	2.470	2.529
P_{e4}	11.438	13.688	13.995	26.451	32.519	33.352
P_{ep1}	14.596	17.500	17.900	5.469	7.725	8.053

Table 5.14: Mean and Peak-to-Peak Pressure Errors for EBF at P_{in} = 100 kPa.

State (K)	Mean Temperature Error			Peak-to-Peak Temperature Error		
	EBF1	EBF2	EBF3	EBF1	EBF2	EBF3
T_{i1}	0.000	0.000	0.000	0.008	0.009	0.006
T_{e1}	0.000	0.000	0.001	0.005	0.006	0.005
T_{i2}	0.001	0.001	0.001	0.015	0.023	0.144
T_{e2}	0.015	0.018	0.018	0.071	0.089	0.091
T_{i3}	0.049	0.060	0.060	0.281	0.361	0.434
T_{e3}	0.355	0.426	0.433	1.138	1.412	1.446
T_{i4}	0.189	0.238	0.245	0.736	0.962	0.990
T_{e4}	3.406	4.018	4.101	13.149	16.080	16.499
T_{ep1}	4.355	5.408	5.550	1.852	1.548	1.500

Table 5.15: Mean and Peak-to-Peak Temperature Errors for EBF at P_{in} = 100 kPa.

5.5 FAULT CLASSIFICATION

The fault classification charts in Tables 5.16 and 5.17 summarize the results of parametric studies in the previous sections. Symbol + represents presence of a significant error, and the number of + symbols indicates relative severity.

Clearance faults (CF's) generally produced a larger error than leakage faults (LF's), which can be used to further isolate faults. A gas leak in claw pumps produced relatively noticeable pressure errors. The maximum mean and peak-to-peak pressure errors (marked with shading) can be a good fault indicator to detect a fault and isolate a fault location except for a gas leak in the first stage Roots blower. Degraded pumping speed in low vacuum indicated a gas leak in the Roots blower; however the mean and peak-to-peak errors of P_{i1} and P_{e1} in low vacuum, as shown in Tables 5.11 and 5.12 were too small to be useful for fault diagnosis.

Exhaust pipe blockage fault (EBF's) affected pressures in the exhaust pipe and the 4^{th} stage exhaust chamber. Faulty clearance in the 4^{th} stage claw pump, however, did not alter exhaust pipe pressure.

Type	Locat'n	Faults	P_{i1}	P_{e1}	P_{i2}	P_{e2}	P_{i3}	P_{e3}	P_{i4}	P_{e4}	P_{ep1}
Excessive Pressure and Temp.	*i1*	CF1		++	++	++	++	++	++	+	
	e1	CF2		++	++	++	++	++	++	+	
	i2	CF3				++	+	+	+		
	e2	CF4				++	+	+	+		
	i3	CF5						++	+		
	e3	CF6						++	+		
	i4	CF7								++	
	e4	CF8								++	
Gas Leak	*i1*	LF1,9	Reduced Pumping Speed S in Low Vacuum								
	e1	LF2,10		++	++	++	++	++	++	+	
	i2	LF3,11			++	++	+	++	+		
	e2	LF4,12				+++	++	++	++	+	
	i3	LF5,13				+	++	++	+	+	
	e3	LF6,14					+	+++	+	+	
	i4	LF7,15						++	++	+	
	e4	LF8,16								+++	
E. Pipe Block	*ep1*	EBF1								++	++
	ep1	EBF2								++	++
	ep1	EBF3								++	++

Table 5.16: Fault Classification Chart Based on Mean Pressure Errors at P_{in} = 100 kPa.

Type	Locat'n	Faults	P_{i1}	P_{e1}	P_{i2}	P_{e2}	P_{i3}	P_{e3}	P_{i4}	P_{e4}	P_{ep1}
Excessive Pressure and Temp.	*i1*	CF1		++	++	++	++	++	++	++	
	e1	CF2		++	++	++	++	++	++	++	
	i2	CF3			++	+++	+	++	+	+	
	e2	CF4			++	+++	+	++	+	+	
	i3	CF5				+	++	+++	+	+	
	e3	CF6				+	++	+++	+	+	
	i4	CF7						++	++	+++	
	e4	CF8						+	++	+++	
Gas Leak	*i1*	LF1,9	Reduced Pumping Speed *S* in Low Vacuum								
	e1	LF2,10		++	++	++	++	++	+	++	
	i2	LF3,11			+++						
	e2	LF4,12				+++					
	i3	LF5,13				++	+++	++			
	e3	LF6,14						+++			
	i4	LF7,15						++	++	++	
	e4	LF8,16								+++	
E. Pipe Block	*ep1*	EBF1								++	+
	ep1	EBF2								++	+
	ep1	EBF3								++	+

Table 5.17: Fault Classification Chart Based on Peak-to-Peak Pressure at P_{in} = 100 kPa.

Chapter 6: Conclusions and Future Work

This work studied a model based fault diagnosis of dry vacuum pumps in the semiconductor industry. This final chapter will summarize this dissertation, review the research contributions, and discuss directions of future research.

6.1 Conclusions and Contributions

1. **Unified Pipe Modeling**: Conventional Knudsen equation and Blasius' throughput model, summarized in Section 2.3.2 are inadequate to cover the entire flow regimes of real world vacuum tubing. Section 2.3.2 to 2.3.4 proposed an unified pipe model tailored for vacuum system modeling, including a turbulent and transition long pipe model based on a novel technique to estimate the Darcy friction factor; a short pipe model capable of describing the molecular and viscous flows; and a numerically efficient and more accurate method to test flow choking. Section 3.4.2 proposed a novel method to model a composite pipe using pressure buffers, and provided heat transfer formulas.

2. **Modeling of a Multi-stage Dry Vacuum Pump**

   a. **Geometric Study of a Cycloidal Roots Blower:** Section 3.2.1 illustrated the structures and working principles of the Roots blower using detailed diagrams. Section 3.2.2 analyzed the rotor and stator geometries and formulated a general cycloidal lobe profile. Appendix A1.1 illustrated the intermeshing of cycloidal bi-lobe rotors. Section 3.2.3 studied gas mixing in the exhaust chamber and proposed a two-control volume model for twin bi-lobe rotors. Section 3.2.4 developed a dimensionless base area and boundary length functions, which enabled easy calculation of the volume and internal area of a pumping chamber with simple mathematical

formulas. Appendix A1.4 proposed a novel method to compute the above dimensionless functions numerically, which improved practical application of the above method.

b. **Geometric Study of a Northey Claw Pump:** Section 3.3.1 studied the structures and working principles of a claw pump, and provided detailed illustrations. Section 3.3.2 formulated a Northey type claw rotor profile and section 3.3.3 defined the control volumes of working chambers. Section 3.3.4 calculated the dimensionless base area and boundary length functions for volume and internal area calculations. Appendix A2.1 addressed difficulties in analytically calculating a chamber volume.

c. **Leakage Modeling of a Roots Blower:** Conventional leakage models based on an isentropic nozzle lacked both geometric rigor and tribological accuracy. This work improved both aspects and developed a highly sophisticated leakage model useful at any vacuum condition. Section 3.2.6.1 defined flank and radial leakages in a Roots blower using detailed illustrations. Appendix A1.5 reviewed Reynolds equation, and section 3.2.6.2 studied gas compressibility and rarefication and modified Reynolds equation tailored for leakage formulation. Sections 3.2.6.3 and 3.2.6.4 developed flank and radial leakage equations suitable for numerical simulation.

d. **Leakage Modeling of a Claw Pump:** The leakage model of a claw pump extended the Roots blower's leakage model to include three sub-models dependent on rotor position. Section 3.3.6.1 defined flank and radial leakages at different rotor positions with detailed illustrations, and analyzed the leakage mechanism with claws engaged. Section 3.3.6.2

proposed a continuously linking function and formulated flank leakage. Section 3.3.6.3 developed a radial leakage model that considered interweaving of claw rotors.

e. **Heat Transfer:** Section 2.2 reviewed heat transfer between two plates based on kinetic gas theory and statistical thermodynamics, and proposed to use a pressure and temperature dependent weighting function [26] in order to combine the transferred heat powers [4] in the viscous and molecular regimes. Sections 3.2.5 and 3.3.5 proposed heat transfer through continuously varying inner areas of working chambers, treating trapped gas as a thermal mass.

f. **Modeling an Inter-Stage Flow:** Section 3.4.1.1 analyzed the structures and working principles of port interfaces. Section 3.4.1.2 defined dimensionless parameters to quantify the size of port openings. Section 3.4.1.3 extended the normal port area formulas to calculate a hydraulic area for viscous throughput, and simplified the hydraulic area formulas via geometric considerations. Section 3.4.1.4 calculated transmission probabilities of three port configurations, and developed a molecular throughput formula for a port interface. Section 3.4.1.5 proposed an inter-stage throughput formula using an isentropic nozzle model for viscous throughput, and the same weighting function as the leakage model.

g. **Modeling a Silencer with a Check Valve:** Dry vacuum pumps typically include a silencer and a check valve to prevent back flow. Section 3.4.3 proposed a pressure buffer with an inlet and a unidirectional outlet to represent a silencer with a check valve in an exhaust pipe.

h. **Systematic Modeling:** The above modular models allow easy assembly of a multi-stage pump model. Section 4.1 reviewed simulation equations module by module, and provided a whole model with references.

3. **Simulation of the Detailed Vacuum Pump Model Including Faults**

a. **Design of a Baseline 4-stage Dry Vacuum Pump Model:** Section 4.2.2 discussed model parameters and defined baseline parameter values. Little data about pump dimensions, clearances, thermal properties, etc., was available in the literature. Hence simulation became a valuable tool to explore and test issues and retrofit sub-models. For instance, the revised dimensionless base area function of a claw pump was not possible without adjusting and revising parameters via simulation, which also confirmed the design practice of real world claw rotors.

b. **Development of a Simulation Technique for a Highly Non-linear and Stiff System:** The vacuum pump models that were developed became so highly non-linear and stiff, that conventional numerical solution techniques failed to integrate. This work tried several numerical packages and tricks in vain. Section 4.2.3 summarized the most successful techniques.

c. **Parameter Turning and Model Validation:** Sections 4.3.1 and 4.3.2 analyzed the simulation results of the baseline dry vacuum pump model, and summarized a parameter tuning process to match the performance specifications of a real world dry vacuum pump used in the semiconductor industry. Section 4.3.3 validated the turned vacuum pump model, which served as a healthy vacuum pump model for fault diagnosis.

4. **Development of a Model Based Health Indicator for the Multi-Stage Dry Vacuum Pump Based on Fault Symptom Classification and Parameter Space**

   a. **Parametric Studies of Common Vacuum Pump Faults:** Section 5.3 discussed common faults of dry vacuum pumps. Section 5.4 simulated three faults: debris, gas leak and exhaust blockage via 27 scenarios, and analyzed pressures, temperatures, mean and peak-to-peak errors and pump performance curves.

   b. **Fault Classification:** Section 5.5 presented two fault classification charts based on parametric studies summarized in section 5.4, and briefly discussed important findings for fault detection and isolation.

6.2 FUTURE DIRECTIONS

The developed dry vacuum pump model excluded an electro-mechanical drive consisting of an induction motor and a gearbox, and an automatic cooling system. Future work will improve the vacuum pump model in those aspects.

Chapter 5 discussed a simple health indicator for fault diagnosis of dry vacuum pumps. Indeed, the model based fault diagnosis of dry vacuum pumps is virgin territory awaiting advanced faulty diagnostic techniques. This work simulated faults using a sophisticated dry vacuum pump model. Applying advanced FDI techniques, which is not possible with a simple model, is a goal for future research.

Appendix

A1.1 Intermeshing of Twin Cycloidal Bi-Lobe Rotors

Figure A1.1 (a) shows how twin cycloidal bi-lobe rotors intermesh at a rotor angle of 0°. The left rotor is perpendicular to the right rotor, and a hypocycloid of the left rotor contacts with an epicycloid of the right rotor. The left and right pitch circles of diameter $2R_p$ share the same rolling circle of diameter $R_p/2$, located inside the left pitch circle but outside the right pitch circle. The contact point of the rotors also coincides with the tracing point on the rolling circle.

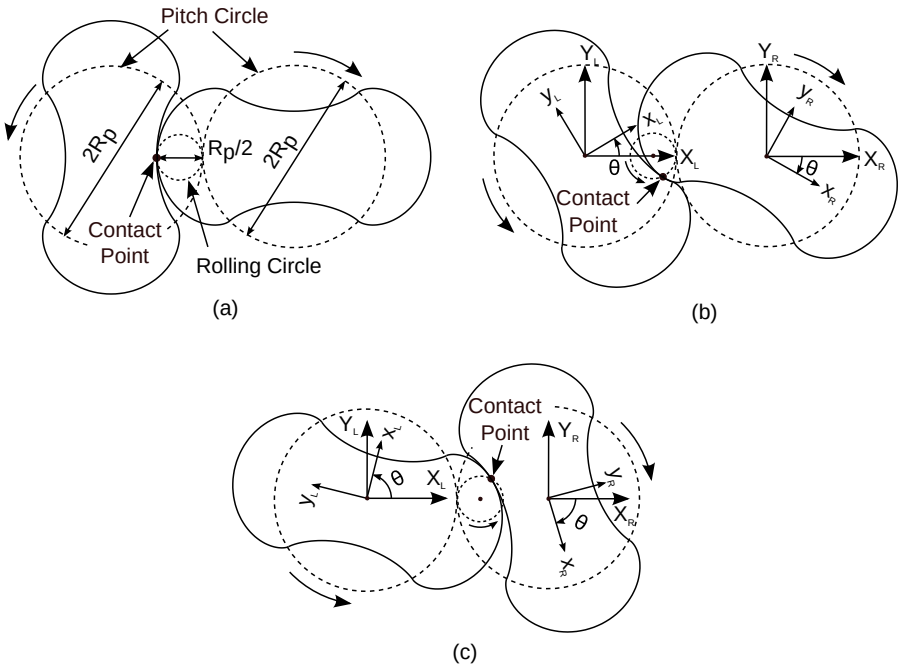

Figure A1.1: Intermeshed Cycloidal Bi-Lobe Rotors.

With the centers of all circles fixed, as θ increases, the rolling circle rolls over the pitch circles without slip. The contact point (solid dot in Fig. A1.1) between the rotors is

represented by a rotating point affixed to the circumference of the rolling circle; that point moves as the rolling circle rolls over the pitch circles. The rotor profiles are formed based on the relative motions of the contact point with respect to the body fixed frames attached to each pitch circle.

Figure A1.1 (b) illustrates how the rotor profiles are drawn for rotor angles $-45° \leq \theta \leq 45°$. The rotor angle θ is defined as the angle between the inertial axes X-Y and the body-fixed axes x-y, attached to the rotor. As θ increases from its initial value of 0 degree in Fig. A1.1 (a), the contact point between the rotors moves counter clockwise along the circumference of the rolling circle, as the circles roll over each other. The ensemble of contact points with respect to the body fixed frames of the left and right rotors forms the lower half of a hypocycloidal curve for the left rotor, and another lower half of an epicycloidal curve for the right rotor. The upper half curves are obtained with rotor angles $-45^{o} \leq \theta \leq 0^{o}$ using a similar procedure.

Figure A1.1 (c) shows the rotor positions for $\theta > 45°$. The epicycloid of the left rotor contacts the hypocycloid of the right rotor; which is a mirror image of Fig. A1.1 (a). The alternating symmetry seen in Figs. (a)-(c) for every θ increment of 90^{o} locates the trajectory of the contact point, which forms the overall profile of the rotors.

A1.2 INSTANTANEOUS MIXING

Instantaneous mixing is assumed to be a closed process without heat transfer, with mixing gasses of same kind, but chemically inert. Applying conservation of energy during a transition, the initial temperature of an exhaust cycle is

$$T_e\big|_{initial} = \left.\frac{m_c u_c + m_e u_e}{c_v\left(m_c + m_e\right)}\right|_{final} = \left.\frac{m_c T_c + m_e T_e}{m_c + m_e}\right|_{final}, \qquad \text{(A1.1)}$$

where subscripts '*initial*' and '*final*' represent the beginning and end of a cycle, and subscripts *c* and *e* denote carry-over volume and composite exhaust chamber.

Via the ideal gas law $PV=mRT$, the initial temperature becomes

$$T_e\big|_{initial} = \left.\frac{P_c V_c + P_e V_e}{P_c V_c / T_c + P_e V_e / T_e}\right|_{final} . \qquad \text{(A1.2)}$$

At the end of a cycle the carry-over volume has pressure and temperature same as the intake chamber:

$$P_c\big|_{final} = P_i\big|_{final} ,$$

$$T_c\big|_{final} = T_i\big|_{final} .$$

The carry-over volume maximizes at the end of a cycle. Equating $CV_{e,min}$ to $CV_{i,min}$, the maximum carry-over volume becomes the difference between the intake volume and the exhaust volume at the final time:

$$V_c\big|_{final} = V_i\big|_{final} - V_e\big|_{final} .$$

Therefore, for reverse-symmetric intake and exhaust chambers, the initial exhaust temperature of Eq. (A1.2) becomes

$$T_e\big|_{initial} = \left.\frac{P_i\left(V_i - V_e\right) + P_e V_e}{P_i\left(V_i - V_e\right)/T_i + P_e V_e / T_e}\right|_{final} . \qquad \text{(A1.3)}$$

The volumetric density of molecules in the composite exhaust chamber at the onset of a new cycle is

$$n_{v,e}\big|_{initial} = \left.\frac{N_e}{V_e}\right|_{initial} = \left.\frac{N_c + N_e}{V_c + V_e}\right|_{final} = \left.\frac{n_{v,c} V_c + n_{v,e} V_e}{V_c + V_e}\right|_{final} , \qquad \text{(A1.4)}$$

where N and n_v denote molecular number and volumetric molecular density, and subscripts c and e represent carry-over volume and exhaust chamber.

Replacing intake and exhaust pressures in Eq. (A1.3) with the Boltzmann expression $P = n_v k_B T$ and canceling Boltzmann's constant k_B in the numerator and denominator gives the initial temperature in terms of the volumetric densities:

$$T_e\big|_{initial} = \left.\frac{n_{v,c}V_cT_c + n_{v,e}V_eT_e}{n_{v,c}V_c + n_{v,e}V_e}\right|_{final} . \tag{A1.5}$$

Substituting Eqs. (A1.4) and (A1.5) for n_v and T in the Boltzmann expression and manipulating the terms renders the initial pressure:

$$\begin{aligned} P_{e1,initial} &= k_B\left(n_{v,e}T_e\right)\big|_{initial} = k_B \left.\frac{n_{v,c}V_c + n_{v,e}V_e}{V_c + V_e}\right|_{final} \left.\frac{n_{v,c}V_cT_c + n_{v,e}V_eT_e}{n_{v,c}V_c + n_{v,e}V_e}\right|_{final} \\ &= \left.\frac{P_cV_c + P_eV_e}{V_c + V_e}\right|_{final} \end{aligned} . \tag{A1.6}$$

For reverse-symmetric pumping chambers, substituting the properties of the carry-over volume into the prior expression yields

$$P_{e1,initial} = \left.\frac{P_i\left(V_i - V_e\right) + P_eV_e}{\left(V_i - V_e\right) + V_e}\right|_{final} = \left.\frac{P_i\left(V_i - V_e\right) + P_eV_e}{V_i}\right|_{final} . \tag{A1.7}$$

The initial volume of the composite exhaust chamber is the sum of the carry-over volume and the exhaust chamber volume at the final time,

$$V_e\big|_{initial} = V_c\big|_{final} + V_e\big|_{final} = \left(V_i\big|_{final} - V_e\big|_{final}\right) + V_e\big|_{final} = V_i\big|_{final} . \tag{A1.8}$$

Similarly, the initial volume of the composite intake volume simplifies to

$$V_i\big|_{initial} = V_i\big|_{final} - V_c\big|_{final} = V_i\big|_{final} - \left(V_i\big|_{final} - V_e\big|_{final}\right) = V_e\big|_{final} . \tag{A1.9}$$

Based on the above discussion, the pressure and temperature of the intake chamber remain the same after separation of the carry-over volume:

$$P_i\big|_{initial} = P_i\big|_{final} \ , \tag{A1.10}$$

$$T_i\big|_{initial} = T_i\big|_{final} \ . \tag{A1.11}$$

A1.3 AREAS UNDER CYCLOIDAL CURVES

Figure A1.2 shows the tracing points p_e and p_h of an epicycloidal curve in (a) and of a hypocycloidal curve in (b) in polar coordinates. In Figs. A1.2 (a) and (b), the rolling circles orbit around and within the pitch circles. The X-Y coordinates of a tracing point depend on the angles θ_e and θ_h from the X_o axis to the centerline of circles, which equal the rotor angle. Here θ_{pe} and θ_{ph} represent the angle to each tracing point with respect to the X_o axis. For multi-lobe rotors, the angle θ_{if} between the initial tracing point p_i and the final tracing point p_f becomes π/N_{lobe}, where N_{lobe} is the number of lobes of a rotor. Here θ_{if} is equal to 90 degrees.

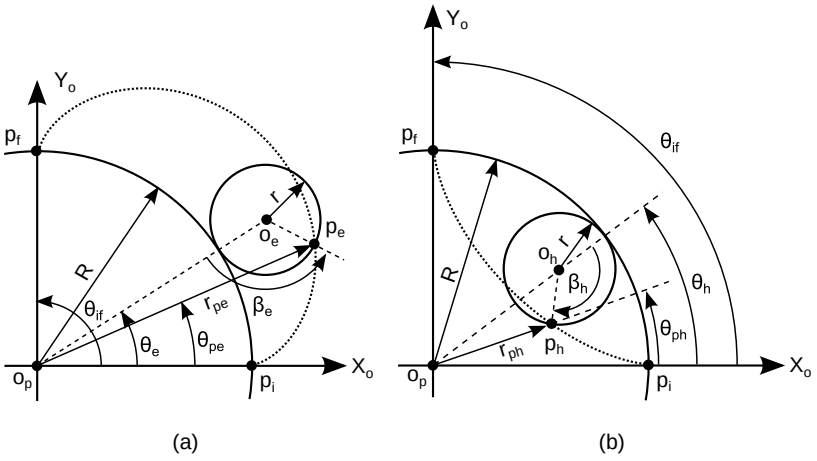

Figure A1.2: Cycloidal Curves in the Polar Coordinates for Bi-Lobe Rotors ($R = R_p$, $r = R_p/2$).

The $r-\theta$ coordinates of the tracing points in terms of the centerline angles θ_e and θ_h render the $r-\theta$ coordinates of the cycloidal curves for a bi-lobe rotor as:

$$r_{pe} = r_{pe}\left(R_p, \theta_e\right) = R_p\sqrt{\frac{13 - 5\cos(4\theta_e)}{8}} = R_p\sqrt{1+\frac{5\sin^2(2\theta_e)}{4}} \quad , \tag{A1.12}$$

$$\theta_{pe} = \theta_{pe}\left(\theta_e\right) = \tan^{-1}\left(\frac{\sin(5\theta_e) - 5\sin(\theta_e)}{\cos(5\theta_e) - 5\cos(\theta_e)}\right) , \tag{A1.13}$$

$$r_{ph} = r_{ph}\left(R, \theta_h\right) = R_p\sqrt{\frac{5 + 3\cos(4\theta_h)}{8}} = R_p\sqrt{1-\frac{5\sin^2(2\theta_e)}{4}} , \tag{A1.14}$$

$$\theta_{ph} = -\tan^{-1}\left(\frac{\sin(3\theta_h) - 3\sin\theta_h}{4\cos^3\theta_h}\right) . \tag{A1.15}$$

The area enclosed by $\overline{o_p p_i}$, $\overline{o_p p_f}$ and an epicycloidal curve is

$$A_{epi\_2lobes} = \int_0^{\pi/2} \frac{1}{2} r_{pe}^2 \left(\frac{d\theta_{pe}}{d\theta_e}\right) d\theta_e = \frac{15\pi}{32} R_p^2 . \tag{A1.16}$$

Similarly, the area surrounded by $\overline{o_p p_i}$, $\overline{o_p p_f}$ and a hypocycloidal curve is

$$A_{hypo\_2lobes} = \int_0^{\pi/2} \frac{1}{2} r_{ph}^2 \left(\frac{d\theta_{ph}}{d\theta_h}\right) d\theta_h = \frac{3\pi}{32} R_p^2 . \tag{A1.17}$$

Therefore, the area of a cycloidal bi-lobe rotor is

$$A_{rotor\_2lobes} = 2\left(A_{epi\_2lobe} + A_{hypo\_2lobe}\right) = \frac{9\pi}{8} R_p^2 . \tag{A1.18}$$

The above calculations can be easily extended for a rotor with N lobes. The results are

$$r_{pe} = R_p\sqrt{1+\frac{\left(1+2N_{lobe}\right)\sin^2\left(N_{lobe}\theta_e\right)}{N_{lobe}^2}} \quad , \tag{A1.19}$$

$$\theta_{pe} = \tan^{-1}\left(\frac{\sin(\theta_e + 2N_{lobe}\theta_e) - (1+2N_{lobe})\sin\theta_e}{\cos(\theta_e + 2N_{lobe}\theta_e) - (1+2N_{lobe})\cos\theta_e}\right), \tag{A1.20}$$

$$r_{ph} = R_p\sqrt{1 - \frac{(1+2N_{lobe})\sin^2(N_{lobe}\theta_h)}{N_{lobe}^2}}, \tag{A1.21}$$

$$\theta_{ph} = -\tan^{-1}\left(\frac{\sin(2N_{lobe}\theta_h - \theta_h) + (1-2N_{lobe})\sin\theta_h}{\cos(2N_{lobe}\theta_h - \theta_h) - (1-2N_{lobe})\cos\theta_h}\right). \tag{A1.22}$$

For base area per lobe, the integral's limits 0 to $\theta_{if} = \pi/N_{lobes}$ yields

$$A_{epi\_N\,lobes} = \int_0^{\pi/N_{lobes}} \frac{1}{2} r_{pe}^2 \left(\frac{d\theta_{pe}}{d\theta_e}\right) d\theta_e = \frac{\pi(2N_{lobe} + 1)(N_{lobe} + 1)}{4N_{lobes}^3} R_p^2 \tag{A1.23}$$

$$A_{hypo\_N\,lobes} = \int_0^{\pi/N_{lobes}} \frac{1}{2} r_{ph}^2 \left(\frac{d\theta_{ph}}{d\theta_h}\right) d\theta_h = \frac{\pi(2N_{lobe} - 1)(N_{lobe} - 1)}{4N_{lobes}^3} R_p^2. \tag{A1.24}$$

A1.4 NUMERICAL METHOD FOR BASE AREA CALCULATION

Numerical estimation of base area is illustrated in Figure A1.3. Four geometric profile arrays, the left and right half-circles c_L and c_R for a stator, and the left and right rotor profiles r_L and r_R, contain vectors of coordinates with respect to the inertial X-Y frame. An array has a starting vector and an ending vector. The starting vector of the left half-circle gives point $p_{i,cL}$ and the ending vector gives point $p_{f,cL}$. A dotted arrow indicates direction of increasing vector indices. The starting vector of a rotor profile is the same as the ending vector, but the same dotted arrow shows the direction of increasing indices on the array. For a left rotor, the starting and ending point is marked as $p_{if,rL}$. The next step finds contact points C_1, C_2 and C_3 by evaluating the minimum distance from a point on a curve to another curve, and seeking the minimum of the minimum distance array. This will produce indices of a contact point on two curve arrays. The remaining task crops the base arrays based on the contact indices and concatenates the array patches

in increasing index order, to insure continuity of the entire boundary of a base area. For example, the boundary of the intake base area can be concatenated as

$$B_{intake} = \overline{p_{if,rL}c_1} + \overline{c_1 p_{f,cL}} + \overline{p_{f,cL}p_{i,cL}} + \overline{p_{i,cR}c_3} + \overline{c_3 p_{if,rR}} + \overline{p_{if,rR}c_2} + \overline{c_2 p_{if,rL}}$$

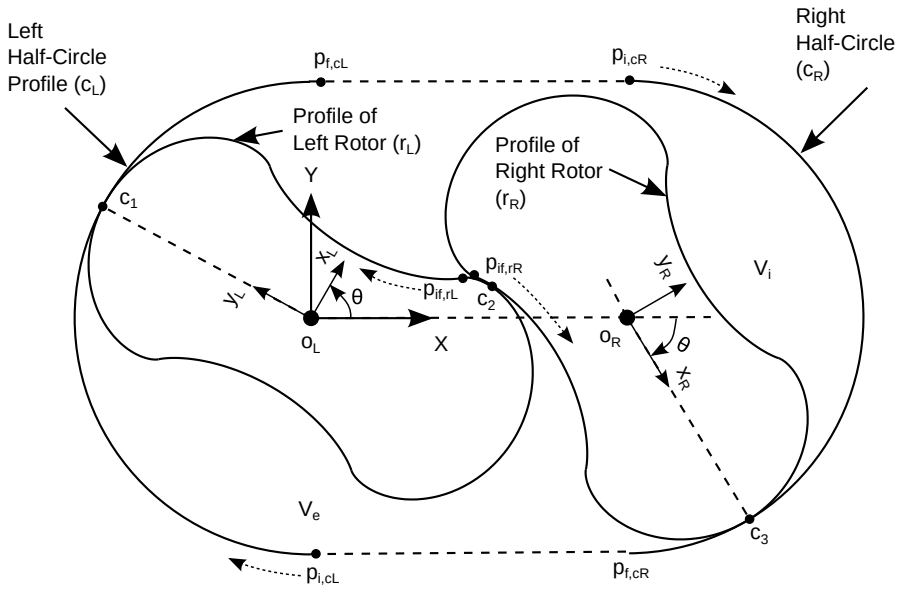

Figure A1.3: Numerical Approach to Calculate Base Areas.

Once a closed boundary is obtained, a numerical scheme can obtain the area enclosed. Matlab's *polyarea* function does such a task. The above process repeats with the new positions of the left and right rotors. Finally, data of base area versus rotor angle is obtained. The boundary length can be saved at each rotor angle, which can allow calculating the side area of a pumping chamber.

A1.5 REYNOLDS EQUATION FOR INTERNAL LEAKAGES OF ROOTS BLOWER

Internal leakage of a Roots blower resembles the thin film flow of a gas journal bearing. This section reviews relevant theories of journal bearings, and obtains the governing equation for leakage suitable for numerical simulations. Thin film flow of a journal bearing with two sliding plates having lubricant in between (see Fig. A1.4) is governed by Reynolds equation [39]:

$$\frac{\partial}{\partial x}\left(\xi\frac{\rho h^3}{12\eta}\frac{\partial P}{\partial x}\right)+\frac{\partial}{\partial z}\left(\frac{\rho h^3}{12\eta}\frac{\partial P}{\partial z}\right)=\frac{\partial(\rho h)}{\partial t}+\frac{\partial}{\partial x}\left(\rho h\frac{u_T+u_B}{2}\right)+\frac{\partial}{\partial z}\left(\rho h\frac{w_T+w_B}{2}\right) \quad \text{(A1.25)}$$

Here the gas rarefication correction factor [40,41] $\xi(Kn,\sigma_{1t})=\left(1-6\frac{2-\sigma_{1t}}{\sigma_{1t}}f_r(Kn)\right)$, σ_{1t} is the tangential momentum accommodation coefficient (TMAC) for one plate, and $f_r(Kn)$ is the gas rarefication function of Knudsen number.

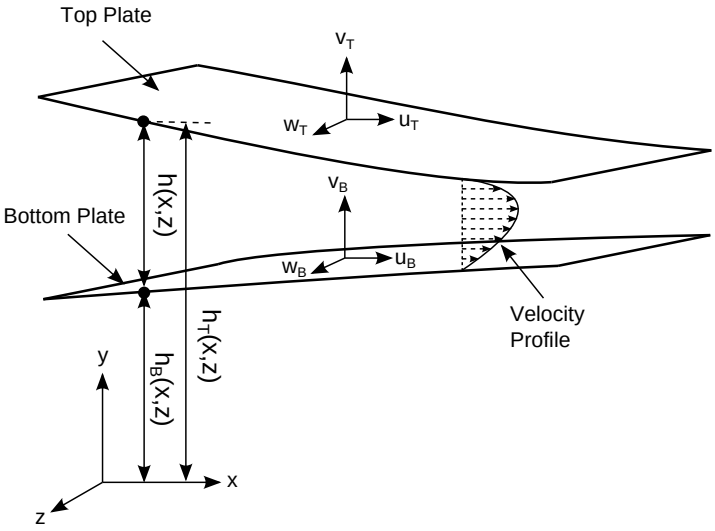

Figure A1.4: Two Sliding Plate Model for the Thin Film Flow.

Journal bearing formulations align the z axis with bearing length, and the y axis with radial direction. The origin of the z axis is typically set at the mid-point of the bearing length. The origin of the x and y axes is placed either at the top of a bearing stator or at the thickest film along the stator, which is offset by an altitude angle. The thin film thickness allows neglect of curvature in the x direction. As a result, tangential position $x \approx R\Theta$ and upper plate tangential speed $u_T \approx R\Omega$ becomes fluid tangential boundary velocity. Other boundary speeds $u_B = w_T = w_B = 0$. Stator radius can be interchanged with rotor radius because of the thin film assumption. The Reynolds equation in the $\theta - y - z$ coordinate system is

$$\frac{\partial}{R^2 \partial\theta}\left(\xi \frac{\rho h^3}{12\eta}\frac{\partial P}{\partial\theta}\right) + \frac{\partial}{\partial z}\left(\frac{\rho h^3}{12\eta}\frac{\partial P}{\partial z}\right) = \frac{\partial(\rho h)}{\partial t} + \frac{\Omega}{2}\frac{\partial}{\partial\theta}(\rho h) \,. \tag{A1.27}$$

The above simplification can be problematic for lobe rotors. The surface speed of a lobe rotor varies along the rotor profile, and has tangential and radial components because normal vectors on the lobe surface usually do not intersect with the center of a rotor.

To approximate the surface speed, the rotor is assumed stationary, while the stator rotates in the opposite direction of the rotor. This assumption will overestimate the surface speed, since the stator has larger radius than the rotor. The error will become progressively worse as a point on the rotating rotor moves away from the point of thinnest clearance between stator and rotor, and the difference in surface speeds increases. However, low compressibility in the affected region will negate the error. Thus solution accuracy does not suffer much due to the speed error.

To modify the Reynolds equation for gas journal bearings, the density variable is replaced with pressure using the ideal gas law, and a quasi-steady state is assumed, allowing the squeeze film term to be neglected. Therefore, the slip modified Reynolds equation for a gas bearing under quasi-steady state operation is

$$\frac{\partial}{R^2\partial\theta}\left(\frac{Ph^3}{12\eta T}\frac{\partial P}{\partial\theta}\xi\left(Kn,\sigma_{1t}\right)\right)+\frac{\partial}{\partial z}\left(\frac{Ph^3}{12\eta T}\frac{\partial P}{\partial z}\right)=\frac{\Omega}{2}\frac{\partial}{\partial\theta}\left(\frac{Ph}{T}\right). \tag{A1.28}$$

To convert to dimensionless form, define dimensionless parameters

$\bar{z}=z/(L/2)$, $\overline{P}=P/P_o$, $\overline{h}=h/c$, $\overline{\eta}=\eta/\eta_o$, and $\overline{T}=T/T_o$,

where L is bearing length, P_o is reference pressure, c is nominal radial clearance, η_o is a reference viscosity, and T_o is a reference temperature. The dimensionless Reynolds equation for gas journal bearings becomes

$$\frac{\partial}{\partial\theta}\left(\frac{\overline{P}\overline{h}^3}{\overline{\eta}\,\overline{T}}\frac{\partial\overline{P}}{\partial\theta}\xi\left(Kn,\sigma_{1t}\right)\right)+\left(\frac{4R^2}{L^2}\right)\frac{\partial}{\partial\bar{z}}\left(\frac{\overline{P}\overline{h}^3}{\overline{\eta}\,\overline{T}}\frac{\partial\overline{P}}{\partial\bar{z}}\right)=\Lambda\frac{\partial}{\partial\theta}\left(\frac{\overline{P}\overline{h}}{\overline{T}}\right), \tag{A1.29}$$

where compressibility number or the bearing number $\Lambda=\frac{6\eta_o\Omega}{P_o}\left(\frac{R^2}{c^2}\right)$ represents the relative importance of Couette flow, if the dimensionless parameters are scaled properly. For journal bearings, such scaling is possible because of the uniform film thickness and the unvarying operation under the atmospheric pressure. However, that is not the case for the lobe rotor. For example, the dimensionless radial clearance for a bi-lobe rotor changes along the lobe profile from around 1000 at the thinnest to 1 at the thickest point. Moreover, the operating pressure of the Roots blower also varies much from atmospheric pressure to low vacuum.

Since the pumping chamber acts as a pressure buffer, radial and the flank leakages do not interact and each leakage can be treated as an independent *1-D* flow. For lobe rotors, out of plane flow is small, and leakage involving the *z* direction can be neglected. Also, isothermal flow can be assumed, and temperature and viscosity treated as constants. Finally, the dimensionless Reynolds equation for flank leakage reduces to

$$\frac{\partial}{\partial\theta}\left(\xi\,\overline{P}\overline{h}^{3}\frac{\partial\overline{P}}{\partial\theta}\right)=\overline{\eta}\Lambda\frac{\partial}{\partial\theta}\left(\overline{P}\overline{h}\right). \tag{A1.30}$$

Solving the *1-D* Reynolds equation for pressure requires integrating Eq. (A1.30) twice with respect to θ. After the first integration, the pressure gradient is proportional to $\overline{h}^{-2}$, and thus the pressure involves finding integrals of $\overline{h}^{-2}$, where $\overline{h}=\overline{Cr}(\cdot)$. Integrals of complicated functions $\overline{C}_r(\cdot)$, i.e.,

$$\int\left[\overline{C}_r\left(\theta_{pe}\right)\right]^{-n}d\theta_{pe} \text{ and } \int\left[\overline{C}_r\left(\theta_{ph}\right)\right]^{-n}d\theta_{ph} \tag{A1.31, A1.32}$$

where $n=1,2,...$

$$\overline{C}_r\left(\theta_{pe}\right)=\frac{C_r\left(\theta_{pe}\right)}{C_{r0}}=1+\frac{3}{2}\frac{R_p}{C_{r0}}-\frac{R_p}{C_{r0}}\sqrt{\frac{13-5\cos\left(4\theta_e\right)}{8}} \text{ for } 0\le\theta_{pe}\le\pi/4 \tag{A1.33a}$$

$$\overline{C}_r\left(\theta_{ph}\right)=\frac{C_r\left(\theta_{ph}\right)}{C_{r0}}=1+\frac{3}{2}\frac{R_p}{C_{r0}}-\frac{R_p}{C_{r0}}\sqrt{\frac{5+3\cos\left(4\theta_h\right)}{8}} \text{ for } -\pi/4\le\theta_{pe}\le 0 \tag{A1.33b}$$

$$\theta_{pe}=\tan^{-1}\left(\frac{\sin\left(5\theta_e\right)-5\sin\left(\theta_e\right)}{\cos\left(5\theta_e\right)-5\cos\left(\theta_e\right)}\right) \text{ and } \theta_{ph}=\tan^{-1}\left(\frac{\sin\left(3\theta_h\right)-3\sin\left(\theta_h\right)}{4\cos^{3}\left(\theta_h\right)}\right)$$

are generally very difficult or intractable. Here $\overline{C}_r(\cdot)$ is the radial clearance between the stator and rotor profiles. Subscripts *h* and *e* stand for hypocycloid and epicycloid. See Fig. A1.2 in Appendix A1.3 for θ definitions and radial coordinate formulas.

No explicit formula for the integral exists because of the peculiar clearance function and nonlinear θ conversion. Even if the θ conversion is neglected, $\int C_r^{-n}(\theta_{pe})\,d\theta_e$ cannot produce an explicit solution. Thus the original clearance function requires a revision.

A2.1 ISSUES WITH ANALYTICAL VOLUME CALCULATION OF THE CLAW PUMP

Figure A2.1 illustrates calculation of exhaust base area as a baseline area minus three pie shaped sections. The baseline area is by line p_{BL}-p_{ARf}, the chord p_{ARf}-p_1, line p_1-o_R, line o_R-p_2, and the chord p_2-p_{BL}. The areas of the right rotor profile to be subtracted from the baseline area are three pie shaped sections enclosed by p_1-p_{ARi}-o_R, p_{ARi}-p_{BRf}-o_R respectively.

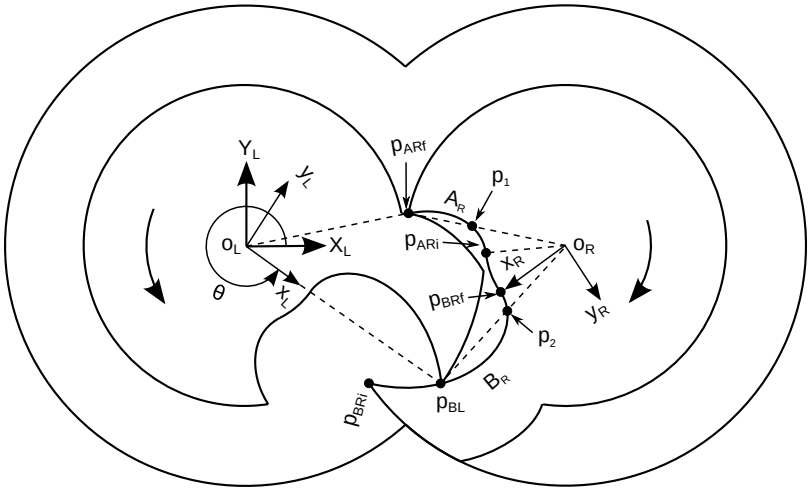

Figure A2.1: Illustrations of Exhaust Area Calculation at $-\theta_{c3} < \theta < -\theta_{c1}$.

The tracing points for the epitrochoidal curves are functions of rotor angle θ. For instance, finding the rotor angle at which p_2 coincides with the tracing point p_{BL} requires solving

$$\theta_{BR} = \tan^{-1}\frac{2r_{ps}\sin\theta_2 - \sin(2\theta_2)}{2r_{ps}\cos\theta_2 - \cos(2\theta_2)} = \tan^{-1}\frac{2r_{ps}\sin\theta - \sin(2\theta)}{2r_{ps}\cos\theta - \cos(2\theta)} \tag{A2.1}$$

for θ_2, which relates rotor angle to p_2.

Here θ_{BR} is the angle to p_{BL} with respect to the x_R-y_R frame, θ is the current rotor angle, and $r_{ps} = R_p / R_s$. Once θ_2 has been obtained, the pie section defined by p_2-p_{BRf}-o_R can be calculated using

$$A_{BR}(\theta) = \int_{\theta_2}^{0} \frac{1}{2} r_{BR}^2 \frac{d\theta_{BR}}{d\theta} d\theta \ , \tag{A2.2}$$

where $r_{BR} = R_s \sqrt{4r_{ps}^2 + 1 - 4r_{ps}\cos\theta}$ and $\frac{d\theta_{BR}}{d\theta} = \frac{4r_{ps}^2 - 6r_{ps}\cos\theta + 2}{\left(2r_{ps}\cos\theta - \cos(2\theta)\right)^2}$.

The main issue is that finding θ_2 in terms of the current rotor angle θ requires solving a nonlinear equation. Since no exact solution exists, a numerical scheme must be employed.

A2.2 DIMENSIONLESS CURVES OF THE CLAW ROTOR PROFILE

Dimensionless parameters are desirable to formulate the base area of the claw pump. The dimensionless form of the claw rotor profile can be defined:

$$\overline{A}_R = \frac{A_R}{R_s} = \begin{bmatrix} 2r_{ps}\cos\theta - \cos(2\theta + \theta_{c1}) \\ 2r_{ps}\sin\theta - \sin(2\theta + \theta_{c1}) \end{bmatrix} \quad for \ -\theta_{c1} \le \theta \le 0 \, , \tag{A2.3}$$

$$\overline{B}_R = \frac{B_R}{R_s} = \begin{bmatrix} 2r_{ps}\cos\theta - \cos(2\theta) \\ 2r_{ps}\sin\theta - \sin(2\theta) \end{bmatrix} \quad for \ -\theta_{c3} \le \theta \le 0 \, , \tag{A2.4}$$

$$\overline{CT}_R = \frac{CT_R}{R_s} = \begin{bmatrix} (2r_{ps} - 1)\cos\theta \\ (2r_{ps} - 1)\sin\theta \end{bmatrix} \ for \ -\theta_{c1} \le \theta \le 0 \, , \tag{A2.5}$$

$$\overline{C}_R = \frac{C_R}{R_s} = \begin{bmatrix} \cos\theta \\ \sin\theta \end{bmatrix} \ for \ 0 \le \theta \le \theta_{c1} \, , \tag{A2.6}$$

$$\overline{D}_R = \frac{D_R}{R_s} = \begin{bmatrix} 2r_{ps}\cos(\theta) - r_{ps}\cos(2\theta - \theta_{c2}) \\ 2r_{ps}\sin(\theta) - r_{ps}\sin(2\theta - \theta_{c2}) \end{bmatrix} for \, 0 \le \theta \le \theta_{c2} \, , \tag{A2.7}$$

$$\overline{E}_R = \frac{E_R}{R_s} = \begin{bmatrix} r_{ps}\cos\theta \\ r_{ps}\sin\theta \end{bmatrix} \ for\ \theta_{c2} \le \theta \le 2\pi - \theta_{c2}\,, \tag{A2.8}$$

where $r_{ps} = R_p / R_s$, $\theta_{c1} = \cos^{-1}\left(\dfrac{3r_{ps}^2 + 1}{4r_{ps}}\right)$, $\theta_{c2} = \cos^{-1}\left(\dfrac{5r_{ps}^2 - 1}{4r_{ps}^2}\right)$ and $\theta_{c3} = \cos^{-1}\left(r_{ps}\right)$.

The dimensionless stator profile can be defined:

$$\overline{F}_R = \frac{F_R}{R_s} = \begin{bmatrix} \cos\theta \\ \sin\theta \end{bmatrix} \ for\ \theta_{c3} \le \theta \le 2\pi - \theta_{c3}\,. \tag{A2.9}$$

A3.1 NONLINEAR ALGEBRAIC PIPE MODEL VIA NEWTON'S METHOD

The main suction and exhaust pipes consist of long pipes, fittings and assorted parts in series. The throughput of a main suction pipe states

$$Q_{sp} = C_{sp}\left(P_c - P_{i1}\right) \tag{A3.1}$$

$$C_{sp} = \left[\sum_{i=1}^{k-1}\left(C\right)_i^{-1}\right]^{-1} \ for\ P_c \ne P_{i1} \tag{A3.2}$$

where C_{SP} is the total pipe conductance, and $\left(C\right)_i$ is the conductance of the ith section, counting from the chamber side. The pressure decrease across the ith pipe section is

$$\Delta P_i = \frac{Q_{sp}}{\left(C\right)_i} \ for\ i = 1\ to\ k-1\,. \tag{A3.3}$$

The upstream and downstream nodal pressures of the i^{th} pipe section are

$$\begin{cases} \left(P_1\right)_i = P_c + \sum_{m=1}^{i}\Delta P_m - \Delta P_i \\ \left(P_2\right)_i = P_c + \sum_{m=1}^{i}\Delta P_m \end{cases} \quad for\ i = 1\ to\ k-1\,, \tag{A3.4}$$

where ΔP_m and ΔP_i are intermediate and i^{th} pressure drops, and the mean pressure is

$$\overline{P}_i = P_c + \sum_{m=1}^{i} \Delta P_m - \frac{\Delta P_i}{2}. \tag{A3.5}$$

For consistency with other conductance formulas in Chapter 2, the intrinsic conductance formula requires revision. The i^{th} molecular conductance is

$$\left(C_{OP,molecular}\right)_i = \frac{P_{tr,intrinsic} \cdot A_c}{4} \sqrt{\frac{8RT_c}{\pi}} \frac{\left(P_1\right)_i}{\Delta P_i} \quad for\ \Delta P_i \neq 0. \tag{A3.6}$$

The Knudsen number of a source flow defined with mean pressure is

$$\left(Kn_c\right)_i = \frac{\pi}{4} \frac{\eta_c}{D} \sqrt{\frac{8RT_c}{\pi}} \frac{1}{\left(\overline{P}_i\right)} \tag{A3.7}$$

where T_c is chamber temperature, and η_c is viscosity. The dimensionless connecting parameter for the i^{th} element is

$$\left(Z_c\right)_i = \left[1 + \sqrt{\frac{\pi}{2}} \frac{1}{\left(Kn_c\right)_i}\right] \left[1 + \frac{21}{17} \sqrt{\frac{\pi}{2}} \frac{1}{\left(Kn_c\right)_i}\right]^{-1}. \tag{A3.8}$$

Calculations of throughput and nodal pressures require solving a set of nonlinear equations

$$F(X) = \left[f_1(X), \ldots, f_k(X)\right]^T = \mathbf{0} \tag{A3.9}$$

where $X = \left[\Delta P_1, \ldots, \Delta P_{k-1}, Q_{sp}\right]^T$,

$$f_i(X) = \begin{cases} C_i\left(\Delta P_1, \ldots, \Delta P_i\right) \cdot \Delta P_i - Q_{sp} & for\ i = 1\ to\ k-1 \\ \sum_{j=1}^{k-1} \Delta P_j - \left(P_c - P_{i1}\right) & for\ i = k \end{cases},$$

and P_c and P_{i1} are boundary pressures at the previous time step. The solution is found using Newton's method

$$X_{p+1} = X_p - \left[\frac{\partial F}{\partial x_j}\right]^{-1}_{X_p} F\left(X_p\right) \quad for \;\; p = 0,1,.... \tag{A3.10}$$

where subscript p is the iteration index.

Initial conditions at startup are set arbitrarily; the previous estimate X_p becomes the initial conditions for the next iteration

$$X_{p+1} = \begin{cases} \left[\Delta P_1\big|_0,...,\Delta P_{k-1}\big|_0, Q_{sp}\big|_0\right]^T & for \;\; p = 0 \\ X_p & otherwise \end{cases} \tag{A3.11}$$

$$\text{where } \Delta P_i\big|_0 = \left(\frac{P_c - P_{i1}}{k-1}\right)\Bigg|_{previous\ time\ step} \quad for\ i = 1\ to\ k-1, \tag{A3.12}$$

$$Q_{sp}\big|_0 = C_{sp}\big|_0 \cdot \left(P_c - P_{i1}\right)\big|_{previous\ time\ step} \quad \text{and} \tag{A3.13}$$

$$C_{sp}\big|_0 = \left[\sum_{i=1}^{k-1}\left\{C_i\left(\Delta P_i\big|_0\right)\right\}^{-1}\right]^{-1} \quad . \tag{A3.14}$$

For computational efficiency, the matrix inversion lemma is used to invert the Jacobian matrix in the form

$$\left[\frac{\partial F}{\partial x_j}\right] = \begin{bmatrix} A & B \\ C & D \end{bmatrix} \tag{A3.15}$$

where A is a *k-1* by *k-1* lower triangular matrix. Column and row vectors $B = \left[-1, ..., -1\right]^T$ and $C = \left[1,...,1\right]$ have *k-1* elements, and scalar $D = 0$. The inversion of lower triangular matrix A can be performed efficiently, then the Jacobian matrix can be inverted using the matrix inversion lemma

$$\left[\frac{\partial F}{\partial x_j}\right]^{-1} = \begin{bmatrix} A^{-1} - A^{-1}\cdot B\cdot\left(C\cdot A^{-1}\cdot B\right)^{-1}\cdot C\cdot A^{-1} & A^{-1}\cdot B\cdot\left(C\cdot A^{-1}\cdot B\right)^{-1} \\ \left(C\cdot A^{-1}\cdot B\right)^{-1}\cdot C\cdot A^{-1} & -\left(C\cdot A^{-1}\cdot B\right)^{-1} \end{bmatrix} . \tag{A3.16}$$

The i^{th} row and j^{th} column element in matrix A is defined as

$$a_{ij} = \frac{\partial C_i(\Delta P_1,...,\Delta P_i)}{\partial \Delta P_j} = \frac{\partial (C_{viscous})_i}{\partial \Delta P_j} + \frac{\partial (C_{molecular})_i}{\partial \Delta P_j}(Z_c)_i + (C_{molecular})_i \frac{\partial (Z_c)_i}{\partial \Delta P_j}. \quad \text{(A3.17)}$$

In general, the conductance formulas are in the following form

$$\frac{\partial}{\partial \Delta P_j}\left[\beta \frac{(\overline{P}_i)^q}{(\Delta P_i)^r}\right] = \begin{cases} \beta \dfrac{(\overline{P}_i)^q}{(\Delta P_i)^r}\left(\dfrac{q}{\overline{P}_i}\right) \text{ for } j \neq i \text{ and } j < i \\ \beta \dfrac{(\overline{P}_i)^q}{(\Delta P_i)^r}\dfrac{(q\,\Delta P_i - 2r\overline{P}_i)}{2\overline{P}_i \Delta P_i} \text{ for } j = i \end{cases} \quad \text{(A3.18)}$$

where β is a constant, and q and r are power exponents. The gradient of the conductance formulas in the viscous regime are:

A.) For laminar flow,

$$\frac{\partial (C_{LCP,viscous})_i}{\partial \Delta P_j} = \begin{cases} (C_{LCP,viscous})_i \left(\dfrac{1}{\overline{P}_i}\right) \text{ for } j \neq i \text{ and } j < i \\ (C_{LCP,viscous})_i \left(\dfrac{1}{2\overline{P}_i}\right) \text{ for } j = i \end{cases}. \quad \text{(A3.19)}$$

B.) For turbulent flow on a smooth surface,

$$\frac{\partial (C_{LCP,viscous})_i}{\partial \Delta P_j} = \begin{cases} (C_{LCP,viscous})_i \left(\dfrac{4}{7\overline{P}_i}\right) \text{ for } j \neq i \text{ and } j < i \\ (C_{LCP,viscous})_i \left(\dfrac{4\Delta P_i/7 - 6\overline{P}_i/7}{2\overline{P}_i \Delta P_i}\right) \text{ for } j = i \end{cases}. \quad \text{(A3.20)}$$

C.) For turbulent flow on a rough surface and a transition flow

$$\frac{\partial (C_{LCP,viscous})_i}{\partial \Delta P_j} = \begin{cases} (C_{LCP,viscous})_i \left(\dfrac{1}{(2+a)\overline{P}_i}\right) \text{ for } j \neq i \text{ and } j < i \\ (C_{LCP,viscous})_i \left(\dfrac{\Delta P_i/(2+a) - 2(1+a)\overline{P}_i/(2+a)}{2\overline{P}_i \Delta P_i}\right) \text{ for } j = i \end{cases}. \quad \text{(A3.21)}$$

D.) For minor loss elements,

$$\frac{\partial\left(C_{OP,viscous}\right)_i}{\partial\Delta P_j}=\begin{cases}\left(C_{OP,viscous}\right)_i\left(\dfrac{1}{2\overline{P}_i}\right) \; for \;\; j\neq i \;\; and \;\; j<i \\ \left(C_{OP,viscous}\right)_i\left(\dfrac{\Delta P_i/2-\overline{P}_i}{2\overline{P}_i\Delta P_i}\right) \; for \;\; j=i\end{cases} . \tag{A3.22}$$

The gradient of the molecular conductance are:

A.) For a long pipe,

$$\frac{\partial\left(C_{LP,molecular}\right)_i}{\partial\Delta P_j}=0 \; . \tag{A3.23}$$

B.) For other pipes,

$$\frac{\partial\left(C_{OP,molecular}\right)_i}{\partial\Delta P_j}=\begin{cases}\dfrac{P_{tr,intrinsic}\cdot A_c}{4}\sqrt{\dfrac{8RT_c}{\pi}}\left(\dfrac{1}{\Delta P_i}\right) \; for \;\; j\neq i \; and \;\; j<i \\ \dfrac{P_{tr,intrinsic}\cdot A_c}{4}\sqrt{\dfrac{8RT_c}{\pi}}\left(P_1\right)_i\left(\dfrac{-1}{\Delta P_i^{\,2}}\right) \;\; for \;\; j=i\end{cases} . \tag{A3.24}$$

The gradient of the dimensionless connecting parameter can be obtained by

$$\frac{\partial\left(Z_c\right)_i}{\partial\Delta P_j}=\frac{\partial\left(Z_c\right)_i}{\partial\left(Kn_c\right)_i}\frac{\partial\left(Kn_c\right)_i}{\partial\Delta P_j} \tag{A3.25}$$

where $\dfrac{\partial\left(Z_c\right)_i}{\partial\left(Kn_c\right)_i}=\left(\dfrac{21}{17}\sqrt{\dfrac{\pi}{2}}-\sqrt{\dfrac{\pi}{2}}\right)\left(\dfrac{21}{17}\sqrt{\dfrac{\pi}{2}}+\left(Kn_c\right)_i\right)^{-2}$ and (A3.26)

$$\frac{\partial\left(Kn_c\right)_i}{\partial\Delta P_j}=\begin{cases}\left(Kn_c\right)_i\left(\dfrac{-1}{\overline{P}_i}\right) \;\; for \;\; j\neq i \;\; and \;\; j<i \\ \left(Kn_c\right)_i\left(\dfrac{-1}{2\overline{P}_i}\right) \;\; for \;\; j=i\end{cases} . \tag{A3.27}$$

Bibliography

[1] Kurita, S. and Blonigan, W. T., 2006, “Load Lock Chamber Having Two Dual Slot Regions,” U.S. Patent 7105463 B2.

[2] Yamagishi, T., 2003, "Semiconductor Manufacturing Device Having Buffer Mechanism and Method for Buffering Semiconductor Wafers," European Patent 1280187 A2.

[3] Pal. et al., 2012, “Vacuum Chambers with Shared Pump,” U.S. Patent 0222813 A1.

[4] Jousten, K., Ed., 2008, *Handbook of Vacuum Technology*, WILEY-VCH, Weinheim, Germany.

[5] Wycliffe, H., 1987, “Mechanical High-vacuum Pumps with an Oil-free Swept Volume,” Journal of Vacuum Science and Technology A, **5**(4), pp. 2608-2611.

[6] Konishi, S. and Yamasawa, K., 1999, “Diagnostic System to Determine the In-service Life of Dry Vacuum Pumps,” Science, Measurement and Technology, IEE Proc. **146**(6), pp. 270-276.

[7] Birch et al, 2007, “Seal Assemblies,” U.S. Patent 7214041 B2.

[8] BOC EDWARDS, 2005, *Instruction Manual: iH Dry Pumping Systems*, A533-50-880 Issue D, West Sussex, UK.

[9] Troup, A. P. and Turrell, D., 1989, “Dry Pumps Operating Under Harsh Conditions in the Semiconductor Industry,” Journal of Vacuum Science and Technology A, **7**(3), pp. 2381-2386.

[10] Lessard, P. A., 2000, “Dry Vacuum Pumps for Semiconductor Processes: Guidelines for Primary Pump Selection,” Journal of Vacuum Science and Technology A, **18**(4), pp. 1777-1781.

[11] Abreu, R. A., Troup, A. P. and Sahm, M. K., 1994, “Causes of Anomalous Solid Formation in the Exhaust Systems of Low-pressure Chemical Vapor Deposition and Plasma Enhanced Chemical Vapor Deposition Semiconductor Processes,” Journal of Vacuum Science and Technology B, **12**(4), pp. 2763-2767.

[12] Troup, A. P. and Dennis, N. T. M., 1991, “Six Years of “Dry Pumping”: A Review of Experience and Issues, Journal of Vacuum Science and Technology A, **9**(3), pp. 2048-2052.

[13] Bahnen, R.. and Kuhn, M., 1993, “Increased Reliability of Dry Pumps Due to Process Related Adaptation and Prefailure Warning,” Vacuum, **44**(5-7), pp. 709-712.

[14] Said, M. S. N., Benbouzid, M. E. H., Benchaib, A, 2000, "Detection of Broken Bars in Induction Motors Using an Extended Kalman Filter for Rotor Resistance Sensorless Estimation," IEEE Transactions on Energy Conversion, **15**(1), pp. 66-70.

[15] Li, P. Goodall, R. and Kadirkamanathan, V., 2004, "Estimation of Parameters in a Linear State Space Model using a Rao-Blackwellised Particle Filter," Proceedings of Control Theory and Applications, **151**(6), pp. 727-738.

[16] Verma, V., 2004, "Tractable Particle Filters for Robot Fault Diagnosis," Ph.D. Thesis, Carnegie Mellon University, PA.

[17] Ljung, L., 1999, *System Identification: Theory for Users*, Prentice Hall, Upper Saddle River, NJ.

[18] Chang, C. and Chen, J., 1995, "Implementation Issues Concerning the EKF-Based Fault Diagnosis Techniques," Chemical Engineering Science, **50**(18), pp. 2861-2882.

[19] Patton, R. J., Lopez-Toribio, C. J. and Uppal, F. J., 1998, "Artificial Intelligence Approaches to Fault Diagnosis," IEE Colloquium on Update on Developments in Intelligence Control, pp. 3/1-3/12.

[20] Isermann, R., 2006, *Fault-Diagnosis Systems*, Springer, Berlin, Germany.

[21] Twiddle, J. Spurgeon, S. K., Kitsos, C. and Jones, N. B., 2006, "A Discrete-Time Sliding Mode Observer for Estimation of Auto-Regressive Model Coefficients with an Application in Condition Monitoring, " Proceedings of the 2006 Inter Workshop on Variable Structure Systems, Alghero, Italy, pp. 127-132.

[22] Twiddle, J. A., Jones, N. B. and Spurgeon, S K, 2008, "Fuzzy Model-based Condition Monitoring of a Dry Vacuum Pump via Time and Frequency Analysis of the Exhaust Pressure Signal," Journal of Mechanical Engineering Science, **222**(2), pp. 287-293.

[23] Jiang, W. Spurgeon, S. K., Twiddle, J. A., Schlindwein, F. S., Feng, Y. Thanagasundram, S., 2007, "A Wavelet Cluster-Based Band-Pass Filtering and Envelope Demodulation Approach with Application To Fault Diagnosis In A Dry Vacuum Pump," Journal of Mechanical Engineering Science, **221**(11), pp. 1279-1286.

[24] Thanagasundram, S., Spurgeon, Schlindwein, F. S., 2008, "A Fault Detection Tool Using Analysis From an Autoregressive Model Pole Trajectory," Journal of Sound and Vibration, **317**(3-5), pp. 975–993.

[25] Floquet, T., Twiddle, J.A., Spurgeon, S. K., 2006, "Parameter Estimation via Second Order Sliding Modes with Application To Thermal Modelling in A High Speed Rotating Machine," Proceedings of the IEEE International Conference on Industrial Technology, pp. 2635-2639.

[26] Ioffe, I. V., Koss, V. A., Gray, M., and Livesey, R. G., 1995, "Modeling of a Multistage Claw Rotor Vacuum Pump," Journal of Vacuum Science and Technology A, **13**(3), pp. 536-539.

[27] Peng, X., Xing, Z., Li, L., and Shu, P., 2002, "Thermodynamic Analysis of the Rotary Tooth Compressor," Journal of Power and Energy, **216**(4), pp. 321-327.

[28] McCarthy, D. J., 1994, "Vibration-Based Diagnostics of Reciprocating Machinery," Ph.D. thesis, MIT, Boston MA.

[29] Galtry, M. A. and Turner, N., 2007, "A System Modelling Approach to Roots Claw Pump Performance Prediction," 51st IUVSTA Workshop on Modern Problems & Capability of Vacuum Gas Dynamics, Djurönäset, Värmdö, Sweden, July 9-12, 2007.

[30] Mcdougald, S. et al., 1974, "An Investigation of the Volumetric. Efficiency of a Roots Blower," International Compressor Engineering Conference at Purdue, West Lafayette, Paper 127.

[31] Ucer, S. and Celik, I., 1980, "Analysis of Flow Through Roots Blower Systems," International Compressor Engineering Conference. Paper 319.

[32] Tong, S.-H. and Yang, D. C. H., 2005, "Rotor Profiles Synthesis for Lobe Pumps with Given Flow Rate Functions, " Journal of Mechanical Design, **127**(2), pp. 287-294.

[33] Joshi, A. M., et al., 2006, "Clearance Analysis and Leakage Flow CFD Model of a Two-Lobe Multi-Recompression Heater," International Journal of Rotating Machinery, **2006**, Article ID 79084.

[34] Hsieh, C.-F. and Hwang, Y.-W., 2005, "Tooth Profile of a Roots Rotor with a Variable Trochoid Ratio," Mathematical and Computer Modelling, **48**(1-2), pp. 19–33.

[35] C-F Hsieh, 2009, "A Study Of The Geometric Design And Gas Port Of The Claw-Type Rotor," Journal of Mechanical Engineering Science, **223**(9), pp. 2063-2069.

[36] Roth, A., 1976, *Vacuum Technology*, North-Holland Pub. Co., NY.

[37] White, F. M., 1998, *Fluid Mechanics*, 4th ed., McGraw-Hill, NY.

[38] Mills, A. F., 1999, *Basic Heat and Mass Transfer*, Prentice Hall, Upper Saddle River, NJ.

[39] Khonsari, M. M. and Booser, E. R., 2008, *Applied Tribology, Bearing Design and Lubrication*, 2nd ed., John Wiley & Sons, West Sussex, England.

[40] Chen, C., 2005, *Rarefied Gas Dynamics Fundamentals, Simulations and Micro Flows*, Springer-Verlag, Berlin, Germany.

[41] Beskok, A., et al., 1996, "Rarefaction and Compressibility Effects in Gas Microflows," Journal of Fluid Engineering, **118**(3), pp. 448-456.

[42] Northey, A. J., 1932, "Rotary Internal Combustion Engine," U.S. Patent 2058817.

[43] Northey, A. J., 1934, "Rotary Compressor or Vacuum Pump," U.S. Patent 2097037.

[44] Shapipov, F., 2004, "Numerical Simulation of Rarefied Gas Flow Through a Thin Orifice," Journal of Fluid Mechanics, **518**, pp. 35-60.

[45] Ohbayashi, T., et al., 2001, "Study on the Performance Prediction of Screw Vacuum Pump", Applied Surface Science, **169-170**, pp. 768–771.

[46] Chen, Y., et al., 2002, "Mathematical Modeling of Scroll Compressors-Part I: Compression Process Modeling," International Journal of Refrigeration, **25**, pp.731-750.

[47] Ishii, N., et al., 2002, "Efficiency Simulations with Consideration of Heat Losses of a R410A Compact Scroll Compressor for Its Optimal Performance", Proceedings of International Compressor Engineering Conference, Purdue University, paper 1598.

[48] Incropera, F. P. and DeWitt, D. P., 2000, *Fundamentals of Heat and Mass Transfer*, 4th ed., Wiley, New York.

[49] Fitzgerald, A. E., et al., 2003, *Electric Machinery*, 6th ed., McGraw-Hill, New York.

[50] BOC EDWARDS, 1998, *Instruction Manual: Drystar GV80 Dry Vacuum Pumps*, A702-11-880 Issue H Original, West Sussex, UK.

[51] Ooi, K. T. and Zhu, J., 2004, "Convective Heat Transfer in a Scroll Compressor Chamber: a 2-D Simulation," International Journal of Thermal Science, **43**, pp. 677-688.

[52] Adair, R. P., et al., 1972, "Instantaneous Heat Transfer to the Cylinder Wall in Reciprocating Compressor", Proceedings of 1972 Purdue Compressor Technology Conference, Purdue University, pp. 521–526.

[53] Hindmarsh, A. C., et al., 2005, "SUNDIALS: Suite of Nonlinear and Differential / Algebraic Equation Solvers," ACM Transactions on Mathematical Software, **31**(3), pp. 363-396.

[54] Cohen, S. D. and Hindmarsh, A. C., 1996, "CVODE, A Stiff/Nonstiff ODE Solver in C," Computers in Physics, **10**(2), pp. 138-143.

[55] Boglietti, A., et al, 2003, "International Standards for the Induction Motor Efficiency Evaluation: a Critical Analysis of the Stray-Load Loss Determination," Proceedings of Industry Applications Conference, **2**, pp. 841-848.

[56] Petry-Johnson, T. T., et al, 2007, "Experimental Investigation of Spur Gear Efficiency," Proceedings ASME 2007 International Design Engineering Technical Conference & Computers and Information in Engineering Conference, Las Vegas, NV, DETC2007-35045.

[57] Mathas, C., 2013, "Temperature Sensors-The Basics," from http://www.digikey.com/us/en/techzone/sensors/resources/articles/temperature-sensors-the-basics.html

[58] NANMAC Corp., 2013, "Comparison of Temperature Sensors and Response Times," from http://www.nanmac.com/documents/sensor-response.pdf

[59] Ackland, K., 1998, "Selecting the Right Infrared Temperature Sensor," from http://www.isa.org/isaolp/journals/pdf/intech/980648.pdf

[60] OMEGA, 2013, "High Speed Industrial Fiber Optic Infrared Transmitter: OS4000 Series," from http://www.omega.com/Temperature/pdf/OS4000_Series.pdf

[61] PCB PIEZOTRONICS, 2013, "Model 112A05 Charge Output Pressure Sensor Installation and Operating Manual," from http://www.pcb.com/contentstore/docs/PCB_Corporate/Pressure/Products/Manuals/112A05.pdf

[62] Pulliam, W. J., et al., 2002, "High-temperature High-bandwidth Fiber Optic MEMS Pressure-sensor Technology for Turbine Engine Component Testing," Proc. SPIE, **4578**, pp. 229-238.

[63] Mercier, D. et al., 2011, "Saw-Pirani Vacuum Sensor with a New Functioning Mode and a Fast Response Time," Proceedings of 2011 16th International Solid-State Sensors, Actuators and Microsystems Conference (TRANSDUCERS), Beijing, China, pp. 902-905.

Vita

Jae-Won Choi was born in Busan, South Korea. He grew up in Busan and attended Busan High School. In 1996, he entered Korea University in Seoul and graduated with honor in February, 2003. He attended Texas A&M University at College Station from Sept. 2003 to August, 2006 to earn a M.S. degree. At TAMU, he studied fault diagnosis of a synchronous generator under the supervision of Prof. Alexander G. Parlos at the Department of Mechanical Engineering. He entered The University of Texas at Austin in September, 2006 to start a Ph.D. study. His Ph.D. research under the supervision of Prof. Michael D. Bryant involved the modeling and model based fault diagnosis of dry vacuum pumps in the semiconductor industry. During his Ph.D. study, he also taught several undergraduate and graduate lecture courses and labs in mechatronics, numerical method, dynamics, control, and digital signal processing. He earned his Ph.D. degree in December, 2013.

Permanent email: jaewon.choi.eng@gmail.com

This dissertation was typed by Jae-Won Choi.